Design, Characterization and On-sky Testing of an Integrated Optics Device for Stellar Interferometry: from Pupil Remappers to Discrete Beam Combiner

Dissertation
zur Erlangung des akademischen Grades
"doctor rerum naturalium"
(Dr. rer. nat.)
in der Wissenschaftsdisziplin Photonik

eingereicht an der
Mathematisch-Naturwissenschaftlichen Fakultät
Institut für Physik und Astronomie
der Universität Potsdam
und
das Leibniz-Institut für Astrophysik Potsdam (AIP)

Abani Shankar Nayak
Potsdam, den 17 Juni 2022

Betreuer:	Prof. Dr. Martin M. Roth
	Prof. Dr. Markus Gühr
1. Gutachter:	Prof. Dr. Martin M. Roth
	Leibniz-Institut für Astrophysik Potsdam
2. Gutachter:	Prof. Dr. Markus Gühr
	Institut für Physik und Astronomie, Universität Potsdam
3. Gutachter:	Priv. Doz. Dr. habil. Andreas Glindemann
	European Southern Observatory, Instrument System Group

Published online on the
Publication Server of the University of Potsdam:
https://doi.org/10.25932/publishup-55874
https://nbn-resolving.org/urn:nbn:de:kobv:517-opus4-558743

Declaration

I declare that this Thesis represents ideas in my own words, and I have adequately cited and referenced the sources whenever others' work is included. According to the University of Potsdam guidelines, I have adhered to all principles of academic honesty, good scientific conduct, and integrity. I have not misrepresented, fabricated, or falsified any idea/data/fact/source in my submission. I also declare that the work presented in this Thesis has not been submitted in parts or whole to any other Univesity or Institute for awarding any degree or diploma.

I understand that any violation of the above will cause disciplinary action against me by the University of Potsdam.

Abani Shankar Nayak
Potsdam, Germany

Dedicated to my parents, brother and beloved teachers

Acknowledgements

Before writing this Section, I would like to give a quote from Hellen Keller: *"Alone, we can do so little; together, we can do so much."* Hence, I am deeply grateful to all the following people who have led me to a successful PhD journey.

I would like to give my sincere thanks to my primary supervisor Prof. Dr. Martin Roth, for guiding me during the pitfalls as a doctoral student. I give my heartfelt thanks to my secondary supervisor Prof. Dr. Markus Gühr, for his indirect support in preparing me towards the completion of the doctoral journey. I am grateful to my current mentor Dr. Kalaga Madhav; his questions and discussions guided me mentally to stay aboard in this journey. It will be incomplete if I do not mention my former mentor, Dr. Stefano Minardi, as I would not have continued this doctoral journey in Germany without him.

During the initial years, I would like to express my profound thanks to Dr. Ettore Pedretti for growing my motivation on the subject, especially on stellar interferometry, and at the same time, in developing the experimental setup. I am very grateful to the scientific atmosphere of Leibniz Institute for Astrophysics Potsdam that helped me in carrying out my research work. The park Babelsberg adjacent to the Institute was a cool visiting place to develop my mental peace.

I extend my passionate gratitude to my collaborating partners: 1) University of Cologne, where I met Prof. Dr. Lucas Labadie, the discussions with him on the research work of this Thesis were really thought-provoking. I thank Dr. Tarun Sharma for carrying out the characterization works at the Telescope. I also cannot forget Dr. Jan Tepper and Thomas Poletti for generating the idea of a broad band response of a DBC. 2) Politecnico di Milano, where I contacted Prof. Dr. Roberto Osellame, who solved the annoying problem of OPD shifts in the experimental setup. It will be rude from my side if I do not mention Simone Piacentini and Dr. Giacomo Corrielli for fabricating the devices using their ULI facility. 3) Heriot-Watt University, where I came in contact with Prof. Robert Thomson for hosting me as a short-time visiting student to carry out some of the activities related to ULI. Once again, I mention Fraser Pike and Dr. Aurélien Benoît for helping me in learning the hands-on of ULI.

I would like to give honest thanks to my colleague Dr. Aline Dinkelaker for proofreading the manuscripts of the journal papers. She helped me in re-establishing the Michelson experimental setup. I also give warm thanks to Sebastian Smarzyk for automating the setup that helped me fast characterize one of the photonic devices.

To proofread the Thesis, I would extend my genuine thanks to Dr. Aline Dinkelaker, Dr. Ajay Singh, Dr. Kalaga Madhav and Brahmadutta Mahapatra. I give sincere thanks to my reviewers and my PhD examination committee members. Facing them would add more value

in disseminating my fundamental concepts of Physics.

I extend my profound gratitude to my AIP colleagues and friends that includes both former and current: Momen Diab, Daniel Bodenmüller, Andreas Stoll, Xijie Luo, Dr. John Davenport, Dr. Eloy Hernandez, Dr. Alan Günther, Dr. Aashia Rahman, Dr. Lu Gao, Dr. Elmar Schmälzlin, Dr. Norberto Castro Rodriguez, Dr. Florian Korinth, Abhishrutha Raghu, Azlizan Soemitro, Dr. Jose Boggio, Yu Wang, Mitali Damle, Adnan, Dr. Pavai and any other names that I might have forgotten. You guys are really awesome, exciting, and cheering.

I also give passionate thanks to new friends and colleagues outside my formal life: Ravi, Shubham, Shraddha, Ishita, Aishwarya, Seeman, Dipti bhai, Ritu bhabhi, Nihar, Deepti bhabhi, Gajanan, Abhishek bhaiya, Sadhana, Akshay and any other names that I may be missing. You guys were really supportive and caring.

It will be incomplete if I do not mention my special friends who gave me moral support during these years of my PhD: Harendra, Kowshik, Ahmed, and Siby. Without you guys, life in Germany would have been lonely and boring.

I would like to give warm thanks to all my friends, teachers, and professors back in India, from schooling to master's time, who always supported me in taking higher education and research as a future option. It will be incomplete if I do not mention my educational institutions, which inspired me to go through this PhD journey. I would also highlight my deity- Sai Baba, from whom I received inner peace and good luck.

Finally, it would be gruesome if I failed to express my deep gratitude to my Bapa- shri. Abhimanyu Nayak, Maa- smt. Binapani Nayak and Bhai- Bhabani (Jonty) for always staying beside me and encouraging me in the never-ending learning process.

Abani Shankar Nayak
Potsdam, Germany

Preface

Stellar interferometry – the concept invented by Albert Michelson in the 1920s is based on the combination of stellar light from two or more telescopes (or apertures) to obtain information about the complex coherence and thereby the brightness distribution of an astronomical object. In other words, complex coherence is sometimes known as complex visibility. There are two popular techniques for combining light: 1) direct detection (or homodyne) and 2) heterodyne. The direct detection technique has two sub-divisions: 1) amplitude interferometry and 2) intensity interferometry. The amplitude interferometry method developed by Michelson relies on obtaining fringes, whose intensity is the square of the sum of the incoming electric fields at the detector. The intensity interferometry method developed by Hanbury Brown and Twiss in the 1950s relies on measuring the modulus of the complex coherence of a source by correlating the intensities of two detectors separated in space. In amplitude interferometry, one can directly measure the amplitude and phase of the complex coherence obtained from a source. In contrast, intensity interferometry measures only the amplitude. Heterodyne stellar interferometry was first demonstrated by Johnson et al. [1] by extending the technique, which was popular in radio interferometry at that time, to optical wavelengths.[i] This technique relies on combining the stellar light with a local oscillator (in the form of a laser) to obtain and record a beat frequency which contains the phase information of the star light. The beat signals from each telescope are then correlated to form the fringes.

Scope – Stellar interferometry finds applications in observational astronomy from the study of fundamental stellar properties to imaging of extragalactic objects. As a result, it covers a wide wavelength range – from as short as X-ray to as long as radio waves. In this sense, it is necessary to define the scope of this Thesis work. Whenever the word *stellar interferometry* or *optical interferometry* or *interferometry* is mentioned, it means I am only discussing *amplitude interferometry* where light from two or more separate apertures are collected and combined using an optics or photonic component at optical wavelengths. As a result, the method of *stellar interferometry* includes the techniques of *aperture masking interferometry*, *pupil remapping interferometry* and *adapative optics* to name a few. The first two techniques will be discussed in Chapter 1, while the latter is not a part of this work. Whenever the word *optical wavelength* or *wavelength* is mentioned, I am generally considering the wavelength range between $0.4-5\,\mu$m, which includes the astronomical bands from B to M. If I am particular about any wavelength range, the astronomical band will be mentioned explicitly. For example, this work shows the results of a photonic device designed, characterized, and tested on-sky at astronomical H-band ($1.5-1.65\,\mu$m).

[i] At $10\,\mu$m.

When I use the word *visibilities*, it refers to the complex coherence of the light, which has both the amplitude and the phase part. But, when I use the word *visibility*, it is strictly the amplitude part which has a range from $0-1$. Thus, I will use *visibility* in a broad context and interchangeably to describe the *fringe visibility* or *visibility amplitude* or *normalized visibility ampltidue* or *fringe contrast*, all of which have range of values in $0-1$. More details on the definitions of these words can be found in Chapter 1.

Content – The majority of the content from Chapter 2 to Chapter 8 is published in my two peer-reviewed journal articles – Refs [2] and [3]. The organization of this Thesis is as follows:

- **Chapter 1** introduces briefly the concept of the van Cittert-Zernike Theorem, which is the mathematical foundation behind image formation through interferometers. The concepts of visibilities, *u–v* plane, non-redundant configuration, and closure phase are outlined. After comprehending the physics behind stellar interferometry, I introduce the scientific motivation with applications in the latest research areas of astronomy and astrophysics. However, these achievements are possible due to ongoing advances in instrumentation and technologies, most notably in fiber and integrated optics (IO)-based platforms leading to the field of *astrophotonics*. Therefore, in this context and the limelight of this Thesis, I have reviewed and outlined the concepts of IO-based beam combiners and pupil remapping interferometry in Section 1.4.

  While this work is related to the fields of *optics* and *photonics*, I did not include all of the background theories of these subjects. I am assuming that the reader has a basic understanding of waveguides, modal analysis, and waveguide manufacturing technologies, to name a few. I recommend readers to go through the Refs [4, 5] for a more thorough understanding of interferometry.

- **Chapter 2** describes the theory separately for coherent reformatters and discrete beam combiner (DBC). Some of the parameters necessary for designing these photonic components are highlighted. I have used the word *coherent reformatters* in a general context which is 3-D single-mode waveguides distributing light from one position to another while maintaining the path length. When *coherent reformatters* are used for collecting the light from a re-imaged pupil of the telescope, they are defined as *pupil remappers*.

- **Chapter 3** describes the design of IO-based *astrophotonics* device that monolithically contains the coherent reformatters and the DBC. Three different designs of IO devices are described.

- **Chapter 4** describes the fabrication of the devices using ultra-fast laser inscription (ULI) and the scientific motivation for 3-D photonic components. I did not fabricate the devices myself and have written this Chapter based on fabrication reports provided by *Politecnico di Milano*.

- **Chapter 5** describes the retrieval of the simulated visibilities from a DBC design when operated in monochromatic and polychromatic light conditions. Impact of various noise sources[ii] on the visibilities are reported. This Chapter supports the characterization results of Chapter 6 and observational results of Chapter 7.
- **Chapter 6** describes the characterization of the devices using a 2-beam interferometric Michelson setup. The retrieval of the visibilities from all three devices is reported. I have interchangeably used the words *bandwidth* and *FWHM* of the bandpass filters used in the experiment.
- **Chapter 7** describes the on-sky tests at the William Herschel Telescope that were done using a different optical setup consisting of a segmented deformable mirror and a microlens array. The visibilities obtained for Vega and Altair from one of the three IO devices are reported.
- **Chapter 8** includes the discussion of the results and the future outlook. Finally, I end my Thesis with **Appendix A** describing a step-by-step procedure for filling the elements of the transfer matrix of a DBC.

Abani Shankar Nayak
Potsdam, Germany

[ii] E.g. Amplitude and phase errors at the input waveguides, photon shot noise, and detector noise.

Abstract

Stellar interferometry is the only method in observational astronomy for obtaining the highest resolution images of astronomical targets. This method is based on combining light from two or more separate telescopes to obtain the complex visibility that contains information about the brightness distribution of an astronomical source. The applications of stellar interferometry have made significant contributions in the exciting research areas of astronomy and astrophysics, including the precise measurement of stellar diameters, imaging of stellar surfaces, observations of circumstellar disks around young stellar objects, predictions of Einstein's General relativity at the galactic center, and the direct search for exoplanets to name a few. One important related technique is aperture masking interferometry, pioneered in the 1960s, which uses a mask with holes at the re-imaged pupil of the telescope, where the light from the holes is combined using the principle of stellar interferometry. While this can increase the resolution, it comes with a disadvantage. Due to the finite size of the holes, the majority of the starlight (typically $> 80\%$) is lost at the mask, thus limiting the signal-to-noise ratio (SNR) of the output images. This restriction of aperture masking only to the bright targets can be avoided using pupil remapping interferometry – a technique combining aperture masking interferometry and advances in photonic technologies using single-mode fibers. Due to the inherent spatial filtering properties, the single-mode fibers can be placed at the focal plane of the re-imaged pupil, allowing the utilization of the whole pupil of the telescope to produce a high-dynamic range along with high-resolution images. Thus, pupil remapping interferometry is one of the most promising application areas in the emerging field of *astrophotonics*.

At the heart of an interferometric facility, a beam combiner exists whose primary function is to combine light to obtain high-contrast fringes. A beam combiner can be as simple as a beam splitter or an anamorphic lens to combine light from 2 apertures (or telescopes) or as complex as a cascade of beam splitters and lenses to combine light for > 2 apertures. However, with the field of *astrophotonics*, interferometric facilities across the globe are increasingly employing some form of photonics technologies by using single-mode fibers or integrated optics (IO) chips as an efficient way to combine light from several apertures. The state-of-the-art instrument – GRAVITY at the very large telescope interferometer (VLTI) facility uses an IO-based beam combiner device reaching visibilities accuracy of better than $< 0.25\%$, which is roughly $50\times$ as precise as a few decades back.

Therefore, in the context of IO-based components for applications in stellar interferometry, this Thesis describes the work towards the development of a 3-dimensional (3-D) IO device – a monolithic *astrophotonics* component containing both the *pupil remappers* and a *discrete beam combiner (DBC)*. In this work, the pupil remappers are 3-D single-mode waveguides

in a glass substrate collecting light from the re-imaged pupil of the telescope and feeding the light to a DBC, where the combination takes place. The DBC is a lattice of 3-D single-mode waveguides, which interact through evanescent coupling. By observing the output power of single-mode waveguides of the DBC, the visibilities are retrieved by using a calibrated transfer matrix ($\{U\}$) of the device. The feasibility of the DBC in retrieving the visibilities theoretically and experimentally had already been studied in the literature but was only limited to laboratory tests with monochromatic light sources. Thus, a part of this work extends these studies by investigating the response of a 4-input DBC to a broad-band light source. Hence, the *objectives* of this Thesis are the following: 1) Design an IO device for broad-band light operation such that accurate and precise visibilities could be retrieved experimentally at astronomical H-band ($1.5-1.65\,\mu$m), and 2) Validation of the DBC as a possible beam combination scheme for future interferometric facilities through on-sky testing at the William Herschel Telescope (WHT).

This work consisted of designing three different 3-D IO devices. One of the popular methods for fabricating 3-D photonic components in a glass substrate is ultra-fast laser inscription (ULI). Thus, manufacturing of the designed devices was outsourced to *Politecnico di Milano* as part of an iterative fabrication process using their state-of-the-art ULI facility. The devices were then characterized using a 2-beam Michelson interferometric setup obtaining both the monochromatic and polychromatic visibilities. The retrieved visibilities for all devices were in good agreement as predicted by the simulation results of a DBC, which confirms both the repeatability of the ULI process and the stability of the Michelson setup, thus fulfilling the *first objective*.

The best-performing device was then selected for the pupil-remapping of the WHT using a different optical setup consisting of a deformable mirror and a microlens array. The device successfully collected stellar photons from Vega and Altair. The visibilities were retrieved using a previously calibrated $\{U\}$ but showed significant deviations from the expected results. Based on the analysis of comparable simulations, it was found that such deviations were primarily caused by the limited SNR of the stellar observations, thus constituting a first step towards the fulfillment of the *second objective*.

Summary

(for non-experts)

The resolution of a telescope, or the ability to separate two point sources, is given by $\sim \frac{\lambda}{A}$, where λ is the wavelength of light, and A is the diameter of the telescope's primary mirror. It is a well-known concept that for a given telescope, if two point objects are separated by $< \frac{\lambda}{A}$, a distinct image of these objects cannot be produced, and the telescope system is known to be diffraction-limited. However, suppose the light is combined from two telescopes separated by a distance B. In that case, the resolution of the system increases by a factor of $\sim \frac{2B}{A}$, thus beating the diffraction limit of a single telescope. Hence, stellar interferometry – the concept developed by Michelson in the 1920s – combines light from two or more telescopes to produce high-resolution images of astronomical targets. The applications of stellar interferometry have made important contributions in astronomy and astrophysics, from the study of fundamental stellar properties to imaging of extragalactic objects.

At the heart of an interferometric facility, a beam combiner is used to combine light from multiple telescopes (or apertures) to obtain high-contrast fringes. In the early days, a beam combiner was as simple as a beam splitter or an anamorphic lens to combine light from 2 apertures (or telescopes) or as complex as a cascade of beam splitters and lenses to combine light for > 2 apertures. However, with the emerging field of *astrophotonics*, interferometric facilities are increasingly employing some form of photonics technologies by using single-mode fibers or integrated optics (IO) chips as an efficient way of combining light from several apertures. To give an example, a technique known as *pupil remapping interferometry* relies on collecting light through a set of single-mode fibers or an IO chip containing single-mode waveguides, which is placed at the re-imaged pupil of the telescope. Later, the light from the fibers or waveguides is combined through a bulk-optics-based or IO-based component to produce a high-dynamic range along with high-resolution images.

Therefore, in the context of IO-based components for applications in stellar interferometry, this Thesis aims at the development of a 3-dimensional (3-D) IO device – a monolithic *astrophotonics* component containing both the *pupil remappers* and a *discrete beam combiner (DBC)*. In this Thesis, the pupil remappers are 3-D single-mode waveguides inscribed in a glass substrate that collect light from the re-imaged pupil of the telescope and feed the light to a DBC, where the beam combination takes place. The DBC is a lattice of 3-D single-mode waveguides, which interact through evanescent coupling. By observing the output power of single-mode waveguides of the DBC, the visibilities required for high-resolution imaging are retrieved using a calibrated transfer matrix of the device. The feasibility of the DBC in retrieving the visibilities theoretically and experimentally had already been studied in the literature but was limited to laboratory tests with monochromatic light sources. Hence, the *objectives* of this Thesis are

the following: 1) To design an IO device for broad-band light operation such that visibilities could be retrieved at astronomical H-band ($1.5 - 1.65\,\mu$m), 2) To experimentally demonstrate accurate and precise visibilities from the IO device that is fabricated using ultra-fast laser inscription technology, and 3) To validate the DBC as a possible beam combination scheme for future interferometric facilities through on-sky testing at the William Herschel Telescope.

Zusammenfassung

Das Auflösungsvermögen eines Teleskops, also die Fähigkeit, zwei Punktquellen voneinander zu trennen, wird durch $\sim \frac{\lambda}{A}$ bestimmt, wobei λ die Wellenlänge des Lichts und A der Durchmesser des Hauptspiegels des Teleskops ist. Wenn bei einem gegebenen Teleskop zwei punktförmige Objekte durch $< \frac{\lambda}{A}$ getrennt sind, kann kein eindeutiges Bild dieser Objekte erzeugt werden und das Teleskopsystem ist somit beugungsbegrenzt. Kombiniert man jedoch das Licht von zwei Teleskopen, die durch einen Abstand B voneinander getrennt sind, erhöht sich die Auflösung um einen Faktor $\sim \frac{2B}{A}$ und überwindet damit die Beugungsgrenze eines einzelnen Teleskops. Daher wird bei der stellaren Interferometrie – deren Konzept von Michelson in den 1920er Jahren entwickelte wurde – Licht von zwei oder mehr Teleskopen kombiniert, um hochauflösende Bilder von astronomischen Objekten zu erzeugen. Die Anwendung der stellaren Interferometrie hat wichtige Beiträge zur Astronomie und Astrophysik geleistet, von der Untersuchung grundlegender Eigenschaften von Sternen bis hin zur Abbildung extragalaktischer Objekte.

Das Herzstück einer interferometrischen Anlage ist ein Strahlkombinierer, der das Licht von mehreren Teleskopen (oder Aperturen) kombiniert, um kontrastreiche Interferenzstreifen zu erhalten. In der Anfangszeit konnte ein Strahlkombinierer ganz einfach sein, wie z.B. ein Strahlteiler oder eine anamorphotische Linse für die Kombination des Lichts von 2 Aperturen (oder Teleskopen), oder sehr komplex, wie z.B. eine Kaskade von Strahlteilern und Linsen, um Licht für > 2 Aperturen zu kombinieren. Mit dem aufkommenden Gebiet der *Astrophotonik* setzen interferometrische Einrichtungen jedoch vermehrt photonische Technologien ein, indem Einzelmoden-Fasern oder ein Chip mit integrierter Optik (IO) verwendet werden, um Licht aus mehreren Aperturen effizient zu kombinieren. Bei der sogenannten *pupil remapping interferometry* Technik (dt etwa: neugeordnete Pupille) wird beispielsweise Licht mit mehreren Einzelmoden-Fasern oder Einzelmoden-Wellenleitern auf einem IO-Chip gesammelt. Diese Komponenten werden an der Position im Strahlengang eingefügt, an der die Pupille des Teleskops abgebildet wird. Anschließend wird das Licht aus den Fasern oder Wellenleitern durch eine Freistrahloptik oder IO-basierte Komponente interferometrisch überlagert, um Bilder sowohl mit hohem Kontrast als auch hoher Auflösung zu erzeugen.

Im Kontext von IO-basierten Komponenten für stellare Interferometrie ist das Ziel dieser Arbeit die Entwicklung eines 3-dimensionalen (3-D) IO-Bauteils - eine monolithische *Astrophotonik*-Komponente, die sowohl die *Pupil Remapper* als auch einen *discrete beam combiner (DBC)* (dt: Diskreten Strahlkombinierer) enthält. In dieser Arbeit sind die Pupil Remapper 3-D-Einzelmoden-Wellenleiter, die in ein Glassubstrat eingeschrieben sind und das Licht von der abgebildeten Pupille des Teleskops sammeln und zu einem DBC leiten, in dem die Kombination

stattfindet. Der DBC ist eine 3-D-Gitteranordnung von Einzelmoden-Wellenleitern, die durch evaneszente Kopplung miteinander wechselwirken. Durch Beobachtung der Ausgangsleistung der Einzelmoden-Wellenleiter des DBCs werden mit Hilfe einer kalibrierten Übertragungsmatrix des Systems die *Visibilities* (dt: Kontrastwerte) ermittelt, die für eine hochauflösende Bildgebung erforderlich sind. Die Eignung von DBCs für die Ermittlung der Kontrastwerte wurde sowohl theoretisch als auch experimentell untersucht und in Fachzeitschriften publiziert. Bisher beschränkten sich diese Untersuchungen jedoch auf Labortests mit monochromatischen Lichtquellen. Die *Ziele* dieser Arbeit sind daher die folgenden: 1) Die Entwicklung eines IO-Bauteils für die Anwendung mit breitbandigem Licht, so dass Kontrastwerte im astronomischen H-Band ($1,5-1,65\,\mu$m) ermittelt werden können, 2) experimentelle Demonstration genauer und präziser Kontrastwerte mit dem IO-Bauteil, welches mit der Femtosekundenlaser-Bearbeitungsmethode hergestellt wird, und 3) Validierung des DBCs als mögliches Konzept für die Strahlkombination für zukünftige interferometrische Anlagen durch On-Sky-Tests am William Herschel Teleskop.

Contents

List of Tables

List of Figures

List of Abbreviations

as	arcsecond
au/a.u.	arbitary units
ABCD	a method used for phase extraction in GRAVITY instrument at VLTI
ADU	analog to digital units
AGN	active galactic nuclei
AO	adaptive optics
APD	avalanche photodiode
AU	astronomical units
AWG	arrayed-waveguide grating
BL	baseline
CAD	computer-aided design
CCD	charged coupled device
CHARA	center for high angular resolution astronomy
CIAO	Coudé infrared adaptive optics
CLEAN	an image reconstruction algorithm in interferometry
CMOS	complementary metal oxide semiconductor
COAST	cambridge optical aperture synthesis telescope
CP	closure phases
CRED2	an NIR camera
dB	decibel
DAFI	dilute aperture fiber interferometer
DBC	discrete beam combiner
DL	delay line
Dragonfly	an instrument for pupil remapping interferometer

Eq	equation
ELT	extremely large telescope
ft	foot (unit of length)
Fig	figure
FFT	fast fourier transform
FIRST	fibered imager for single telescope
FLUOR	fibered link unit for optical recombination
FWHM	full width half maximum
GI2T	grand interférométré a 2 télescopes
GRAVITY	a 4-telescope IO beam combiner at VLTI
H-R	Hertzsprung-Russell
in	inch (unit of length)
IL	insertion loss
IO	integrated optics
IONIC	an IO beam combiner visitor instrument at VLTI
IOTA	infrared optical telescope array
IPA	isopropyl alcohol
I2T	interférométré a 2 télescopes
JWST	James Webb space telescope
ly	light-year
MEM	an image reconstruction algorithm in interferometry
MFD	mode-field diameter
MLA	microlens array
MONA	a beam combiner at CHARA
MSE	mean squared error
NACO	an adaptive optics system
NIR	near infrared
NIRISS	near-Infrared imager and slitless spectrograph
NN	nearest neighbour interaction
NNN	next-nearest neighboure interaction

NLLS	non-linear least square
NPOI	navy precision optical interferometer
NTT	new technology telescope
OPD	optical path difference
OPL	optical path length
PaL	path length
PIC	photonic integrated circuit
PIONIER	a 4-telescope beam combiner at VLTI
PSF	point spread function
P2VM	pixel-2-visibility matrix
rms	root-mean-square
Ref	reference
DM	segmented deformable mirror
SCAO	single conjugate adaptive optics
SHARP	a NIR camera installed at NTT
SMF	single mode fiber
SNR	signal-to-noise ratio
SR	Strehl ratio
ULI	ultra-fast laser inscription
UV	ultraviolet
VLT	very large telescope that consists of using only 1 out of 4 unit telescopes
VLTI	very large telescope interferometer
vs	versus
V2PM	visibility-2-pixel matrix
WG	waveguide
WHT	William Herschel Telescope
YSOs	young stellar objects
ZBLAN	a type of fluorozirconate glass

List of Symbols

A_i	amplitude of the electric field at the i^{th} location
c	speed of light
E_i	electric field at the i^{th} location
$f'(z)$	first derivative of the function, $f(z)$
$f''(z)$	second derivative of the function, $f(z)$
I_d	dark current
L	interaction length of the DBC
L_c	coupling length for two system of WGs
m_k	magnitude of the star at astronomical K-band
N_e	number of electrons per pixel
N_p	number of photons per pixel
N_t	number of telescopes
P	power associated with the optical wave
r_0	Fried parameter
R	resolving power of the spectrometer, unless stated otherwise
R_c	radius of curvatuare of a spline function
t_e	exposure time of the camera
T_a	atmospheric transfer function
T_i	instrumental transfer function
T_s	temperature of stellar surface
u, v, w	ground coordinates
$\{U\}$	transfer matrix of the DBC
V_{ij}	visibility amplitude
α, β, ζ	sky coordiantes

γ	normalized complex visiblity
Γ	complex visibility
δ	optical path delay in dimensions of length
Δn	refractive index change between the core and the cladding
$\Delta\Theta$, $\Delta\Theta_{tel}$, $\Delta\Theta_{int}$	angular resolution, for a single telescope, for an interferometer
$\Delta\lambda$	bandwidth or FWHM of the light
ε_i	an error term in the phase of an object
ε_{PaL}	threshold for the path length matching
ε_{R_c}	threshold for the R_c
θ_s	angular extent of a source
κ, κ_D, κ_H	coupling coefficient, in diagonal direction, in horizontal direction
λ	wavelength of the light
λ_0	center wavelength of the light
Λ_{coh}	coherence length of the interferometer due to finite bandpass
ν	frequency of the light
σ_λ	rms wavefront error in units of length
τ_0	atmosperic time constant
ϕ_{ij}	visibility phase
Φ_{ijk}	closure phase

List of Publications

International Journals

1. **Abani Shankar Nayak**, Lucas Labadie, Tarun Kumar Sharma, Simone Piacentini, Giacomo Corrielli, Roberto Osellame, Éric Gendron, Jean-Tristan M. Buey, Fanny Chemla, Mathieu Cohen, Nazim A. Bharmal, Lisa F. Bardou, Lazar Staykov, James Osborn, Timothy J. Morris, Ettore Pedretti, Aline N. Dinkelaker, Kalaga V. Madhav, and Martin M. Roth, "First stellar photons for an integrated optics discrete beam combiner at the William Herschel Telescope," Appl. Opt. 60, D129-D142 (2021)

2. Aurelién Benoît, Fraser A. Pike, Tarun K. Sharma, David G. MacLachlan, Aline N. Dinkelaker, **Abani S. Nayak**, Kalaga Madhav, Martin M. Roth, Lucas Labadie, Ettore Pedretti, Theo A. ten Brummelaar, Nic Scott, Vincent Coudé du Foresto, and Robert R. Thomson, "Ultrafast laser inscription of asymmetric integrated waveguide 3 dB couplers for astronomical K-band interferometry at the CHARA array," J. Opt. Soc. Am. B 38, 2455-2464 (2021)

3. **Abani Shankar Nayak**, Thomas Poletti, Tarun Kumar Sharma, Kalaga Madhav, Ettore Pedretti, Lucas Labadie, and Martin M. Roth, "Chromatic response of a four-telescope integrated-optics discrete beam combiner at the astronomical L band," Opt. Express 28, 34346-34361 (2020)

International Conferences

1. **Abani Shankar Nayak**, Tarun Kumar Sharma, Lucas Labadie, Simone Piacentini, Giacomo Corrielli, Roberto Osellame, Éric Gendron, Jean-Tristan M. Buey, Fanny Chemla, Mathieu Cohen, Nazim A. Bharmal, Lisa F. Bardou, Lazar Staykov, James Osborn, Timothy J. Morris, Ettore Pedretti, Aline N. Dinkelaker, Kalaga V. Madhav, Martin M. Roth, "First on-sky results with an interferometric discrete beam combiner (DBC) at the William Herschel Telescope," Proc. SPIE 11446, Optical and Infrared Interferometry and Imaging VII, 114461D (13 December 2020)

2. Fraser A. Pike, Tarun K. Sharma, Aurélien Benoît, David G. MacLachlan, Aline N. Dinkelaker, **Abani S. Nayak**, Kalaga Madhav, Martin M. Roth, Lucas Labadie, Ettore Pedretti, Theo A. ten Brummelaar, Nicholas J. Scott, Vincent Coudé du Foresto, Robert R. Thomson, "K-band integrated optics beam combiners for CHARA fabricated by ultrafast laser inscription," Proc. SPIE 11446, Optical and Infrared Interferometry and Imaging VII, 114460K (13 December 2020)

3. Robert J. Harris, Tarun Kumar Sharma, John J. Davenport, Philipp Hottinger, Theodoros Anagnos, **Abani Shankar Nayak**, Andreas Quirrenbach, Lucas Labadie, Kalaga V. Madhav, Martin M. Roth, "NAIR: Novel Astronomical Instrumentation through photonic Reformatting," Proc. SPIE 11451, Advances in Optical and Mechanical Technologies for Telescopes and Instrumentation IV, 1145108 (13 December 2020)

4. **Abani Shankar Nayak**, Simone Piacentini, Tarun Kumar Sharma, Giacomo Corrielli, Roberto Osellame, Lucas Labadie, Stefano Minardi, Ettore Pedretti, Kalaga Madhav, Martin M. Roth, "Integrated optics-interferometry using pupil remapping and beam combination at astronomical H-band," Proc. SPIE 11203, Advances in Optical Astronomical Instrumentation 2019, 112030V (3 January 2020)

5. Simone Piacentini, Giacomo Corrielli, **Abani Shankar Nayak**, Tarun Kumar Sharma, Kalaga V. Madhav, Ettore Pedretti, Stefano Minardi, Lucas Labadie, Roberto Osellame, "Integrated discrete beam combiner with a pupil remapper for stellar interferometry (Conference Presentation)," Proc. SPIE 11287, Photonic Instrumentation Engineering VII, 112870B (9 March 2020)

6. Simone Piacentini, Giacomo Corrielli, **Abani Shankar Nayak**, Tarun Kumar Sharma, Kalaga V. Madhav, Andrea Adami, Ettore Pedretti, Stefano Minardi, Lucas Labadie, Roberto Osellame, "Femtosecond laser writing of 3D polarization insensitive integrated devices for astrophotonics (Conference Presentation)," Proc. SPIE 11270, Frontiers in Ultrafast Optics: Biomedical, Scientific, and Industrial Applications XX, 112700S (9 March 2020)

7. S. Piacentini, G. Corrielli, **A. S. Nayak**, E. Pedretti, S. Minardi and R. Osellame, "Direct Writing of 3D Integrated Photonic Circuits for Astrophotonics," 2019 Conference on Lasers and Electro-Optics Europe & European Quantum Electronics Conference (CLEO/Europe-EQEC), Munich, Germany, 2019, pp. 1-1

8. Robert J. Harris, Jan Tepper, John J. Davenport, Ettore Pedretti, Dionne M. Haynes, Philipp Hottinger, Theodoros Anagnos, **Abani Shankar Nayak**, Yohana Herrero Alonso, Pranab Jyoti Deka, Stefano Minardi, Andreas Quirrenbach, Lucas Labadie, Roger Haynes, "NAIR: novel astronomical instrumentation through photonic reformatting," Proc. SPIE

10706, Advances in Optical and Mechanical Technologies for Telescopes and Instrumentation III, 107060L (10 July 2018)

9. Ettore Pedretti, Romina Diener, **Abani Shankar Nayak**, Jan Tepper, Lucas Labadie, Thomas Pertsch, Stefan Nolte, Stefano Minardi, "Beam combination schemes and technologies for the Planet Formation Imager," Proc. SPIE 10701, Optical and Infrared Interferometry and Imaging VI, 107012O (9 July 2018)

This page was intentionally left blank.

Chapter 1

Principles of stellar interferometry

This Chapter outlines the concept of van Cittert-Zernike theorem, visibilities, u–v plane, non-redundant configuration, and closure phases. After a brief introduction into the physics of stellar interferometry, the motivation behind this technique is presented and its applications in current exciting research areas of astronomy and astrophysics. Finally, with the utilization of photonics technologies in astronomical instruments, the recent developments in pupil remapping interferometry and integrated optics-based beam combiners are indicated.

1.1 van Cittert-Zernike theorem

The partial theory of coherence is a well-known concept in optics, and a rigorous theory can be found in the standard textbook of Born and Wolf [18, Chapter 10]. The van Cittert-Zernike theorem, first established by van Cittert and later more generally by Zernike, is thus an extension of the coherence theory in describing the interference and diffraction properties from an extended incoherent quasi-monochromatic light source. It provides a relationship between the complex degree of coherence and the intensity distribution of the source, which is given by a Fourier transformation. Mathematically, the relationship is written as [4, Chapter 2][19]:

$$\Gamma(u,v) = \int d\alpha\, d\beta\, A(\alpha,\beta)\, F(\alpha,\beta)\, e^{-2\pi \mathrm{i}(\alpha u+\beta v)}. \tag{1.1}$$

The term $\Gamma(u,v)$ is a complex quantity, also known as the complex degree of coherence or the complex visibility of the source. The plane consisting of u,v is known as the $u-v$ plane or the Fourier plane, i.e. the plane when the sky coordinates (α,β) containing the source is projected perpendicularly[i] to the ground coordinates (u,v) containing the baseline vector, B, formed by a pair of telescopes. The schematic of the working principle of an idealized two-telescope interferometer is shown in Fig. 1.1. The coordinates u,v are defined as:

$$\left.\begin{aligned} u &= \frac{B_x}{\lambda} \\ v &= \frac{B_y}{\lambda} \end{aligned}\right\}. \tag{1.2}$$

$F(\alpha,\beta)$ is the source intensity which has units of incident power per unit area per solid angle in the sky. $A(\alpha,\beta)$ is the effective cross-sectional area of the telescope where the light is collected. Then the product $d\alpha\, d\beta\, F(\alpha,\beta)A(\alpha,\beta)$ has dimensions of power. Therefore, from Eq. (1.1), the complex visibility $\Gamma(u,v)$ has the dimensions of power.

[i] Along the line of sight $\hat{\zeta}$. See Fig. 1.1.

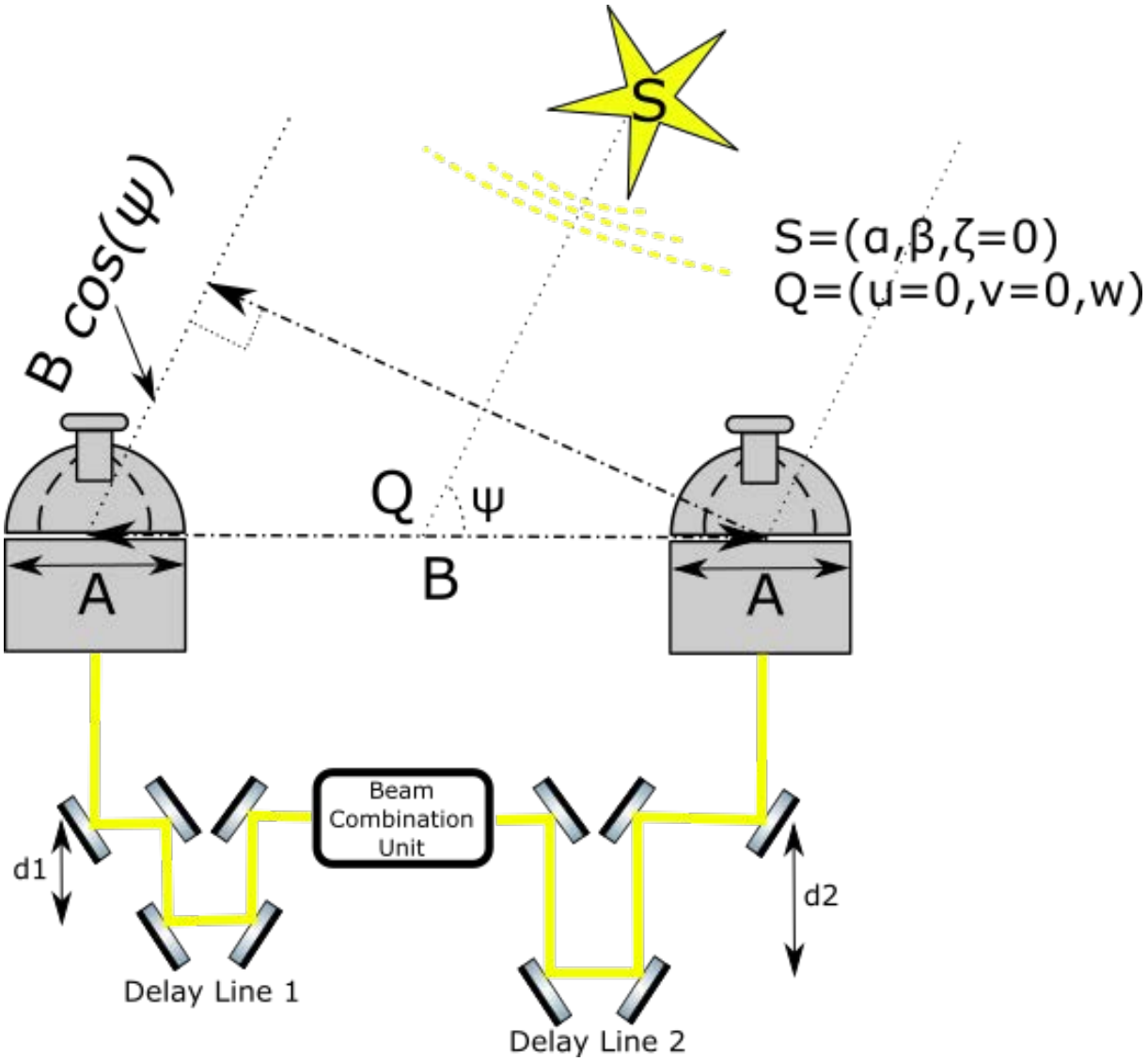

Figure 1.1: A schematic of an idealized 2-telescope interferometer. Light from the source S with coordinates $(\alpha, \beta, \zeta = 0)$ is collected by the two telescopes, each with a cross-sectional area A and separated by a baseline B. The light is sent to a beam combination unit consisting of several optical components and a detector, where fringes are recorded for high-resolution imaging. The geometric path delay $B\cos(\psi)$ is compensated by two delay lines, d1 and d2. The point Q is the center of the interferometer with coordinates $(u = 0, v = 0, w)$ such that $\hat{w} \parallel \hat{\zeta}$.

Following Eq. (1.1), one can define a normalized, dimensionless visibility given by:

$$\gamma(u,v) = \frac{\int d\alpha\, d\beta\, A(\alpha,\beta) F(\alpha,\beta)\, e^{-2\pi \mathrm{i}(\alpha u+\beta v)}}{\int d\alpha\, d\beta\, A(\alpha,\beta) F(\alpha,\beta)} = \frac{\Gamma(u,v)}{\Gamma(0,0)}. \tag{1.3}$$

γ defined above is a complex quantity. Here, $|\gamma| = V$ is the visibility amplitude, and $\mathrm{Arg}(\gamma) = \phi$ is the visibility phase. The squared law detectors typically used in optical interferometry setups measure the normalized fringe power, which is the fringe power relative to the total power of the source. Therefore, the power P at the detector is:

$$P(u,v,\delta) = P_0(1 + \Re[\gamma(u,v) e^{\mathrm{i}k\delta}]). \tag{1.4}$$

Where $P_0 = \Gamma(0,0)$. $\delta = d1 - d2 + \varepsilon$ is the optical path delay introduced by the delay line of the interferometer, such that P can be measured by varying δ. From Eq. (1.4), if one measures P for at least two values of δ, the normalized object visibility γ can be recovered within a multiplicative constant [19]. Once γ is extracted, known models of the intensity distribution of different sources[ii] can be applied to estimate the stellar diameter of the source. The imaging techniques from radio interferometry have been extended and extensively used at optical wavelengths to produce high-resolution images of stellar targets. Some of the image reconstruction algorithms used in optical interferometry, known as CLEAN and MEM, work on the basic principle of inverse Fourier transform of Γ and *a priori* information of the object to form images [4, Chapter 13].

In his classic paper, Michelson [20] coined the word *visibility* of fringes as the apparent contrast between the bright (P_{max}) and dark (P_{min}) areas of the fringes. It is also known as the Michelson fringe visibility and using Eq. (1.3), Eq. (1.4), it is defined as:

$$V = |\gamma| = \frac{P_{max} - P_{min}}{P_{max} + P_{min}}. \tag{1.5}$$

In this work, the word *visibility* will be used in a broad context and interchangeably to describe the *fringe visibility* or *visibility amplitude* or *normalized visibility amplitude* or *fringe contrast*, all of which have values in the range of $0-1$. Thus, visibility measures the degree of coherence of the light, which has a range of $0-1$. If $V = 1$ for a source, it is completely

[ii] For example point, uniform disk, Gaussian symmetry, etc.

coherent. If $V = 0$, the source is said to be completely incoherent. All other intermediate values between 0–1 make the source partially coherent. For a point source[iii] at monochromatic wavelength λ_0, $V = 1$ implying that the light waves received by the interferometer[iv] have a definite phase relationship at any spatial point along the wave train. The point source produces a good quality interference fringe, where the contrast of the fringe is used as a measure to define its quality. This is shown as example in Fig. 1.2a, where $|\gamma| = V = 1$ and $\phi = 0$ for all inverse spatial frequencies ($\sim \lambda/B$).[v] In the example shown, the point source is assumed to be at the zenith[vi] as observed from the center of the interferometer. From Eq. (1.4) and Eq. (1.5), the power recorded by the interferometer in terms of P_0 is also shown in the lower row of Fig. 1.2a for $V = 1$.

On the other hand, an extended source can be thought of as a superposition of several point sources, emitting waves independently, and there may not be any correlation between the waves. As a result, the contrast of the fringes starts degrading, implying $V < 1$. This situation is shown for a uniform disk with diameter a in Fig. 1.2b. One can think of $|\gamma|$ of the uniform disk as the Fraunhofer diffraction pattern of a circular aperture produced by a pair of circular holes [21, Chapter 12].[vii] Assume a circular source fixed on the sky subtending an angle θ_s with the baseline of the interferometer as shown in Fig. 1.1 that can vary. If the baseline decreases,[viii] the waves from the source are coherent, implying $V = 1$. As B increases, the source becomes partially coherent, implying a decrease in the contrast of fringe power in Eq. (1.4). This scenario is shown in the lower row of Fig. 1.2 for two cases: 1) A unresolved or a coherent source that has $V = 1$, and 2) A resolved or partially coherent source with $V = 0.5$. When $B = 1.22\frac{\lambda_0}{\theta_s}$, the fringes completely disappear with zero power at the detector. Thus, one measures B to find the angular size θ_s. In fact, this principle was applied by Michelson to precisely calculate the diameter of a star, Betelgeuse (α Orionis) [22], for the very first time.

From Eq. (1.5), the fringe visibility V equals the modulus of the object visibility γ, is an ideal scenario. In any real interferometer, one has to consider two dominant noise sources: the atmosphere and the instrument itself. As a result, the object visibility (V_o) differs from the fringe visibility (V_f). Using the convolution theorem, one can write [23]:

$$V_f = T_i T_a V_o. \tag{1.6}$$

[iii] Source that is spatially unresolved by the interferometer.

[iv] Assuming a pair of telescopes.

[v] Following the convention of [4, Chapter 2][5, Chapter 3], in this work, spatial frequency is defined as $\frac{B}{\lambda}$, unit is rad^{-1}, and inverse spatial frequency is defined as $\frac{\lambda}{B}$, unit is rad.

[vi] $\Psi = 90^\circ$ in Fig. 1.1.

[vii] The pair of holes are analogous to the two telescopes in an interferometer setup as shown in Fig. 1.1.

[viii] It does not imply that $B = 0$, where no fringes are detected.

Where T_i,T_a are the interferometric efficiencies[ix] due to instrument and atmosphere, respectively. An accurate knowledge of both T_i, T_a is required in order to have a good estimate of V_o. It is possible to perform a suitable calibration of T_i from a well-designed interferometer. Obtaining T_a is more difficult, as it is a random variable caused by the phase corrugation in the wavefront due to the atmosphere. One way to calibrate T_a is by taking a large number of short duration images, which freezes the atmosphere and recovers the Fourier components of the target [24]. This technique was first developed by Labeyrie and is also known as *speckle imaging* [25]. However, since this method is highly dependent on atmospheric turbulence, it creates difficulties in calibrating the optical transfer function of the telescope [16]. This well-known issue in long baseline interferometry has been addressed using single-mode fibers, which is discussed in detail in Section 1.4.3.

It is to be noted that in the above discussion, ideal interference fringes obtained from the source were assumed.[x] However, all interferometers currently operating have a finite passband or bandwidth. The optical components used in the interferometers have a finite transmission, allowing only a certain wavelength range from $\lambda_0 - \frac{\Delta\lambda}{2}$ to $\lambda_0 + \frac{\Delta\lambda}{2}$, where $\Delta\lambda$ is the bandwidth of an interferometric system. As a result, the fringe observed by Eq. (1.4) does not occur at all values of δ, but over a finite length, also known as the coherence length given by:

$$\Lambda_{coh} = \frac{\lambda_0^2}{\Delta\lambda}. \tag{1.7}$$

It indicates that to have good contrast fringes (i.e. $V = 1$), the path delay, δ, introduced by the two arms of the interferometer in Fig. 1.1 has to be matched with a precision in the physical scale of Λ_{coh}, typically of the order of few nm. It can be seen that Λ_{coh} depends solely on the finite bandwidth of an interferometric system.

1.2 Arrangement of telescopes in an optical interferometer

The telescopes in an optical interferometer are arranged spatially such that a good coverage of the $u-v$ plane is obtained. In addition, the telescopes are located non-redundantly to have a good SNR associated with the spatial frequency in the interferogram. One such optical interferometer facility – the very large telescope interferometer (VLTI) [26] located in Chile – is shown in Fig. 1.3. In the next two sections, the concept of the $u-v$ plane and a distinction

[ix] Sometimes known as transfer function.

[x] Interference fringes are present at all delay line values, δ.

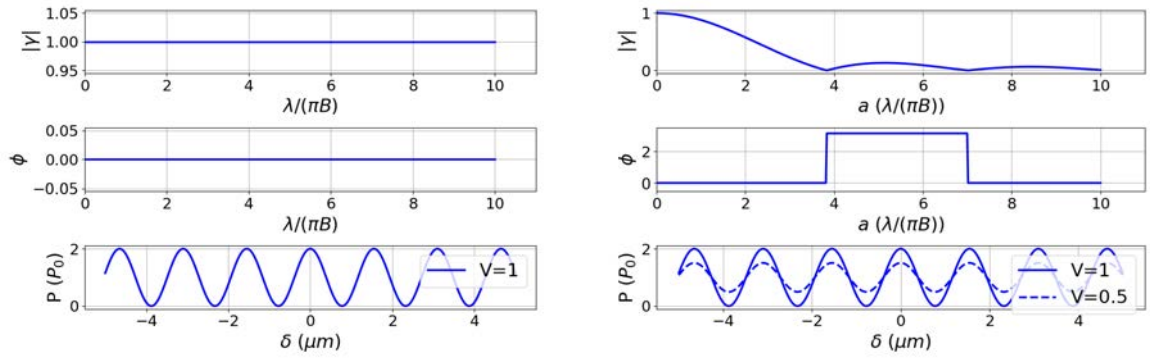

(a) (b)

Figure 1.2: Visibilities for two of the common source types: (a) Point. (b) Uniform disk with diameter a. *Upper row:* $|\gamma| = V$ as a function of $\lambda/(\pi B)$. *Middle row:* $\text{Arg}(\gamma) = \phi$ as a function of $\lambda/(\pi B)$. *Lower row:* power observed by a detector in a two-telescope interferometer as a function of path delay (δ) introduced by the delay line. The legend on the *right* figure shows the Michelson fringe visibility for two sources: 1) An unresolved source ($V = 1$), and 2) A resolved source ($V = 0.5$). (see Section 1.1 for details).

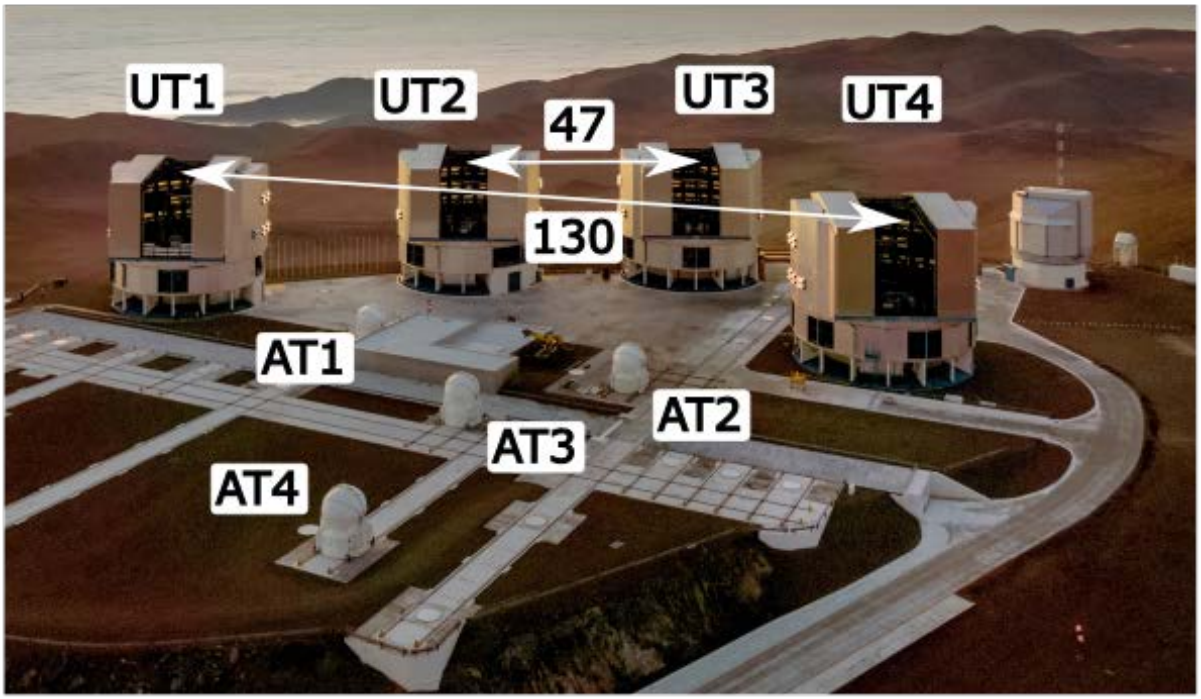

Figure 1.3: A photograph showing the very large telescope interferometer (VLTI) facility situated on Cerro Paranal in the Atacama desert of Chile. The four unit telescopes (UTs), each having a diameter of 8 m, are marked in the photograph. The longest and shortest baselines formed by the four UTs are shown in meters. The four auxiliary telescopes (ATs), each having a diameter of 1.8 m, are also marked. The UTs are fixed, but the ATs can move along the white tracks to increase the u–v coverage and, at the same time, maintain non-redundancy in combining stellar light. Image retrieved from Ref [6].

between redundant versus non-redundant configuration will be outlined, which are relevant for understanding the design of the pupil remappers in Chapter 3.

1.2.1 *u–v* plane

The Eq. (1.1) gives the object-image relationship behind stellar interferometry. It can be seen that forming the image of a stellar object requires a set of discrete baseline measurements B_i (see Fig. 1.1), such that a discrete set of $\Gamma_i(u_i, v_i)$ can be obtained. These discrete visibilities are then inverted using a Fourier transform to estimate the brightness distribution of the source. Thus, the accuracy of the image synthesis is a function of coverage of the (u, v) coordinates in the Fourier plane.

Consider the plane shown in Fig. 1.4a where an interferometer is formed from 4 telescopes with baselines ranging from 25–150 m. This plane is also known as the aperture plane, where all six possible baselines formed by the 4 telescopes are shown in different colors.[xi] The complementary Fourier plane (or $u-v$ plane) is shown in Fig. 1.4b, which corresponds to an object's position at a declination of 45° and an hour angle of 0°.[xii] It is to be noted that the coordinates in the $u-v$ plane are dependent on the hour angle and declination of the object's position, and the rules of coordinate transformations can be found in Ref [27, Chapter 4]. The six unique baselines of Fig. 1.4a are mapped to 12 single points in Fig. 1.4b, which correspond to both the positive and the negative spatial frequency points due to the Hermitian property of the Fourier transform. To solve the ill-posed image synthesis problem, one has to measure finitely many discrete sets of $\Gamma_i(u_i, v_i)$. Since the spatial frequency in Eq. (1.2) is dependent on B_i and λ_0, filling the $u-v$ plane can be done in two ways: 1) By varying B_i, and 2) By varying λ_0.

To change B_i, one takes advantage of the rotation of the stellar object in the sky as shown in Fig. 1.4c. In some cases, the telescope positions can be changed, e.g. the four 1.8 m auxiliary telescopes at the VLTI facility [26] can be relocated to different positions as shown in Fig. 1.3, which changes the B_i, thus the $u-v$ coverage. In addition to the sky rotation of the object, one can disperse the light as shown in Fig. 1.4d or vary the observed λ_0 from the stellar object using a set of optical filters. Instruments such as GRAVITY [28], and PIONIER [29] at VLTI rely not only on the sky rotation but also on the dispersion of the collected light to increase the $u-v$ coverage.

[xi] For N telescopes in an interferometer, there are ${}^{N}C_2$ pairwise baselines and ${}^{N}C_3$ closure phase triplets. The closure phase will be discussed in Section 1.3.

[xii] The coordinates of a celestial sphere are given by (hour angle, declination), which describes the position of any astronomical object. The hour angle has a range from $-180°$ to 180°, while declination has a range from 0° to 90°.

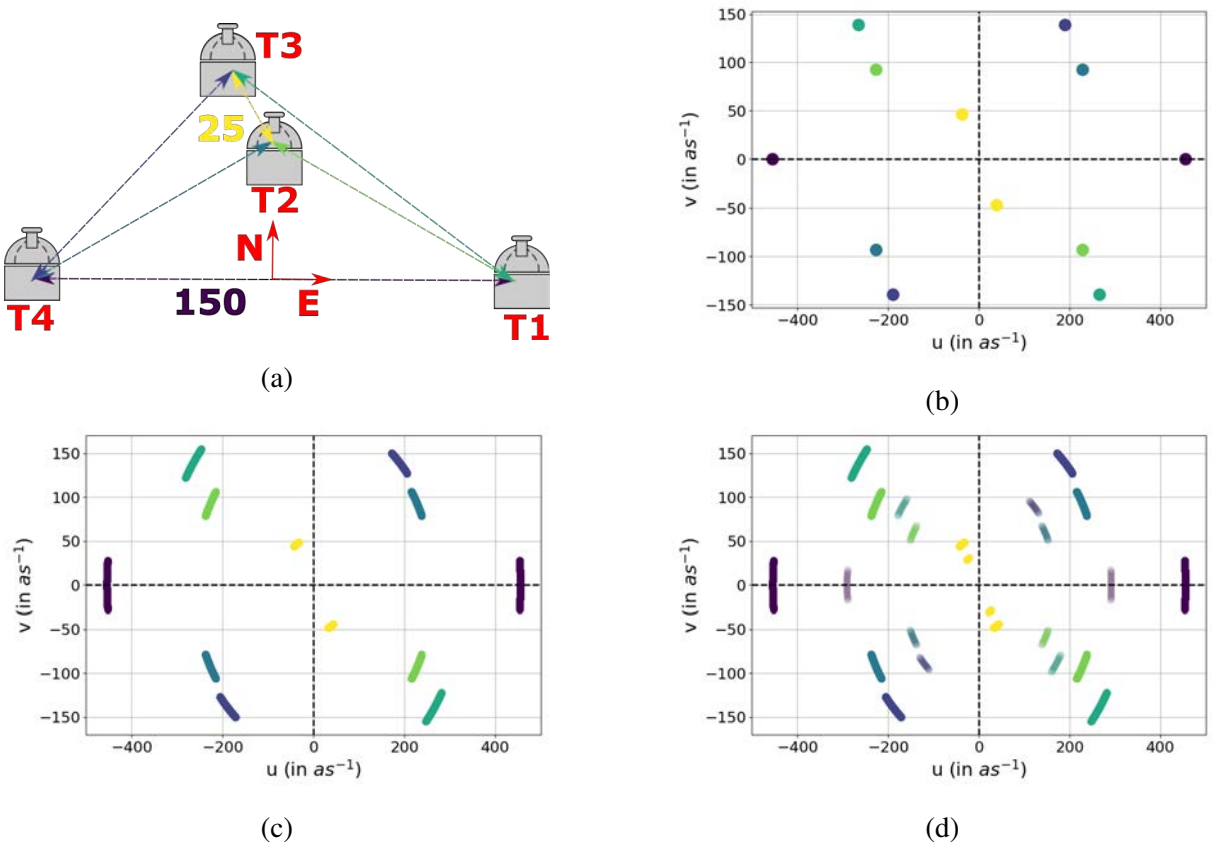

Figure 1.4: (a) Arrangement of 4 telescopes in the aperture plane. The origin is marked as (E, N). The numbers show the shortest and the longest baseline of the arrangement in meters. (b) Snapshot of the 12 spatial frequency points (both positive and negative) in the Fourier plane corresponding to the arrangement shown in (a) for an object's position at a declination of 45° and an hour angle of 0°. The color points show the respective baselines. The units are in arcsecond inverse. (c) $u-v$ coverage of the interferometer assuming that it is tracking the object at a declination of 45° over a range of hour angles from $-5°$ to 5°. (d) $u-v$ coverage of the interferometer with the same assumptions as in (c), but with the dispersion of the collected light. The faint color tracks are for the dispersion direction towards a longer wavelength.

1.2.2 Redundant versus non-redundant configuration

Both Eq. (1.1) and Eq. (1.2) suggest that a set of B_i leads to an unique determination of Γ_i, and its associated spatial frequency is given by (u_i, v_i). Thus, redundancy in interferometers is defined as *a number (R)* when some (u_i, v_i) are repeated in the Fourier plane. Consider an arrangement of three telescopes shown in Fig. 1.5 that differentiates between non-redundant and redundant configurations. In the redundant case, identical baselines produce fringes with the same spatial frequency that cannot be distinguished. As a result, the power associated with the spatial frequency in the interferogram adds incoherently and follows a random walk [30]. Though most of the interferometers across the globe are placed non-redundantly, some of the facilities such as NPOI [31] have partially redundant arrays to uniquely determine the Fourier phases by a method known as *baseline bootstrapping* [32].[xiii]

If SNR_r is the signal-to-noise ratio of a spatial frequency at the interferogram for redundant configuration and SNR_{nr} for that of a non-redundant configuration. Then, assuming additive noise from the turbulence of the atmosphere, mathematically, the relationship is [33]:

$$\frac{SNR_{nr}}{SNR_r} \geq \frac{\sqrt{R}+1}{\sqrt{R+2\sqrt{R}}}. \tag{1.8}$$

It is to be noted that Eq. (1.8) is always satisfied as R increases.

1.3 Closure phase

All ground-based telescopes are susceptible to atmospheric effects, and so are the arms of an interferometer. Atmospheric turbulence creates phase errors that produce various ill effects, such as limiting the maximum useful size of the telescope diameter, affecting the long integration time on the detector, and setting severe limitations on the sensitivity. The phase errors also cause phase shifts in the observed fringes of an interferometer, which erase information about the true phase arising from the stellar object. Due to the loss of this phase information, the imaging of non-centrosymmetric objects is not possible because these objects rely on the Fourier phase information encoded in the true phase of the interferometer fringes [4, Chapter 13]. As a result, the imaging becomes limited to simple objects such as disks or round stars. One way to mitigate such phase errors introduced by the atmosphere is through closure phases (CPs).

[xiii] A method to find unknown phase from known phases and closure phase.

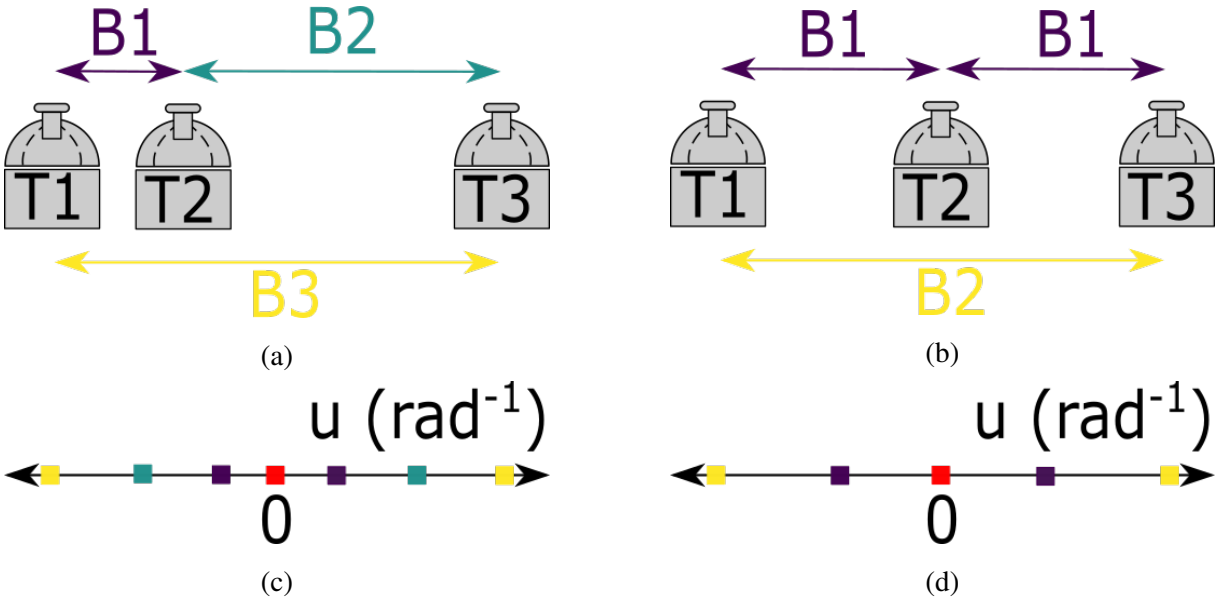

Figure 1.5: (a) Non-redundant arrangement of three telescopes. (b) Redundant arrangement of three telescopes. (c) Spatial frequencies corresponding to the arrangement in (a), where the color points show the respective baselines. All six frequencies (both positive and negative) are marked for the 3-telescope configuration. The units are in radian inverse. (d) Spatial frequencies corresponding to the arrangement in (b). Two of the frequencies are repeated and therefore redundant. From Eq. (1.8), SNR_r is lower than SNR_{nr} by a factor of 0.87.

Consider Fig. 1.6, which shows the turbulent atmosphere above a three-telescope configuration. The phase error can be written mathematically as $\phi_{ij} + \varepsilon$, where ϕ_{ij} is the true phase, and ε is the error term from the atmosphere. The observed phase (ϕ^0_{ij}) at the individual telescopes is then written as:

$$\left.\begin{aligned} \phi^0_{12} &= \phi_{12} + \varepsilon_2 - \varepsilon_1 \\ \phi^0_{23} &= \phi_{23} + \varepsilon_3 - \varepsilon_2 \\ \phi^0_{31} &= \phi_{31} + \varepsilon_1 - \varepsilon_3 \end{aligned}\right\}. \tag{1.9}$$

Hence, the closure phase, which is the sum of three phases around a closed triangle is:

$$\Phi_{123} = \phi^0_{12} + \phi^0_{23} + \phi^0_{31} = \phi_{12} + \phi_{23} + \phi_{31}. \tag{1.10}$$

Thus, the closure phase defined in Eq. (1.10) is an important interferometric observable,

which is immune to phase errors induced either by the atmosphere or by the optical components present in an interferometer. The idea of CP was first introduced by Jennison [34] in the context of radio interferometry to obtain stable phases, but Rogstad [35] is usually credited with extending the feasibility of CP techniques at optical wavelengths. The robustness of CP measurements implies that it alone can be used with the existing imaging techniques to produce high-contrast images of stellar objects [36, 37].

1.4 Scientific motivation

The key attraction of a stellar interferometer is the high-angular resolution that can be achieved by combining light from different telescopes. Unlike a single telescope (tel) of diameter A, where the resolution is given by $\Delta\Theta_{tel} \sim \frac{\lambda}{A}$, for an interferometer (int) with separation or baseline B, the resolution is given by $\Delta\Theta_{int} \sim \frac{\lambda}{2B}$. As a result, the resolution of an interferometer is higher than that of a single telescope by a factor $\sim \frac{2B}{A}$. On the other hand, unlike the size of a single telescope is limited to few tens of meters, an interferometer can have long baselines up to a few hundred meters, thus producing high-contrast images of astronomical targets. Today the interferometer facility, CHARA [38] has the largest baseline of 330 m and produces $\Delta\Theta_{int} \sim 0.5$ mas[xiv] in astronomical H-band[xv], which can resolve a 1.8 m tall man standing on the moon.[xvi]

Astronomy is an observational science, and the theories of stellar formation and evolution rely on obtaining a set of measurements that are the basic parameters of a star.[xvii] These parameters are the basis for testing the evolutionary stellar models. However, many of these parameters are not well known and difficult to measure. In some cases, parameters can be measured using traditional astronomy techniques. One example is doppler spectroscopy, a widely used technique in astronomy to indirectly infer the chemical composition, radius, and orbital period of a star from measuring changes in the frequency of the spectral lines. Interferometry, however, is a direct method that can provide precise measurements of stellar sizes and orbital periods. By combining angular measurements and distances, astronomers can now measure stellar radii with an accuracy of $< 1\%$, and often the precision is set by the distance determination,[xviii] which limits the overall measurement of the actual stellar diameter [40]. The majority of the stars, particularly in the hydrogen burning main sequence of the Hertzsprung-Russell (H-R) diagram, have angular extents from $0.1 - 10$ mas, which is much smaller than the diffraction

[xiv] 1 mas $= \frac{0.001^\circ}{3600}$.

[xv] Assuming, $\lambda_0 = 1.55\,\mu$m.

[xvi] A 1.8 m tall man standing on the moon subtends an angle of ~ 1 mas, as seen from the earth.

[xvii] E.g. temperature, luminosity, chemical composition, mass, and size.

[xviii] In astronomy, distances are measured using parallax, luminosity measurements from either a cepheid variable or from a supernova explosion, to name a few [39].

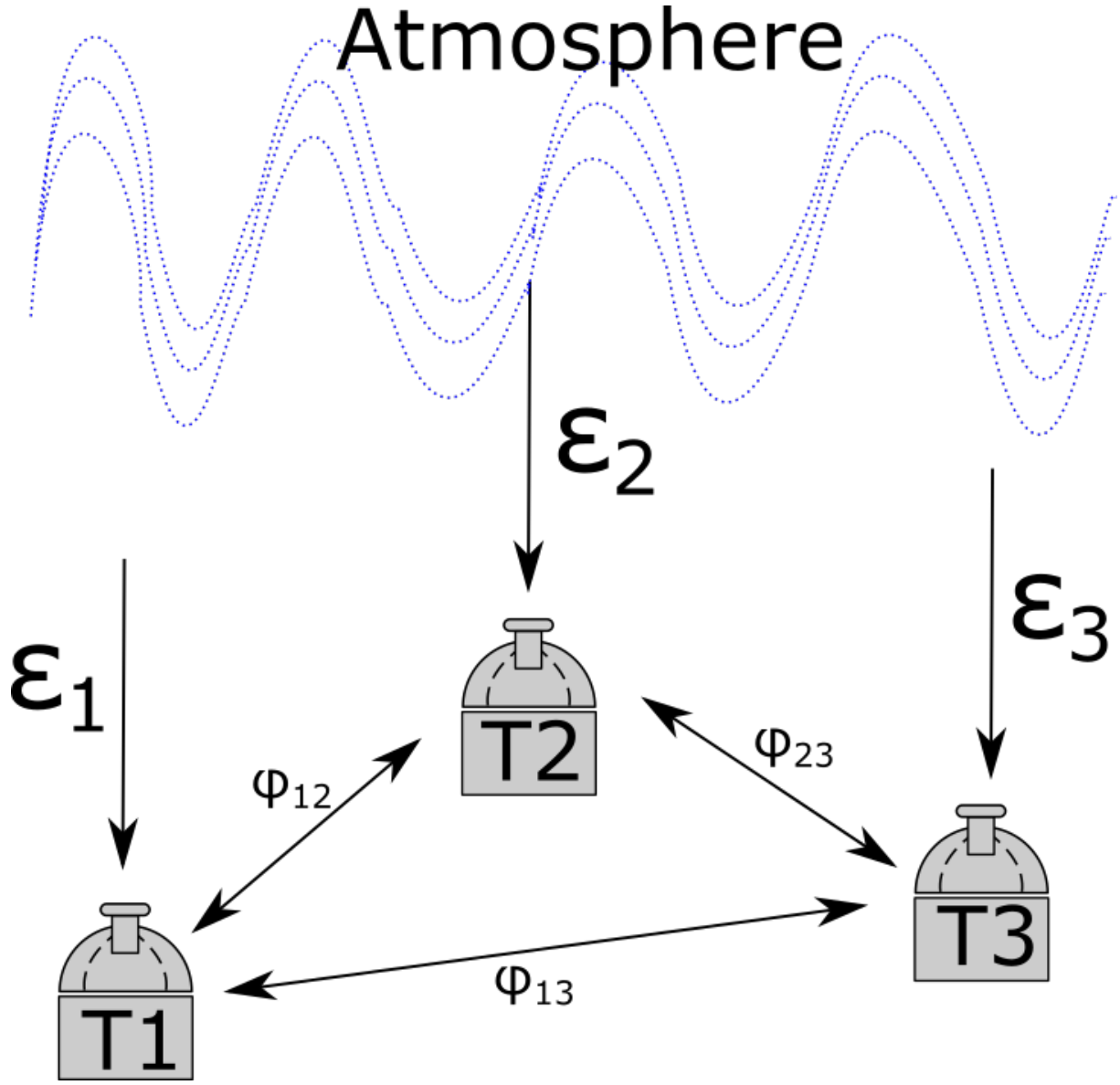

Figure 1.6: The turbulent atmosphere above the interferometer introduces phase errors (ε) at the individual telescopes. As a result, the observed phase at the arm of each two-telescope interferometer is corrupted by an amount $\phi_{ij} + \varepsilon_j - \varepsilon_i$. However, in closure phase, the phase errors cancel out to give $\phi_{12} + \phi_{23} + \phi_{31}$.

limit of even the single largest existing telescope. At this point, long-baseline interferometry is the only direct technique able to resolve not only galactic targets but also beyond extra-galactic objects [41], making stellar interferometry one of the most important tools of our time to address urgent science questions in astronomy.

In the following few pages, the history of stellar interferometry will be outlined. Scientific results obtained using interferometers ranging from basic measurement of stellar diameters to the latest research on the detection of exoplanets will be indicated.

History – The first step towards modern interferometry could be dated back to 1868 in France when Hippolyte Fizeau outlined the basic concept of stellar interferometry on how interference of light could be used to measure the size of the stars. The technique was applied by Édouard Stephan where a mask with two holes was placed at an existing largest telescope[xix] in Marseille Observatory. However, at that time, the achievable $\Delta\Theta_{int}$ was insufficient to resolve even the largest and brightest of the known stars. Later, Albert Michelson developed the mathematical framework for stellar interferometers [20] and is usually credited for founding modern interferometry. Along with Pease, Michelson measured the diameter of α Orionis (Betelgeuse) by building a 20-feet interferometer across the top of the 100 in. telescope on Mount Wilson [22]. Later, Mount Wilson became a choice site for building interferometric facilities such as Mark III (now closed) and CHARA [38], usually due to its excellent atmospheric conditions. Although Michelson has invented stellar interferometry independently, the question arises: Was he influenced by the prior works of Fizeau and Stéphan? Interested readers can read [4, Appendix A] for this exciting history behind stellar interferometry.

Stellar diameters – In the early days, one of the main applications of the stellar interferometer was to measure the diameter of the stellar objects. This led to the direct calculation of the temperature (T_s) of the stellar surfaces, as one can measure the apparent luminosity from the photometry and angular sizes from the interferometry. Empirical calibration of T_s as a function of the spectral type of a star is considered to be necessary since T_s is a fundamental parameter in stellar astrophysics, especially on the H-R diagram [42]. While the giant stars are easy targets due to their large angular sizes and luminosities, interferometric measurements of the lower-mass dwarfs and hotter main sequence remain incomplete. The CHARA interferometer has been used to study the K- and M-dwarfs, but the accuracy of the model in estimating the true stellar radii had errors of $\geq 15\%$ [43]. For such dwarf stars, it was found out that the atmosphere is a vital function of metallicity.[xx] Recently, the systematic errors in predicting the radius improved to $\leq 5\%$ by incorporating the metallicity parameter and recalibrating the stellar models [44].

[xix] It was an 80 cm reflecting telescope built by Léon Foucault.

[xx] Defined as the difference between the common logarithm of the ratio of a star's iron abundance and that of the Sun. It is denoted by [Fe/H].

Stellar atmospheres – Stellar photospheres are known to be limb-darkened, which happens due to the optical depth effects. Limb-darkening can be seen in the Sun, where the center appears bright and as one goes away from the center towards the perimeter,[xxi] it appears to be dimmer as well as redder than the center. As a result, to correctly estimate the angular sizes, stellar models have to be recalibrated for incorporating limb-darkening effects. The main difficulty for limb-darkening studies lies in the precise observations that have to be made beyond the first null of a uniform disk (see Fig. 1.2b) to detect the limb-darkening effects [42]. Measuring limb-darkening is difficult because the fringe contrast beyond the first null is lower than the central lobe. The precise measurements required to detect limb-darkening were made using the Mark III interferometer on Arcturus (α Boo, K1III) as shown on Fig. 1.7a and Fig. 1.7b, by employing a novel phase-referencing technique to increase the SNR beyond the first null. The detected results also agreed well with the theoretical models [7]. Along with limb-darkening effects, interferometers have been used to study the photospheres of cool giants,[xxii] especially the Mira variables.[xxiii] The COAST interferometer was first used to detect the pulsation of an O-rich Mira, R Leonis, at visible wavelengths that had good agreement with the previously measured light curves [45]. It was found that the pulsations in the Mira variables are due to the presence of H_2O molecules in the photosphere, causing a significant increase in the apparent sizes at IR-wavelengths [42]. Another O-rich Mira, R Aquarii, was dramatically larger at 3.1 μm than at shorter wavelengths, as shown in Fig. 1.7c [8].

Stellar surfaces – Interferometers have been used to investigate 'hotspots' on red giants and supergiants [42], with Betelgeuse being one of the most well-known examples. Hotspots are hot patches on the photosphere of a star, which may be due to shock waves caused by pulsation or convection in its outer layers, and are yet still a mystery [46]. Some of the hotspots appear in the visible wavelengths but disappear in the near-IR. Multi-wavelength studies suggest that these hotspots for M-spectral stars are due to inhomogeneous TiO molecules present in patches causing visible light to pass through it but absorbing in the near-IR [47]. Unlike 'hotspots', 'sunspots' are cool areas caused by strong surface magnetic fields that inhibit convection. The CHARA interferometer has been used to image the magnetically active star ζ Andromedae, confirming the existence of a controversial, dark polar sunspot, which indicates that a solar-type dynamo cannot produce these patterns [48].

Binary systems – Interacting binaries are stars that orbit each other so closely that tidal effects become important. As a result, each star's gravitational field distorts the outer layers of the other, which leads to mass transfer between them. These systems are of significant interest because strong binary interactions are thought to produce: 1) Standard-candle Type Ia supernovae, and 2) A binary system of a pulsar and black hole [40]. The final states in

[xxi] i.e. the limb.

[xxii] Mostly M spectral types.

[xxiii] A class of pulsating stars.

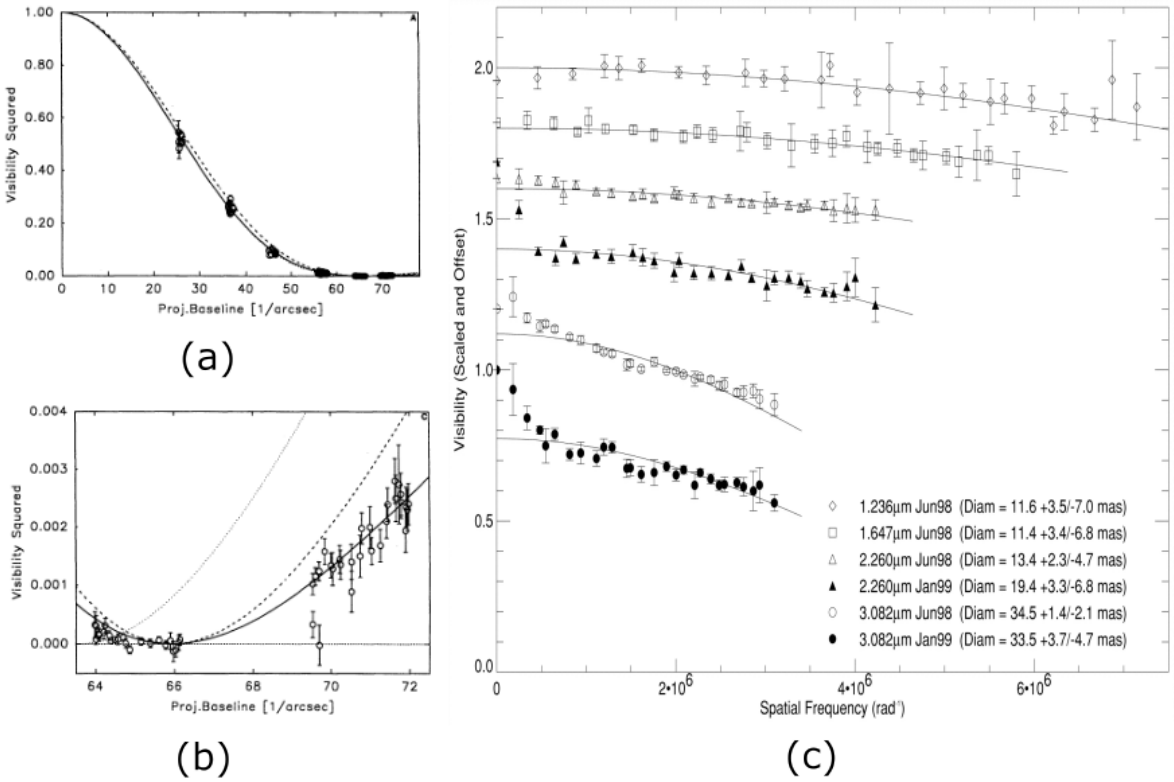

Figure 1.7: (a) The visibility data and model fitting of a limb-darkened star, Arcturus, with respect to projected baseline length obtained from the Mark III interferometer. (b) A zoomed view of (a) around the first null/zero. The dotted line is a uniform disk model which gives the best fit to the data on short baselines but has large errors beyond the first null. The dashed line is also a uniform disk model, but with the first null taken into account, which has a better estimate than the dotted line. The solid line is a limb-darkened model, which estimates the diameter to be ~ 21.1 mas. (c) Visibility data of a Mira variable, R Aquarii, at different wavelengths, which was observed using aperture masking interferometry (see details in Section 1.4.2) on the Keck telescope. For clarity, the visibility plots are offset by multiples of 0.2 to separate the various data sets. The solid curve shows the best-fitting uniform disk model with reported diameters in the legend. At $\lambda_0 \sim 3.1\,\mu$m, there is a diameter increase roughly by a factor of 2 when compared to shorter wavelengths, which is due to the molecular emission produced at the photospheres of cool giants. The results of (a), (b), and (c) suggest that depending on the types of stellar astrophysics studies; one has to precisely recalibrate the stellar models taking into account various effects such as limb-darkening, pulsations, formations of molecular lines, and oblateness of stars, to name a few with the observational visibility data. Images (a) and (b) retrieved from Ref [7], Image (c) retrieved from Ref [8].

interacting binaries are hard to predict due to difficulties in tracking their angular momentum exchange and the lack of direct detection techniques [40]. Interferometers have been used to image an interacting binary, β Lyrae, as shown in Fig. 1.8, revealing the gravitational distortion between the bright mass donor and the faint gainer with a thick planar disk surrounding the star system [9]. Another interacting hydrogen-deficient binary, ν Sagittarii, was also imaged, revealing the thick flat disk around the system [49].

Circumstellar environments – Interferometers have been used to probe the stellar environment in order to study the gas and dust around stars that might not be uniformly distributed and may be changing with time. One example is about studying the Balmer line emission (H_α) around Be stars. The term 'Be stars' is used to describe stars that are hot and non-supergiants, have spectral type B, with H_α spectrum emission, presumed to be fast rotators spinning at 200 km/s, and have a sizeable stellar wind with a high mass-loss rate. Be stars are an essential source of UV photons that are ionizing the interstellar environment, thus playing an essential role in the heating of the gas as well as the formation of radiative shocks in the interstellar medium [50]. The envelope of a Be star, γ Cas, was first resolved using the I2T interferometer [51].[xxiv] Later, the high spectral resolution of GI2T uncovered the asymmetric H_α emission of the Be stars, which are one-sided and time-varying [53]. Recent studies using interferometric measurements suggest that these asymmetries could be due to the outburst of the central star or due to a decrease in the radiative force at the base of the photosphere [54].

Young stellar objects (YSOs) – YSOs are stars in the first phase of their lives before they enter the main-sequence of the H-R diagram [55]. YSOs are formed by the contraction of molecular clouds. The term describes a class of objects that includes protostars, proto-stellar disks, Herbig-Haro objects, and pre-main-sequence stars, the study of which plays an essential role in understanding star and planet formation. Interferometry is the key to studying the inner regions ($\sim$ 1 AU) of these YSOs. The first YSO to be resolved was the Herbig Ae/Be star,[xxv] AB Aurigae with the IOTA facility. The interferometric data could consistently be fitted with a visibility model that assumes circumstellar material lying in a flattened structure with a large central hole around AB Aurigae [56]. Interferometric studies were also conducted for some of the Herbig Ae stars by the VLTI interferometer, where compositional analysis of the innermost ($\sim$ 2 AU) dusts surrounding these stars were performed. Results showed that the composition of the dust varied with the disc radii, and the spectrum of the inner disk showed surprising similarity with our solar system comets [57].

Active galactic nuclei (AGN) – AGNs, which have long puzzled astronomers, are now understood to be active supermassive black holes at the center of the galaxies that emit jets and

[xxiv] It is to be noted that I2T was the first stellar interferometer built by Antoine Labeyrie, which used two small telescopes separated by 12 m. The I2T facility obtained its first fringes from Vega, thus building the foundations for long baseline stellar interferometry at optical wavelengths [52].

[xxv] A pre-main-sequence star of spectral types A or B.

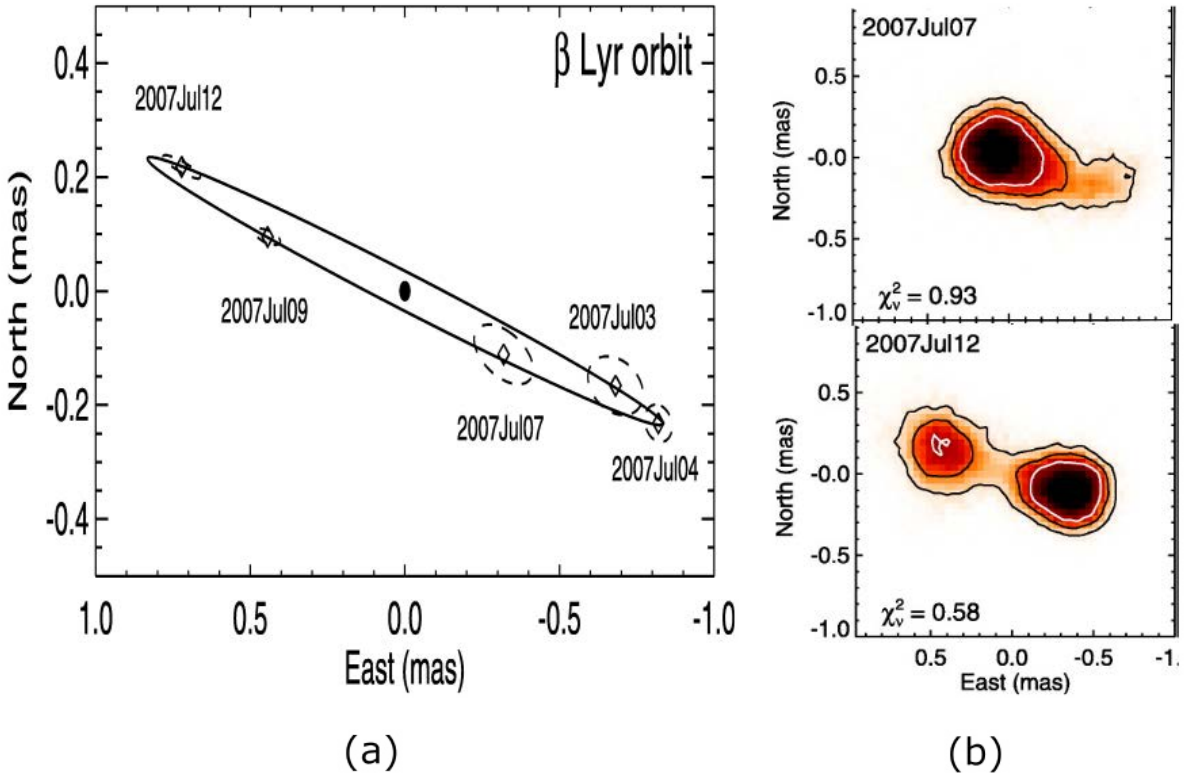

Figure 1.8: (a) The astrometric orbital motion of an interacting binary, β Lyrae, obtained with the CHARA facility. The solid line is the best-fit orbit of the system. A filled dot in the center indicates the donor. Positions of each epoch are shown by open dots, which are surrounded by their error ellipses in dashed lines. (b) Reconstructed images of the binary system. Two different epochs are mentioned in the top left corner of each image. Darker colors correspond to higher intensity, and the darker component is the donor. The contours in the images correspond to 0.3, 0.6, and 0.9 of the peak intensity. The goodness of the fit, χ^2, of each image is shown in the bottom left corner. The separation of the stars in the system in the top and bottom images is 0.34 mas and 0.754 mas, respectively. These results show the gravitational distortion of the bright mass donor and the faint component with an elongated planar disk surrounding the star system. Images (a) and (b) retrieved from Ref [9].

winds, which have an electromagnetic spectrum from X-rays to radio waves [58]. AGNs have a doughnut-shaped structure (sometimes called as torus) of gas and dust that orbits around supermassive black holes. The particles in the torus periodically rub together, which generates heat as well as light and ejects materials along very strong magnetic fields into jets and winds. AGNs have several classifications based on their distances from Earth: Seyfert galaxies are nearby, while Quasars[xxvi] are very distant, point-like sources. The VLTI has been used to resolve several of the nearest Seyfert galaxies (e.g. NGC 3783 [59], NGC 1068 [60] and Circinus galaxy [60]). The results of the dust structures show that these galaxies contain an elongated inner component that is embedded in a larger dust distribution, thus confirming the torus structure of the AGNs.

Galactic center – The recent 2020 Nobel prize in physics was awarded for the discovery of a supermassive black hole (Sgr A^*) at the center of our Milky Way Galaxy.[xxvii] From the analysis of orbits of more than two dozen stars and the measurements of size and motion of the central compact source, Sgr A^* is found to be a massive black hole of about $\sim 10^6 M_\odot$. The GRAVITY instrument at VLTI has been mostly used to observe the galactic center of our Milky Way by studying the relativistic orbital parameters of one of the stars – S2 around the Sgr A^*, and also to track down the motion of Sgr A^* flares on short timescales [10]. Interferometric results as shown in Fig. 1.9 of the highly elliptical,[xxviii] 16-year orbital period of star S2 around Sgr A^* reveals that near the pericenter,[xxix] the star has an orbital speed of 7650 Km/s[xxx] [11]. It also has a Schwarzschild precision of $\approx 12'$ per orbital period [62]. Thus, the model fitting of the relativistic orbital parameters of the star, S2, implies that the observational data cannot be merely explained by pure Newtonian dynamics but by correction terms from General relativity – the theory developed by Einstein almost a century ago.

Exoplanets – Exoplanets are planets outside the solar system, which come in a wide variety of sizes – from gas giants comparable with Jupiter to rocky planets as big as Earth or Mars. Using direct imaging, the GRAVITY instrument at VLTI was first used to detect a gas giant, HR8799 e, and its precise orbital path along with surface gravity, temperature, radius, and mass of the exoplanet was calculated [63]. When fully operational, the recently launched space based-telescope James Webb space telescope (JWST, see Fig. 1.11a) will have an aperture masking interferometry mode to enable mid-IR characterization as well as search for the exoplanets [64].

[xxvi] Derived from the term 'quasi-stellar radio sources'.

[xxvii] Interested readers can follow the works of Genzel et al. and references therein, which explains the theoretical and observational work on central massive black holes [61].

[xxviii] Ecentricity $= 0.88$.

[xxix] At 120 AU $\approx$ 1400 Schwarzschild radius.

[xxx] Roughly $\sim 3\%$ of c.

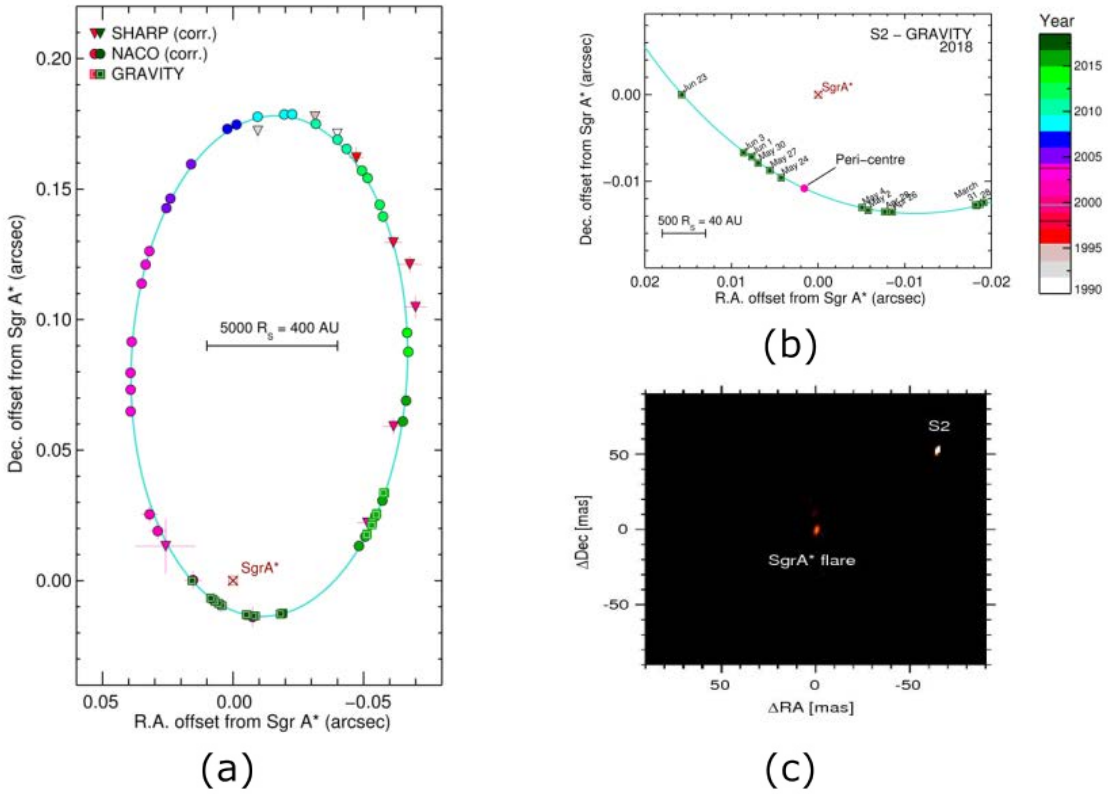

Figure 1.9: Monitoring of the astrometric orbital motion of S2 around the supermassive black hole, Sgr A^* at the center of our Milky Way Galaxy. (a) The projected orbit of the star S2 on the sky relative to Sgr A^*, where Sgr A^* is shown as a brown crossed square at the origin. Triangles and circles with 1σ uncertainties denote the SHARP and NACO instrument position measurements at the NTT and VLT, respectively. Green squares denote the GRAVITY measurements at the VLTI. (b) A zoomed picture around the pericenter of the S2/Sgr A^* system in 2018 was taken using the GRAVITY instrument. The cyan curve shows the best-fitting S2 orbit to the data, including the effects of General relativity. The color bar shows the time scale. (c) Reconstructed image during the flaring of Sgr A^* and the star S2 system. The peak brightness during the flare was ≈ 15 mag. The flares are light emissions due to the electronic transitions caused by mass loss of very close orbit stars around Sgr A^*, and the mass loss mechanism is caused due to the friction [10]. Images (a) and (b) retrieved from Ref [11], while Image (c) retrieved from Ref [12].

1.4.1 New technologies and techniques

The applications of stellar interferometry presented in the previous section have made substantial contributions in the exciting research areas of astronomy and astrophysics, including the precise measurement of stellar diameters, imaging of stellar surfaces, the study of circumstellar disks around YSOs, predictions of Einstein's General theory of relativity at the galactic center and the direct search for exoplanets to name a few. All these were possible due to the active implementation of new technologies and techniques that have pushed the limits of sensitivity and calibration precision of current interferometers. In this section, the novel techniques and technologies that are most relevant in the context of this Thesis will be introduced.

One of the important implementations of novel technology was the use of single-mode fibers in stellar interferometers, which greatly enhanced the calibration precision on visibilities.[xxxi] E.g. the FLUOR [65] instrument that uses single-mode fibers for combining light at IOTA had visibilities uncertainties of $< 1\%$, which was a real breakthrough. While combining light from two telescopes using fibers is straightforward, combining light from multiple telescopes is a challenge. The light from multiple telescopes must be split and combined many times. As a result, precise matching of path lengths in optical fibers must be maintained to reduce the spurious effects of differential chromatic dispersion and polarization. An elegant solution to this problem, while maintaining the advantages of spatial filtering, is the use of integrated optics-based beam combiners, which is described in detail in Section 1.4.4. Recently, the term *astrophotonics* is generically used to describe the ongoing advancements in photonics technology for astronomical instrumentation [66, 67]. Another critical advancement in increasing the sensitivity of interferometers is by applying adaptive optics (AO) on ground-based telescopes, which corrects for the wavefront perturbations caused by the atmosphere. However, AO has its limitations in producing high fidelity images due to the difficulties in calibrating the PSF of an AO system. The calibration problem of the PSF comes from the high spatial frequency terms, which include finite spatial bandwidth and non-common path errors from the AO system [68]. This PSF calibration problem is mitigated in interferometry by using masks in the pupil plane of the telescope (see Section 1.4.2) or using a technique known as phase referencing. The phase referencing interferometry [69] is extensively used in the VLTI, where two stars[xxxii] are picked up in the interferometric field-of-view, and fringes are obtained simultaneously for both the stars. The fringes obtained on the reference star are then used to calibrate the target star. As a result, bias-free[xxxiii] and precise visibilities of the faint target star are measured.

Drastic progress has also been made for the spectroscopic capabilities of an interferome-

[xxxi] The spatial filtering advantage offered by single-mode fibers is discussed briefly in Section 1.4.3.

[xxxii] E.g. one could be a bright reference and the other could be a faint target star.

[xxxiii] T_i, T_a terms $\rightarrow 1$ in Eq. (1.6).

ter, which can be achieved by dispersing the light using a prism or diffraction grating to probe molecular lines[xxxiv] in the stellar atmosphere. Lastly, the technological advancement in detectors has pushed the sensitivity limits of current interferometers. Due to the respective cutoff wavelengths, Si is the preferred material of choice in the visible, InGaAs in the near-IR, and HgCdTe in near-IR and mid-IR wavelengths. Generally, near-IR detectors have high readout noise, which can be substantially reduced by using avalanche photodiodes (APDs). There are two different technologies for capturing images digitally: charged coupled device (CCD) and complementary metal-oxide semiconductor (CMOS). Whether CCD or CMOS-based image sensors should be used depends on the type of application, where either one or the other technology can be advantageous.

To give an example of how the different technologies and techniques that were described above are used in a cutting-edge instrument, some key features of the GRAVITY instrument [28, 12] at VLTI are briefly described. The GRAVITY instrument works in the astronomical K-band (2.1 μm). It utilizes the technique of phase referencing, and at its heart are two 4-telescope beam combiner devices[xxxv] based on planar integrated optics. The device's inputs are fed by single-mode fibers, which allow for accurate polarization control and monitoring of differential OPD between the target and reference star. Each of the unit telescopes in VLTI is equipped with the IR adaptive optics system – CIAO – to correct the atmosphere. The stellar light is captured in detectors made of HgCdTe, which are APDs with an effective readout noise of $< 1e^-$ rms. With these subsystems in place, the GRAVITY instrument can perform phase referencing interferometry of faint objects with a limiting magnitude of $m_k \approx 17$ mag, within an integration time of a few tens of minutes. The instrument reaches visibility accuracy of $< 0.25\%$, closure phase accuracy of $< 0.5^0$, multi-wavelength interferometric imaging with a spectral resolving power of $R \approx 4500$, and differential astrometry with a few μas precision [12].

1.4.2 Aperture masking

The use of masks in the telescope pupil to mitigate unknown phase errors from the atmosphere was proposed by Rhodes et al. [70]. The concept was extended to optical interferometry and demonstrated by Baldwin et al. [71], where they placed a mask with three non-redundant holes in a re-imaged pupil plane of the telescope. The experiment was performed at the University of Hawaii 88-inch Telescope on Mount Kea, where visibility amplitude and closure phase measurements were made on β Ori and β Tau. Later, Haniff et al. were the first to obtain diffraction-limited images of λ Peg (a single star) and ϕ And (a binary system) at the 2.5 m

[xxxiv] E.g. CO, H_2O.

[xxxv] One device for bright reference and one for faint target star.

Issac Newton Telescope on La Palma using four non-redundant holes in the aperture mask [36]. In that time, several other groups also obtained diffraction-limited images of stellar targets from visibility and closure phase measurements using three or more holes in the mask placed at the aperture plane [72, 37]. Thus, aperture masking[xxxvi] is an interferometry technique where a mask with holes is placed in the re-imaged pupil plane of a telescope. The light emanating from the holes is then combined for high-contrast imaging of ground-based telescopes.

More recent examples of aperture masking include measurements with the Keck I Telescope (see Fig. 1.10), where morphologies of dusty envelopes around YSOs and the circumstellar shrouds surrounding evolved giants and supergiants were revealed [13, 73]. From spectro-interferometric measurements, Mira variables were studied allowing to probe the atmospheric structure, including zones of H_2O, CO, OH and dust formation [74, 75]. There are also measurements where optical interferometry data from multiple facilities were combined to increase the $u-v$ coverage, thus allowing imaging of both the star and the surrounding dust shell [73]. In one case, the data from the Keck aperture masking and the IOTA data were combined to study the deviations in the dust shells, and the photospheres of the most evolved M spectral stars [76]. Finally, aperture masking is not limited to ground-based telescopes but has been implemented on the recently launched space-based telescope JWST in the instrument named 'NIRISS', which contains a mask with seven non-redundant holes (see Fig. 1.11) [77]. In this mode, JWST will detect the thermal emission of young massive planets and will permit the mid-IR characterization of exoplanets [64].

Despite the exciting science cases and results delivered by aperture masking, it still suffers several disadvantages. Most of the holes in the masks have to be arranged such that it reduces the redundancy noise given by Eq. (1.8), thus posing constraints on the number of holes that can be used in the mask. This results in low-throughput of the incident starlight, typically 80-90 % of the light is lost at the mask [30]. Furthermore, due to the finite size of the holes in the masks, atmospheric phase noise is still present. While this can be mitigated by reducing the size of the holes, this would further limit the SNR of the instrument.

Hence, to tackle these problems in aperture masking, the advances in fiber and optical waveguide technologies have led several separate groups to independently propose a new imaging methodology: Pupil remapping interferometry – one of the applications of *astrophotonics* in interferometry.

[xxxvi] Sometimes known as aperture synthesis or synthesis imaging.

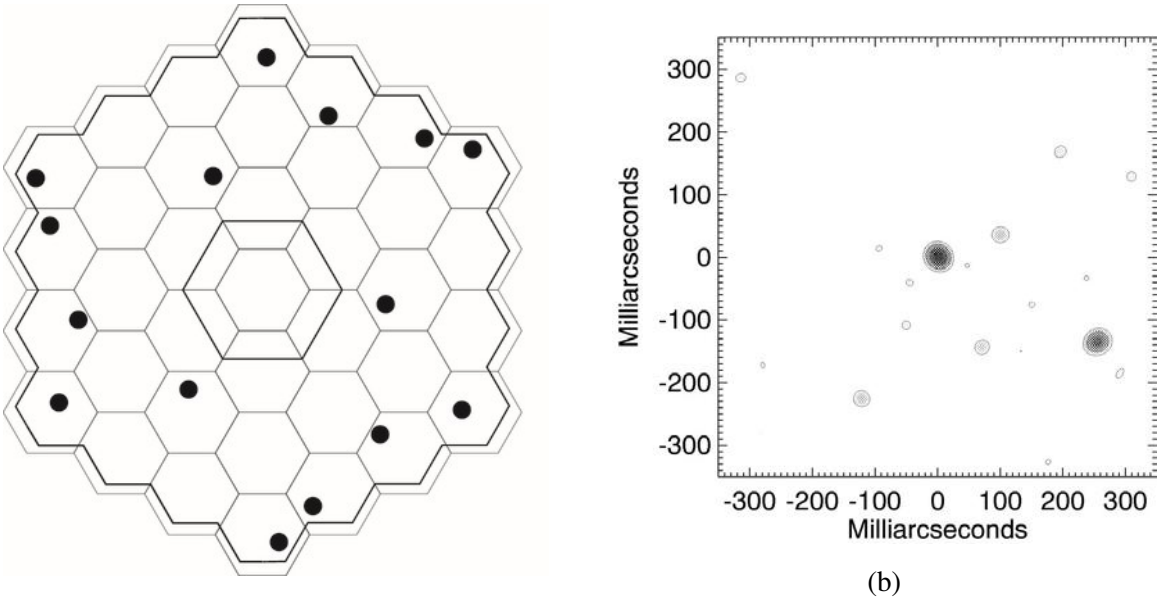

(a) (b)

Figure 1.10: (a) Aperture masking on the 10 m Keck telescope. The black spots are the diffraction-limit holes, which are superimposed on the segmented mirror of the Keck telescope. (b) Reconstructed astronomical K-band image of the binary star 126 Tau with a separation of 287 mas. The logarithmic contour levels, at 0.2 %, 2 %, 20 %, and 70 % of the peak, show the noise features in the map. Images retrieved from Ref [13].

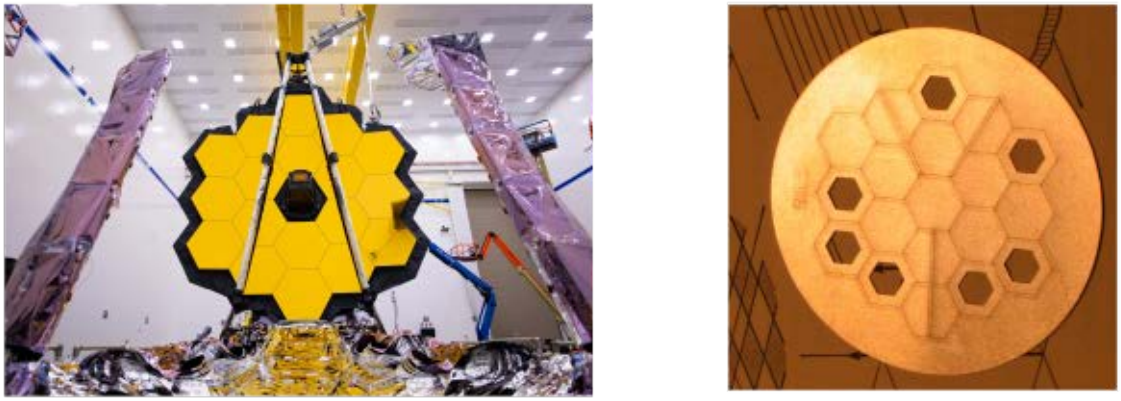

(a) (b)

Figure 1.11: (a) The primary mirror of the James Webb space telescope (JWST) with a diameter of 6.5 m. The JWST is recently launched and is currently in operation. (b) A prototype of the non-redundant mask that will be used in the NIRISS instrument of the JWST. The mask has seven hexagonal holes with the transmission of $\sim$ 15% of the light incident on the mask. The holes are smaller than the re-imaged pupil to allow for misalignment error in the optical system. Images (a) and (b) retrieved from Refs [14] and [15], respectively.

1.4.3 Pupil remapping

As mentioned in Section 1.1, one of the main challenges in long-baseline interferometry at optical wavelengths is the calibration of fringe visibility, especially the atmosphere transfer function T_a in Eq. (1.6). The difficulty can be overcome by the use of single-mode fibers, which spatially filter the incident beam [78, 79]. One should recall that the beam profile propagating inside a single-mode fiber is determined by the waveguide physical properties and not by the incoming wavefront. The phase of the wavefront across the guided beam of the fiber is constant, and the guided beam, therefore by definition, is coherent [80, Chapter 7]. Due to atmospheric turbulence, the field amplitude distribution at the telescope's focal plane varies with time. If a single-mode fiber is placed at the focal plane, then depending on the field distribution due to the atmosphere, the intensity of the coupled beam also varies. Thus, single-mode fiber transforms the incoming wavefront phase corrugations into outgoing intensity fluctuations of the coupled light. It is to be noted that, unlike wavefront perturbations, the intensity fluctuations can be easily monitored and calibrated against the effects of atmospheric distortion. Single-mode fibers for stellar interferometry were first implemented in the FLUOR [81] instrument at IOTA, which has demonstrated accurate visibility measurements with statistical errors of $< 1\%$ over a dozen of stars [23].

Thus, pupil remapping combines the aperture masking technique with single-mode fiber technology for the high-angular resolution of a single telescope. In other words, the pupil remapping technique uses single-mode fibers to map the input pupil to a non-redundant output pupil, thus turning any single ground-based telescope into a multiple-beam interferometer (see Fig. 1.12). The light from each pair of single-mode fibers at the output pupil corresponds to a unique spatial frequency component such that complex visibility is measured and calibrated. Thus, high-dynamic range and high-contrast images of astronomical targets are reconstructed from the unique visibilities by exploiting Fourier techniques that are already well-established for long baseline interferometry [82].

The advantages of pupil remapping system are as follows: 1) Unlike aperture masking, the entire pupil area of the primary mirror of the telescope can be used [16], 2) The use of single-mode fibers filters out atmospheric turbulence effects by spatially filtering the output beam [23], 3) The output fibers are placed in a non-redundant pupil configuration, which gives unique spatial frequencies [33]. Therefore, this technique removes both the atmospheric distortion and redundancy noise, thus allowing for a perfect calibration of the degraded wavefront. The technique also takes advantage of the intrinsic angular resolution of the telescope and enhances the SNR due to the large photon collecting capability [83].

The first proposal for a single telescope pupil remapping interferometer was based on

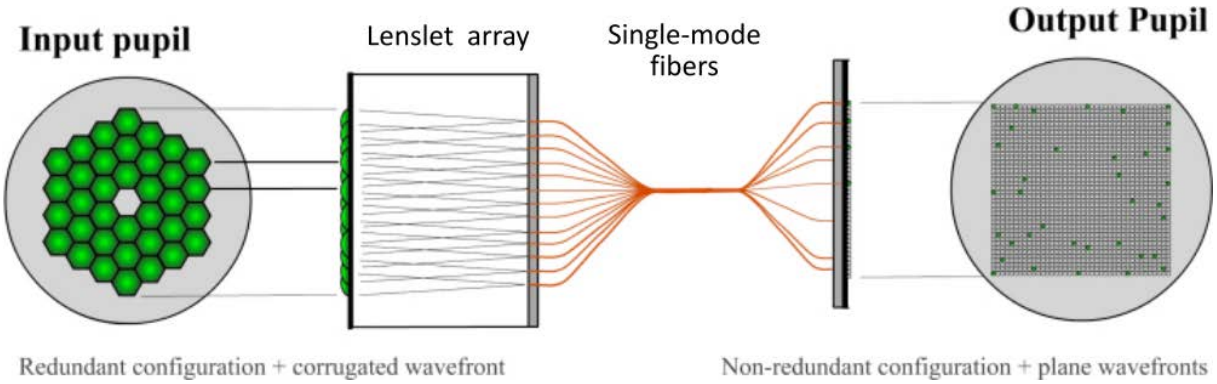

Figure 1.12: A conceptual design of a pupil remapping setup. The input pupil is shown as 36 hexagonal green segments arranged in a hexagonal pattern. The input pupil is mapped to a lenslet array (shown in black), arranged in the same hexagonal pattern as the input pupil. At the back focal plane of the lenslet array, there are 36 single-mode fibers (shown in orange) that rearrange into a non-redundant output pupil configuration. Each lenslet eases the coupling of the subpupil beam into a single-mode fiber. The green spots in the output pupil show the fiber ends. Each pair of subpupils in the input pupil corresponds to a single spatial frequency component in the output pupil. Assuming the input wavefront is corrugated due to the atmosphere, the spatial filtering offered by single-mode fibers forces the field distribution across the fiber to be uniform. The emergent wavefront from the fiber is therefore coherent. Image retrieved from Ref [16].

an instrument concept known as DAFI [84, 79], which appeared in the late 1990s. A decade later, papers were published from Perrin et al. [16] and Lacour et al. [82], exploring the technical and scientific aspects of such a pupil remapping concept with quantitative projections of performance, SNR, and dynamic range for a working device [30]. Later, two independent projects, namely the French "FIRST" and the Australian "Dragonfly", started their work independently on single-telescope pupil remapping interferometer from the initial conceptual design (see Fig. 1.12) to develop a laboratory prototype. The FIRST instrument relies on single-mode fibers as pupil remappers following the simulation works of Perrin et al. [16]. The FIRST instrument has already been demonstrated in the laboratory [83], and on-sky [85], showing promising results under real observing conditions, thus validating the concept of fiber-based pupil remapping interferometry. The spectroscopic capability has also been demonstrated, showing the power of FIRST to provide valuable spectral information for the characterization of binary systems [86].

On the other hand, the Dragonfly instrument is an integrated optics (IO)-based pupil remapping interferometer, where single-mode waveguides are fabricated using ULI and are embedded in a single miniaturized monolithic chip [30]. The on-sky experiments with the Dragonfly instrument have been completed [87], and laboratory prototypes with improved throughput and stable closure phases have already been developed, which are foreseen to be implemented in a second-generation instrument for sensitive observations of exoplanetary systems [88]. Re-

cently, a 3-D pupil remapping interferometer was connected to a nulling interferometer[xxxvii] that was written monolithically using ULI. This so-called "GLINT" instrument was successfully tested on-sky, measuring the angular diameter of various stars [90]. More recently, a laboratory prototype is realized, achieving a standard deviation in CP of $< 1^\circ$ and demonstrating advanced hybridization and packaging techniques. The prototype uses different integrated photonics fabrication platforms, where a 3-D 8-input pupil remapper device written using ULI is connected with a planar 8-port ABCD pairwise beam combiner written using lithography, along with necessary injection optics for coupling of light, into a single integrated monolithic device [91].

Therefore, in the context of stellar interferometry and the need for enabling high-angular resolution of ground-based telescopes, one of the main goals of this Thesis is to develop an IO-based pupil remapping interferometer. The pupil remappers are connected to a discrete beam combiner (see Section 1.4.4) to form a compact and monolithic IO device. The device will retrieve the complex visibilities to allow high-contrast images of astronomical targets. In the following section, IO-based beam combiners are discussed, which form an important aspect of this work.

1.4.4 Integrated optics-based beam combiners

Integrated optics (IO) is a technology that aims at fabricating integrated optical devices (sometimes called photonic integrated circuits (PICs)) on a single substrate. These PICs can contain several different optical components for manipulating light, thus analogous to electronic circuits. Some of the optical components in PICs could be as simple as a single-mode waveguide for transporting light from input port to output port and as complex as an arrayed-waveguide grating (AWG) consisting of a cascade of single-mode waveguides for wavelength multiplexing or demultiplexing applications. The fabrication of PICs takes advantage of contemporary CMOS technologies, which are already well-established and mature in the semiconductor industry. The advantages of IO components over their bulk optic counterparts are manifold: 1) Complex structures serving multiple functions can be manufactured in compact sizes, 2) Less sensitive to environmental fluctuations,[xxxviii] 3) No additional mechanical alignment is required

[xxxvii] Nulling interferometry – first proposed by Bracewell [89] is a technique of manipulating the phases of the individual beams such that the light interferes destructively, as opposed to conventional interferometry technique where light interferes constructively [90]. Thus, the starlight is effectively 'nulled' out for a star-planet system, and the light from the faint off-axis planet remains. As a result, the technique is used for detecting faint circumstellar materials and companions, which finds applications for exoplanet searches and zodiacal dust disc characterizations [42].

[xxxviii] E.g. thermal drift, moisture, and vibrations.

other than injecting-in or ejecting-out light, 4) Less weight, 5) Low power requirements, and 6) Possibility of batch fabrication with reduced cost. However, IO components also have challenges, such as higher losses than free-space optics, limited wavelength coverage, dispersion, and birefringence.

The concept of IO beam combiners for applications in astronomical interferometry was first proposed by Kern et al. [78]. They pointed out: 1) The advantage of spatial filtering offered by single-mode waveguides, and 2) Simple optical layouts offered by IO beam combiners that could be designed in case of light combination from multiple telescopes. Later, Berger et al. [92] manufactured a two-telescope beam combiner along with two photometric outputs on a standard glass substrate using ion-exchange technology. The group reported first white-light fringes with a contrast of 78% and a throughput of $\sim 43\%$ were obtained at astronomical H-band ($1.54\,\mu$m), which demonstrated the feasibility of IO-based beam combiners for astronomical interferometry. This group also developed the IONIC instrument that consisted of a two-telescope IO-based beam combiner, which was tested at the VLTI to obtain fringe contrasts of 85% [93]. Later, the IONIC instrument was upgraded to IONIC3 [94] that consisted of a three-telescope IO-based beam combiner and was installed at the IOTA facility. The IONIC3 instrument was used for imaging of binary system Capella (α Aur), resolving the disks of the two stars [95]. It was also used to study several YSOs, where it was found that a few of them had skewed disks, potentially due to the presence of stellar halos [96]. The success of IONIC and IONIC3 led to the commissioning of the GRAVITY [97, 28] and PIONIER [29] instruments that consisted of four-telescope IO-based beam combiners for the VLTI at the astronomical K- and H-band, respectively. The GRAVITY beam combiner – an *astrophotonics* component – has been used to study many exciting research areas of astrophysics, one being the observations of our Galactic center [12], which was discussed in detail in Section 1.4. It is clear that combining light with many beams using bulk optics requires dozens of beam splitting and combining components as shown in Fig. 1.13a, which is a three-telescope CLIMB combiner [17] at the CHARA facility. However, integrated optics devices such as GRAVITY, as shown in Fig. 1.13b, have proven to miniaturize this process, where the whole optical table is now replaced by a single chip of few cm lengths, with a near-perfect beam combination and little alignment.

Depending on the specific design, beam combiners use different ways to encode the fringes as well as to route and interfere with the baselines. The fringes can be encoded either spatial, temporal, or matricial. In contrast, the baselines can be encoded either all-in-one, partial or pairwise.[xxxix] It is the subject of debate whether one architecture of the beam combiner is more favorable than the other. A more thorough investigation would be needed here to address this point, which is beyond the scope of this work.

[xxxix] Interested readers can follow Refs. [98, 99] to learn more about fringe and baseline encoding techniques in IO-based beam combiners.

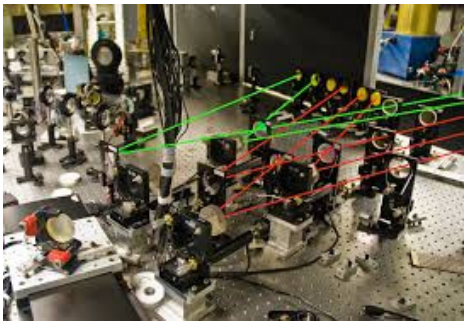

(a)

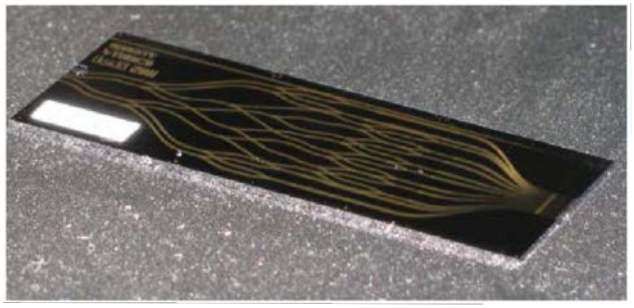

(b)

Figure 1.13: Picture showing the size comparison between a bulk optics- and IO-based beam combiner. (a) The three-telescope CLIMB combiner at the CHARA facility constitutes several mirrors, compensators, and beam splitters. The red optical path shows one CLIMB combiner, while the green one shows another. (b) The four-telescope GRAVITY combiner at the VLTI facility. It is an IO device consisting of several couplers, phase shifters, and splitters performing the same functions as its bulk counterpart. Though the number of telescopes of CHARA and VLTI is different, the physical size of the IO chip is a few cm, which is $\sim 100\times$ smaller than the CLIMB combiner. Images (a) and (b) retrieved from Refs [17] and [12], respectively.

To give an example of a beam combiner architecture including aspects of encoding, the beam combiner that the GRAVITY instrument uses will briefly be described. The GRAVITY instrument at VLTI uses a pairwise combiner with matricial encoding. Looking at the skeleton layout of the GRAVITY combiner in Fig. 1.14, it can be observed that the four input waveguides are spatially arranged to form six baseline pairs using optical functions consisting of both 33/66 splitter and 50/50 splitter. Each baseline pair is then fed to other optical functions: phase shifter and X-coupler, which finally terminates into four single-mode waveguides. These four output waveguides follow an *ABCD* method for extracting the unknown phase of the object. For each baseline, the power P_m at the m^{th} output waveguide of the ABCD-based combiner (see Fig. 1.14) can be expressed as:

$$P_m \propto V_o \cos(\phi_o + \phi_m). \tag{1.11}$$

Where $m = A, B, C, D$ with $\phi_A = 0$, $\phi_B = \frac{\pi}{2}$, $\phi_C = \pi$, $\phi_D = \frac{3\pi}{2}$; V_o is amplitude and ϕ_o is phase of the complex visibility of the object. Using trigonometry identitites, one can find the unknown phase ϕ_o:

$$\phi_o = \tan^{-1}\left(\frac{P_D - P_B}{P_A - P_C}\right). \tag{1.12}$$

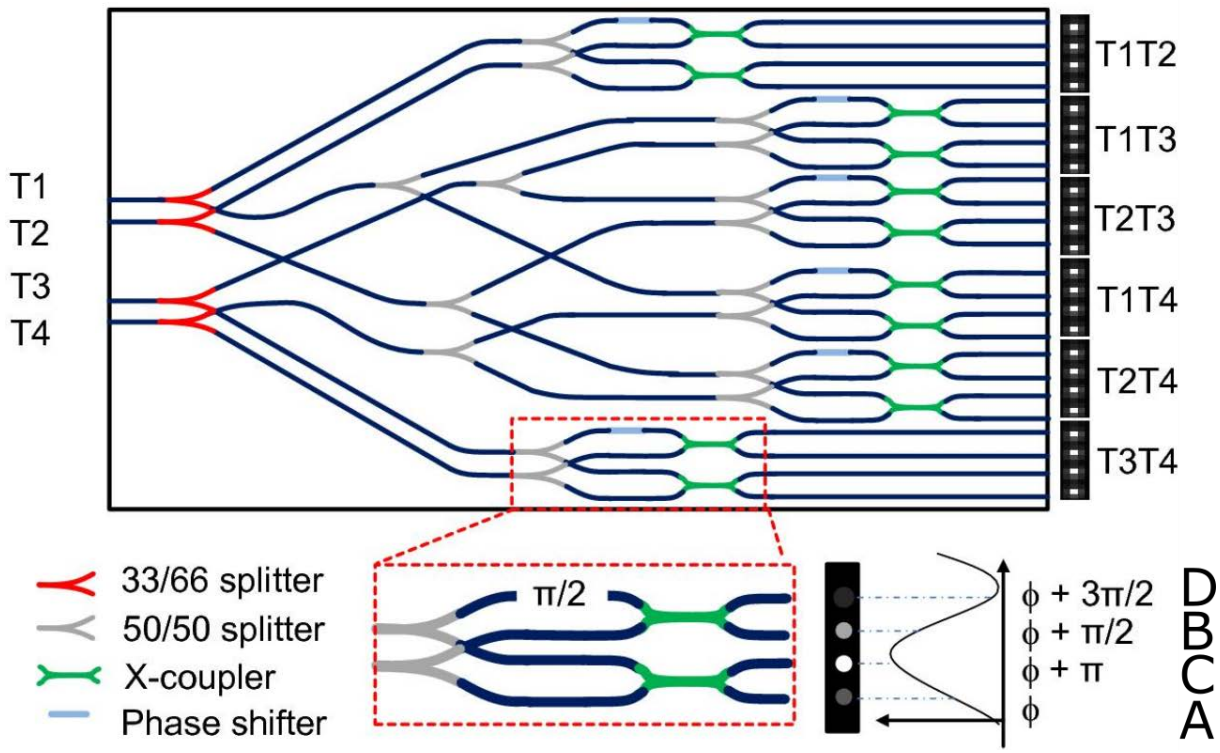

Figure 1.14: The skeleton layout of the 4-telescope IO-based GRAVITY beam combiner, which consists of important optical functions, such as 33/66 splitter, 50/50 splitter, X-coupler, and phase-shifter. All pairwise baseline combinations can be seen next to the outputs at the top-right. Each pairwise combination has four output single-mode waveguides, which follows an *ABCD* method of extracting the unknown phase of an object. The *ABCD* method shown at the bottom-right records the four intensities of light at the same time, where the light at each output has a phase difference (relative to output A) of 0°,90°,180° and 270°, respectively. Thus, using Eq. (1.11) and Eq. (1.12), one can calculate the unknown phase. Image retrieved from Ref [12].

Thus, the ABCD method used in the GRAVITY combiner extracts ϕ_o by using different phase states in quadrature[xl] at the same time. Unlike IONIC or IONIC3 combiners that need a temporal modulation or scanning element, GRAVITY is a static beam combiner. Therefore, it encodes the fringes matricially with a pairwise combination in terms of baseline.

IO combiners based on planar lithography technology are the most developed devices so far,[xli] which have already been tested on-sky and are even commissioned in facilities such as VLTI. The limitation of planar-based IO beam combiners is that they cannot be easily scaled to combine light from many telescopes. In doing so, a cascade of waveguides, Y-splitters, and X-couplers are needed, which could increase the crosstalk between the output waveguides and reduce the SNR of the measured visibility. Recently, an 8-input pairwise *ABCD* combiner

[xl] In other words, a relative phase difference of 0°,90°,180° and 270°, respectively.

[xli] E.g. IONIC, IONIC3, GRAVITY, and PIONIER, to name a few.

was experimentally demonstrated with a CP standard deviation of $\sim 0.9^{\circ}$, but visibility values were not reported [91]. Another limitation of planar IO components lies in the exploitation of the fundamental properties of photons as it is manipulated only in two spatial dimensions, which restricts the data-carrying capacity in telecommunications and computing applications [100]. Finally, the choice of materials is minimal for manufacturing planar IO components, which are primarily on silica or silicon platforms. The transparency window of silica/silicon-based substrate is well-suited for optical telecommunications bands that predominantly lie in the visible to near-IR wavelengths. However, the observation wavelength of interest in astronomy ranges from X-rays to radio waves. Not all astronomical wavelength bands can be covered by silica/silicon-based materials.

The above limitations have motivated the photonics community to exploit the remaining spatial dimension. Hence, the need for 3-D PICs has been growing among several research groups as well as commercial enterprises [101]. One popular technology for fabricating 3-D photonic structures is ultra-fast laser inscription (ULI), where a laser is focused inside a transparent material, leading to refractive index changes. By moving the substrate relative to the focused laser, waveguides can be created that guide the light spatially in 3-D. The motivation to use ULI technology to fabricate the 3-D PICs that are used in this work is discussed in detail in Chapter 4.

In the context of developing IO-based beam combiners, this work focuses on discrete beam combiner (DBC) [102], which are 3-D lattices of single-mode waveguides that are evanescently coupled to each other. In the earlier works of Refs [102, 103, 104], it has been shown that such a DBC – an *astrophotonics* component combines light from multiple telescopes and simultaneously extract the visibilities of an object, and can thus be used as an IO-beam combiner either for pupil remapping of a telescope or for long-baseline interferometry. The DBC is an all-in-one combiner because the light from all telescopes interacts simultaneously. Mathematically, all-in-one implies that the electric field at the output of the DBC can be written as the linear superposition of N input electric fields. This number of input electric fields, N, equals the number of telescopes. The arrangement of single-mode waveguides in a DBC creates fixed phase states at the same time, leading to retrieval of the unknown phase of the object, ϕ_o. Unlike the GRAVITY combiner that works with the *ABCD* method, where ϕ_o given by Eq. (1.12) is a simple expression due to only four outputs, a DBC has $> N^2$ outputs. As a result, deriving an expression as simple as Eq. (1.12) for the DBC is not straightforward. To overcome this difficulty, the transfer matrix method is used instead, which has been developed for multi-field interferometric beam combination [105] to extract the complex visibilities. Therefore, DBC encodes the fringes matricially with the all-in-one combination. The DBC is at the core of this work, which is discussed in detail in Section 2.2 and the subsequent Chapters.

This page was intentionally left blank.

Chapter 2

Theory

This Chapter describes separately the theory of *coherent reformatters* and *DBC*. For design and manufacturing, a spline technique is implemented to equalize the optical paths of the coherent reformatters. The mathematics and theory of the spline functions are briefly presented. Then, the principle of DBC under monochromatic and polychromatic illumination is described. A numerical method based on the Crank-Nicolson scheme is described to solve the coupled-mode equation of the zig-zag lattice of the DBC. This method is applied to find the interaction length, coupling coefficient, and input configurations for a 4-input DBC based on zig-zag geometry such that a low conditioned transfer matrix is obtained.

It is to be noted that Section 2.2.1 of this Chapter is published in Nayak et al. [2].

2.1 Coherent reformatters

Photonic reformatters utilize photonic components such as single-mode waveguides or fibers that distribute light from one spatial point to another. Photonic reformatters can be broadly classified as coherent or incoherent, which depends on the level of detected optical field at the device's output [106]. Incoherent reformatting implies that only the intensity at the output light is measured, whereas coherent reformatting implies that both amplitude and phase at the output light are measured [107]. Coherent reformatters are needed for applications in high angular resolution astronomy where phase information is crucial, whereas applications for incoherent reformatters are most common in spectroscopy. In high-resolution spectroscopic applications, loss of the phase information contained in the input field of the device is crucial to achieving a uniform, time-averaged point spread function (PSF) at the spectrograph [106].

Coherent reformatters are 3-D single-mode waveguides that distribute the light between one set of positions to another while retaining the same path length. The tolerance required for the path length difference depends on the observing wavelength. The required path lengths in the instrument have to be matched within the coherence length of the light passing through the turbulent atmosphere. The coherence length of the light through the atmosphere is roughly $\approx 50\,\mu$m [87] in near-IR wavelengths. Thus, it is sufficient to match the path lengths up to 0.1 μm giving a phase error of 0.4 rad at 1.6 μm, where in reality phase errors of < 1 rad are expected to obtain good quality astronomical images [108, Chapter 2]. In this work, coherent reformatters are designed in the context of pupil remapping as discussed in Section 1.4.3, such that an IO device can be realized to combine the stellar light coherently.

2.1.1 Spline technique

The construction of the coherent reformatters is motivated by the work of Charles et al.[109], which uses spline functions for defining the path of a 3D waveguide. The details of the algorithm for implementing a spline function are given in the Ref [110, Chapter 5]. However, some important definitions in understanding the spline function are outlined here. A polynomial curve with N-1 order can be interpolated using the non-linear least square (NLLS) technique for any N points in space, but the curve may exhibit large oscillations. To avoid such polynomial wiggle, a piece-wise continuous cubic function can be used, such that a smooth curve is interpolated for N+1 points (see Fig. 2.1). Hence, for N+1 points, where $a = x_0 < x_1 < x_2 \cdots < x_N = b$; there exists N cubic polynomials $S_k(x)$ with coefficients $s_{k,0}, s_{k,1}, s_{k,2}, s_{k,3}$ that satisfy the following properties [110, Chapter 5]:

I $S(x) = S_k(x) = s_{k,0} + s_{k,1}(x - x_k) + s_{k,2}(x - x_k)^2 + s_{k,3}(x - x_k)^3$ for $x \in [x_k, x_{k+1}]$ and $k = 0, 1, \cdots, N-1$.

II $S(x_k) = y_k$ for $k = 0, 1, \cdots, N$.

III $S_k(x_k + 1) = S_{k+1}(x_k + 1)$ for $k = 0, 1, \cdots, N-2$.

IV $S'_k(x_k + 1) = S'_{k+1}(x_k + 1)$ for $k = 0, 1, \cdots, N-2$.

V $S''_k(x_k + 1) = S''_{k+1}(x_k + 1)$ for $k = 0, 1, \cdots, N-2$.

For each cubic polynomial $S_k(x)$ there are four unknown constants $(s_{k,0}, s_{k,1}, s_{k,2}, s_{k,3})$; hence there are 4N coefficients to be determined. The properties from I to V gives 4N-2 conditions. The endpoint constraints set the remaining two conditions, thus giving a unique spline curve between N+1 points. The endpoint constraints also determine the type of spline curve passing through the points. This work mainly focusses on "clamped spline" where the two end-point constraints are given by $S'(a) = 0$ and $S'(b) = 0$.

The theory described above for 2-D space can be now be extended to a 3-D space. A vector curve $r(t)$ in terms of unit vectors $\hat{\mathbf{i}}, \hat{\mathbf{j}}, \hat{\mathbf{k}}$ can be written as: $r(t) = f(t)\hat{\mathbf{i}} + g(t)\hat{\mathbf{j}} + h(t)\hat{\mathbf{k}}$, where parameter $t \in \mathbb{R}$. Hence, for a 3-D spline function, one can write the vector curve, $r(z)$ for $z \in \mathbb{R}$ such that the following equations are satisfied simultaneously:

$$r(z) = f(z)\hat{\mathbf{i}} + g(z)\hat{\mathbf{j}} + h(z)\hat{\mathbf{k}}. \tag{2.1}$$

$$f(z) = S^x_k(z) = s^x_{k,0} + s^x_{k,1}(z - z_k) + s^x_{k,2}(z - z_k)^2 + s^x_{k,3}(z - z_k)^3. \tag{2.2}$$

$$g(z) = S^y_k(z) = s^y_{k,0} + s^y_{k,1}(z - z_k) + s^y_{k,2}(z - z_k)^2 + s^y_{k,3}(z - z_k)^3. \tag{2.3}$$

$$h(z) = z. \tag{2.4}$$

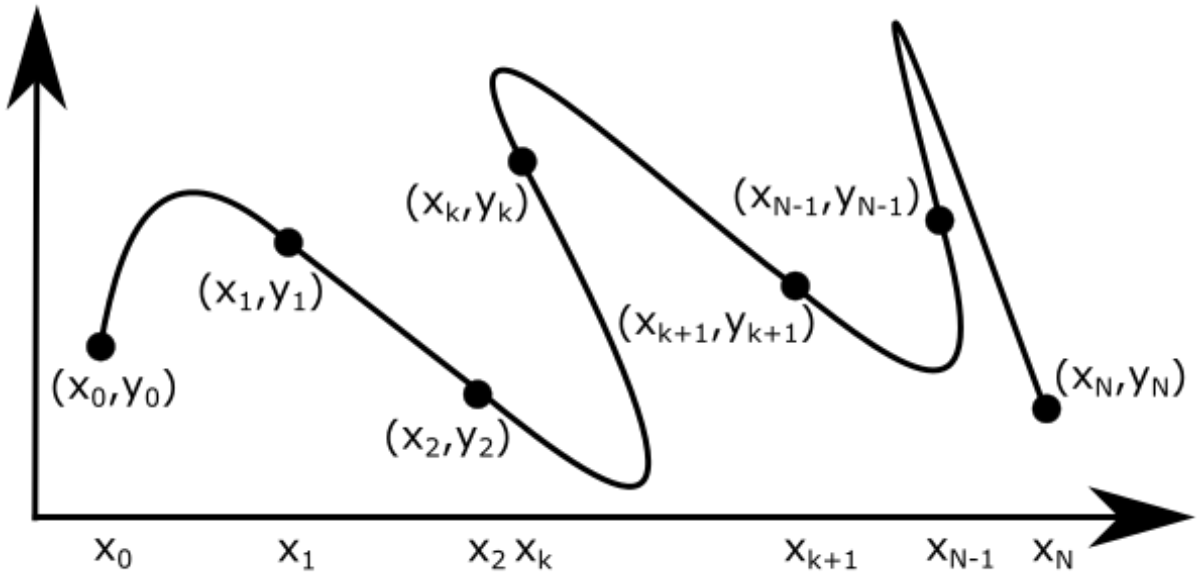

Figure 2.1: A smooth, continous and piecewise cubic spline function passing through N+1 points.

In writing Eq. (2.2) and Eq. (2.3), properties I to V described above have to be satisfied simultaneously. Thus Eq. (2.1) is a 3D spline curve in the interval $[(x_k, y_k, z_k), (x_{k+1}, y_{k+1}, z_{k+1})]$. The path length (*PaL*) of such a curve is given by:

$$PaL = \sqrt{f'(z)^2 + g'(z)^2 + h'(z)^2}. \tag{2.5}$$

The radius of curvature of the curve, which has a dimension of length, is given by:

$$R_c = \left(\frac{|r'(z) \times r''(z)|}{|r'(z)|^3} \right)^{-1}. \tag{2.6}$$

A small radius of curvature R_c results in a tight bend. Therefore, for a linear straight curve, minimum $R_c \to \infty$. The theory and definitions described above are demonstrated in Fig. 2.2. The blue and the green dashed curves are constrained by the fixed endpoints, but they are not path length matched. The path matching is ensured by the red curve passing through the same endpoints as that of the green curve. Table 2.1 reports the path length of the three curves and shows that the difference in the path length between the red and blue curves is ≈ 0.01 units.

It is to be noted that although the blue and red curves are path length matched, no restrictions were given to the radius of curvature. As a result, the minimum R_c for the red curve has the lowest value compared to the other two in Table 2.1. In Chapter 3 and Chapter 4, it will

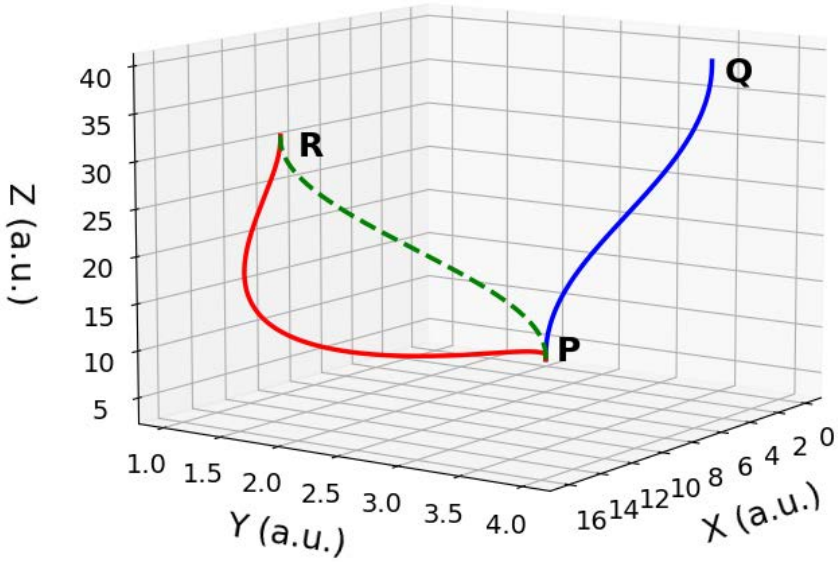

Figure 2.2: Spline curves passing through three different paths. The goal is to match the path length of (P,Q) with (P,R). This is ensured by the blue and the red curve. The *PaL* and R_c values are shown in Table 2.1.

be shown that it is desirable to increase the minimum R_c to avoid both the bending and the transition losses of 3-D waveguides (WGs) that are fabricated using ULI. Thus, the *PaL* and minimum R_c are the two parameters that will be further constrained in Chapter 3 to increase the throughput of the coherent reformatters. One can ensure this by using two user-specified parameters – ε_{PaL} and ε_{R_c} as:

$$\Delta(PaL) = |PaL_1 - PaL_2| \leq \varepsilon_{PaL}. \tag{2.7}$$

$$\mathbf{min}\,(R_c) \geq \varepsilon_{R_c}. \tag{2.8}$$

2.2 Discrete beam combiners

A general solution of the light propagating in an array of evanescently coupled waveguides is given by the Floquet-Bloch theorem [111]. Due to periodic perturbation seen by the light

Curve	*PaL*	**min** (R_c)
Blue	37.97	42
Green dashed	29.65	12
Red	37.96	0.5

Table 2.1: Parameters of the spline curves as shown in Fig. 2.2. **min** (R_c) reports the minimum radius of curvature. The units are arbitary.

waves, the evolution of the electric fields in the array of waveguides can be written as a superposition of a finite set of discrete modes. As a result, when the light beam is launched in one of the waveguides present in a lattice, the intensity at the output of the array follows a discrete diffraction pattern, which is different from the diffraction pattern observed in free-space [112]. However, the discrete diffraction pattern can be engineered, unlike its free-space counterpart, thus interesting phenomena of anomalous diffraction, Bloch oscillations, and discrete solitons can be studied [113].

On a similar attempt, Minardi and Pertsch [102] first studied the complex visibilities of an astronomical target retrieved from a two-dimensional array of waveguides. As mentioned in Section 1.4.4, DBC is a 3-D photonic lattice consisting of an array of WGs that are evanescently coupled to each other. The theory, design, manufacturing, and experimental characterization have been extensively studied in the works of Minardi et al. [114, 103, 115, 104, 116], but these were limited only to laboratory tests with a monochromatic light source. As a result, the theoretical treatment of the transfer matrix of the DBC was missing under the influence of a broadband light. Therefore this work extends the research by defining the "quasi-monochromatic transfer matrix" of the DBC, which is necessary for visibility retrieval of any light source, and verifying the study both through simulation and experiment.

2.2.1 Principle

Monochromatic – From the discussion of Section 1.4.4, the principle of DBC is that it encodes the fringes matricially with an all-in-one combination in terms of baseline encoding. As a result, the electric field at the m^{th} output waveguide can be written as a linear superposition of N input fields by (see pictorial representation of Fig. 2.3):

$$E_m = \sum_{i=1}^{N} U_{mi} E_i. \tag{2.9}$$

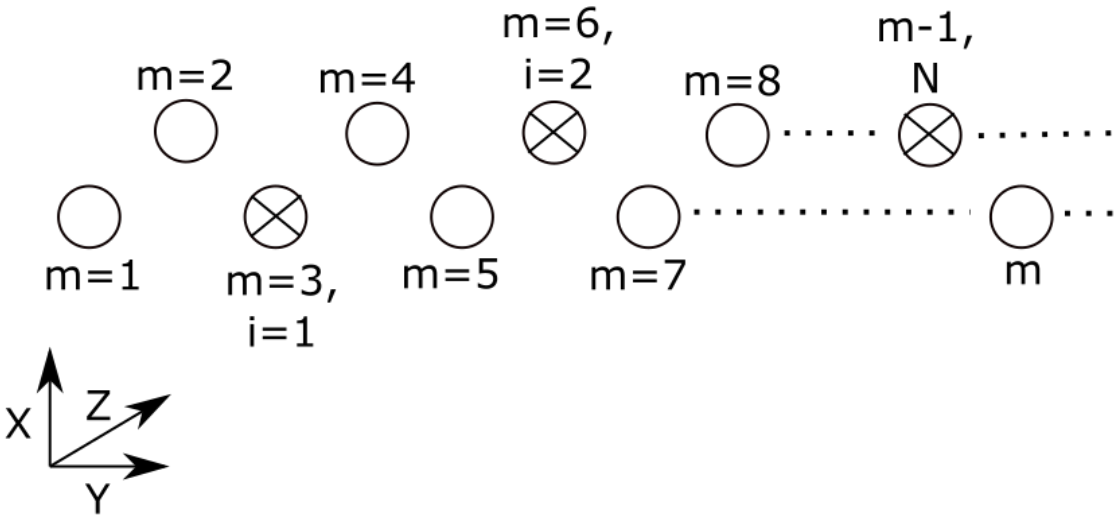

Figure 2.3: A 2-D sketch showing the waveguides of a DBC arranged in a zig-zag geometry. The waveguides are numbered from 1 to m, while the input electric field positions marked with cross are numbered from $i = 1$ to $i = N$. The light propagates in the WGs along the z-direction, which is going into the page. One can see Fig. 2.5 for its 3-D representation.

Where $\{U\}$ is the transfer matrix of the DBC. Assuming unit area, the power at the m^{th} output waveguide can be expressed as a correlation of output electric field as:

$$P_m = \Big\langle \Big(\sum_{i=1}^{N} U_{mi} E_i \Big) \Big(\sum_{j=1}^{N} U_{mj}^* E_j^* \Big) \Big\rangle. \tag{2.10}$$

Where $< \cdot >$ denotes the average and $*$ denotes the complex conjugate over the quantities. Expanding the above equation, one obtains:

$$P_m = \sum_{i=1}^{N} \Big\langle |U_{mi}|^2 |E_i^2| \Big\rangle + 2 \sum_{i=1}^{j-1} \sum_{j=2}^{N} \Re \Big\langle U_{mi} E_i U_{mj}^* E_j^* \Big\rangle. \tag{2.11}$$

Where $\Re$ denotes the real part of the complex quantity. The second term in the above equation is expanded in terms of self-coherence (Γ_{ii}) and mutual-coherence terms (Γ_{ij})[i] as:

$$P_m = \sum_{i=1}^{N} |U_{mi}|^2 \Gamma_{ii} + 2 \sum_{i=1}^{j-1} \sum_{j=2}^{N} [\Re(U_{mi} U_{mj}^*) \cdot \Re\Gamma_{ij} - \Im(U_{mi} U_{mj}^*) \cdot \Im\Gamma_{ij}]. \tag{2.12}$$

[i]The definitions for Γ_{ii} and Γ_{ij} are given in the **Polychromatic** heading.

Where $\Im$ denotes the imaginary part of the complex quantity. The above equation can also be represented in matrix form by:

$$\overrightarrow{P} = V2PM \cdot \overrightarrow{J}. \tag{2.13}$$

The $\overrightarrow{J}$ in Eq. (2.13) are the complex coherence terms and are represented in Eq. (2.14). The $\overrightarrow{P}$ (power output vector) and $\overrightarrow{J}$ are linked through the $M \times N^2$ matrix known as the Visibility-to-Pixel Matrix (V2PM) [105]. It is to be noted that V2PM is also the transfer matrix[ii] of the DBC, and it will be used interchangeably in this work.

$$\overrightarrow{J} = (\Gamma_{11}, \ldots, \Gamma_{NN}, \Re\Gamma_{12}, \ldots, \Re\Gamma_{1N}, \ldots, \Re\Gamma_{N-1N}, \Im\Gamma_{12}, \ldots, \Im\Gamma_{1N}, \ldots, \Im\Gamma_{N-1N})^T. \tag{2.14}$$

Eq. (2.13) is over-determined[iii] and the V2PM possesses a Moore-Penrose pseudo-inverse matrix,[iv] which can be applied to the output vector $\vec{P}$ to extract the coherence functions. Since it is a pseudo-inverse problem, the robustness of the retrieval process of $\vec{J}$ by the inverted V2PM can be gauged by the condition number (CN [117]), which describes the propagation and amplification of errors from $\vec{P}$ to $\vec{J}$. Ideally a low condition number[v] of the V2PM is desirable. It is therefore important to design and characterize the V2PM of the system since a low CN of the V2PM ensures that the retrieved quantities (i.e. $\vec{J}$) obtained after the inversion are less sensitive to external perturbations of the optical system. The coupling strength, excitation sites, and the interaction length between the WGs are carefully chosen to get a low-conditioned V2PM, which will be discussed in Chapter 2.2.2. A low conditioned V2PM is achieved by the presence of next-nearest coupling [115], which will be the goal for the fabrication of DBC devices using ULI in Chapter 4.

Polychromatic – The V2PM approach described above is strictly valid for monochromatic light. The operation of V2PM for a light source with bandwidth is now considered. The coherence terms are defined as:

$$\Gamma_{ii}(\tau) = < \overrightarrow{E_i}(t) \overrightarrow{E_i}(t+\tau)^* > . \tag{2.15}$$

$$\Gamma_{ij}(\tau) = < \overrightarrow{E_i}(t) \overrightarrow{E_j}(t+\tau)^* > = \sqrt{\Gamma_{ii}(0)} \sqrt{\Gamma_{jj}(0)} e^{i2\pi\nu\tau} = \sqrt{\Gamma_{ii}} \sqrt{\Gamma_{jj}} e^{i2\pi\nu\tau}. \tag{2.16}$$

[ii] Sometimes denoted by $\{U\}$.

[iii] The device has more outputs M than the square of the number of inputs N.

[iv] Known as Pixel-2-Visibility matrix (P2VM).

[v] CN = 1.

Where $\Gamma_{ii}(\tau)$ is the self-coherence which describes the correlation of the electric field at the m^{th} WG from the i^{th} input WG and $\Gamma_{ij}(\tau)$ is the mutual-coherence of m^{th} WG, where τ is the difference in the time delay between the j^{th} WG and the i^{th} input WG. The monochromatic frequency of the light is denoted by ν. Eq. (2.15) and Eq. (2.16) are substituted in Eq. (2.12) and integrated over the frequency range of the light:

$$P_m(\nu) = \int_{\nu_1}^{\nu_2} \left[\sum_{i=1}^{N} |U_{\mathrm{mi}}(\nu)|^2 \Gamma_{ii} + 2 \sum_{i=1}^{j-1} \sum_{j=2}^{N} \sqrt{\Gamma_{\mathrm{ii}}} \sqrt{\Gamma_{\mathrm{jj}}} |U_{\mathrm{mi}}(\nu) U_{\mathrm{mj}}^{*}(\nu)| \cos(2\pi\nu\tau + \phi_{\mathrm{mij}}(\nu)) \right] d\nu. \tag{2.17}$$

Where $\phi_{mij} = \tan^{-1}\left[\frac{\Im(U_{mi}U_{mj}^{*})}{\Re(U_{mi}U_{mj}^{*})}\right]$ represents the phase of the {U} matrix. The {U} matrix contains frequency-dependent modal amplitudes of the electric field and solving the integral in Eq. (2.17) is cumbersome. However, for a light centred at ν_0 with a bandwidth $\Delta\nu$, and assuming narrow bandwidth of $\frac{\Delta\nu}{\nu_0} \ll 1$ [18, Chapter 10], the frequency dependency of $U_n(\nu)$ can be neglected in the narrow bandwidth approximation. Thus, the integration of Eq. (2.17) is performed to get:

$$P_m(\nu) = \sum_{i=1}^{N} \langle |U_{\mathrm{mi}}|^2 \rangle \Gamma_{\mathrm{ii}} \Delta\nu + 2 \sum_{i=1}^{j-1} \sum_{j=2}^{N} \langle |U_{\mathrm{mi}} U_{\mathrm{mj}}^{*}| \rangle \sqrt{\Gamma_{\mathrm{ii}} \Gamma_{\mathrm{jj}}} \Delta\nu \frac{\sin(\tau\Delta\nu\pi)}{\tau\Delta\nu\pi} \cos(\pi(\nu_1 + \nu_2)\tau + \phi_{\mathrm{mij}}). \tag{2.18}$$

Eq. (2.18) is valid for any generalized multi-field integrated optics beam combiner, and it will be shown that Chapter 5 and Chapter 6 support the above consideration. It describes the temporal evolution of fringes at the m^{th} output WG where, in reality, any light source doesn't contain a single frequency but has a finite width. Eq. (2.18) also tells that the visibility retrieval using P2VM requires a certain degree of achromaticity within which the frequency dependence of {U} can be neglected. Now, the calibration procedure of the V2PM under polychromatic illumination is briefly described. However, a detailed step-by-step procedure for the calibration of the V2PM is described in Appendix A.

Under monochromatic illumination, the calibration of the V2PM matrix described by Eq. (2.13) is carried out by filling the first N columns with the square modulus of the field transfer function and the remaining N(N-1) columns with the real and imaginary parts of the product of the field transfer function. In other words, the first N columns are filled with the normalized photometry of the output channels by exciting one input at a time. The remaining N(N-1) columns are filled with the temporal fringes by exciting two inputs at a time and adding a known phase delay between them. Generally, a photometric correction procedure (see Ref [103] or Appendix A for details) is followed, where one gets rid of the photometric transmission terms (Γ_{ii} and $\sqrt{\Gamma_{ii}\Gamma_{jj}}$) in Eq. (2.18) for m^{th} WG to extract the amplitude and phase that goes in filling the elements of the V2PM. Hence, Eq. (2.18) is photometrically corrected to get:

$$P_{\mathrm{m}} = |U_{\mathrm{mi}} U^{*}_{\mathrm{mj}}| \frac{\sin\left(\pi\delta\frac{\Delta\lambda}{\lambda_0^2}\right)\cos\left[\pi\delta\left(\frac{1}{\lambda_1}+\frac{1}{\lambda_2}\right)+\phi_{mij}\right]}{\pi\delta\frac{\Delta\lambda}{\lambda_0^2}}, \quad i \neq j. \tag{2.19}$$

In Eq. (2.19), the notation $\delta = c\tau$ is used for converting the frequency bandwidth to wavelength bandwidth using $\Delta\nu = c\frac{\Delta\lambda}{\lambda_0^2}$. A NLLS fitting is performed to the photometrically corrected interferogram given by Eq. (2.19). The *amplitude* $= |U_{mi}U^{*}_{mj}|$ and *phase* $= \phi_{mij}$ of the complex transfer function is extracted for each of the M output WGs, hence filling the N(N-1) columns of the V2PM. Thus, the above method for the V2PM calibration leads to a more robust result in extracting the visibilities using narrow bandwidth light sources. In this context, such a V2PM is also defined as a *quasi-monochromatic* V2PM.

Since, the $\vec{J}$ is extracted from the P2VM, the normalized amplitude V_{ij} (i.e. the Michelson fringe visibility) and its phase ϕ_{ij} is calculated from:

$$\left.\begin{aligned} V_{ij} &= \sqrt{(\Re\gamma_{ij})^2 + (\Im\gamma_{ij})^2} \\ \phi_{ij} &= \tan^{-1}\left(\frac{\Im\gamma_{ij}}{\Re\gamma_{ij}}\right) \end{aligned}\right\} \quad \mathrm{i} \neq \mathrm{j}. \tag{2.20}$$

Where,

$$\gamma_{ij} = \frac{\Gamma_{ij}}{\sqrt{\Gamma_{ii}\Gamma_{jj}}}, \; i \neq j. \tag{2.21}$$

The closure phase is also calculated directly from the visibility phase as:

$$\Phi_{ijk} = \phi_{ij} + \phi_{jk} - \phi_{ik}\,. \tag{2.22}$$

The above notations of V_{ij}, ϕ_{ij}, γ_{ij}, Φ_{ijk} are commonly used in astro-interferometry [103, 104, 118], and are used also extensively in this work.

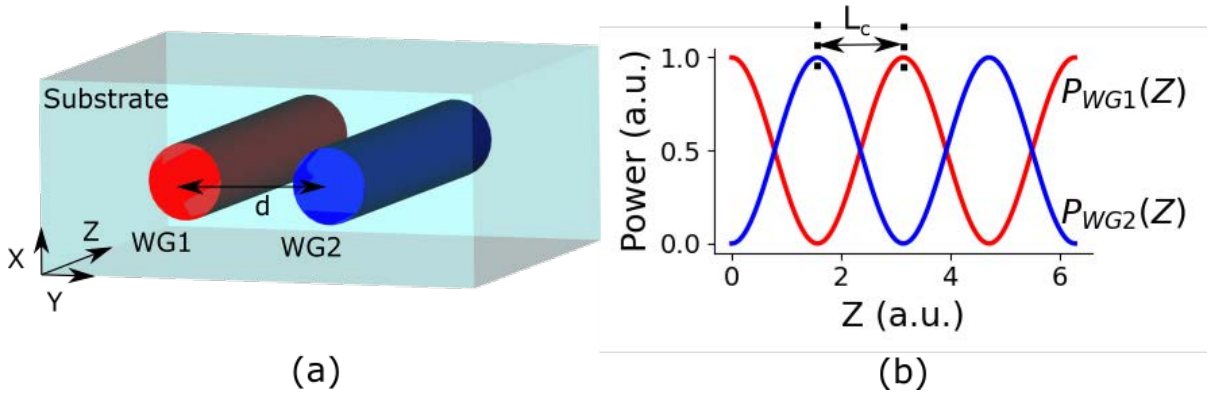

Figure 2.4: (a) Two waveguides separated by a separation d that are weakly interacting with each other through evanescent coupling. (b) Solving Eq. (2.23) with the assumption that $\kappa_{12} = \kappa_{21} = 1$ and optical power for WG1 equals 1 at $z = 0$ (i.e. $P_{WG1}(0) = 1$), the optical power periodically exchanges between both the WGs. L_c is defined as the coupling length period when power from WG1 completely transfers to WG2.

2.2.2 Numerical method

In this part, a method is suggested to numerically solve a system of m waveguides in a DBC. Consider the case of two waveguides that are interacting weakly through evanescent coupling as shown in Fig. 2.4a. In this weak approximation, the total field of the system is written as a superposition of individual waveguide modes. As a result in matrix form, the coupled-mode equations describing the amplitude (A) of the fundamental mode for waveguide 1 and 2 are written as [119, Chapter 8][80, Appendix E]:

$$\mathrm{i}\begin{bmatrix} \frac{dA_1}{dz} \\ \frac{dA_2}{dz} \end{bmatrix} = \begin{bmatrix} 0 & \kappa_{12} \\ \kappa_{21} & 0 \end{bmatrix} \begin{bmatrix} A_1 \\ A_2 \end{bmatrix}. \tag{2.23}$$

In writing Eq. (2.23), the difference in the propagation constant (i.e. $\Delta\beta = \beta_1 - \beta_2$) is assumed to be zero. β_1 and n_1 are the progagation constant and refractive index of the fundamental mode respectively, propagating inside WG1, when WG2 is not present. The same applies to β_2 and n_2 for WG2. The coupling coefficients are defined as:

$$\kappa_{12} = \frac{k_0^2}{2\beta_1} \frac{\int_{-\infty}^{\infty}\int_{-\infty}^{\infty} \psi_1^* \Delta n_2^2 \psi_2 \, dx\, dy}{\int_{-\infty}^{\infty}\int_{-\infty}^{\infty} \psi_1^* \psi_1 \, dx\, dy}. \tag{2.24}$$

$$\kappa_{21} = \frac{k_0^2}{2\beta_2} \frac{\int_{-\infty}^{\infty}\int_{-\infty}^{\infty} \psi_2^* \Delta n_1^2 \psi_1 \, dx\, dy}{\int_{-\infty}^{\infty}\int_{-\infty}^{\infty} \psi_2^* \psi_2 \, dx\, dy}. \tag{2.25}$$

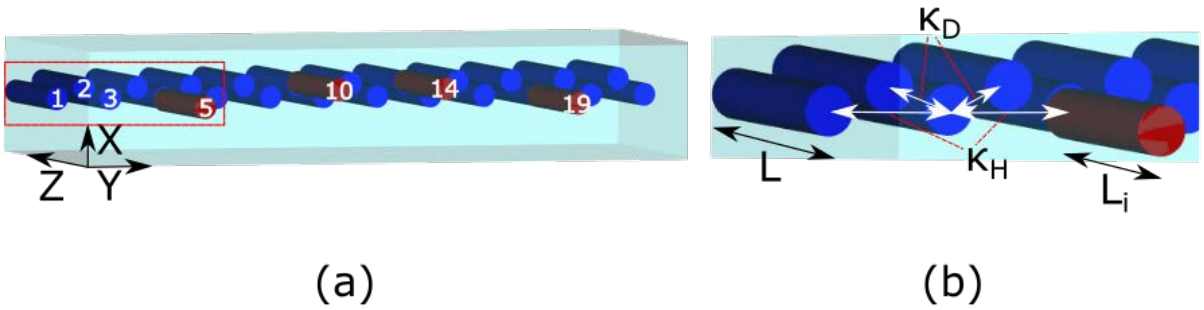

Figure 2.5: (a) 3-D representation of a 4-input and 23-output waveguides of a DBC based on zig-zag geometry in a glass substrate. The input waveguides of the DBC are shown in red, which are at input positions 5, 10, 14, and 19. (b) A zoomed view of the red rectangle part is shown in (a). L is the interaction length of the DBC, L_i is the length of the input waveguides. κ_D is the coupling co-efficient along a diagonal direction corresponding to NN interaction. In contrast, κ_H is the coupling co-efficient along a horizontal direction corresponding to NNN interaction.

Δn_1 and Δn_2 are the differences in the refractive index and defined as follows:

$$\Delta n_1^2 = n^2 - n_1^2. \tag{2.26}$$

$$\Delta n_2^2 = n^2 - n_2^2. \tag{2.27}$$

In the above equations, n is the effective refractive index of the fundamental mode due to presence of both WG1 and WG2. Now the coupled mode equations can be generalized to a system composed of m number of WGs as:

$$\mathrm{i}\begin{bmatrix} \frac{dA_1}{dz} \\ \frac{dA_2}{dz} \\ \vdots \\ \frac{dA_m}{dz} \end{bmatrix} = \begin{bmatrix} \kappa_{11} & \kappa_{12} & \dots & \kappa_{1m} \\ \kappa_{21} & \kappa_{22} & \dots & \kappa_{2m} \\ \vdots & \vdots & \ddots & \\ \kappa_{m1} & \dots & \dots & \kappa_{mm} \end{bmatrix} \begin{bmatrix} A_1 \\ A_2 \\ \vdots \\ A_m \end{bmatrix}. \tag{2.28}$$

For a DBC, where the waveguides are arranged in a zig-zag configuration one assumes only nearest neighbour (NN) and next-nearest neighbour (NNN) interaction as showin in Fig. 2.5.

The coupling coefficients are NN = κ_D and NNN = κ_H. Hence, Eq. (2.28) is written as:

$$\mathrm{i}\begin{bmatrix} \frac{dA_1}{dz} \\ \frac{dA_2}{dz} \\ \vdots \\ \frac{dA_m}{dz} \end{bmatrix} = \begin{bmatrix} 0 & \kappa_D & \kappa_H & 0 & \dots & 0 \\ \kappa_D & 0 & \kappa_D & \kappa_H & \dots & 0 \\ \vdots & & \ddots & & & \vdots \\ 0 & & \dots & & & 0 \end{bmatrix} \begin{bmatrix} A_1 \\ A_2 \\ \vdots \\ A_m \end{bmatrix}. \tag{2.29}$$

In compact form, Eq. (2.29) is written as [102]:

$$\mathrm{i}\frac{dA_m}{dz} = \frac{\pi}{2L_c}\sum_{l=1}^{m} C_{ml}A_l. \tag{2.30}$$

L_c is the coupling length where a complete transfer of optical power takes place from one WG to another in a system of two waveguides interacting with each other as shown in Fig. 2.4b. In Eq. (2.30), the matrix containing the coupling coefficients C_{ml} are dimensionless. A crank-Nicolson method [120] is used to solve Eq. (2.30) numerically. The following quantities from the Crank-Nicolson method are now defined:

$$\frac{dA_m}{dz} = \frac{A_k^{j+1} - A_k^j}{\Delta z}. \tag{2.31}$$

$$A_l = \frac{1}{2}(A_k^{j+1} + A_k^j). \tag{2.32}$$

A_k^j is the amplitude of the k^{th} waveguide at j^{th} step and A_k^{j+1} is the amplitude after $(j+1)^{th}$ step. The above two equations are now substituted in Eq. (2.30) and rearranged to form:

$$A_k^{j+1} = \left(1 + \mathrm{i}\frac{\pi\Delta z}{4L_c}\sum_{l=1}^{m} C_{ml}\right)^{-1}\left(1 - \mathrm{i}\frac{\pi\Delta z}{4L_c}\sum_{l=1}^{m} C_{ml}\right)A_k^j. \tag{2.33}$$

Eq. (2.33) can be solved for the field amplitudes of k^{th} waveguide after $(j+1)^{th}$ step given the initial value of the amplitude at j^{th} step. Thus, A_k^{j+1} are the elements of the $\{U\}$ by substituting it in Eq. (2.12). The goal is to find the minimum CN of the DBC, which gives the best injection sites [115] and the best inetraction length of the DBC [121].

For a 4-input DBC based on zig-zag geometry, it is already found out that there have to be 23-output waveguides to achieve the optimum SNR [104] as shown in Fig. 2.5. To achieve the minimum CN of $\{U\}$, the input injection sites were already found to be at locations 5, 10,

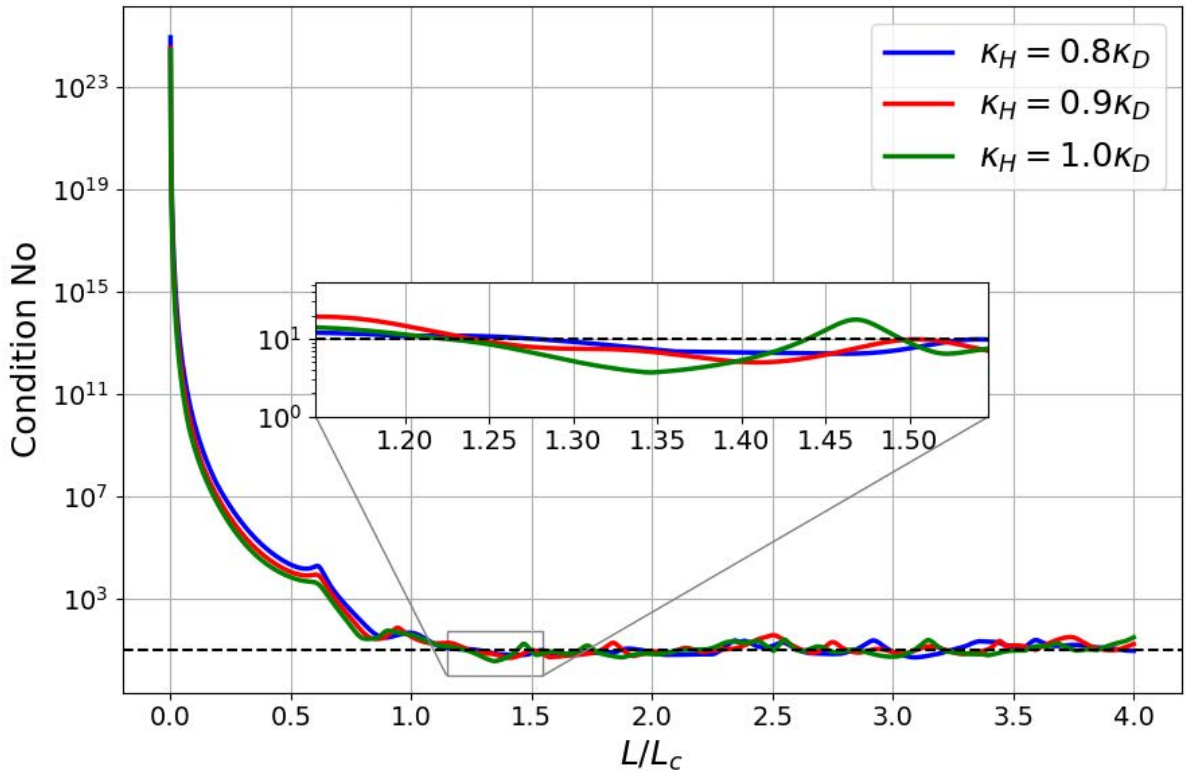

Figure 2.6: Variation of CN along the length of the device. The legend shows κ_H. The black line shows the CN = 10. The inset shows a zoomed view around $\frac{L}{L_c} = 1.35$.

14, and 19. In Fig. 2.6, the variation of CN is shown along the length of the DBC. The length is normalized in terms of coupling length. The values of the minimum CN are reported in Table 2.2a. It can be seen that the CN decreases as the ratio of $\frac{\kappa_H}{\kappa_D}$ reaches its maximum value = 1. This conclusion is also reported in Ref [115], where due to the presence of NNN (= κ_H) term, the CN reaches its minimum because of greater diversity in retrieved phases. The effect of phase diversity is also known as phase symmetry breaking, which is necessary to have fewer errors from the V2PM inversion to retrieve the coherence functions simultaneously.

The effect of different configurations on CN along the length of the device is shown in Fig. 2.7 and reported in Table 2.2b. It can be seen that the CN attains a global minimum only for the configuration 5-10-14-19. The variation of CN is worst for the configuration 20-21-22-23 that has the highest value of the minimum CN obtained from all possible configurations. The 20-21-22-23 configuration corresponds to all four input sites serially located at one end of the DBC. Similarly, configuration 1-8-9-13 corresponds to the median value of the minimum CN obtained from all possible configurations.

$\frac{\kappa_H}{\kappa_D}$	CN	$\frac{L}{L_c}$
0.8	5.20	3.09
0.9	4.97	1.41
1.0	3.69	1.35

(a)

Configuration	CN	$\frac{L}{L_c}$
20-21-22-23	21.12	3.53
1-8-9-13	6.41	2.55
5-10-14-19	3.69	1.35

(b)

Table 2.2: (a) The minimum CN as a function of $\frac{\kappa_H}{\kappa_D}$. The coresponding $\frac{L}{L_c}$ value is reported, where the minimum CN has occured, assuming the configuration 5-10-14-19. (b) The minimum CN as a function of various configurations. The corresponding $\frac{L}{L_c}$ value is reported, where the minimimum CN has occured, assuming $\frac{\kappa_H}{\kappa_D} = 1$.

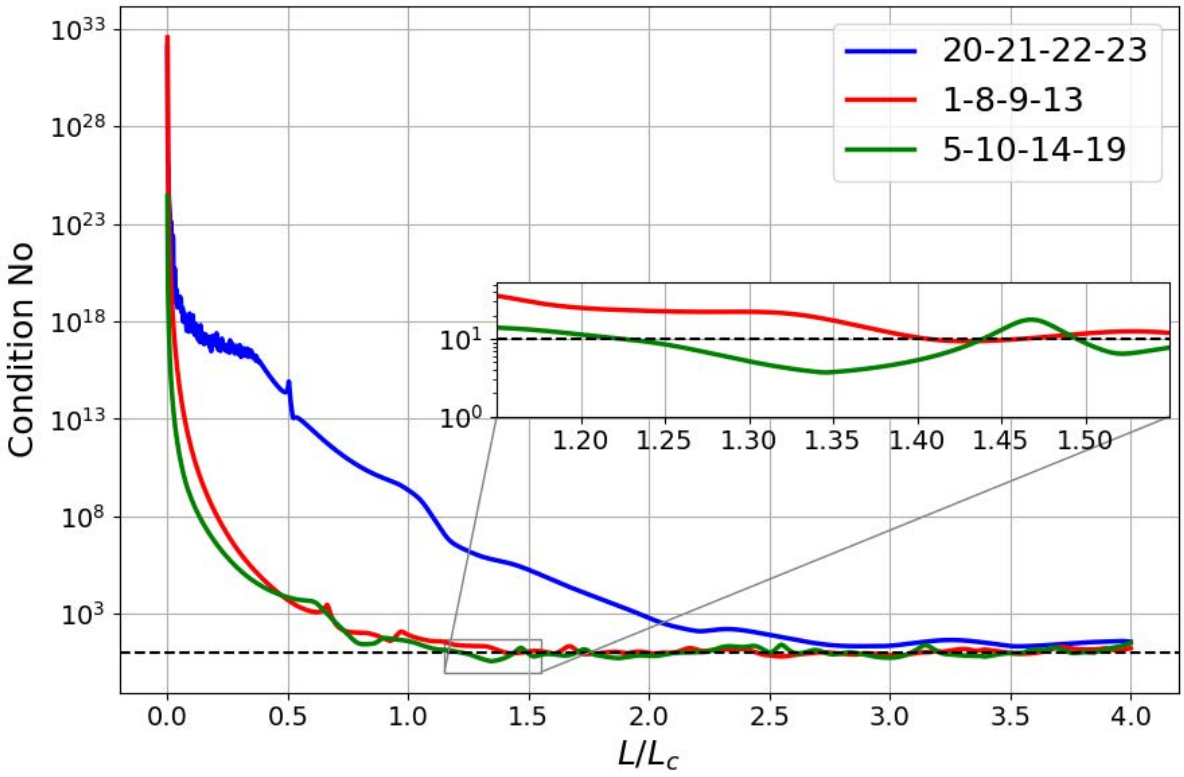

Figure 2.7: Variation of CN along the length of the device. The legend shows different configurations for $\frac{\kappa_H}{\kappa_D} = 1$. The inset shows a zoomed view around $\frac{L}{L_c} = 1.35$.

This page was intentionally left blank.

Chapter 3

Design

In this Chapter, the parameters obtained from Chapter 2 are used for designing an IO based-*astrophotonics* device that monolithically contains the coherent reformatters and the DBC. Three different devices are designed as follows: 1) Device-A consisting of 4-input non-redundant pupil remappers connected with the 4-input DBC, 2) Device-B is a replica of Device-A, but have coherent reformatters that spatially distribute the 23-outputs of the DBC for doing spectro-interferometric measurements, and 3) Device-C consisting of an 8-input non-redundant pupil remappers connected with two 4-input DBCs that are stacked vertically. These three devices are designed in such a way that a pupil remapping experiment at the WHT can be performed, which will be discussed in detail in Chapter 7.

3.1 4-input pupil remappers with DBC

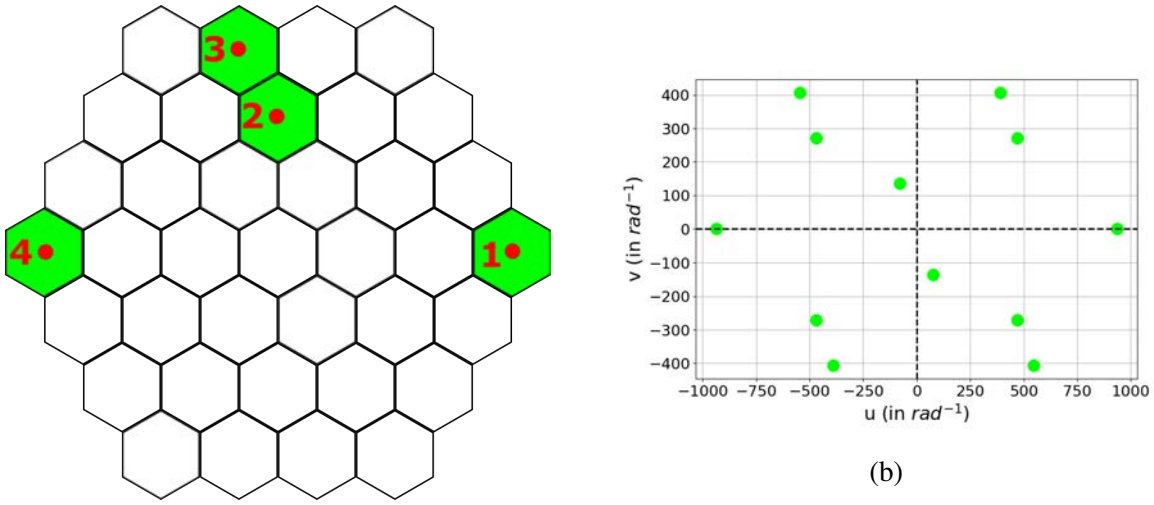

(a) (b)

Figure 3.1: (a) Conjugation of the hexagonal-shaped segmented DM with the 4-input Pupil remappers (shown in red). The segments of the DM as shown in green will only be used to couple light into the pupil remappers, while the remaining ones will steer out the light. (b) A Snapshot of the 12 spatial frequencies (both positive and negative) in the $u-v$ plane corresponding to the arrangement shown in (a) assuming an object's position at a declination of 90° and an hour angle of 0° with $\lambda_0 = 1.6\,\mu$m. The units are in radian inverse.

For performing the pupil remapping experiment, one requires two optical components – a deformable mirror (DM) and a microlens array (MLA). One can see the experimental setup in Fig. 7.1 and Fig. 7.2. The pupil remappers are located at the back-focal plane of the MLA. As a result, Fig. 3.1a shows the 37 hexagonal segments of the DM plane, which will be conjugated with the MLA plane. The pitch of the individual lenslet in the MLA $= 250\,\mu$m, thus the distance between the baseline 1-4 $= 1.5$ mm. The red numbering and dots show the augmented

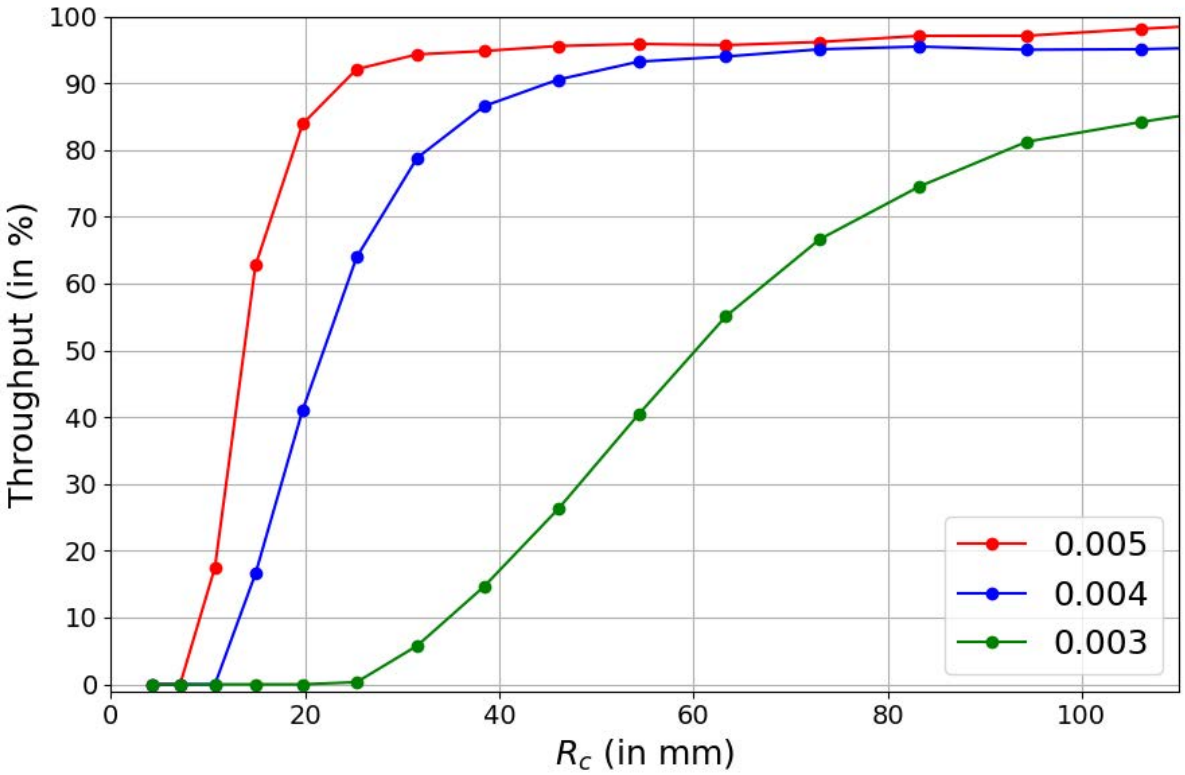

Figure 3.2: Throughput vs R_c. Here, R_c equals minimum radius of curvature for a coherent reformatter. The legend shows the refractive index change Δn between the core and the cladding. The 3-D waveguide is assumed to be a step-index profile. The dimension of the WG is $5.0\,\mu$m $\times$ $6.4\,\mu$m.

positioning of the 4-input pupil remappers. The green segments are selected from the DM, such that the light from these segments is coupled into the pupil remappers. The green segments were chosen in a non-redundant way such that both the low and high- Fourier components are accessible. The corresponding $u-v$ plane at 1.6 μm is shown in Fig. 3.1b.

Eq. (2.7) and Eq. (2.8) are used to design the pupil remappers connecting the DBC, where $\varepsilon_{PaL} = 0.1\,\mu$m and $\varepsilon_{R_c} = 30\,$mm. The minimum radius of curvature[i] was set at 30 mm to increase the overall throughput of the device. The bending and transition losses tend to be higher at a lower radius of curvature [109], thereby decreasing the throughput of the spline WGs. Fig. 3.2 shows the throughput vs the minimum radius of curvature for three different refractive index changes (Δn) between the core and cladding that was simulated in RSoft. The Δn is assumed to be a step-index profile, and the details of the WG parameters that are used to launch light in RSoft can be found in Chapter 5. It can be seen that the $\mathbf{min}\,(R_c)$ value at which the 50 % drop in the throughput occurs decreases as Δn increases. In other words, to increase the throughput of the WG at low Δn, the $\mathbf{min}\,(R_c)$ has to be increased substantially. The 4-input

[i]Denoted by $\mathbf{min}\,(R_c)$.

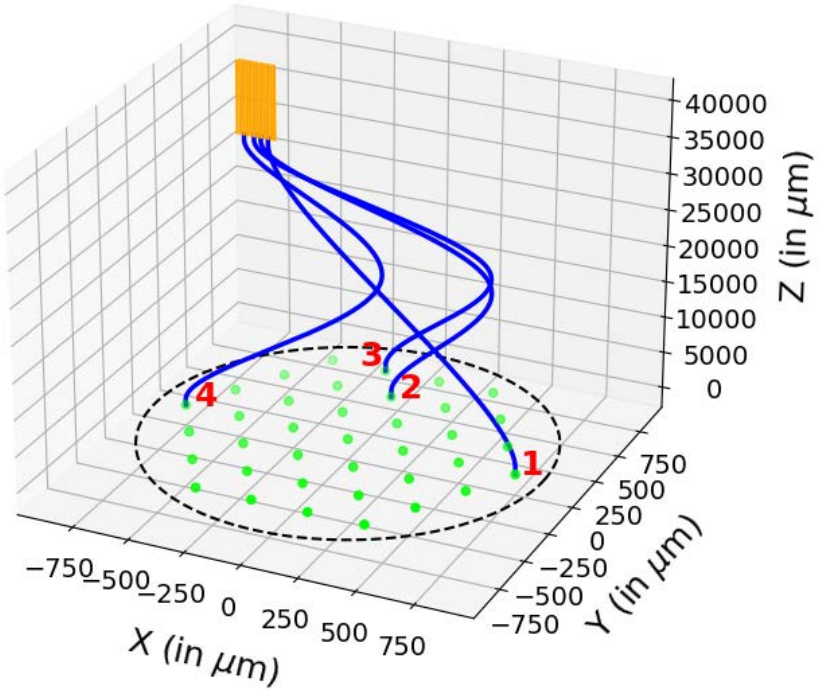

Figure 3.3: 4-input pupil remappers along with DBC (shown in orange). The green dots arranged in a hexagonal pattern are the augmented focal spots of the MLA. Only the numbered focal spots are coupled to the 4-input pupil remappers. The black circle shows an augmented re-imaged pupil of a telescope.

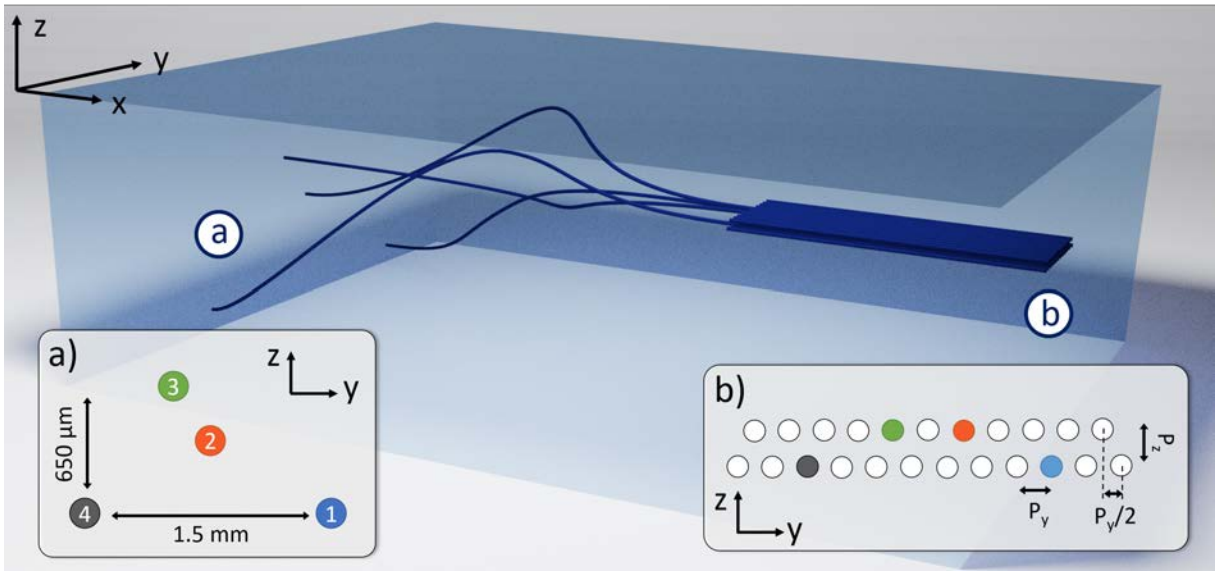

Figure 3.4: CAD drawing of the 4-input pupil remappers along with the DBC (not to scale). (a) Section showing the arrangement of the four input waveguides of the pupil remapper. The input face of the pupil remapper is placed behind the back focal plane of the MLA, which will be conjugated with the segmented deformable mirror (see Fig. 3.1a). (b) Section of the zig-zag DBC. The four input waveguides are highlighted in color, together with the horizontal and vertical pitches of the array.

pupil remappers connecting the DBC are shown in Fig. 3.3 and its CAD drawing is shown in Fig. 3.4. The parameters of the pupil remappers are shown in Table 3.1. The numbers indicate that the 4-input remappers are path length matched with higher **min** (R_c), and at the same time maximizing the throughput of the pupil remappers.

Another device was designed where the output of the DBC was reformatted coherently and arranged linearly. The CAD drawing of the fan-out device is shown in Fig. 3.5, and this device will be used for the on-sky test at WHT. The output reformatting is done to make the output modes more distinguishable since they can be arranged with higher separations. Moreover, it would make a spectral measurement easier since the output light could be vertically dispersed

Input number	PaL (in μm)	**min** (R_c) (in mm)
1	30,050.87	88
2	30,050.93	41
3	30,050.93	40
4	30,050.95	46

Table 3.1: Parameters of the 4-input pupil remappers as shown in Fig. 3.3. **min** (R_c) reports the minimum radius of curvature.

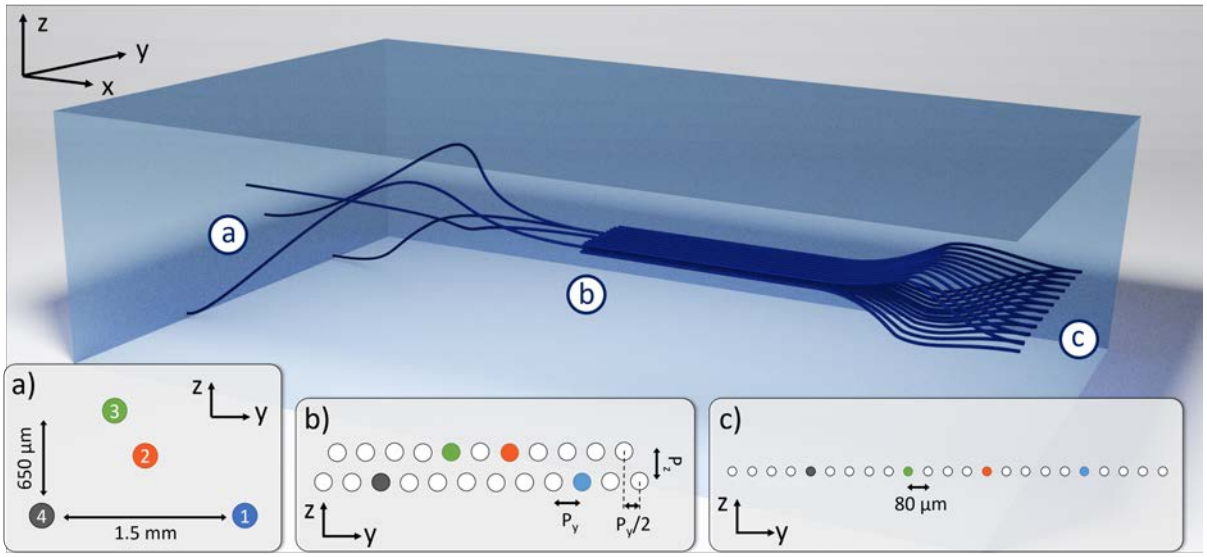

Figure 3.5: CAD drawing of the 4-input pupil remappers along with the outputs of the DBC that are reformatted spatially (not to scale). (a) Section showing the arrangement of the four input waveguides of the pupil remapper. The input face of the pupil remapper is placed behind the back focal plane of the MLA, which will be conjugated with the segmented deformable mirror (see Fig. 3.1a). (b) Section of the zig-zag DBC. The four input waveguides are highlighted in color, together with the horizontal and vertical pitches of the array. (c) The output section of the device after performing the reformatting of the WGs spatially. The waveguides are linearly arranged with a separation of 80 μm.

without the risk of modal cross-talk. Like the pupil remapper, the output of the DBC was designed with spline functions, implementing an isotropic expansion of the array for keeping the coupling uniform between the nearest neighboring waveguides. Since in the first part of the expansion, the waveguides are still slightly coupled, the interaction length of the DBC was reduced correctly to obtain the same effective length.

3.2 8-input pupil remappers with 2×4-input DBC

The concept to scale beyond 4-input pupil remappers is also tested to identify the advantage of the third dimension such that complex reformatting could be done without waveguide crossovers. This will result in a 3-D network of waveguides that can be routed from one spatial dimension to another, delivering high-data transmission capacity of IO chip for telecommunication applications [100]. Furthermore, due to 3-D capability, one can utilize the whole pupil of the telescope to increase the SNR, which will produce high-fidelity images in stellar interferometry. Fig. 3.6a shows the 8-input pupil remappers that were selected, and the corresponding

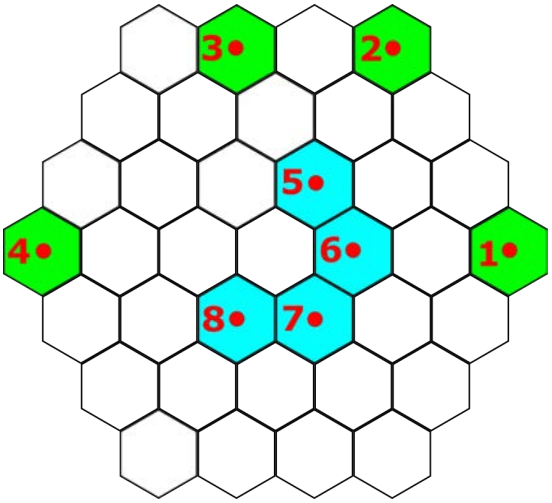

(a)

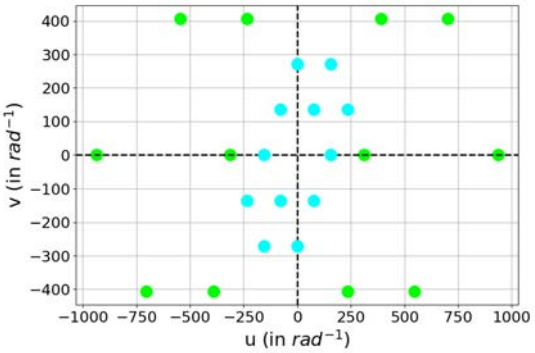

(b)

Figure 3.6: (a) Conjugation of the hexagonal-shaped segmented DM with the 8-input Pupil remappers (shown in red). The segments of the DM as shown in green and cyan will only be used to couple light into the pupil remappers, while the remaining ones will steer out the light. (b) A Snapshot of the 24 spatial frequencies (both positive and negative) in the $u-v$ plane corresponding to the arrangement shown in (a) assuming an object's position at a declination of 90° and an hour angle of 0° with $\lambda_0 = 1.6\,\mu$m. The units are in radian inverse.

$u-v$ plane is shown in Fig. 3.6b.

Fig. 3.7 shows the design of 8-input pupil remappers and Fig. 3.8 shows its CAD drawing. The pupil remappers for the configuration 1-2-3-4 feeds one of the 4-input DBC, while the configuration 5-6-7-8 feeds another 4-input DBC. Both the DBCs are separated vertically by 70 μm, such that they can be re-imaged simultaneously on the camera in the Michelson setup, which will be used for the characterization of the device in Chapter 6. The device was designed so that the configuration 5-6-7-8 corresponds to lower-order Fourier components, while the configuration 1-2-3-4 corresponds to higher-order Fourier components. The parameters of the pupil-remappers are shown in Table 3.2. It can be seen that the 8-input pupil remappers are path length matched, as set by $\varepsilon_{PaL} = 0.1\,\mu$m. The minimum radius of the curvature is well above the threshold set by $\varepsilon_{R_c} = 30\,$mm, which implies excellent throughput achieved by the pupil remappers. It is to be noted that when the number of pupil remappers is increased, there will be chances of intersection points between the waveguide paths. One has to carefully implement this in an algorithm to avoid such waveguide crossovers.

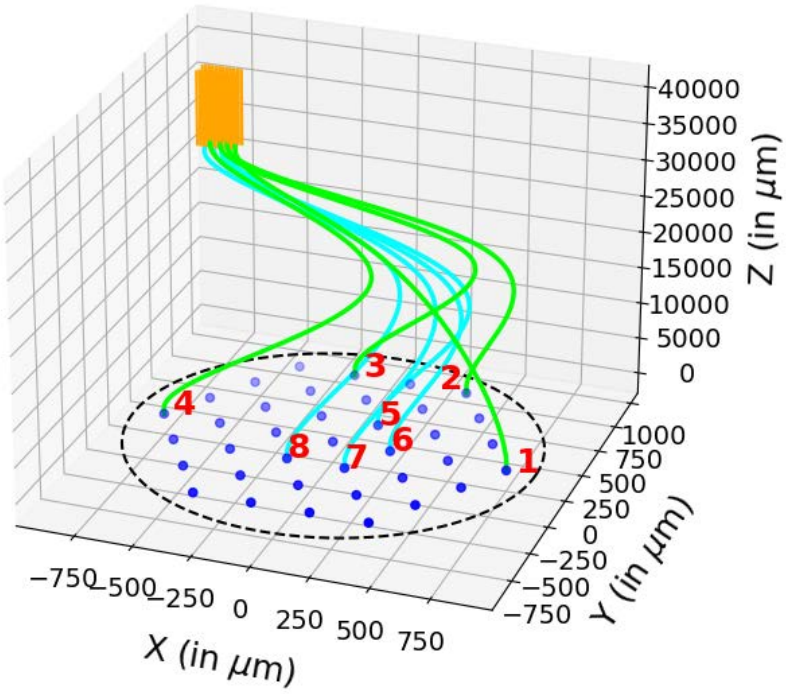

Figure 3.7: 8-input pupil remappers along with two DBCs (shown in orange). The blue dots arranged in a hexagonal pattern are the augmented focal spots of the MLA. Only the numbered focal spots are coupled to the 8-input pupil remappers. The black circle shows an augmented re-imaged pupil of a telescope.

Input number	PaL (in μm)	**min** (R_c) (in mm)
1	30,060.10	66
2	30,060.06	35
3	30,060.07	35
4	30,060.07	43
5	30,060.10	38
6	30,060.06	40
7	30,060.06	42
8	30,060.06	40

Table 3.2: Parameters of the 8-input pupil remappers as shown in Fig. 3.7. **min** (R_c) reports the minimum radius of curvature.

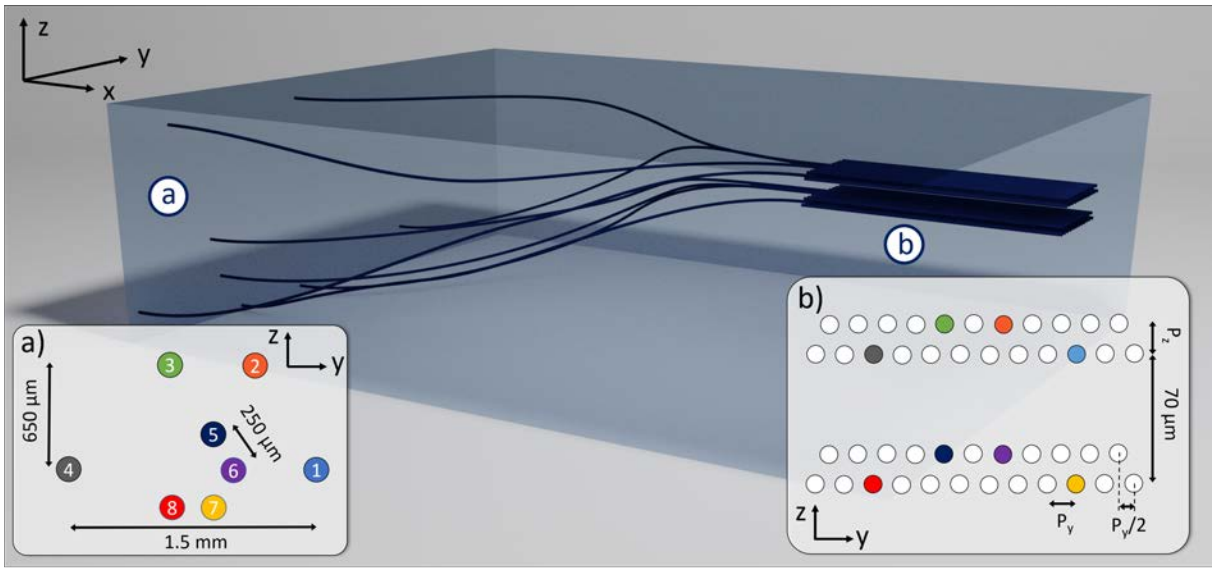

Figure 3.8: CAD drawing of the 8-input pupil remappers along with the two DBCs that are placed vertically at a separation of 70 μm (not to scale). (a) Section showing the arrangement of the eight input waveguides of the pupil remapper. The input face of the pupil remapper is placed behind the back focal plane of the MLA, which will be conjugated with the segmented deformable mirror (see Fig. 3.6a). (b) Section of the zig-zag DBCs that are stacked vertically with a separation of 70 μm. The eight input waveguides are highlighted in color, together with the horizontal and vertical pitches of the array.

This page was intentionally left blank.

Chapter 4

Fabrication of devices using ultra-fast laser inscription

This Chapter describes the fabrication of devices to realize 3-D PICs using ULI. The design parameters obtained from Chapter 3 were sent to *Politecnico di Milano* for the fabrication of the devices using their state-of-the-art ULI facility. It is to be noted the design parameters were further optimized by the *Politecnico di Milano*, but the parameters obtained from Chapter 3 served as a starting point for them to fabricate these 3-D IO based-*astrophotonics* devices.

The findings of Section 4.2 and Section 4.3 was explicitly done by the *Politecnico di Milano*. Section 4.2 is published in Nayak et al. [3], while Section 4.3 is written on the basis of a report provided by them.

4.1 Motivation

The building block of an optical device/circuit is the optical waveguide, which enables low-loss light propagation and is thereby used to connect components and devices [122, Chapter 6]. The mature CMOS technology that consists of lithography and etching methods have already produced 2-D planar waveguides with a propagation loss of $\sim 1 - 10\,\mathrm{dB/m}$ on silica/silicon nitride/silicon based-substrates, as these materials are compatible and well-established with the commercial foundries and generic platforms [123]. However, in the context of IO based-beam combiners, it was discussed in Section 1.4.4 that planar based IO have limitations in terms of scalability [91], choice of materials [124], wavelength coverage [104] and data-carrying capacity [100]. As a result, to overcome the problems of planar based-IO components, in recent decades, there has been growing interest in the 3-D PICs among several research groups, and commercial enterprises [101].

There are three main fabrication technologies to realize 3-D photonic circuits. The first technology uses multilayer stacking and coupling of planar photonic circuits, which exploits the mature and precise wafer-scale lithographic process [125]. Using this technology, 3D high-performance photonic devices such as waveguides, microrings, multi-mode interference power splitters, AWGS, and cascaded directional couplers have been fabricated at telecom wavelengths [126, 127]. The second technology is using a 3-D printer, where waveguides and multi-mode interference devices have been fabricated [128, 129]. Since most of the 3-D printing of waveguides uses polymer materials, bio-degradable based-polymer waveguides find immense applications in medicine [130]. The third technology uses an ultra-fast laser for inscribing freeform shaping of 3D photonic circuits with arbitrary contours and formations inside a substrate [125]. However, there are two main methods for fabricating 3-D photonic circuits using an ultra-fast laser. One method uses the concept of two-photon polymerization that focuses a laser in a photosensitive resist. It later undergoes a chemical etching process to obtain the required photonic structure [131, 132]. Such methods have been used in the realization of hybrid multi-chip

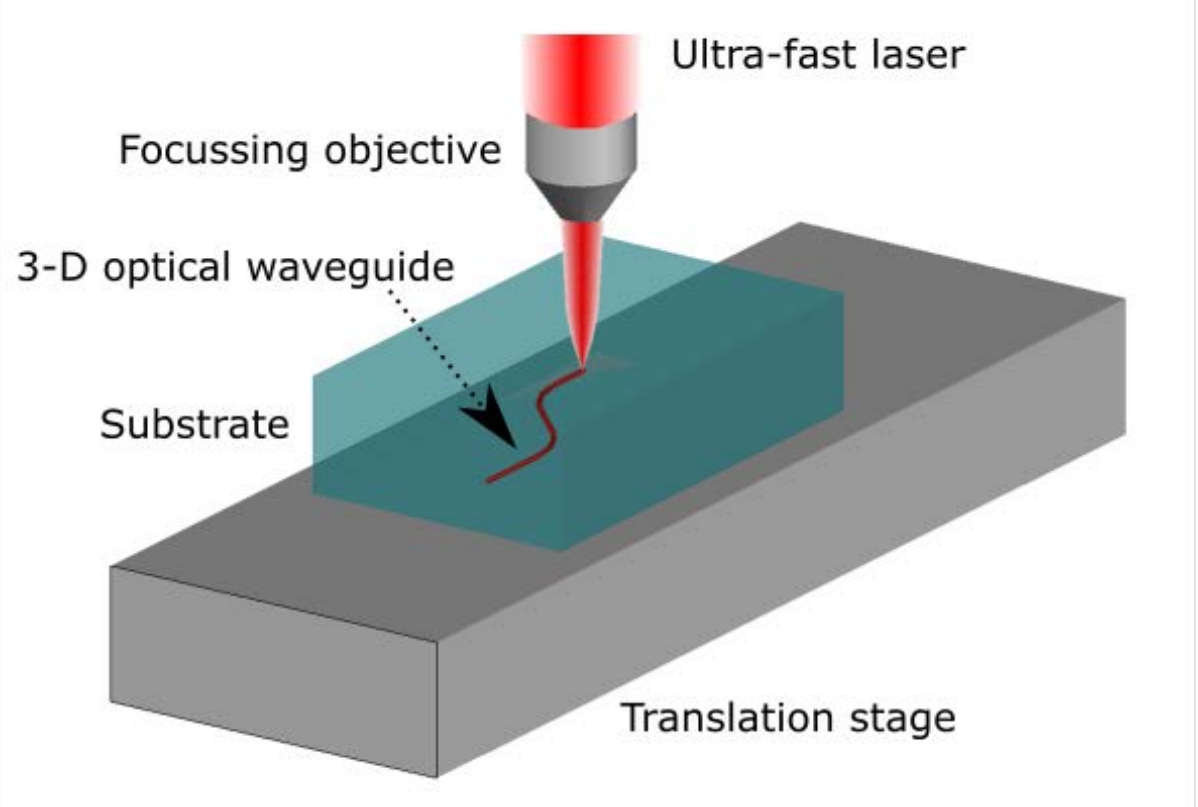

Figure 4.1: An ULI setup where an ultra-fast laser (pulse duration of a few hundred of fs) is focussed through an objective into a glass substrate. The glass substrate sits on a translation stage that is moved spatially to write 3-D photonic circuits in the substrate.

modules, where photonic wire bonds are used for efficient coupling between photonic chips [133], and realization of microstructures for microfluidic cooling of the chips [134], thereby increasing the performance of next-generation photonic circuits. Another method for ultra-fast laser uses the concept of multi-photon absorption that focuses the laser in transparent materials without any chemical etching step, thus leading to a variety of phase and structural changes in a spatially selective manner (see Fig. 4.1) [135]. This method of writing photonic structures have found applications in *astrophotonics* [67, 66], optical communication, quantum photonics, optofluidics, and sensing, to name a few [101].

In the context of astronomical interferometry, ULI based-*astrophotonics* devices have already been demonstrated in the laboratory and tested on-sky using a variety of materials at different astronomical bands. Some of the examples include: 1) Mid-IR beam combiner at L-band ($3-4\,\mu$m) with visibility contrast of $>90\%$ have been demonstrated on ZBLAN substrate [124], 2) An IO pupil remapping interferometer, "Dragonfly" instrument was successfully tested on-sky at H-band ($1.55\,\mu$m) [87], 3) A nulling interferometer, "GLINT" instrument was also successfully tested on-sky measuring the angular diameter of various stars [90], 4) DBCs have been experimentally verified by retrieving the visibilities both at Visible [103] and L-band [104], and 5) Recently, a K-band ($2.0-2.4\,\mu$m) two-telescope beam combiner was developed

using ULI to replace the existing beam combiner – MONA at CHARA facility [136, 137]. Hence, these examples necessitate that ULI is the only efficient technology for fabricating the photonic structures of Chapter 3.

As mentioned earlier, this work is one of the examples of an *astrophotonics* component for stellar interferometry applications, where the pupil remapping interferometers have to be arranged in 3-D geometry. These are connected to the 3-D photonic lattice of the DBC and fulfill both the restriction of path length matching and the minimum radius of curvature for 3-D WGs. Thus this task is realizable only with a 3-D PIC; therefore, the efficient and reliable method of fabricating this state-of-the-art photonic structure monolithically is through ULI.

4.2 Process parameters

For the fabrication of the device, a cavity-dumped Yb:KYW source was employed, delivering pulses with a central wavelength of 1030 nm, duration of 300 fs, and repetition rate of 1 MHz [138]. The optimal inscription process for obtaining low-loss single-mode waveguides at 1550 nm consisted of focusing the laser beam with a power of 620 mW through a 50x, 0.6 NA microscope objective inside an alumino-borosilicate glass (Eagle XG by Corning), translated by an air-bearing motion stage (Aerotech FiberGlide 3D) at a speed of 40 mm/s [139]. The translation was performed six times for each waveguide to increase the induced refractive index contrast. After inscription, the device was subjected to thermal annealing, consisting of 1-hour long heating step up to 750 °C, followed by slow cooling, first with a rate of -12 °C/h down to 630 °C, then with a rate of -24 °C/h down to 500 °C, followed at the end by a natural cooling down to room temperature. This treatment reduces both the waveguides' birefringence and the losses since it releases the internal stresses generated during the laser inscription [140, 141]. The result of the complete fabrication process is a single-mode waveguide suitable for operation at 1550 nm with propagation losses of about 0.2 dB/cm, a $1/e^2$ mode dimension of $8.5 \pm 0.3\,\mu\text{m} \times 9.0 \pm 0.3\,\mu\text{m}$, and a birefringence value below 5×10^{-6}. It is worth noting that the fabricated waveguides showed very similar performances regardless of the inscription depth, allowing, therefore, the fabrication of a pupil remapper with almost identical waveguides. However, when increasing the inscription depth, so for waveguides more buried in the glass, a reduction of the vertical offset was observed between the center of the guiding structure and the point where the inscription laser was focused. This effect is probably related to the dissimilar focusing conditions occurring at different depths due to spherical aberrations [101]. Since this offset change could lead to a misalignment between the focal spot of the telescope segments and the device inputs, a depth-dependent correction factor was applied to the vertical coordinates of the 4 input waveguides during the writing process.

After the optimization of the inscription parameters, preliminary zig-zag DBCs were fabricated, and the dependence on the waveguide distance of the planar (κ_H) and diagonal coupling coefficients (κ_D) were studied. The coupling coefficient is defined as the angular frequency of the optical power beating in a system composed of two evanescently-coupled waveguides (see Fig. 2.4). With an in-plane pitch of $16\,\mu$m and a separation between the planes of $13.3\,\mu$m, the same value for both coupling coefficients were obtained, equal to $1\,\text{cm}^{-1}$ at 1550 nm. In a system of two coupled waveguides, such a value would guarantee a full optical power transfer after a length of about 1.5 cm. With this value, the interaction length of the combiner was set to 20 mm, to provide the lowest condition number of the V2PM according to Chapter 2. It was already discussed in Chapter 2 that a low condition number of the V2PM is obtained when $\kappa_H = \kappa_D$ with $L = 1.35\,L_c$. These geometric parameters for the fabrication of the DBC with pupil remapper and fan-out were employed, which was used in the on-sky experiment. However, similar geometric parameters were also employed when the other two devices[i] were manufactured. The characterization of the device with horizontally and vertically polarized light provided the same output distributions, thus validating its polarization insensitivity [142]. Finally, by coupling the device with an SMF-28 fiber, the insertion losses were measured to be lower than 3 dB for all the four inputs, corresponding to a transmission of $\sim 50\,\%$.

[i] Device-A and Device-C as discussed in Chapter 3.

(a)

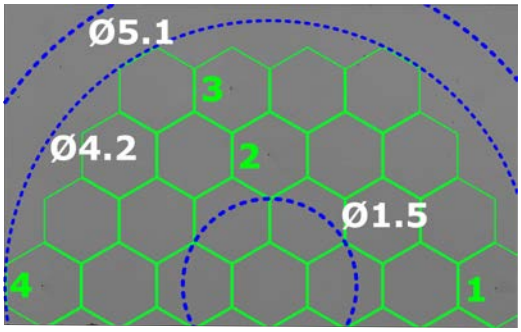

(b)

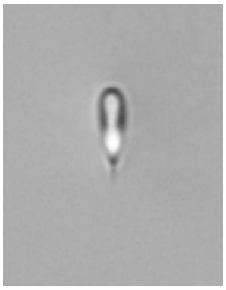

(c)

(d)

Figure 4.2: Images showing parts relevant to the integrated optics chip and its interface with the segmented deformable mirror *(not to scale)*. (a) Integrated optics chip inscribed in an alumino-borosilicate glass from *Politecnico di Milano*. The chip contains several devices with the geometry shown in Fig. 3.5 but differing in the DBC length ranging from $18-22\,\mathrm{mm}$. The device used for on-sky operation is shown in the micrographs (b)–(d). The waveguides are faintly visible in scattered light. (b) Input facet of the chip. Dimensions shown in white are in mm. The four input waveguides can be barely seen. The image is overlaid with a green grid showing the projection of a hexagonal-shaped segmented deformable mirror (DM) used to couple light into the waveguides (see Fig. 3.1a). The numbering of the input pupil remappers is also marked. The innermost and outermost blue overlay shows the projection of 1.2 m obscuration, and 4.2 m primary of the WHT, respectively. The middle blue overlay shows the DM with 4.2 mm diameter. (c) A magnified view of the single-mode waveguide written in the device using ULI. (d) Output facet showing the linear arrangement of 23 waveguides of the device.

The photonic chip with the fan-out DBC device[ii] as received from *Politecnico di Milano* is

[ii]This device as shown in the CAD drawing of Fig. 3.5 was used to collect stellar photons at the WHT, which will be discussed in details in Chapter 7.

shown in Fig. 4.2a. This chip contained three fan-out devices with a differing length of the DBC for $L = 18, 20, 22$ mm. The vertical spacing between the horizontal planes was fixed at $13.3\,\mu$m. The chip also contained a pupil remapper region but without the DBC. There were several straight waveguides along with the y-z position of the chip (see Fig. 3.5) for easy alignment and knowing which device is being injected with the light. The microscopic images of the device, where the first stellar photons were collected, are shown in Fig. 4.2, which corresponds to a DBC interaction length of 20 mm.

4.3 Insertion loss measurement

A precise measurement of the insertion losses of the device could be challenging due to its closely spaced 23 outputs. As the DBC spreads the light to its neighboring waveguides by evanescent coupling, only the 4-input pupil remappers fabricated with the same geometry as the DBC were considered for measuring the losses. This performed measurement would give a reliable estimation of the losses of the device as a whole. In this way, since the injected light remained confined in only one waveguide without spreading in the array, the insertion loss could be measured easily by coupling the output waveguides with an SMF-28 fiber and measuring the transmitted optical power. The insertion loss (IL) is calculated as follows:

$$IL = -10 \log \frac{P_{out}}{P_{in}}. \tag{4.1}$$

Where P_{in} is the input power of the injection fiber and P_{out} is the output power of the exit fiber. For the sake of completeness, the values for the 4 input pupil-remappers are listed in Table 4.1. The differences among the inputs can be explained if one considers that they experience different radii of curvature and different inscription depths in the chip. Similar IL values are reported for the other two devices.

Input number	IL (in dB)
1	3.0
2	3.0
3	2.6
4	2.4

Table 4.1: Insertion loss of the 4-input pupil remappers fabricated using ULI. The measurements were peformed by *Politecnico di Milano*.

This page was intentionally left blank.

Chapter 5

Simulation results

This Chapter presents the simulation results for the retrieval of the visibilities and the closure phases for a 4-input DBC with the design parameters obtained both from Chapter 2 and Chapter 4. The influence of noise – in the form of amplitude and phase errors at the input waveguides of the DBC, photon shot noise, detector noise, and the effect of long exposure time of the camera on the visibilities and the CP are studied. Some of the results in Section 5.3 are published in Nayak et al. [2], whereas the entire results of Section 5.4 are already published in Nayak et al. [3].

5.1 Simulation setup

Several assumptions were made to set up the simulation in RSoft. Only the DBC region as shown in Fig. 3.5b is simulated. It is assumed that there are negligible phase errors either from the pupil remappers (see Fig. 3.5a) or the coherent reformatters (see Fig. 3.5c) because these regions were path length matched. As the WGs of the DBC are single-mode, the fundamental mode can be approximated to a Gaussian function irrespective of the shape of the WGs or their refractive index profile [143, 144, 145]. The refractive index profile of the WGs written using ULI has a complex geometry [109], and a profilometer is required to calculate the exact profile. However, one can work with a step-index profile which is a good first-order assumption given the Gaussian approximation of a single-mode WG [143, 144]. The MFD of the WG from Chapter 4 was $8.5\,\mu$m $\times$ $9.0\,\mu$m. A Gaussian fitting of the fundamental mode of the WG was performed, taking into account the MFD. Thus the following values were obtained from the simulation at 1550 nm: 1) The refractive step-index difference between the core and cladding was 0.0067 and 2) Dimension of the single-mode WG was $5.0\,\mu$m $\times$ $6.4\,\mu$m. The material dispersion of the WG was also taken into account by doing a Sellmeier fitting of the empirical refractive indices given by the manufacturer.[i] The horizontal separation of the WG was kept at $16\,\mu$m from Chapter 4, whereas a vertical offset of $14.29\,\mu$m was used to make sure that $\frac{\kappa_H}{\kappa_D} = 1$. This would obtain a low CN of the V2PM at 1600 nm as discussed in Chapter 2. The coupling length (L_c) at 1600 nm was found to be 15.143 mm and the interaction region of the DBC was kept at $L = 1.346 L_c$. For the simulation, 51 equally spaced monochromatic wavelengths were launched in the range $(1.45, 1.75)\,\mu$m with a spacing of 6 nm between two successive wavelengths to calculate the wavelength response and bandwidth response of the V2PM. The results of the retrieved visibilities are discussed in the subsequent sections.

[i] The substrate is an alumino-borosilicate glass which is a proprietary material from Corning company and sold under the name Eagle 2000.

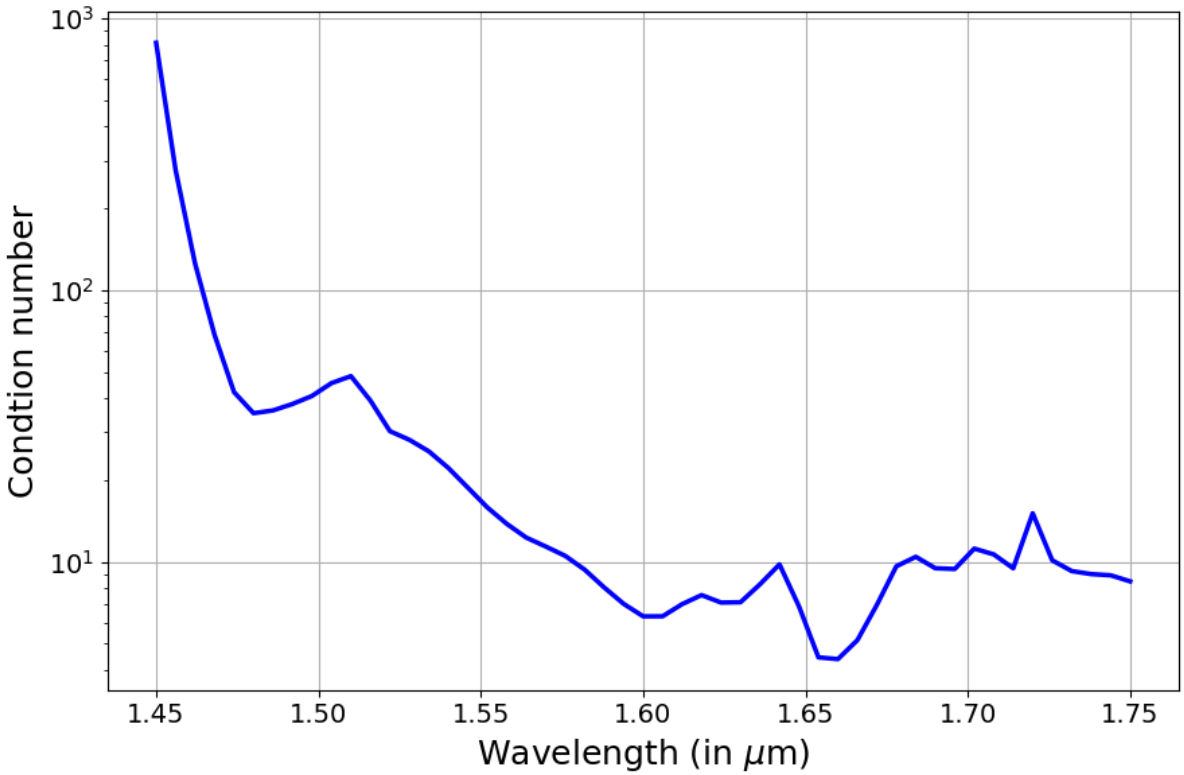

Figure 5.1: Variation of condition number as a function of wavelength.

5.2 Monochromatic visibilities

The variation of CN as a function of wavelength in the range $(1.45, 1.75)\,\mu$m is shown in Fig. 5.1. The CN decreases exponentially with increasing wavelength. For $\lambda \geq 1.55\,\mu$m, the mean of the CN = 9.3 and standard deviation = 3.1 which gives a variation of 33 % from the mean value. It is to be noted that though the device was designed at $\lambda_0 = 1.6\,\mu$m, the minimum of the CN occurred at a slightly longer wavelength, which was at $1.66\,\mu$m. The CN alone doesn't give a conclusive statement about the accuracy of the V2PM in retrieving the visibilities [103]. Hence, the P2VM will be applied to the $\vec{P}$ of the DBC, and the extracted visibilities will be shown.

The complex visibility of the model from Eq. (2.19) is defined as:

$$\gamma(\delta) = \frac{\sin\left(\pi\delta\frac{\Delta\lambda}{\lambda_0^2}\right)\exp\left[\mathrm{i}\pi\delta\left(\frac{1}{\lambda_1}+\frac{1}{\lambda_2}\right)\right]}{\pi\delta\frac{\Delta\lambda}{\lambda_0^2}}. \tag{5.1}$$

Where, δ is the known path delay between the interfering arms. It is to be noted that

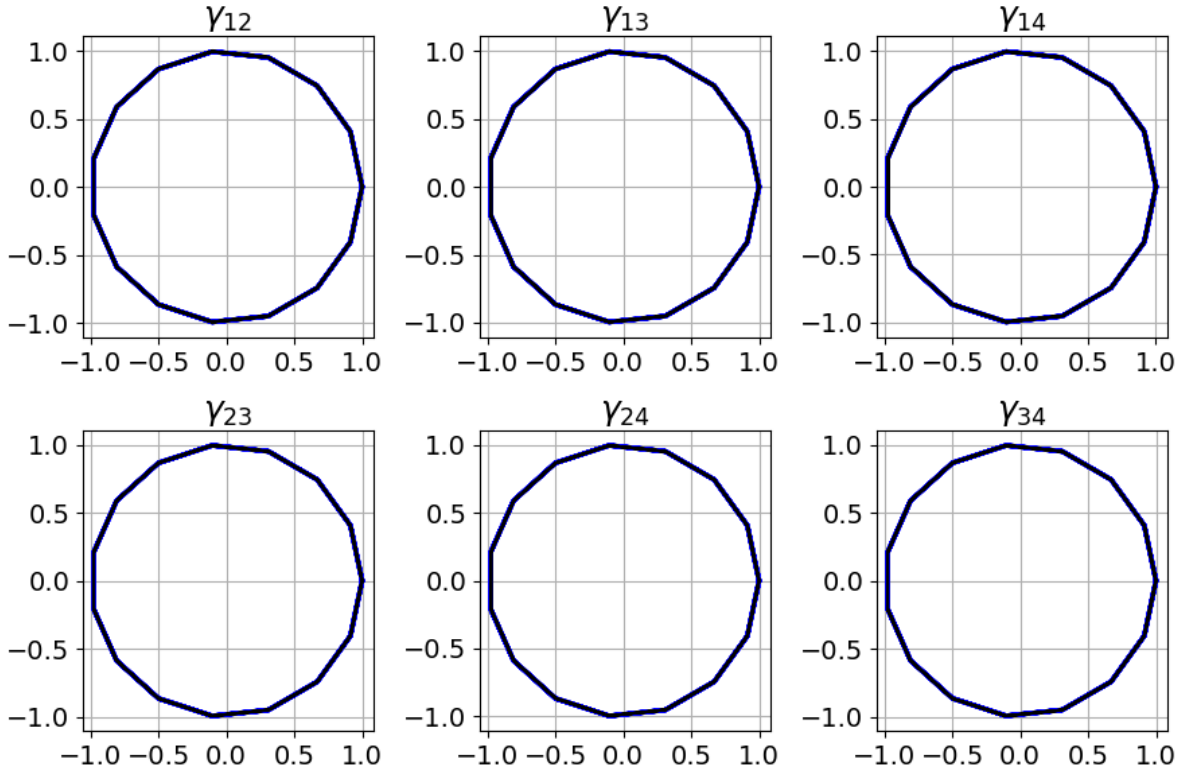

Figure 5.2: Retrieved visibility amplitudes (in blue) at $\lambda_0 = 1.6\,\mu$m. Black is the theoretical curve. x-axis: $\Re\gamma$, y-axis: $\Im\gamma$.

for the monochromatic light assumed in this section, $\Delta\lambda = 0$ thus, $\frac{\sin(\cdot)}{(\cdot)} \to 1$ and $\lambda_1 = \lambda_2$ in Eq. (5.1). The model defined above will be used as theoretical complex visibility of any light source for the rest of the work.

The retrieved visibility amplitudes and phases are shown in Fig. 5.2 and Fig. 5.3, respectively. The black curve shown in both the figures is the theoretical value as given by Eq. (5.1), and the blue curve is the retrieved value obtained from the DBC. To quantify the goodness of fit between the retrieved values and the model, a quantity – mean squared error (MSE) is defined [146, Chap 20]:

$$MSE = \frac{1}{n}\sum_{i=1}^{n}(Y_i - \hat{Y}_i)^2. \tag{5.2}$$

Where, n is the number of samples, Y_i is a vector of observed values, and $\hat{Y}_i$ is a vector of predicted (i.e. theoretical) values as given by Eq. (5.1). For an excellent fit, the MSE should be $= 0$. The MSE is calculated between the retrieved value in blue and theoretical value in black for visibility amplitudes as shown in Fig. 5.2. For all the pairwise combinations, the MSE is in the range (1.16×10^{-7}, 20.7×10^{-7}). Also, the MSE for retrieved phases in Fig. 5.3 for all

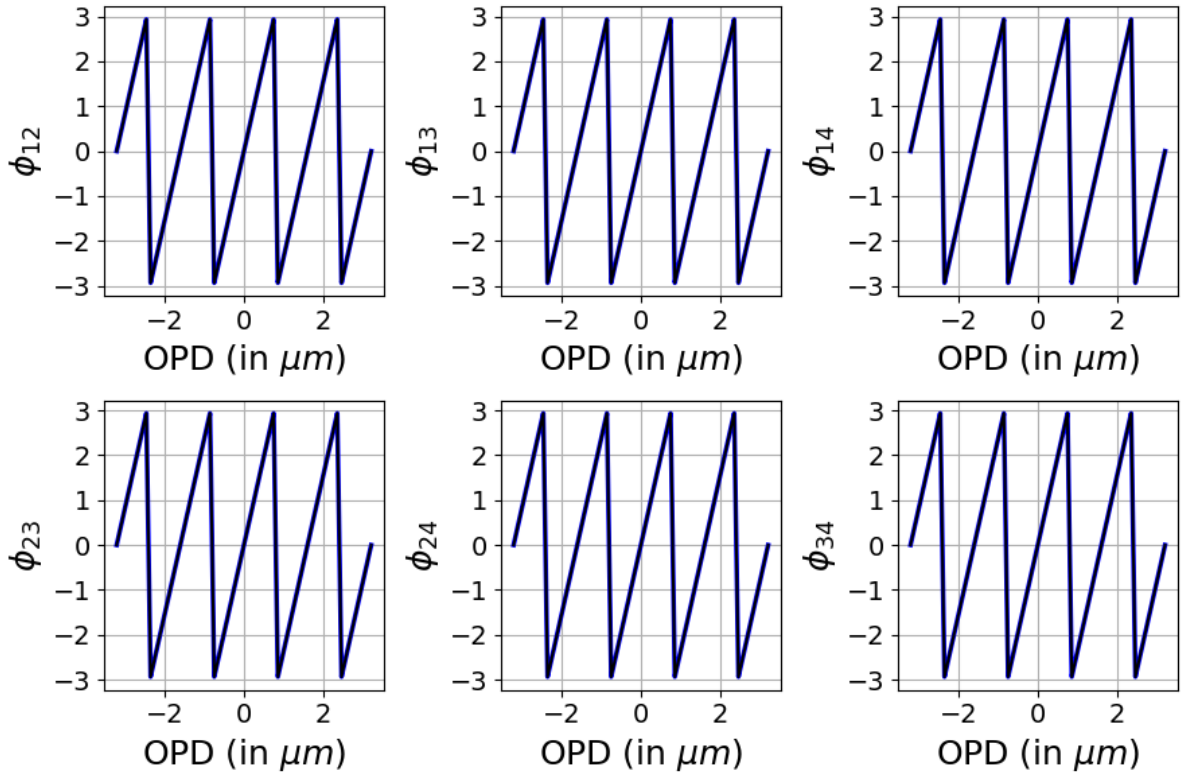

Figure 5.3: Retrieval of visibility phases (in blue) at $\lambda_0 = 1.6\,\mu$m. Black is the theoretical curve.

combinations is in the range $(1.3\times10^{-8}, 6.8\times10^{-7})$. Thus, it indicates that the theoretical curve well replicates the retrieved value at $\lambda_0 = 1.6\,\mu$m, as MSE ≈ 0. The MSE at shorter wavelengths (i.e. $\lambda < 1.55\,\mu$m) were higher in orders of magnitude when compared with $\lambda_0 = 1.6\,\mu$m. This is due to the high CN at shorter wavelengths, and as mentioned in Chapter 2, CN is a quantity that directly indicates the stability of a matrix.

In the above results, the retrieved visibilities are calculated from the calibrated V2PM. Therefore, one extracts the CP from Eq. (2.22), and unique CP can be calculated for each of the pairwise baselines. From Fig. 5.2, the visibility pair γ_{23} corresponds to the best baseline as it has the lowest MSE. Therefore, the CP corresponding to γ_{23} is shown in Fig. 5.4. It is evident from Fig. 5.4 that the retrieved value in blue does not match the theoretical curve in black. The MSE was in the range (5.9, 8.3). Since the MSE for CP is higher than that of visibility phases, the calculation of CP directly from the calibrated P2VM does not provide a feasible result. However, in the next section, it will be shown that when the same calibrated P2VM is used to extract the visibilities of 4-input light beams that are all injected simultaneously, the CP provides a feasible result.

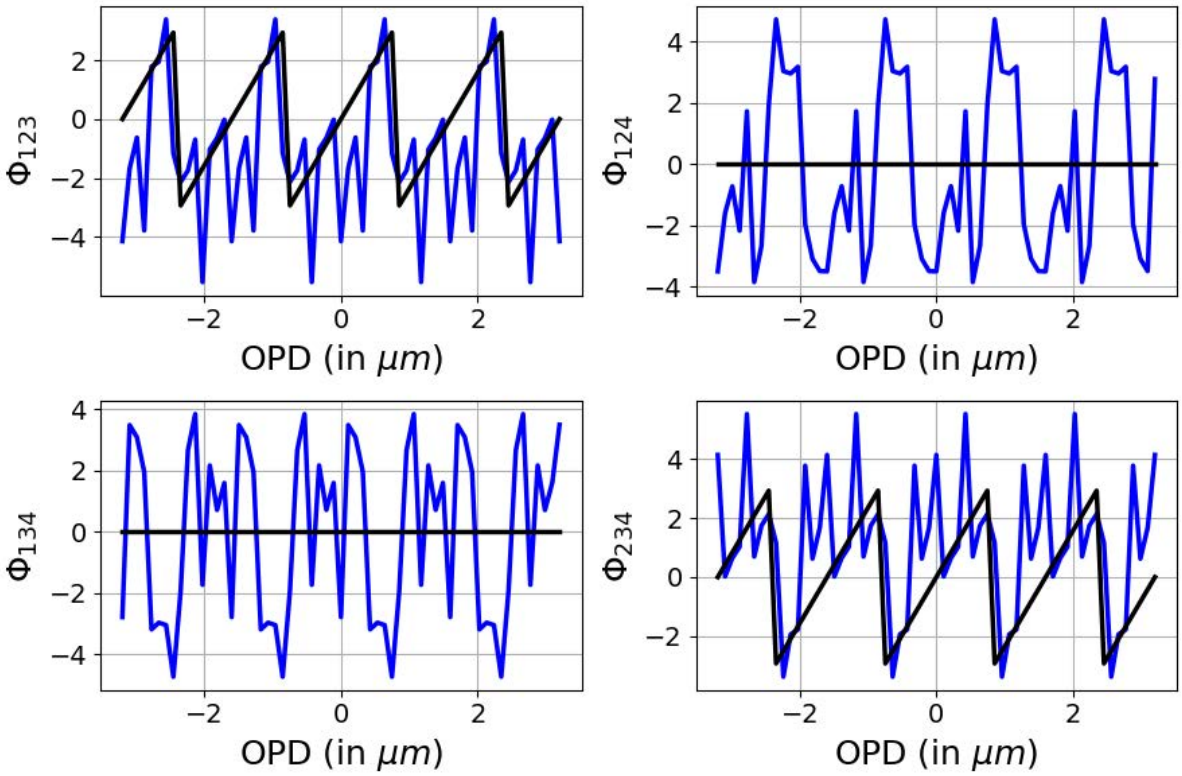

Figure 5.4: Retrieval of closure phases (in blue) for the best visibility pair, γ_{23} at $\lambda_0 = 1.6\,\mu$m. Black is the theoretical curve.

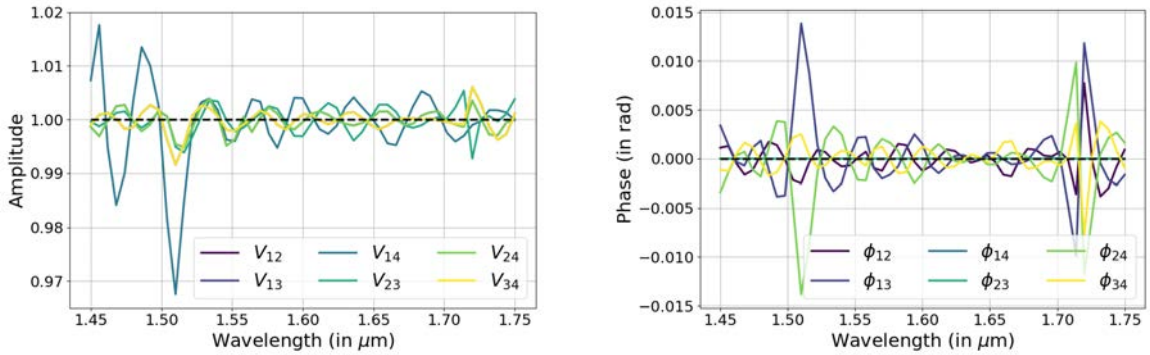

(a) (b)

Figure 5.5: Retrieved visibilities as a function of wavelength when 4-input beams are injected simultaneously into the DBC device. Black is the theoretical curve. (a) Visibility amplitudes. (b) Visibility phases.

5.2.1 Simultaneous injection of 4-input light beams

It is desirable to simultaneously inject 4-input light beams into the device, firstly to study the response of the P2VM in retrieving the visibilities, and secondly to simulate an interferometric array of Telescopes for Chapter 7. Here, 4-input beams are injected simultaneously. The phase delay between all the 4-input beams is assumed to be zero, and the amplitude also is assumed to be 1.

With the assumptions mentioned above, images are obtained from RSoft at each wavelength sample. Then, the output power vectors extracted from these images are applied to the corresponding P2VM – the one obtained from Fig. 5.1 and then, the visibilities are extracted. The visibility amplitude and phase are shown in Fig. 5.5a and Fig. 5.5b, respectively. The visibility amplitude agrees well with the theoretical value in black, except at shorter wavelengths (i.e. $\lambda < 1.55\,\mu$m), the amplitude value is deviated up to 2 decimal places. The same holds for visibility phases as well. However, these variations in the visibility amplitude and phase are minimal and can be neglected in the present context.

The retrieved closure phase is shown in Fig. 5.6. There are similar deviations in the CP, but it is slightly better when compared to the visibility phase. To get a feasible result of the closure phase from the calibrated P2VM, injecting all 4-input light beams simultaneously is desirable. Similar results in the next sections are shown when the DBC device will be injected with a real light source with a bandwidth.

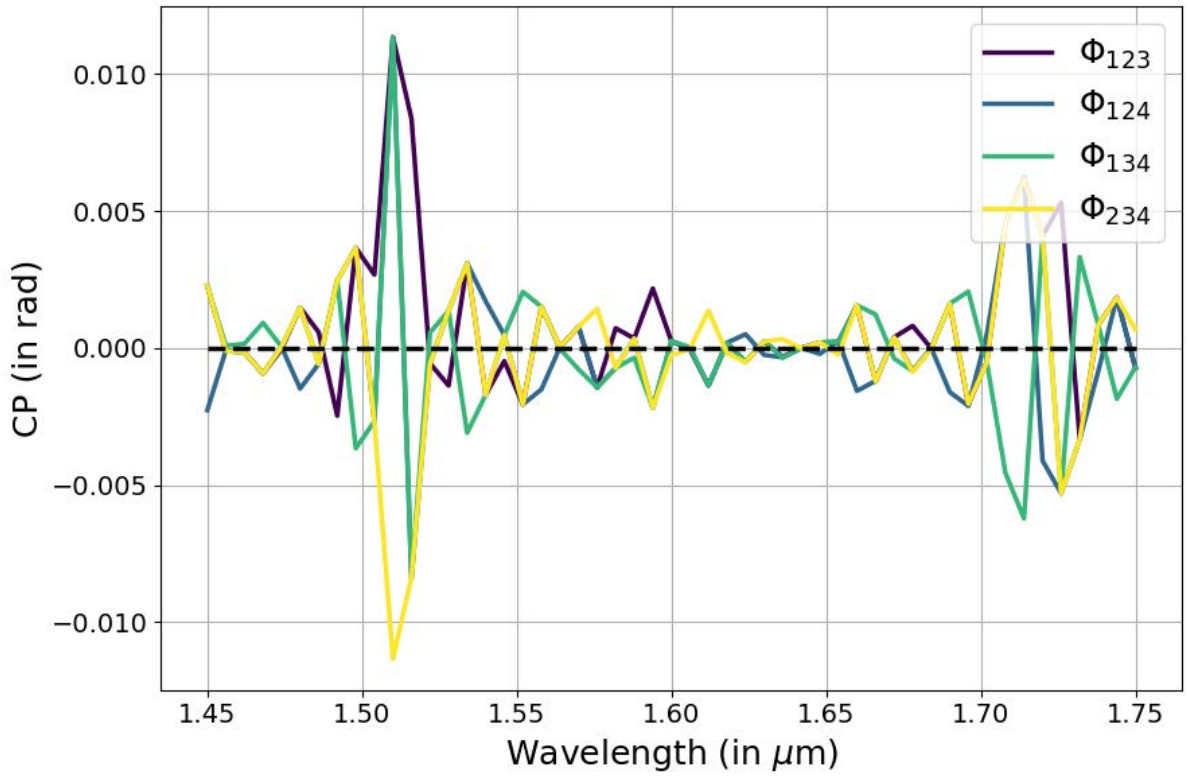

Figure 5.6: Retrieved CP as a function of wavelength when 4-input beams are injected simultaneously into the DBC device. Black is the theoretical curve.

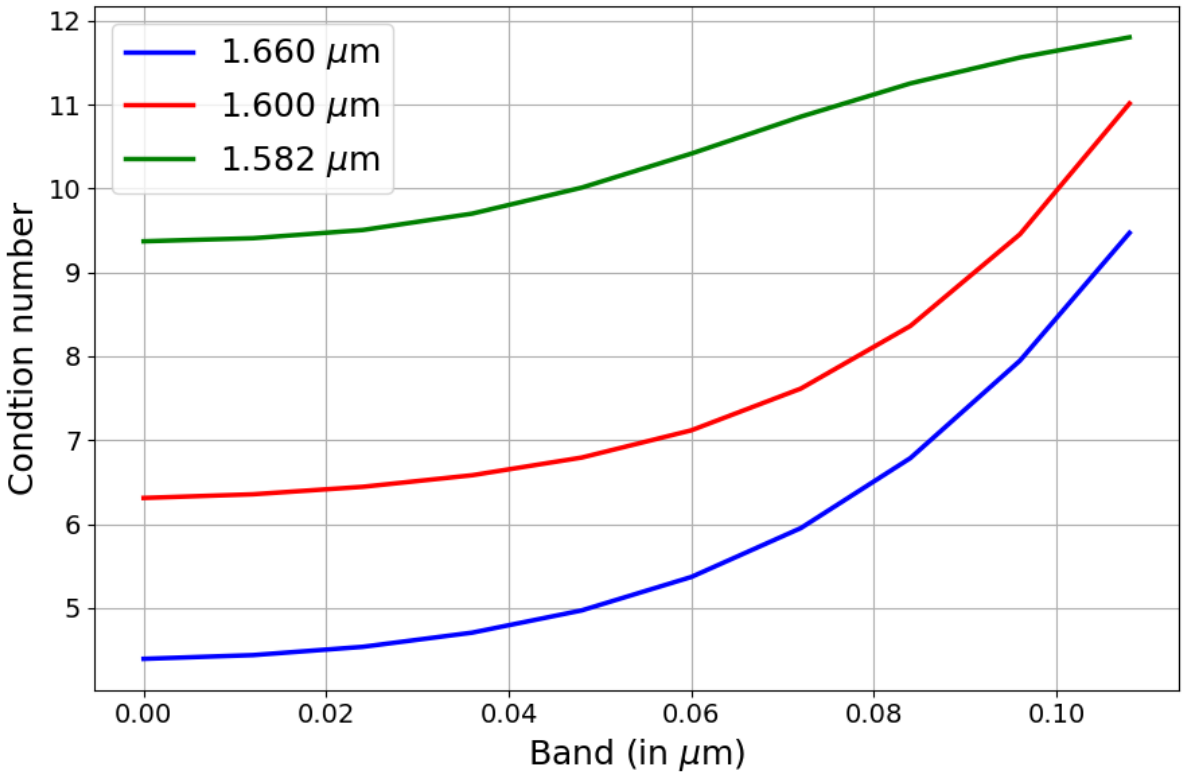

Figure 5.7: Variation of condition number as a function of bandwidth for three different central wavelengths.

5.3 Polychromatic visibilities

In the previous section, the visibilities obtained at monochromatic wavelengths are ideal, where a Dirac delta function represents the light source at any particular frequency. But, in reality, any light source has a certain finite bandwidth. Hence, the visibilities presented in this section are more robust than those presented for an ideal monochromatic light source. The variation of CN as a function of finite bandwidth of the source is shown in Fig. 5.7 for three different centered wavelengths. It can be seen that the condition number increases monotonically as bandwidth increases, and the dependence is polynomial. At increasing bandwidths, the modal fields describing the V2PM become chromatic, affecting the matrix elements, thus increasing the CN. At bandwidth = 0, it represents the CN of the ideal monochromatic wavelength as shown in Fig. 5.1. This concludes that it is often desirable to find the best operating wavelength of a DBC device by searching the lowest CN with respect to monochromatic wavelength. Furthermore, keeping the bandwidth as low as possible avoids inversion errors from the P2VM.

The retrieved visibility amplitude for a light centred at 1.6 μm, bandwidth of 48 nm is shown in Fig. 5.8. A zoomed view of 10 μm around the central lobe is shown in the inset to

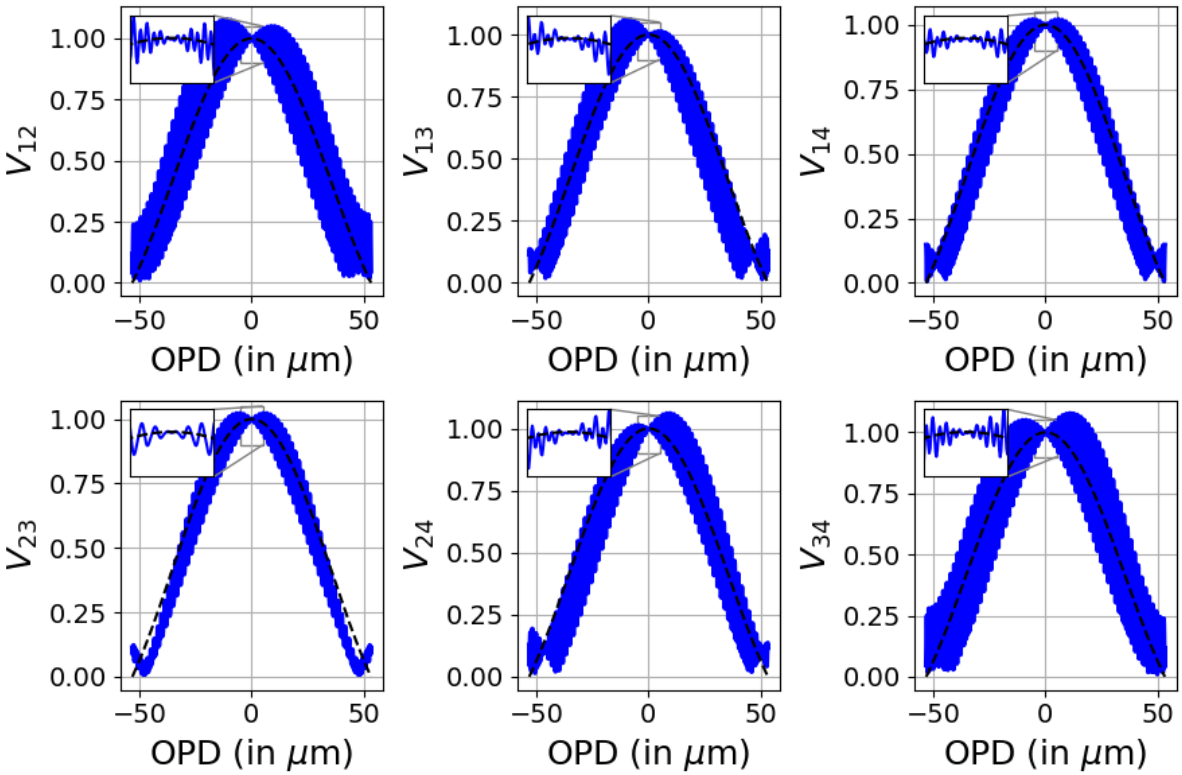

Figure 5.8: Retrieved visibility amplitude for a light source centred at 1.6 μm, bandwidth of 48 nm. The inset shows a zoomed view of 10 μm showing periodic oscilations around the theoretical curve in black.

show the periodic oscillations around the theoretical curve in black as predicted by Eq. (5.1). The frequency of these oscillations is $\sim \frac{\lambda}{2}$ indicating a phase difference of π between the real and imaginary parts of the complex visibilities retrieved from the P2VM. In principle, the phase difference between the real and imaginary parts should be $\frac{\pi}{2}$, which is represented by the black curve in Fig. 5.8. The amplitude of the periodic oscillation is maximum when the residual phase difference between the real and imaginary part equals π, which happens at increasing bandwidths. For the sake of clarity, the retrieved phases for an OPD of 20 μm are shown in Fig. 5.9. At 0 OPD, a perfect correlation exists between the retrieved values in blue and theoretical values in black. However, moving away from 0 OPD, the phase decorrelation of individual wavelength increases with increasing bandwidth. This results in a phase accumulation of π between the real and imaginary parts of the complex visibilities as one departs away from 0 OPD. It was also found that the phase decorrelation becomes worst with increasing bandwidth.

To quantify the error between the retrieved and theoretical values, MSE is calculated. The MSE for the visibility amplitude for all pairwise combinations from Fig. 5.8 is in the range (0.006, 0.014). This range of MSE for visibility amplitude is $\sim 10^5\times$ higher in order of magnitude than obtained at the monochromatic wavelength that was shown in Section 5.2. The increase in MSE is due to the phase errors obtained from the quasi-monochromatic P2VM

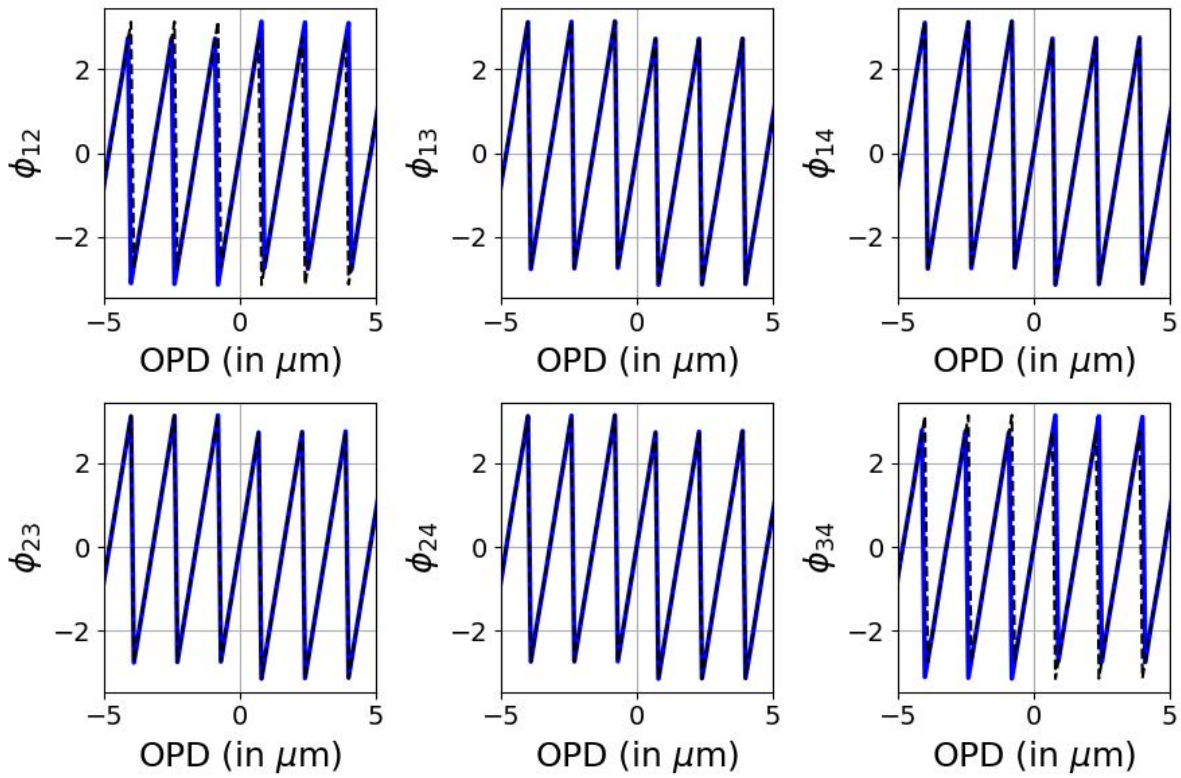

Figure 5.9: Retrieved visibility phase for a light source centred at 1.6 μm, bandwidth of 48 nm. A zoomed view of 10 μm around the central lobe is shown.

due to the finite bandwidth of the source. One can see that Eq. (5.1) is not adapted to predict the high frequency oscillations as seen from the retrieved values of Fig. 5.8, thus increasing the MSE of visibility amplitude for the polychromatic case when compared to the monochromatic case.

The MSE for the visibility phase from Fig. 5.9 has a range of (1.34, 3.72), which is $\sim 100\times$ higher in order of magnitude when compared to the range of the visibility amplitude. This implies that the retrieved visibility phase is more sensitive to phase errors when compared to the visibility amplitude. Though a perfect match between the prediction and retrieved values is seen for a difference of $10\,\mu$m, it is not the case when the whole OPD of $\sim 102\mu$m is taken into account. One can easily calculate the predicted phase from Eq. (5.1) since a known phase – δ is defined by the simulation. It was found that at the endpoints – far away from the OPD, the retrieved phase is not well predicted by the Eq. (5.1) which leads to an increase in MSE. The finite chromaticity of the V2PM as discussed in Chapter 2 can also lead to numerical errors that may pretend as phase errors in the retrieved visibility phases.

It is believed that a more rigorous estimator – introducing a phase term in the exponential part of Eq. (5.1) and accounting for the phase mismatch between the model and retrieved values can reduce the MSE. But, this is not the goal of the Thesis. The goal is to verify if the characterization results of Chapter 6 are well-explained and understood from this simulation section. Therefore, two of the outcomes from this section will be extensively used in Chapter 6: 1) High frequency oscillations in the polychromatic visibilities when characterizing all three different devices[ii] with a broadband light source, and 2) Retrieved visibility phase is more sensitive to phase errors resulting in higher MSE when compared to visibility amplitude.

However, the MSE increases with increasing bandwidth. This implies that the frequency dependence of $U_n(\nu)$ cannot be neglected, thus limiting the bandwidth operation of the DBC. The pair V_{23} had the lowest MSE for both the retrieved amplitudes and the phases. Hence for the sake of completeness, the closure phase for the pair V_{23} pair is again calculated, which was not as expected. The MSE was worse and higher than the visibility phase. This concludes that the CP that is directly calculated from the calibrated P2VM does not provide a feasible result – a consistent result with what was found in Section 5.2.

5.3.1 Simultaneous injection of 4-input light beams

This section will study the impact of retrieved visibilities from the DBC for a broadband light source when all the 4-input beams are injected simultaneously. Two scenarios will be con-

[ii] As mentioned in Chapter 3.

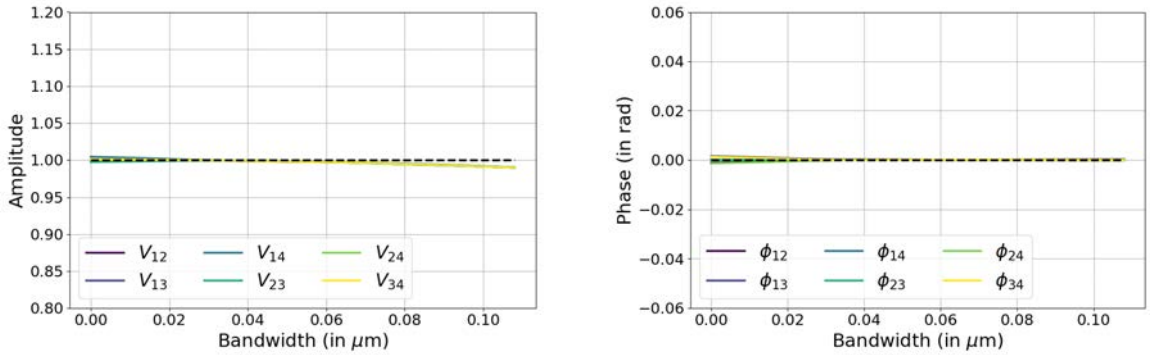

(a) (b)

Figure 5.10: Retrieved visibilities as a function of bandwidth when 4-input beams are injected simultaneously into the DBC device at $\lambda_0 = 1.6\,\mu$m. Black is the theoretical curve. (a) Visibility amplitudes. (b) Visibility phases.

sidered: 1) When there is no phase delay between the 4-input beams when they are injected simultaneously,[iii] and 2) When there is a phase delay in one of the 4-input beams, but all of them injected simultaneously.[iv]

5.3.1.1 Static injection

The amplitude of all 4-input beams injected simultaneously is assumed to be 1 and phase to be 0. The power extracted from the output images of the RSoft is summed as given by Eq. (2.17). This is done because the input light now considered contains a finite bandwidth. The summed power vectors are now applied to the P2VM obtained from Fig. 5.7 that is centered at $1.6\,\mu$m and then, the visibilities are retrieved. The visibility amplitude and phase is shown in Fig. 5.10a and Fig. 5.10b, respectively. The retrieved values match the theoretical black curve well, except at larger bandwidths, the amplitude value slightly deviates from the theoretical value. However, the visibility phase is nearly constant and matches well with the theoretical black curve.

The retrieved closure phase is shown in Fig. 5.11, and the retrieved values match well with the theoretical black curve. It can be seen that the variation of CP is nearly constant with increasing bandwidths. These results show that the variation of visibilities and CP are nearly constant with increasing bandwidth in an ideal scenario. However, when various noise sources are taken into account, it will be shown in Section 5.4 that the visibilities and CP do not match the expected values.

[iii] Known as a static injection.
[iv] Known as a dynamic injection.

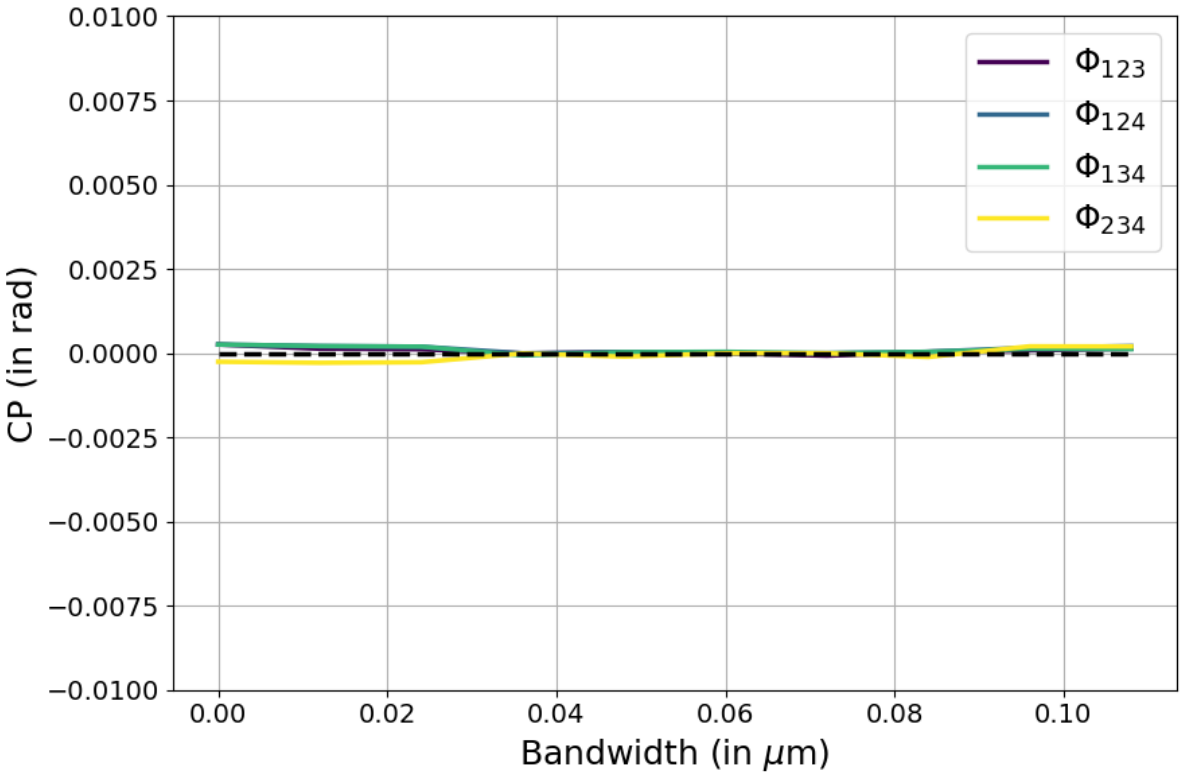

Figure 5.11: Retrieved CP as a function of bandwidth when 4-input beams are injected simultaneously into the DBC device at $\lambda_0 = 1.6\,\mu$m. Black is the theoretical curve.

5.3.1.2 Dynamic injection

The assumption for Section 5.3.1.1 holds in this section as well, but now a linear phase ramp is also added, especially to input numbered 4. For the sake of representation of visibilities, the results will be shown when a fixed P2VM is obtained at $\lambda_0 = 1.6\,\mu$m and $\Delta\lambda = 48\,$nm. The retrieved visibility amplitude is shown in Fig. 5.12. Since the input numbered 4 is delayed, the visibilities (i.e. V_{14}, V_{24}, V_{34}) follow a sinc function given by Eq. (2.19), which is the characteristics for a broad-band light source. The remaining three visibilities have a constant magnitude of 1. However, due to the finite bandwidth of the light source, the retrieved visibilities have phase errors which are seen in the form of high frequency oscillations in Fig. 5.12. The reasoning for these phase errors is already mentioned in Section 5.3, and these phase errors become more prominent with increasing bandwidth.

Similarly, the visibility phase is shown in Fig. 5.13 for a zoomed view of 10 μm around the center OPD. It can be seen that as phase ramp was applied in input numbered 4, the phase ramps are successfully retrieved for phase pairs ϕ_{14}, ϕ_{24}, and ϕ_{34}. The remaining phase pairs are expected to be 0. It was found that the MSE for the visibility phase was higher than that of visibility amplitude. This is attributed due to the increase in phase errors as one goes away from zero OPD, and as a result, retrieved phases are more sensitive to phase errors leading to higher MSE when compared to retrieved amplitudes.

As pointed out in Chapter 2, the CP is robust to external phase errors arising from a common origin. To prove this fact, the closure phase is shown in Fig. 5.14. It can be seen that the closure phases for all the triplets are close to 0 rad. It was found out that the MSE for CP was of the same order of magnitude as that for the visibility phase.

The above results conclude that though there are induced phase errors at the input of the DBC, the visibilities and CP can be retrieved from the P2VM up to a reasonable accuracy matching well with the theoretical values. But, the MSE for all the three quantities (i.e. visibility amplitude, visibility phase, and CP) increases with increasing bandwidth, which indicates the bandwidth limitation of the DBC.

5.4 Impact of noise on visibilities

[v]In the above sections, ideal detectors are assumed. From Chapter 2 and in the above sections, monochromatic light is assumed as a wavelength – λ_0 and bandwidth – $\Delta\lambda = 0$, while the

[v]The readers are asked first to read Chapter 7 and then read this section to have a better understanding of the noise sources.

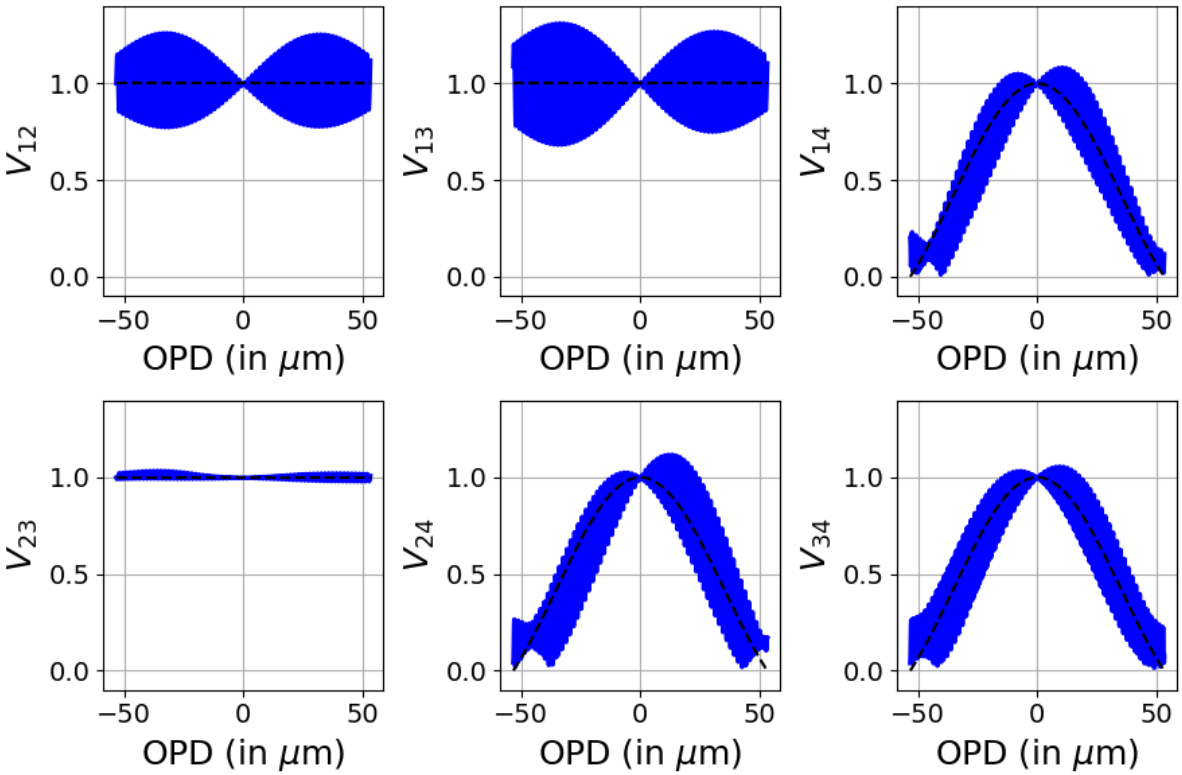

Figure 5.12: Retrieved visibility amplitude when 4-input beams are injected simultaneously into the DBC device. Black is the theoretical curve. Here, a phase ramp is applied to input numbered 4.

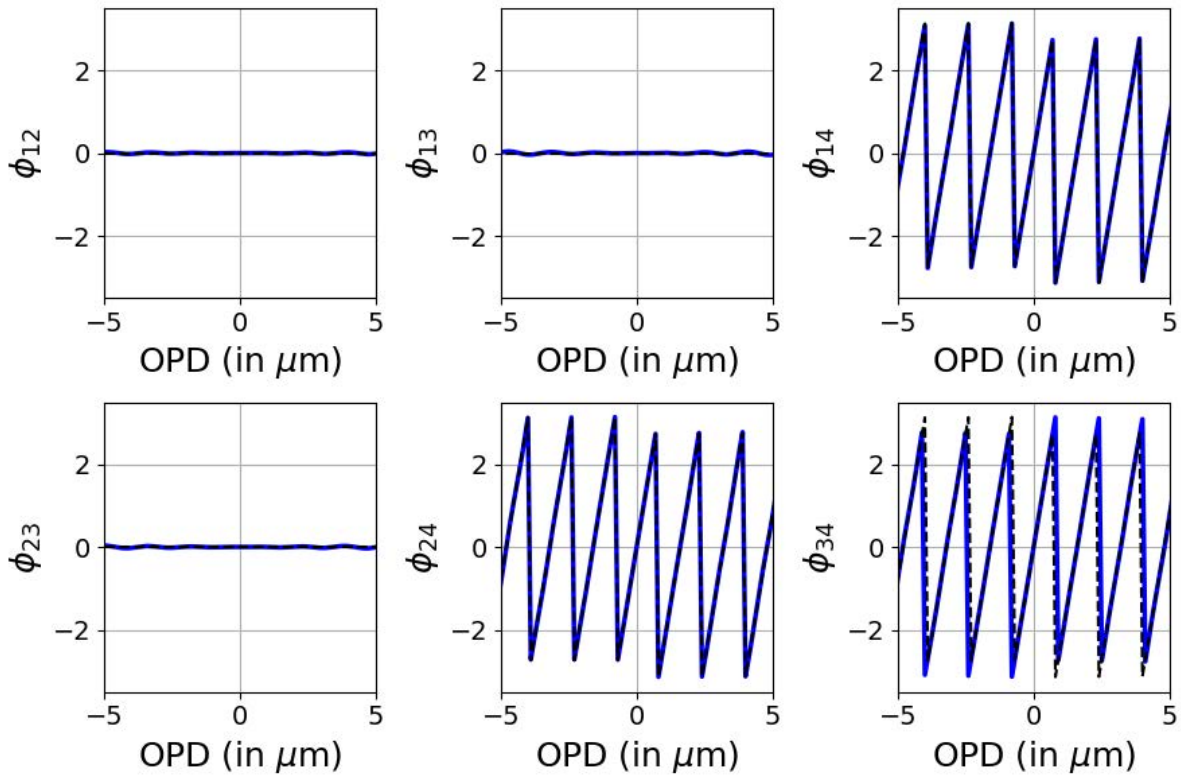

Figure 5.13: Retrieved visibility phase when 4-input beams are injected simultaneously into the DBC device. Black is the theoretical curve. Here, a phase ramp is applied to input numbered 4.

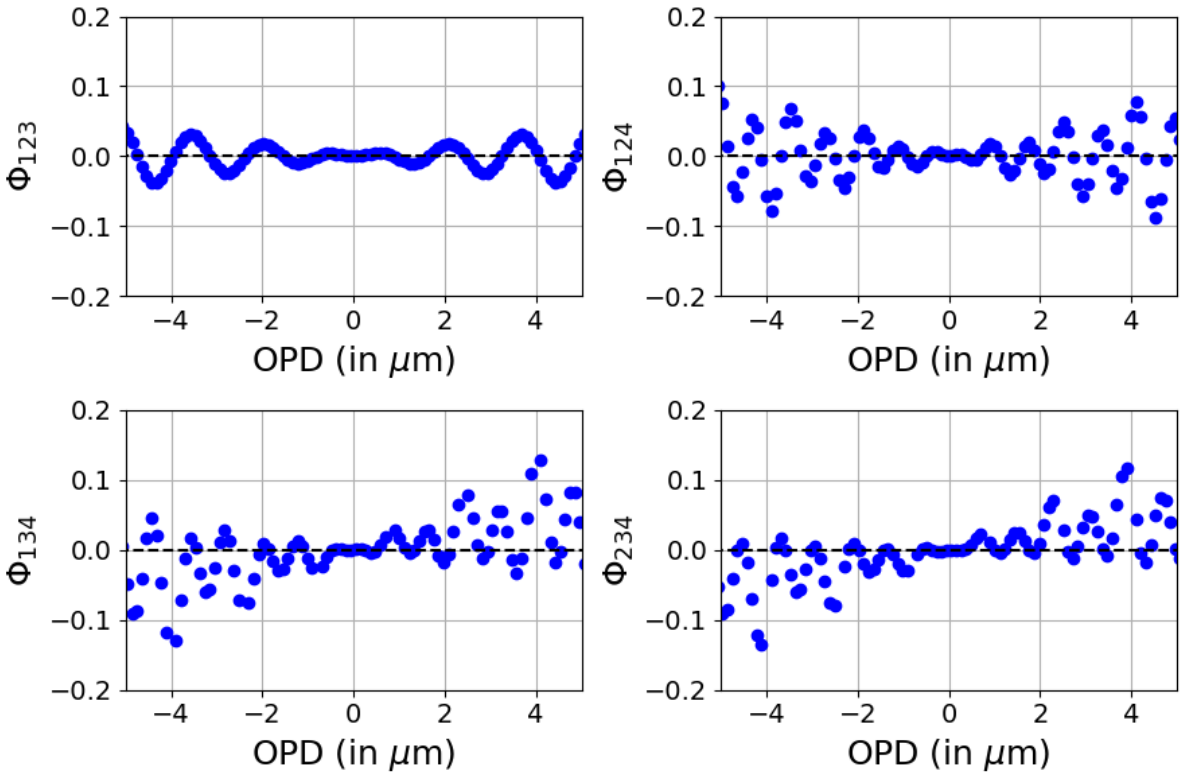

Figure 5.14: Retrieved CP when 4-input beams are injected simultaneously into the DBC device. Black is the theoretical curve. Here, a phase ramp is applied to input numbered 4.

polychromatic light is assumed to behave as $\frac{\lambda_0}{\Delta\lambda} \ll 1$. As a result, the visibilities and CP are retrieved with excellent accuracy from a DBC, whether the light source is monochromatic or polychromatic. It is well known that the visibilities describing the degree of coherence get degraded due to the presence of different noise sources such as finite bandwidth of the light source, wavefront tilts, aberrations of optical surfaces, non-ideal detectors, and polarization mismatch [4, Chapter 3]. The effect of finite bandwidth of a light source and induced phase errors at the inputs of the DBC have already been studied in the above sections of this chapter.

While conducting the lab characterization in Chapter 6, it will be seen that the retrieved experimental visibilities are comparable to theoretical values. But, during the on-sky tests in Chapter 7, the retrieved visibilities are significantly dispersed from the expected values. Therefore in this section, a simulation is carried out to understand better the on-sky results of Chapter 7 and their deviations from the expected values. Hence in a real-time environment, it is essential to study the impact of some of these noise sources on the retrieved visibilities in the context of a DBC.

Following Section 5.2.1, the 4-input electric fields are injected simultaneously into the DBC device using RSoft. But, now, both the amplitude and phase of the electric field are statistically varied[vi] with respect to time. The power vectors extracted from these statistical variations of the input electric fields are applied to the P2VM centered at $1.6\,\mu$m, and then, the visibilities are retrieved.

The statistical variation of the input electric field gives a simplistic representation of an adaptive optics (AO) system, where the wavefront corrected by the AO has both phase and amplitude errors. A quantity named Strehl ratio (SR) is defined, which tells about the quality of the wavefront correction by an AO system. Mathematically, SR is written as:

$$SR = \exp\Big(-\Big(\frac{2\pi\sigma_\lambda}{\lambda}\Big)^2\Big). \tag{5.3}$$

Where, σ_λ is the rms wavefront error in the units of length. Hence, it follows that the higher the SR, the better is the quality of wavefront correction of an AO system.

It is underlined that a simulation taking fully into account the properties of the experimental setup described in Chapter 7 is beyond the scope of the present work. Consequently, the description of the electric fields being launched in the present analysis is simplified. From the SR of $\sim 30\%$ delivered by adaptive optics system of the WHT – CANARY (see Chapter 7), a wavefront error of $\lambda/5.7$ root-mean-square (rms) is derived. The relative phases between the four input electric fields are varied using a random Gaussian distribution with a standard deviation of $2\pi/5.7$. The amplitude fluctuations at the four inputs are accounted in the form of a

[vi] The probability density function of the histogram follows a Gaussian distribution.

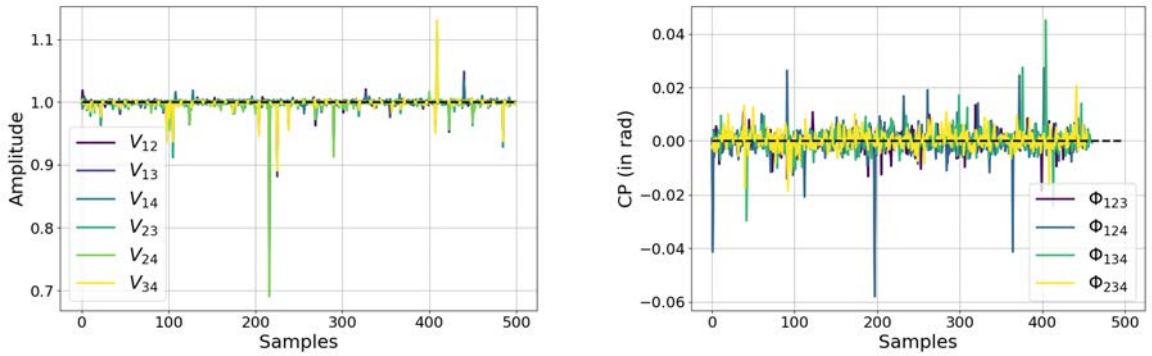

(a) (b)

Figure 5.15: Retrieved visibilities with four input beams coupled into the DBC device. Both the amplitudes and phases vary following a statistical Gaussian distribution. Black is the theoretical curve. (a) Visibility amplitudes. (b) Closure phases.

random Gaussian distribution with a mean of one and a standard deviation of 0.3, with strictly positive amplitude values. In the subsequent sections, the results of the simulation study are shown.

5.4.1 Input amplitude and phase errors

A 500 realizations of the output images of the DBC produced by RSoft were obtained, and the images were applied to the simulated P2VM described above to extract the visibilities. The retrieved visibility amplitude is shown in Fig. 5.15a, and the amplitude values for all the visibility pairs are in the range 0.996 ± 0.017 to 1.001 ± 0.006. The closure phase values are shown in Fig. 5.15b. For a small subset (i.e. $< 10\%$) of samples, $\pm 2\pi$ phase jumps are obtained, which are likely due to numerical errors, and are thus removed in Fig. 5.15b. It is observed that the CP values are consistent with 0° for all the triplets. When testing SR = 0.5, it was found that, as expected, an even lower dispersion for the retrieved amplitudes and CP values. These results suggest that the effect of amplitude and phase residual errors from the AO should be negligible compared to other noise sources.

In the next sections, additional noise sources are taken into account and considered only one visibility amplitude and one closure phase for a clearer demonstration of the resulting effects. The visibility V_{14} and the closure phase Φ_{234} is selected, which have the lowest mean squared error in Fig. 5.15.

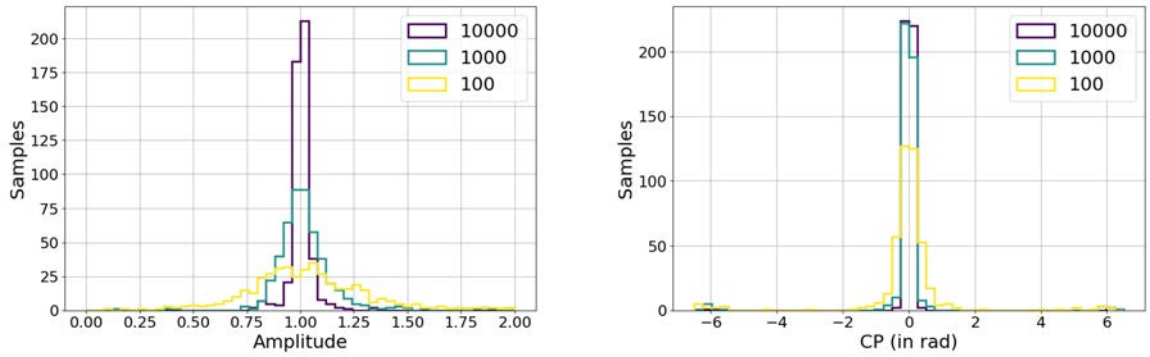

(a) (b)

Figure 5.16: Histogram of the retrieved visibilities for different levels of photon shot noise. The legend shows the mean number of photons N_p per pixel. (a) V_{14}. (b) Φ_{234}.

5.4.2 Photon shot noise

As the output intensity images provided by RSoft are normalized, the images are multiplied by a constant factor to get the number of photons (N_p) per pixel. Thus, a random Poisson distribution with a mean of N_p photons per pixel is now applied to the output image of DBC containing the intensity of the complex electric fields to obtain the required photon shot noise.

By setting N_p to the values 10^2, 10^3 and 10^4, different histograms of the visibility amplitude for the pair V_{14} are obtained as shown in Fig. 5.16a. It can be seen that the standard deviation of the visibility amplitude distribution increases for low N_p where the effects of photon noise become more significant. As a result, there is a spread in the visibility amplitude distribution as N_p decreases. The histogram plot for the CP triplet Φ_{234} in Fig. 5.16b also shows a gradual increase of the standard deviation for decreasing N_p. In addition to the photon noise, the detector noise is added to the DBC outputs, and the impact of visibilities is studied in the next section.

5.4.3 Detector noise

The simultaneous contribution of the photon noise and detector noise is now considered. For the latter, two main components are included: 1) read-out noise; 2) dark current (I_d). To implement these noises in the intensity images obtained from RSoft, N_p in Section 5.4.2 is converted into number of electrons N_e using the 90% quantum efficiency of the CRED2[vii] when operated at

[vii]CRED2 is an NIR camera from the company – First Light Imaging. This camera will be used for on-sky test in Chapter 7.

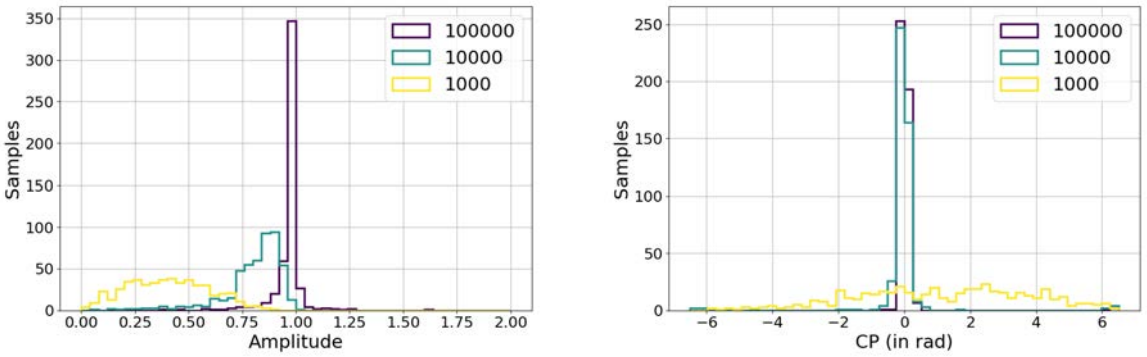

(a) (b)

Figure 5.17: Histogram of the retrieved visibilities for different levels of photon shot noise along with added detector noise. The legend shows the N_p per pixel. (a) V_{14}. (b) Φ_{234}.

$-40\,^{\circ}$C [147]. After N_e is calculated, a Gaussian random distribution for the read-out electrons with a standard deviation of $22\,e^-$ per pixel is added [148], and a Poisson random distribution for dark current with a mean of $600\,e^-/s$ per pixel [147] is also added. Successively, N_e is converted to ADU by multiplying it with the gain of the camera, which is $0.49\,\mathrm{ADU}/e^-$ [147]. Since $I_d \propto t_e$, the on-sky $t_e = 250\,\mathrm{ms}$ giving an $I_d = 150\,e^-$ per pixel is considered from Chapter 7, where t_e is the exposure time of the camera. The distribution of the retrieved vsibility amplitude is shown in Fig. 5.17a for three scenarios of N_p.

In comparison to the photon-noise dominated case (see Section 5.4.2), the inclusion of the detector noise produces a more extensive spread of the interferometric quantities with a decreasing number of photons N_p, but also shifts the peak of the visibility amplitude distribution towards V$<$1. The spread of the CP histograms in Fig. 5.17b is also significantly impacted when including the detector noise in the low photon regime. As one may have expected, this implies that in the low flux regime, the detector noise in the experiment, especially in Chapter 7 becomes dominant along with photon noise. This is a major source of signal degradation in the retrieval process of the coherence vector. In the next section, the effect of longer t_e on the retrieved visibility amplitude is discussed.

5.4.4 The effect of $t_e > \tau_0$

The use of adaptive optics acting as a fringe tracker allows in principle to increase the integration time t_e beyond the characteristic coherence time of the atmosphere τ_0. In the absence of AO correction, the standard deviation of the phase between the sub-apertures of the longest baseline 1-4 for the observing conditions reported in Table 7.3 is estimated to be $\sim 1.6\,\lambda$ [5, Eq. (4.45)], while it is only $0.2\,\lambda$ with the AO correction. However, with an SR $\sim 30\%$, the level of residual

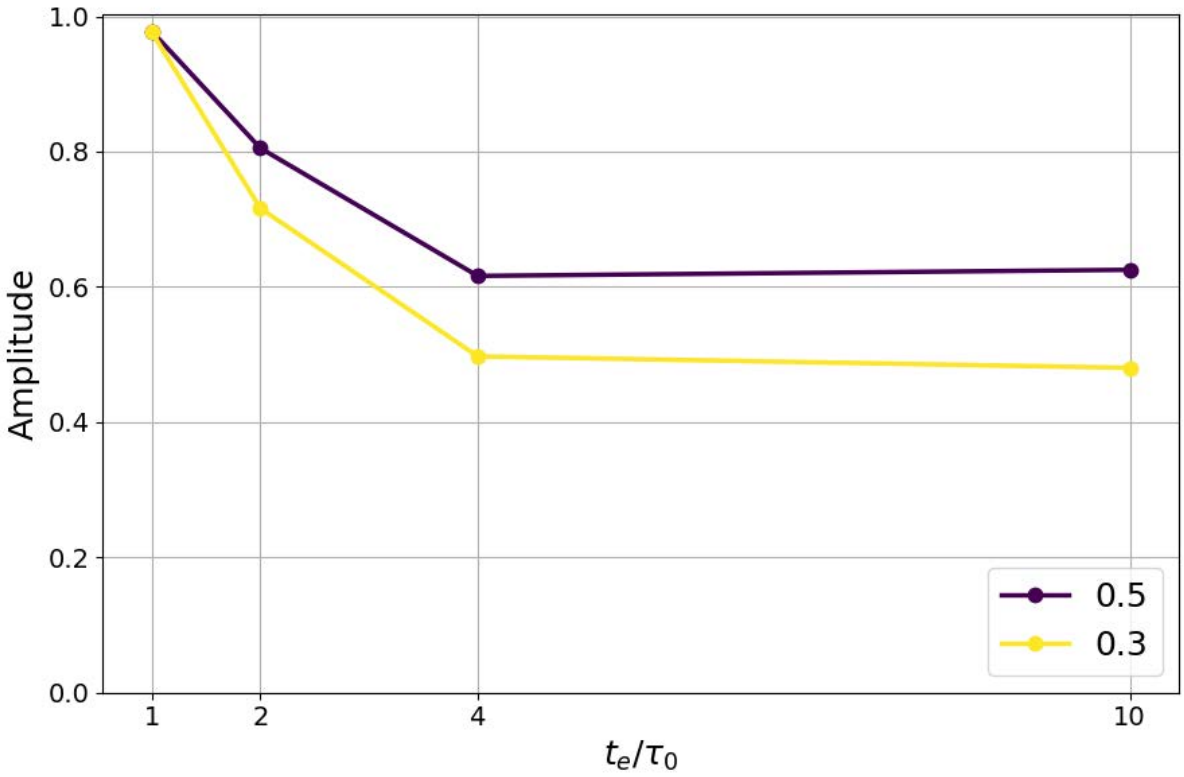

Figure 5.18: Median value of the retrieved visibility amplitude (V_{14}) as a function of the exposure time. The legend shows the Strehl Ratio. Here the case n=1 assumes $t_e = 30$ ms with $N_p = 10^4$ photons per pixel.

phase error may produce fringe smearing, which causes the retrieved visibility amplitudes to be smaller than unity.

To simulate the effect of longer t_e on a squared law detector, an intensity summation over n samples obtained in Section 5.4.1 is taken and fulfilling $n = \frac{t_e}{\tau_0}$. The photon shot noise and detector noise is also taken into account, and tested for $n = 1, 2, 4, 10$. The median value of the retrieved visibility amplitude for the pair V_{14} is shown in Fig. 5.18 for SR = 0.3 and 0.5. The case $n = 1$ corresponds to $t_e = 30$ ms with $N_p = 10^4$ photons per pixel. The clear effect of fringe smearing due to partial AO correction is observed in Fig. 5.18, suggesting that the chosen value of the exposure time contributes to the drop in the visibility amplitude in Chapter 7.

This page was intentionally left blank.

Chapter 6

Characterization of devices

This Chapter presents the interferometric characterization results of the three different IO based-*astrophotonics* devices using a 2-beam Michelson setup. For all the devices, results of monochromatic and polychromatic visibilities are shown. A polarization study is also done to verify the polarization independent behavior of the DBC device fabricated using ULI. These characterization results were necessary to find the best suitable device that could be operated for the on-sky test in Chapter 7.

6.1 2-beam Michelson setup

The fabricated devices received from *Politecnico di Milano* were characterized to verify its interferometric response. For doing the interferometric characterization of the devices, a semi-automatic 2-input Michelson setup was used as shown in Fig. 6.1. Though the input facet of the device is arranged in a pupil remapper configuration, the filling of the V2PM elements requires excitation of at most two input beams. Hence, the 2-input Michelson setup is sufficient to characterize these devices containing the DBC. The same 2-beam Michelson setup had been used to characterize a 6-input DBC [149]. Thus, the 2-input Michelson setup can characterize the V2PM of an N-input DBC. The goal of the device characterization is as follows: 1) To observe temporal fringes in all the output waveguides of the DBC for all pairwise combinations, and 2) To obtain a low-conditioned V2PM of the device to extract the visibilities.

There are various opto-mechanical and electrical components in the Michelson setup shown in Fig. 6.1. The setup starts with a collimator to give a parallel light beam from a fiber-fed laser source. The collimated light then passes through a polarizer to select the suitable polarization, hitting the 50:50 beam splitter (BS). Between the path of the polarizer and beam splitter, there is an adjustable pinhole (APH) for controlling the diameter of the collimated beam, and there is also a band-pass optical filter inserted only when doing the broadband characterization. The transmitted light from the beam splitter went through a mirror (M2), and reflected light went through M1. The two mirrors (M1 and M2) are placed on a kinematic mirror mount controlled through a computer (COMP). Behind M2, there is a motorized delay line controlled through COMP to give a known phase delay in one of the setup arms to obtain the required temporal delay. There are electronic shutters controlled by COMP in front of M1 and M2, which can block/unblock the beam paths to excite the input WGs of the device. The light from both the mirrors (M1 and M2) is passed via BS through lenses L1 and L2, which reduces the beam diameter by a factor of 2. The reduced beam falls on a NIR Mitutoyo objective (OBJ1),[i] which has a long working distance of 30.5 mm. Thus, the OBJ1 allows a focused spot of $\sim 12\,\mu$m, which couples the light to the single-mode WGs of a photonic chip (DEV).

[i]Model no: M Plan Apo NIR 10x.

The DEV sits on a 5-axis translational stage from Luminos,[ii] which is controlled manually to align the device with the focused spot from OBJ1. A vacuum holder between the chip and the Luminos mount stabilizes the chip from any thermo-mechanical vibrations. The diffracted light from the device's output is collected by another Mitutoyo objective (OBJ2).[iii] Then, the light from OBJ2 is focused onto a computer-controlled InGaAs NIR camera (IR CAM) from Raptor Photonics[iv] to record the output image of the photonic device.

The camera, two shutters, two kinematic mirror mounts, and the delay line are synchronously controlled using an interface written in Python. Thus, the Michelson setup is semi-automated for characterizing the device to obtain the required V2PM.

6.2 Procedure

After placing the photonic chip on the Luminos mount, the laser is switched on, shutter S2 is blocked while S1 is unblocked, and the light from mirror M1 is allowed to fall on the chip. The chip is manually moved in 5-axis through Luminos mount to couple the light in one of the input WGs of a device by observing at the camera. As the light couples into one of the input WGs, the outputs of the DBC are seen in the camera. This gives a rough idea of the device's coordinates in the chip, which otherwise is not visible to one's naked eye. The positions of the Luminos mount are further fine-tuned manually to increase the counts of the camera. After the light is coupled[v] into one of the input WGs of the device, the beam path from M1 is now placed roughly at the center of the device that contains the pupil remappers. Then, a raster scan is started to find the input positions of the device by blocking either of the two mirrors. In the initiation of the raster scan through the python interface, the camera records the device's output. As one of the input WGs is coupled with the incoming light, the output of the device flashes, increasing the intensity momentarily in the camera. As a result, the camera counts (i.e. ADU) increase. When there is no coupled light, ADU decreases. Thus, a 2D map is obtained from the raster scan for each of the input beams giving the coordinates of the input WGs of the device as shown in Fig. 6.2. The coordinates of the input position of the WGs are stored and retrieved later to perform the interferometric characterization of the device. The naming convention of Fig. 6.2 will be used throughout in Section 6.3 and in Section 6.4.

For an N-input device, there will be ${}^{N}C_2$ terms describing the pairwise pairs. For each of

[ii] Model no: P5A-LM-M-M-M-M-H-N-SI

[iii] Model no: M Plan Apo NIR 100x and 20x, which also have a long working distance of 12 and 20 mm, respectively. Either of the two OBJ2 can be used depending on the device to be imaged.

[iv] Model no: Ninox SWIR 640

[v] One sees a maximum in the counts of the camera.

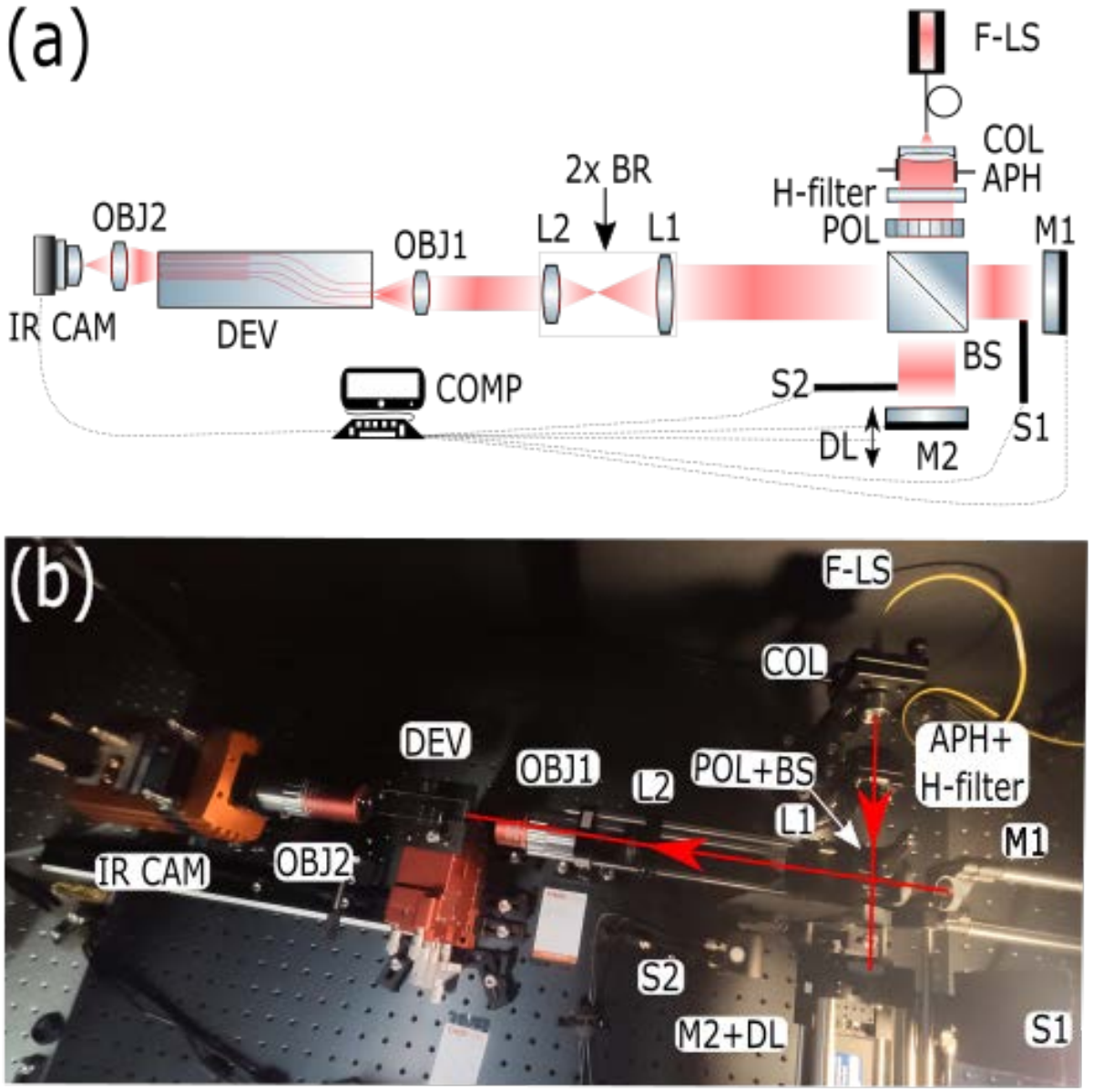

Figure 6.1: (a) A schematic of the 2-beam interferometric Michelson setup *(not to scale)*. The black dotted lines shows various components that are being controlled using the computer. The following acronyms are used, F-LS: fiber-coupled laser source; COL: collimator; APH: adjustable pin hole; H-filter: H-band filter (Two separate filters are used: 1) $\lambda_0 = 1.55\mu$m, $\Delta\lambda = 40$nm, 2) $\lambda_0 = 1.6\mu$m, $\Delta\lambda = 50$nm); POL: polarizer; BS: beam splitter; M: mirror; S: shutter; DL: delay line; L: lens; OBJ: objective; DEV: IO based-astrophotonics device; IR-CAM: infrared camera; COMP: computer. The focal lengths are: $f1 = 100$mm, $f2 = 50$mm. (b) Photograph of the experimental setup as installed in the lab. The red beam shows the light path from the fiber-coupled laser source to the IO device.

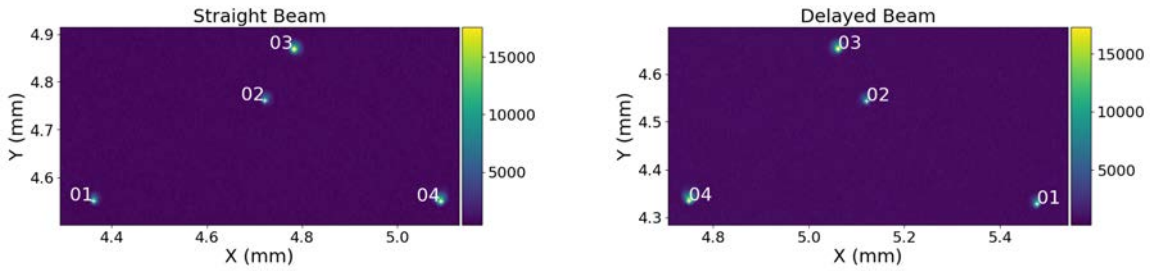

(a) (b)

Figure 6.2: Input maps that are obtained from the Michelson Characterization Setup. (a) Straight beam corresponds to when M1 is open, and M2 is closed. (b) Delayed beam corresponds to when M2 is open, and M1 is closed. It can be seen that the input maps obtained from the mirrors M1 and M2 are flipped horizontally. The color bar shows the ADU value of the 14-bit camera.

the baseline pair, three individual measurements are obtained: 1) By exciting two input beams at a time and delaying the mirror M2 to record the temporal fringes; 2) By exciting one input beam with blocking M1 and unblocking M2 to record photometry from M1; and 3) By exciting one input beam with unblocking M1 and blocking M2 to record the photometry from M2. This process is followed to avoid coupling errors when data is obtained from one baseline to another. Hence, in the present setup, $3^N C_2$ individual measurements are obtained to get a robust V2PM while filling the elements. The photometry from M1, which is unaltered by any coupling errors due to the presence of delay line, goes in the first N columns (i.e. V2PM having $M \times N^2$ elements) for any N-input, M-output DBC device.[vi]

While recording the temporal fringes, the delay line and the camera are controlled synchronously using the python interface. The camera's frame rate is 100 Hz, but while recording the output images of the DBC, the camera was set to record a stack of frames at every $0.25\,s$. When monochromatic light[vii] is used, a travel range of $15\,\mu$m for the delay line is used with 300 samples. But, when polychromatic light[viii] is used, a travel range of $300\,\mu$m for the delay line is used with 5700 samples. The broadband light source is based on spontaneous amplified emission with a constant spectral range from 1528 nm to 1608 nm. Also, while using the broadband light source, two separate band-pass filters are used: 1) center $= 1600\,$nm, FWHM $= 50\,$nm; and 2) center $= 1550\,$nm, FWHM $= 40\,$nm. In the remaining sections of Chapter 6, the results will be shown for all three devices taken each at monochromatic light and polychromatic light.

[vi] Readers can follow Appendix A on filling the elements of a V2PM that is recorded experimentally.
[vii] A tunable laser source from Tunics.
[viii] A broadband light source Amonics.

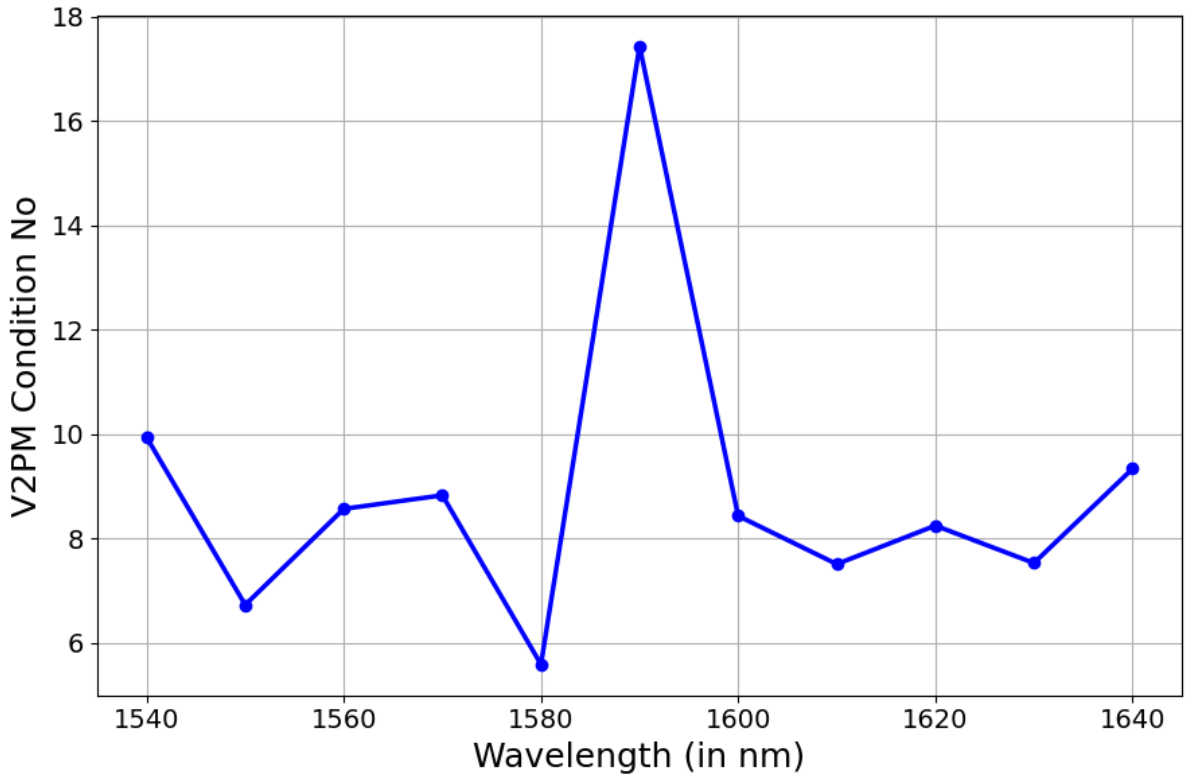

Figure 6.3: Variation of CN vs Wavelength.

6.3 4-input pupil remappers with DBC

6.3.1 Retrieval of monochromatic visibilities

The CN as a function of wavelength is shown in Fig. 6.3. The mean of the CN across the wavelength range = 8.75 and standard deviation = 2.42, which implies a variation of 27 % from the mean CN value. Due to the same orders of magnitude of the CN across the wavelength, it can be concluded that the variation of the CN is almost constant across the astronomical H-band of the device.

The retrieved complex visibility across the wavelength range is shown in Fig. 6.4. There are deviations for γ_{13} and γ_{14} for some of the wavelengths, and it is due to the errors that have happened while performing the experiment. These deviations are due to improper photometric subtraction while filling the V2PM elements, which might have happened due to the systematic errors from the kinematic mirror mounts affecting the flux of coupled light injected into the device.

For the sake of better representation, the retrieved visibility phase is shown in Fig. 6.5 at

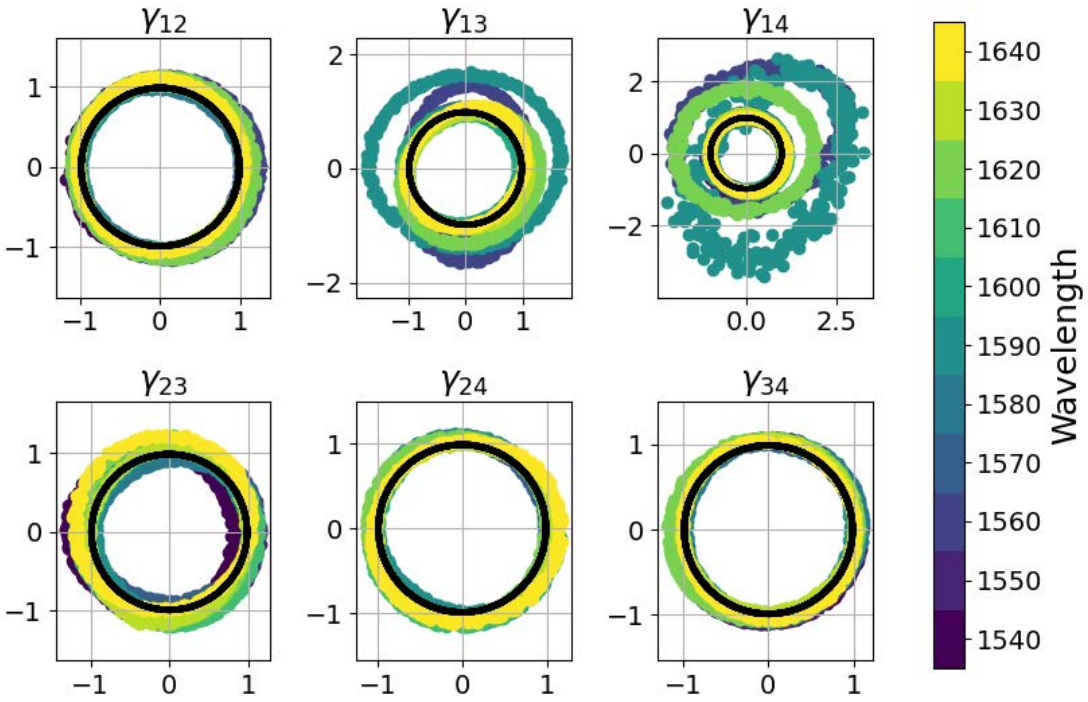

Figure 6.4: Complex visibilities across the Wavelength. Theoretical value is shown in black. x-axis: $\Re\gamma$, y-axis: $\Im\gamma$.

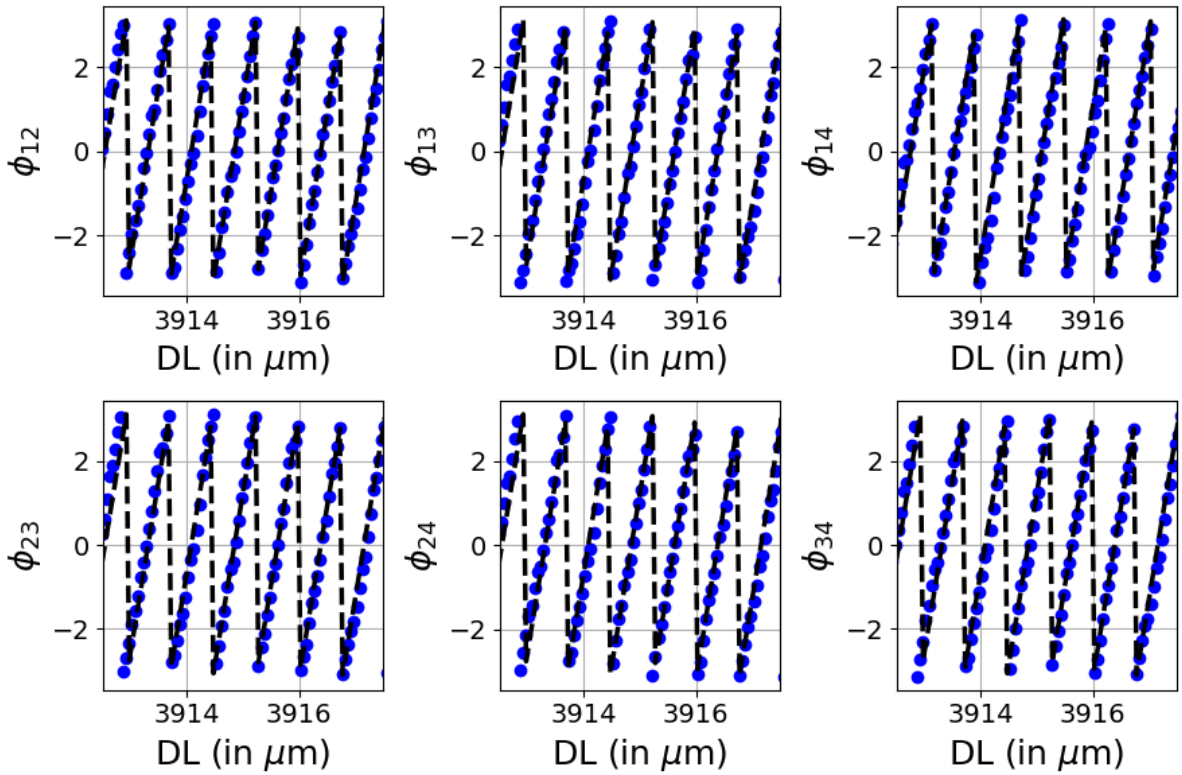

Figure 6.5: Visibility phase for $\lambda_0 = 1.6\mu$m. Theoretical value is shown in black. A zoomed view of $5\,\mu$m is shown. The x-axis values are absolute as recorded by the DL.

$\lambda_0 = 1.6\,\mu$m. The absolute delay line position was in the range (3907.5, 3922.5) μm, which was set in the controller, and a zoomed view of 5 μm is shown in Fig. 6.5. It is to be noted that the DL range is dependent on the user and on the alignment of the experimental setup as shown in Fig. 6.1. In Section 6.3.2, it will be seen that there will be shifts in the central OPD of the central packet of V_{ij} due to long arms of the Michelson setup in Fig. 6.1. Here, a tunable laser source is used that has an extremely narrow linewidth and thus has a long coherence length. Therefore, it is hard to predict precisely the central OPD of the experimental setup.

In order to compare the quality of retrieval with the expected value as given by Eq. (5.1), the MSE is calculated from Eq. (5.2) and shown in Fig. 6.6. Though the range of MSE values for the monochromatic visibilities in Section 5.2 were far much better than the ones shown in Fig. 6.6, one should take several experimental factors into account. One of them is the non-linearity of the delay line positioning. As a mechanical process moves the delay line, the precision of the motor itself might have been too coarse or too fine that might have led to systematic errors in the delay line control. The coupling of the light to the pupil remappers' input due to the delay line's positioning is also not perfect, adding random phase errors. These systematic and random errors from the delay line will manifest in the retrieved visibilities producing huge deviation from the prediction as given by Eq. (5.1) – thus leading to higher MSE. As seen from Chapter 5, the retrieved visibilities are also affected the most as one departs away from zero

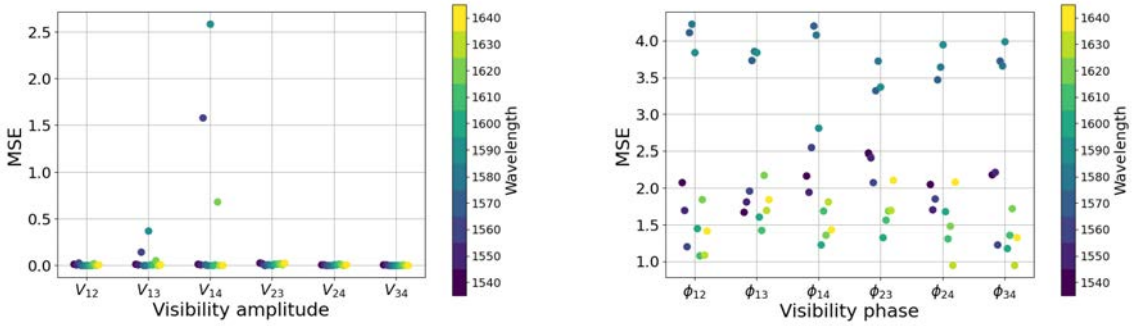

(a) (b)

Figure 6.6: MSE. (a) Visibility amplitude. (b) Visibility phase.

OPD, leading to higher MSE. One should also not forget about the non-ideal detectors used in the setup that might affect the visibilities as seen in Section 5.4.

The above factors are some external phase errors, and as pointed out in Chapter 5, the retrieved visibility phase is more sensitive to these phase errors. That's why the retrieved visibility phase has higher MSE in Fig. 6.6b when compared to MSE of retrieved amplitude in Fig. 6.6a. One should note that such phase errors are inevitable with the present experimental setup. These reasonings will be applied to the rest of the Chapters to discuss higher MSE arising from the experiment.

It was already discussed in Chapter 5 that CP calculated directly from the calibrated P2VM yields an unstable solution with large uncertainties. To prove this fact, the CP was calculated for the best visibility pair V_{34} that had the lowest MSE at $\lambda_0 = 1.6\,\mu$m. The variation of CP is shown in Fig. 6.7. As shown in the theoretical black curve, there is a phase ramp for Φ_{134}, Φ_{234} triplets, which contains the baseline pair 3-4, while the remaining two triplets are 0. However, the CP has a large deviation compared with the theoretical value. It was found that the MSE for the retrieved CP triplets was relatively higher when compared to retrieved visibility phases. Thus, it is verified that the CP calculated directly from the calibrated P2VM have large uncertainties – a result that was consistent from Chapter 5.

6.3.2 Retrieval of polychromatic visibilities

The H-band filter at $\lambda_0 = 1600\,$nm with an FWHM of 50 nm was used to retrieve the polychromatic visibilities of the device. The DL in the Michelson setup was changed such that the white light fringe envelope could be observed in all the 23 output WGs of the DBC. It was found

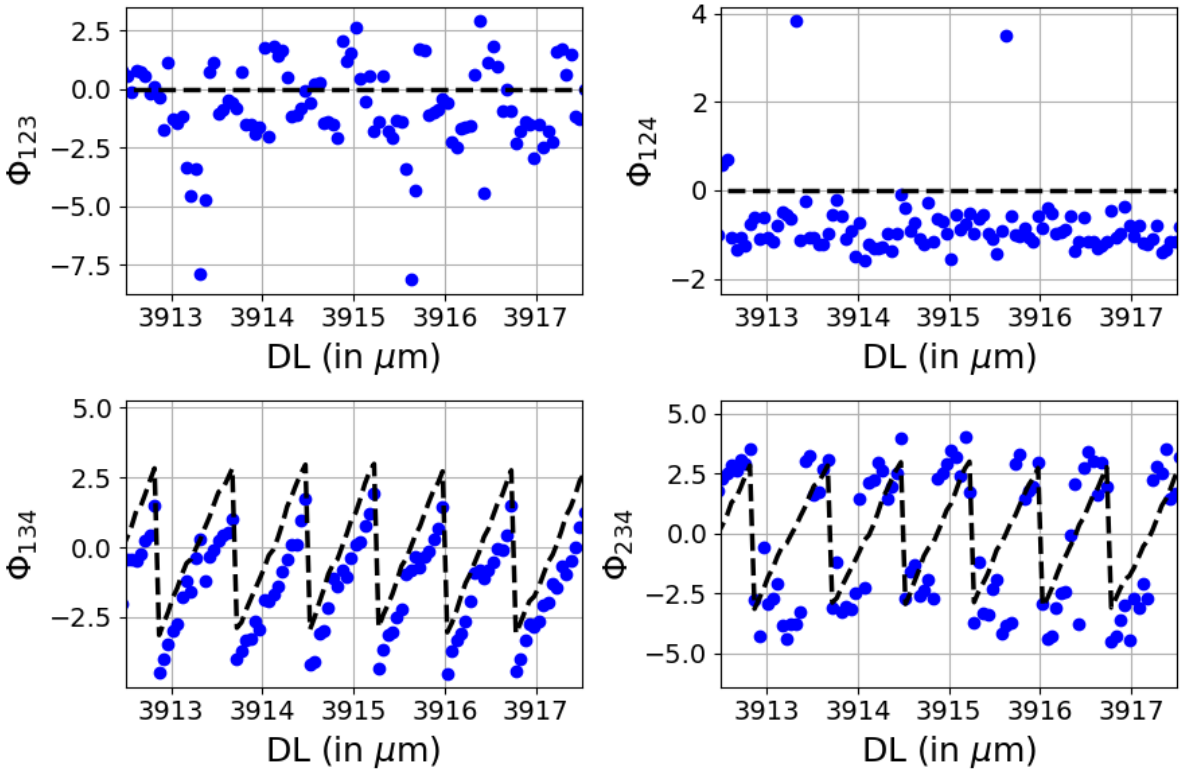

Figure 6.7: Closure phase for $\lambda_0 = 1.6\,\mu$m. Theoretical value is shown in black. A zoomed view of $5\,\mu$m is shown. Here, there is a phase delay in one of the arms of baseline pair 3-4.

out due to the tip-tilt of the mirror mount and long arm of the Michelson,[ix] there were shifts in the central OPD. This has also to do with the input facet of the pupil remapper, which has the largest length of 1.5 mm and shortest length of 0.25 mm. However, due to the symmetry of the input pupil remapper, the shifts in the OPD could be easily found out.

The visibility amplitude obtained from the device is shown in Fig. 6.8 with a CN of 8.2. In the inset, the central OPD is shown along with high frequency oscillations as explained in Chapter 5. From the symmetry of the device as shown in Fig. 6.2, V_{14} and V_{23} are almost at the centre of the optical path in Fig. 6.1. Hence, the central OPD for these pairs are roughly the same with a difference of $\approx 1\mu$m. The pairs V_{12} and V_{13} had an OPD which is less than the central OPD of V_{14} and V_{23}. This means the optical path length between M1 and the OBJ1 is more than the actual path length that was set for the pairs V_{14}, V_{23}. As a result, to compensate for the long path length between M1 and OBJ1, the path length between M2 and BS has also to become longer. Therefore, according to the convention used in Fig. 6.1, the reading of the DL position decreased for V_{12}, V_{13} when compared with V_{14}, V_{23}. A similar conclusion is drawn for visibility pairs – V_{23}, V_{34}, which have an increased reading of the DL position when compared with V_{14}, V_{23}.

The visibility phase is shown in Fig. 6.9 for a zoomed view of 5 μm around the center. A close match between the predicted and retrieved values can be seen in the plots around the central OPD. But, it is not the case when the entire OPL consisting of 5700 samples is considered. The experiment was repeated with another H-band filter at $\lambda_0 = 1550$ nm with an FWHM of 40 nm to retrieve the polychromatic visibilities. The CN was 7.4, which is less when compared to the bandwidth of $\Delta\lambda = 50$ nm. As inferred in Chapter 5, the CN increases with increasing bandwidth that is also seen experimentally. The visibility data for $\Delta\lambda = 40$ nm is not shown here, but a comparison of MSE using both the filters is shown in Fig. 6.10.

Though the MSE reported for polychromatic visibilities in Section 5.3 have the same order of magnitude as the one shown in Fig. 6.10. But, one should not forget about the experimental factors in the form of external phase errors described in Section 6.3.1 that might apply here as well. Mainly, the MSE for the retrieved phase is higher than the retrieved amplitude, which is due to: 1) Systematic errors from the DL, 2) Coupling errors due to the positioning of the DM, 2) Retrieval errors from the quasi-monochromatic P2VM due to the finite bandwidth of light as mentioned in Section 5.3, and 3) Non-ideal detectors. However, the MSE using both the filters are of the same orders of magnitude in visibility amplitude and visibility phase. This implies that the quality of the retrieved visibilities from the DBC device is at least independent to light source that has a moderate bandwidth – a result that is also conferred in Chapter 5.

[ix] The long arm refers to the distance between OBJ1 and either of the mirrors (i.e. M1 or M2).

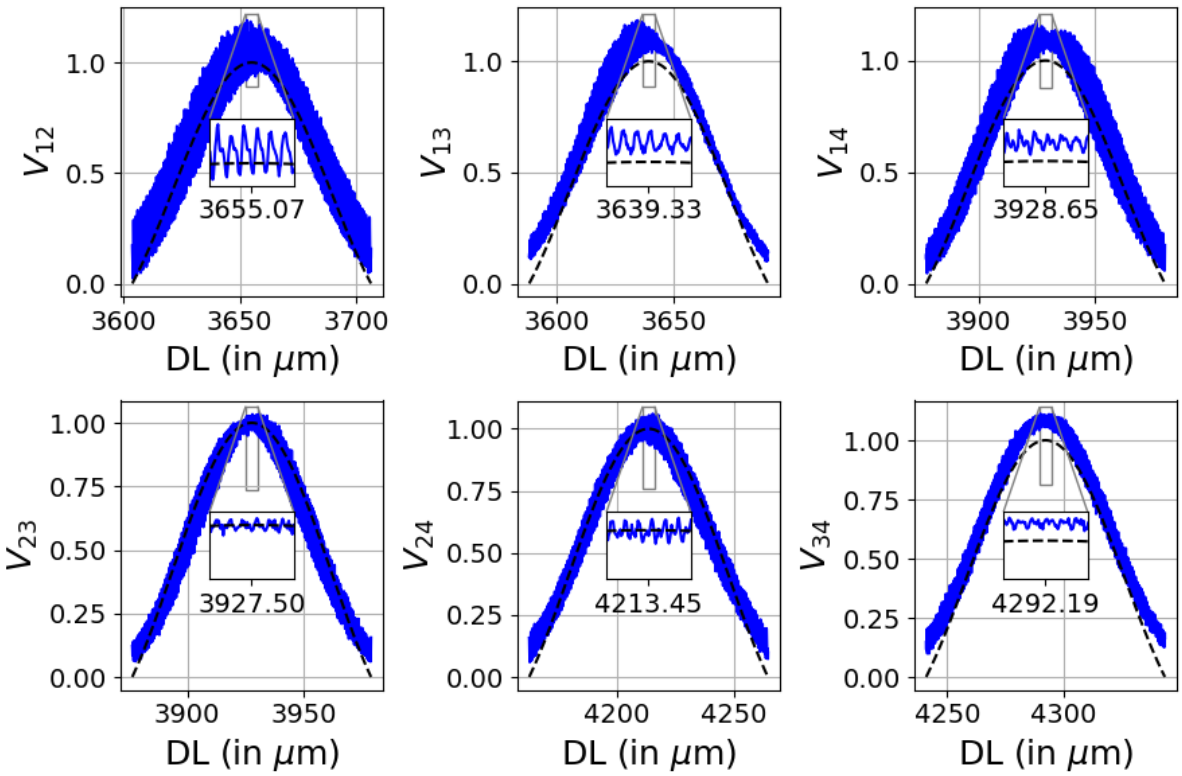

Figure 6.8: Visibility amplitude for $\lambda_0 = 1600\,\text{nm}$ and FWHM of 50 nm. Theoretical value is shown in black. A zoomed view around the center is shown in the inset, which indiciates the central OPD of each of the visibility pair from the experiment. The x-axis values are absolute as recorded by the DL.

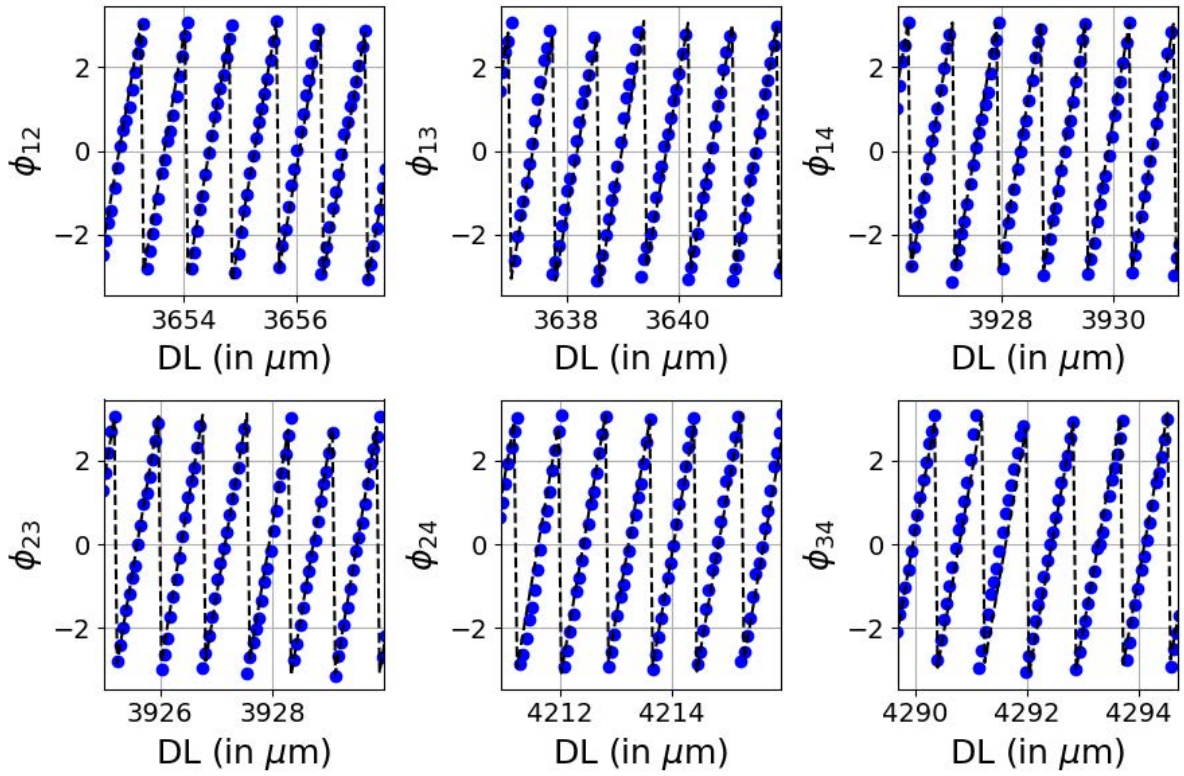

Figure 6.9: Visibility phase for $\lambda_0 = 1600\,\text{nm}$ and FWHM of 50 nm. Theoretical value is shown in black. A zoomed view of $5\,\mu$m is shown. The x-axis values are absolute as recorded by the DL.

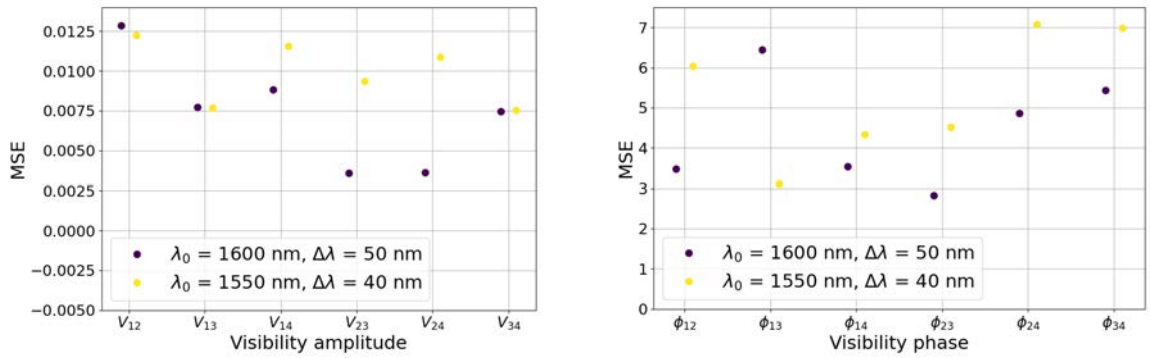

(a) (b)

Figure 6.10: MSE with the legend showing two H-band filters. (a) Visibility amplitude. (b) Visibility phase.

6.4 4-input pupil remappers with DBC and reformatters

The characterization procedure and the analysis of results in Section 6.3 are extended to this section as well. It is to be reminded that the outputs of the DBC device in this section are coherently reformatted in a linear spatial arrangement. This device will be used to record the first stellar photons, which will be discussed in detail in Chapter 7.

6.4.1 Retrieval of monochromatic visibilities

The variation of the CN across the wavelength range is shown in Fig. 6.11. The mean of the CN = 10.62 and the standard deviation = 1.54 across the considered wavelengths, which implies a variation of 15 % from the mean CN value. The order of the magnitude of the CN is roughly the same when compared to the values of Section 6.3, indicating that the reformatters at the output ends of the DBC induce negligible phase differences. This is important for stellar interferometry because any additional detected phase will bias the true phase of the object. The retrieved visibility amplitude from the device is shown in Fig. 6.12. The complex visibility pair γ_{14} performs slightly worse than other visibility pairs, which might have come from the systematic errors of the experiment. For the sake of clarity, the visibility phase at $\lambda_0 = 1600\,\text{nm}$ is shown in Fig. 6.13 for a zoomed view of 5μm. It can be seen that the absolute delay line position in Fig. 6.13 is different when compared to Fig. 6.5. As pointed out in Section 6.3, the reading of the DL is absolute and user-specific. Thus, the change in the DL position is attributed to the use of a different IO chip in Fig. 6.1. It is to be noted that the coupling conditions will change during the replacement of the chip. The overall length of the IO chip is also different when compared to the IO chip of Section 6.3. These factors will result in changing the absolute delay line position. However, it is to be reminded that the travel range of the delay line and the number of frames acquired by the camera are kept fixed.

The quality of the retrieval of the visibilities is measured using MSE, which is shown in Fig. 6.14 both for visibility amplitude and phase. The MSE for visibility phase is higher than MSE for visibility amplitude, which is due to systematic errors from the DL, coupling errors due to the positioning of DL, retrieval errors from the P2VM, and non-ideal detectors – the reasons already mentioned in Section 6.3.1. However, comparing Fig. 6.14 with Fig. 6.6, it can be seen that the MSE for both the devices is roughly the same, at least in the order of magnitude. Thus it concludes that the reformatters at the output ends of the DBC are path length matched experimentally up to a good accuracy, which implies that the devices fabricated using ULI are reliable.

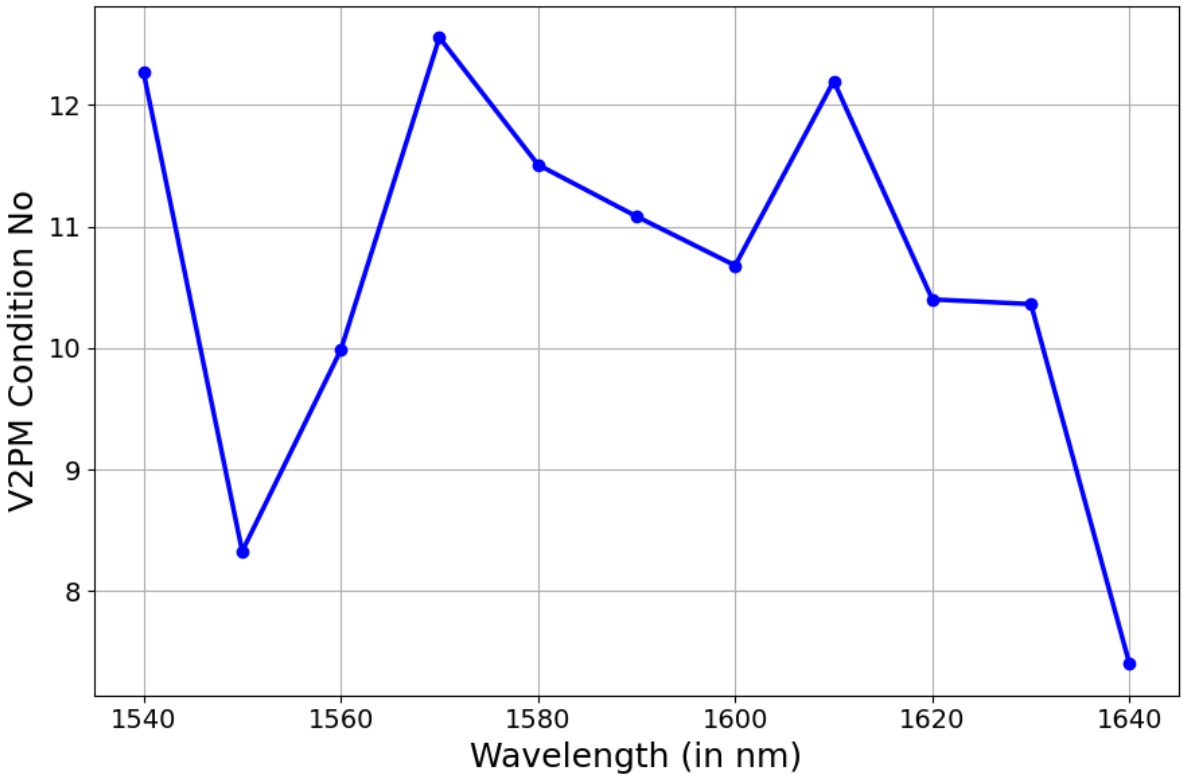

Figure 6.11: Variation of CN across the wavelength.

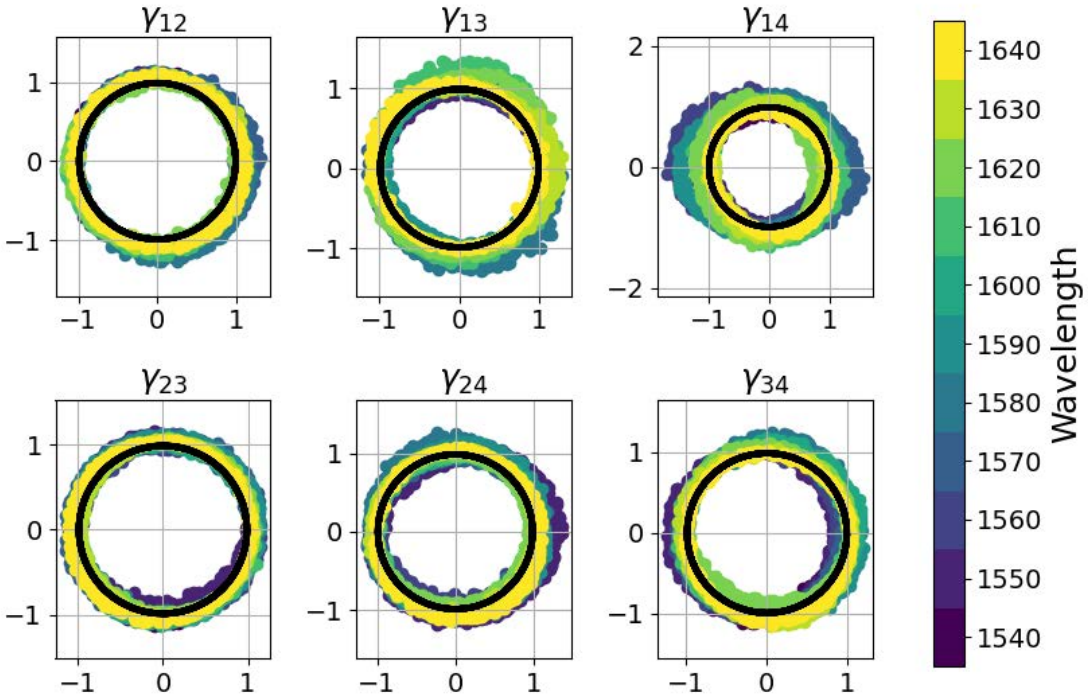

Figure 6.12: Complex visibilities across the wavelength. Theoretical value is shown in black. x-axis: $\Re\gamma$, y-axis: $\Im\gamma$.

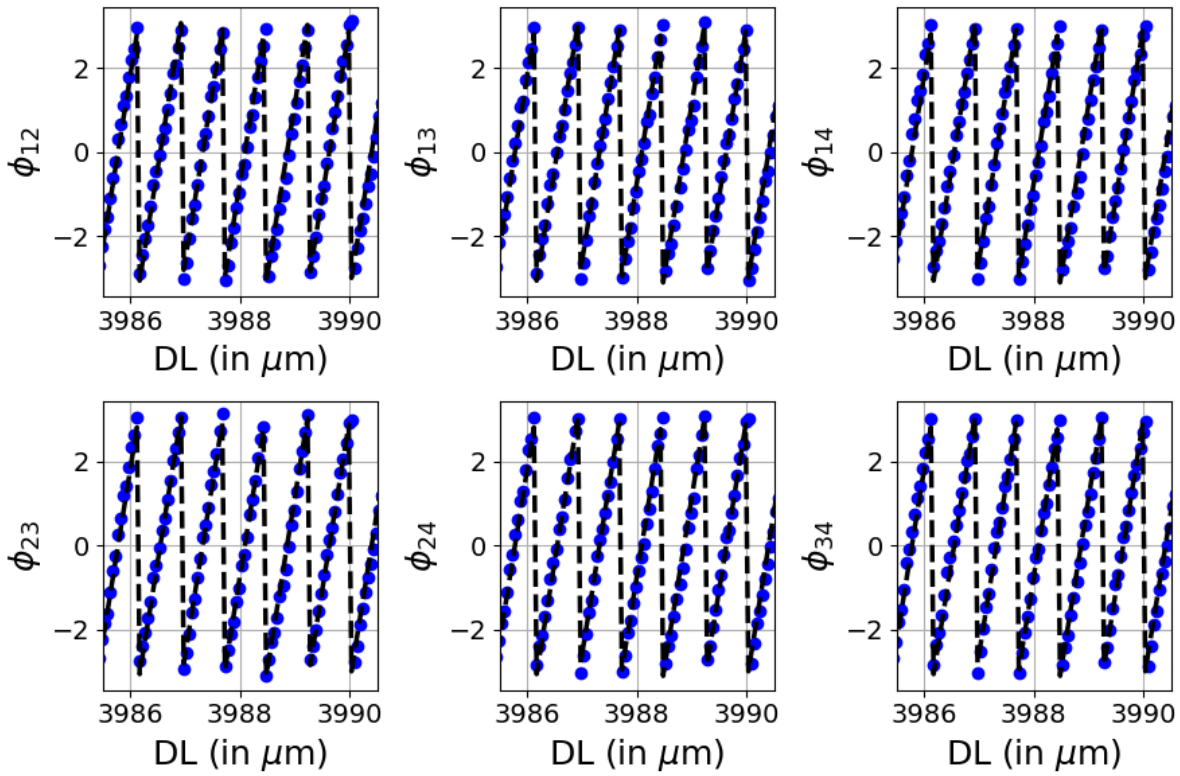

Figure 6.13: Visibility phase for $\lambda_0 = 1.6\,\mu$m. Theoretical value is shown in black. A zoomed view of $5\,\mu$m is shown. The x-axis values are absolute as recorded by the DL.

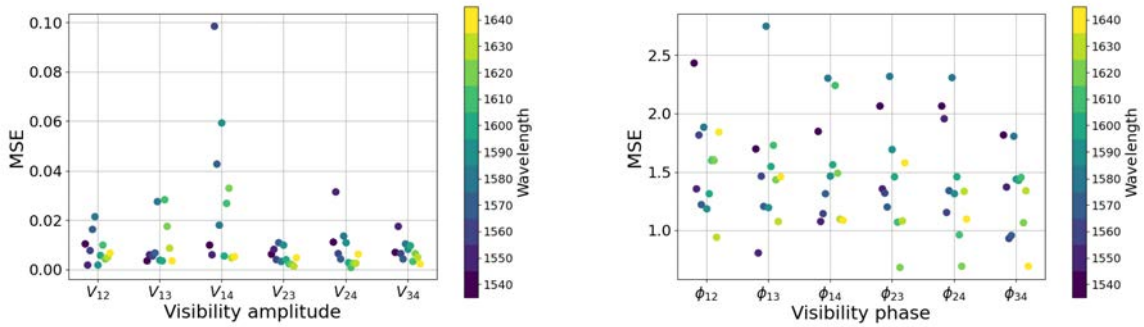

(a) (b)

Figure 6.14: MSE. (a) Visibility amplitude. (b) Visibility phase.

6.4.2 Retreival of polychromatic visibilities

The visibility amplitude obtained using the H-band filter for $\lambda_0 = 1600$ nm, $\Delta\lambda = 50$ nm is shown in Fig. 6.15 that has a CN of 11.4. The center OPD is shown in the inset. As discussed in Section 6.3, the shifts in the central OPD between the baselines are seen in the insets of Fig. 6.15. This is due to the differential tip/tilt of the kinematic mirror mounts that couples light into the device. The long arms of the setup in Fig. 6.1 also play a significant role by inducing optical path delays in the form of central OPD that shifts between the baselines as seen in the inset of Fig. 6.15. From the symmetry of the pupil remappers, the visibility pair V_{14} and V_{23} corresponds to the position of the beam path when the tip/tilt of the kinematic mirror mounts are "balanced".[x]

The central OPD for V_{12}, V_{13} are less when compared to the central OPD of V_{14}, V_{23}. This is due to the "unbalanced" tip/tilt of the kinematic mirror mounts, which effectively increases the OPL between the mirrors and the OBJ1 in Fig. 6.1. Hence according to the convention, the reading of the DL position decreases. Similar conclusion holds for visibility pairs – V_{24} and V_{34}.

The visibility phase is shown in Fig. 6.16. The experiment is repeated for $\lambda_0 = 1550\,$nm, $\Delta\lambda = 40\,$nm, but the visibility data is not shown here. The CN was 8.2, which is less when compared to $\Delta\lambda = 50$ nm. As inferred from Chapter 5, the CN increases with increasing bandwidth. The comparison for MSE using both the filters is shown in Fig. 6.17. It can be seen that the quality of the retrieval is roughly the same in order of magnitude for both the filters, be it visibility amplitude or phase. This implies that the quality of the retrieved visibilities is almost equal when operating at moderated bandwith – a result that is already inferred from Section 6.3 and Chapter 5. Comparing Fig. 6.10 and Fig. 6.17, it can be seen that the MSE are roughly the same for both the devices, whether the outputs of the DBC are reformatted or not. This concludes that the reformatters induce negligible phase errors and indicate the good reliability of the devices fabricated using ULI.

6.5 8-input pupil remappers with 2×4-input DBC

The Michelson setup of Fig. 6.1 is also used to characterize the transfer matrix and extract the visibilities for the 8-input pupil remappers with the design shown in Fig. 3.8. The 8-input pupil remapper chip was placed and aligned in the setup to find the input WGs from the raster scan. Fig. 6.18 shows the input map of the pupil remapper from the raster scan, where all the

[x] It refers to the optical path delay from the mirrors to the objective. Thus, "balanced" implies when the optical path delay from M1 to OBJ1 equals that from M2 to OBJ1 (see Fig. 6.1).

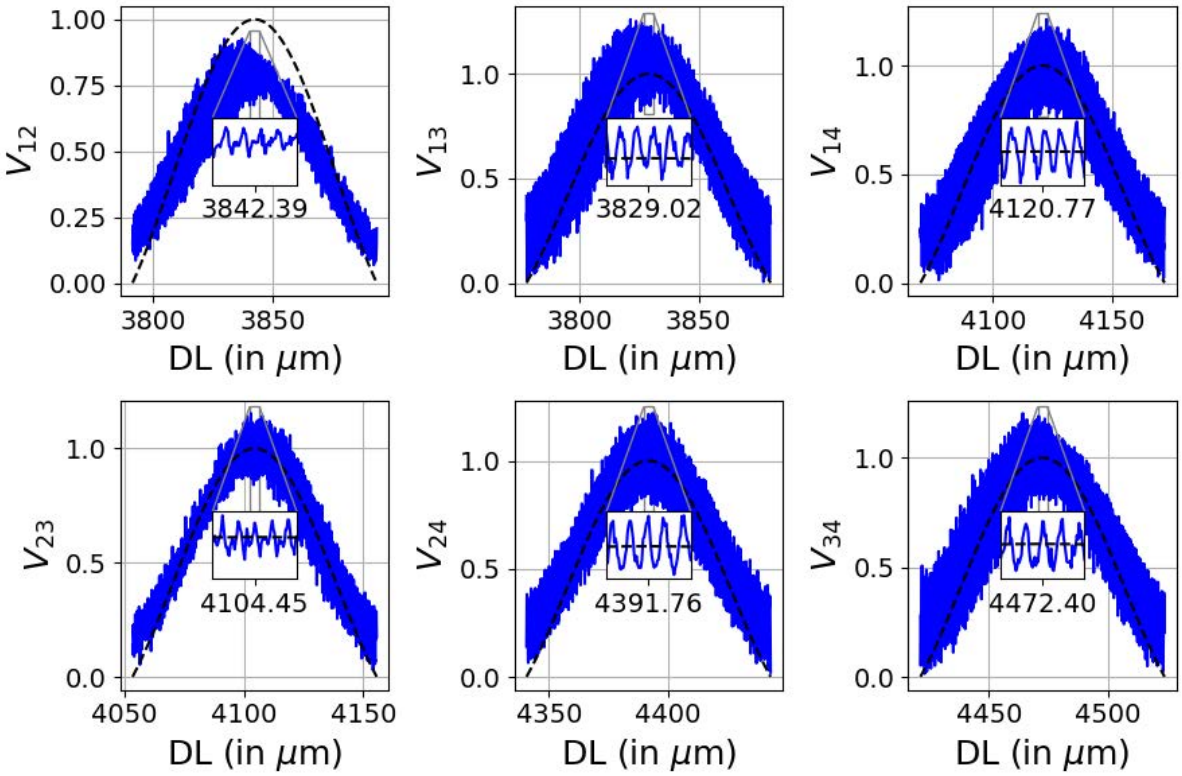

Figure 6.15: Visibility amplitude for $\lambda_0 = 1600\,\text{nm}$ and FWHM of 50 nm. Theoretical value is shown in black. A zoomed view around the center is shown in the inset. The x-axis values are absolute as recorded by the DL.

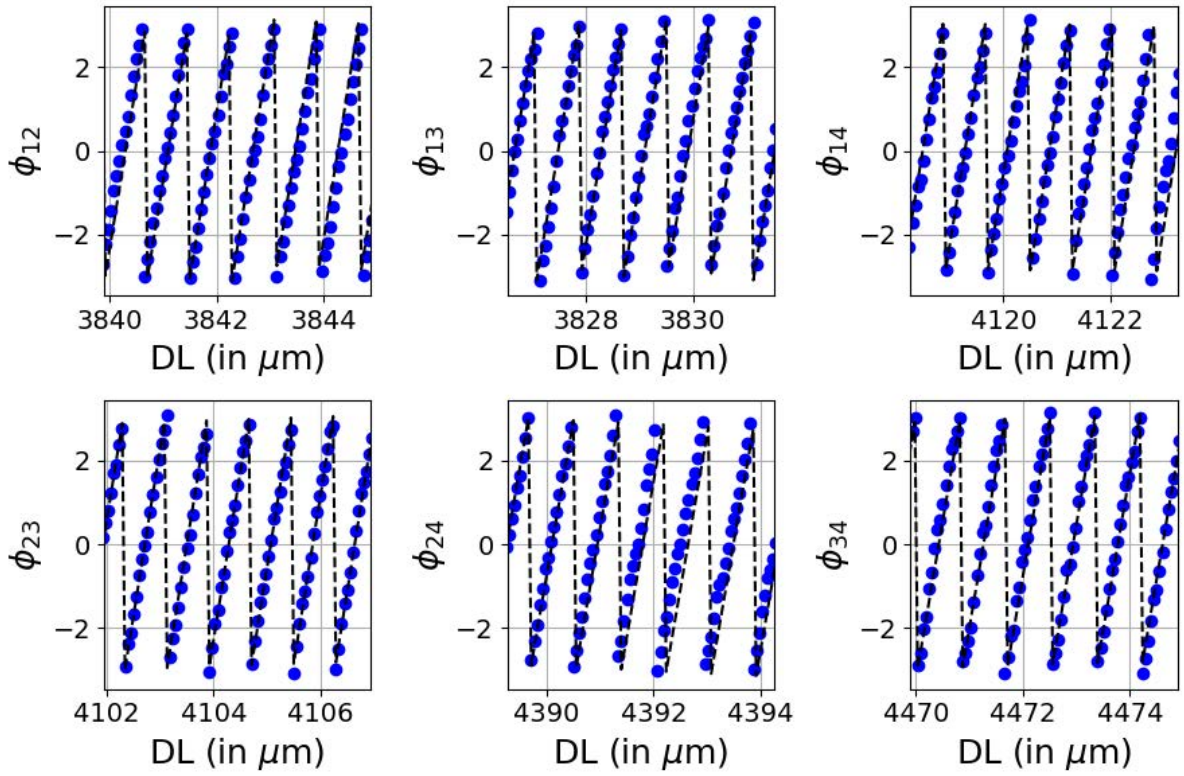

Figure 6.16: Visibility phase for $\lambda_0 = 1600\,\text{nm}$ and FWHM of $50\,\text{nm}$. Theoretical value is shown in black. A zoomed view of $5\,\mu\text{m}$ is shown. The x-axis values are absolute as recorded by the DL.

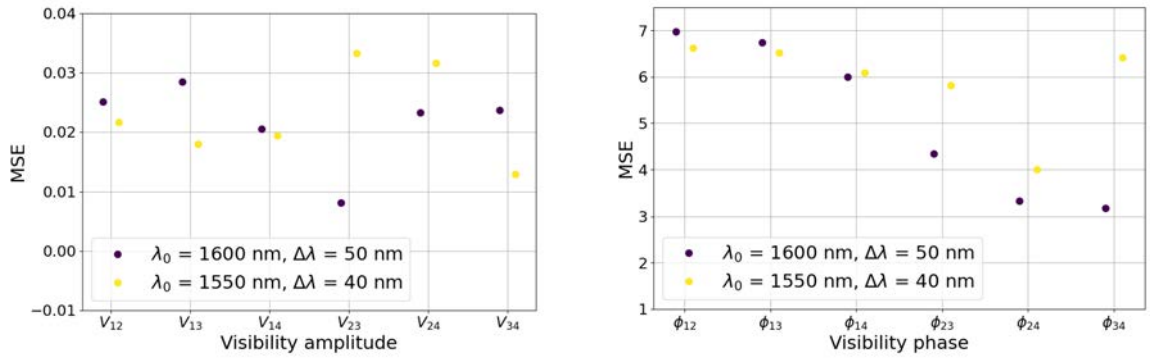

(a) (b)

Figure 6.17: MSE with the legend showing two H-band filters. (a) Visibility amplitude. (b) Visibility phase.

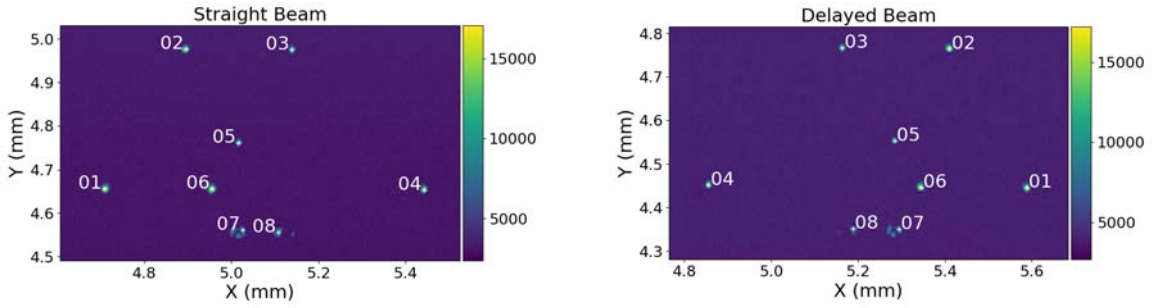

(a) (b)

Figure 6.18: Input maps that are obtained from the Michelson Characterization Setup. (a) Straight beam corresponds to when M1 is open, and M2 is closed. (b) Delayed beam corresponds to when M2 is open, and M1 is closed. The color bar shows the ADU value of the 14-bit camera.

8-inputs spots are visible and numbered. It can be seen that the inputs numbered 7 and 8 have a non-circular spot. The first thought was that it could be due to dust particles present in the input facet of the IO chip. So, the chip was cleaned with IPA, and the alignment of the chip was also repeated many times. But, to the surprise – the inputs numbered 7 and 8 always had a non-circular spot confirming that these were due to the fabrication errors from the ULI. Since these two waveguides are located at the extreme bottom of the chip,[xi] the laser spot of the ULI could have been defocussed, resulting in the non-circular spot of the input WGs.

The 8-coordinates of the pupil remappers are extracted, stored, and later used to carry out the calibration of the V2PM. The naming convention shown in Fig. 6.18 will be used in the remaining sections of this Chapter. The results of the monochromatic and polychromatic visibilities are discussed in the subsequent sections using the same analysis as that of Section 6.3 and Section 6.4.

6.5.1 Retrieval of monochromatic visibilities

The retrieved visibility amplitude for both the DBCs at $\lambda_0 = 1600\,\text{nm}$ are shown in Fig. 6.19 and Fig. 6.20. The theoretical black curve matches well with the retrieved values. The CN of the V2PM for both the DBCs were 10.8 and 11.2, which are comparable to the CN obtained both in Section 6.3 and Section 6.4. The retrieved visibility phase for both the DBCs for a 5 μm path length at $\lambda_0 = 1600$ nm are shown in Fig. 6.21 and Fig. 6.22. The MSE for the visibility amplitude for all 12 combinations is in the range $(1.1, 6.6) \times 10^{-3}$. Similarly, the MSE for the

[xi] Located $\approx 1.06\,\text{mm}$ measured from the top surface of the chip

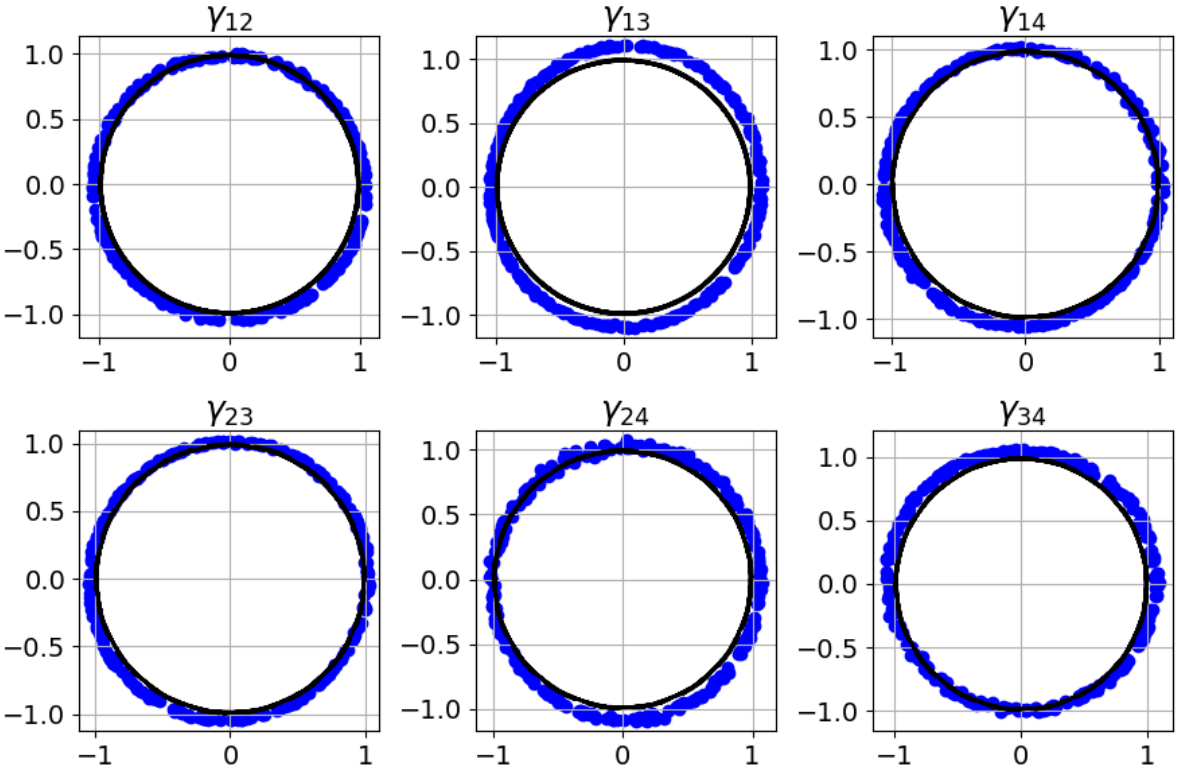

Figure 6.19: Complex visibilities for $\lambda_0 = 1600\,\text{nm}$. Theoretical value is shown in black. x-axis: $\Re\gamma$, y-axis: $\Im\gamma$.

visibility phase for all the 12 combinations is in the range $(0.8, 1.4)$. The MSE for the visibility phase is higher than the visibility amplitude, which is due to systematic errors of the delay line, coupling errors due to the positioning of the delay line, retrieval errors from the P2VM, and non-ideal detectors in the experiment – the reasons already outlined in Section 6.3.1. However, the MSE, either for visibility amplitude or phase for all the 12 combinations, have the same order of magnitude.

Following Fig. 6.18 that indicated the imperfection of the bottom two input waveguides of the device, it was expected that the two DBCs that are fabricated at different heights in the substrate might be different. There could be laser-induced stress and different focussing conditions of the laser spot at different heights resulting in the two DBCs having slightly different geometrical and optical properties. But, as the calculated MSE across the 12 visibility pairs has the same order of magnitude, it indicates that the two DBCs at different heights have almost identical optical properties. Thus, it implies the fabrication advantage of the ULI in writing such 3-D devices, where identical photonic devices can be written at different depths. One can also conclude that though the pupil remappers numbered 7 and 8 in Fig. 6.18 are visually different, but the amplitude and phase errors induced by them are negligible during the experiment, thus leading to similar MSE values across the 12 visibility pairs.

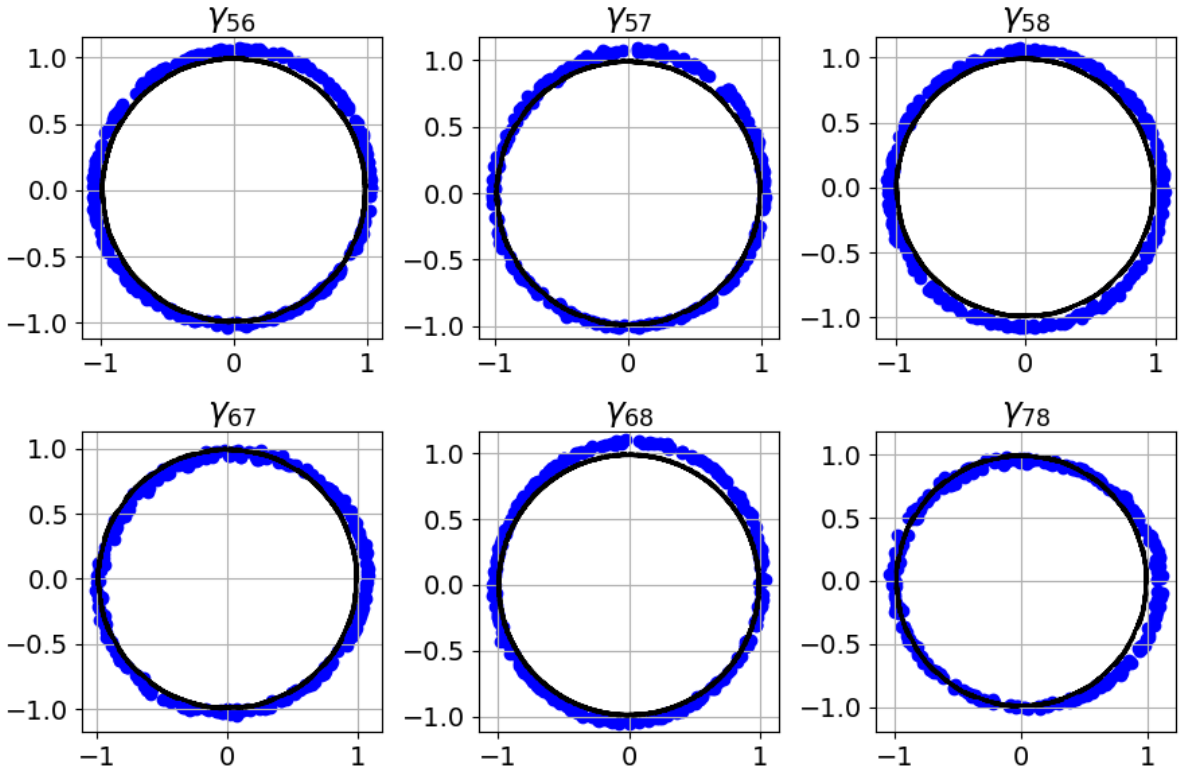

Figure 6.20: Complex visibilities for $\lambda_0 = 1600\,\text{nm}$. Theoretical value is shown in black. x-axis: $\Re\gamma$, y-axis: $\Im\gamma$.

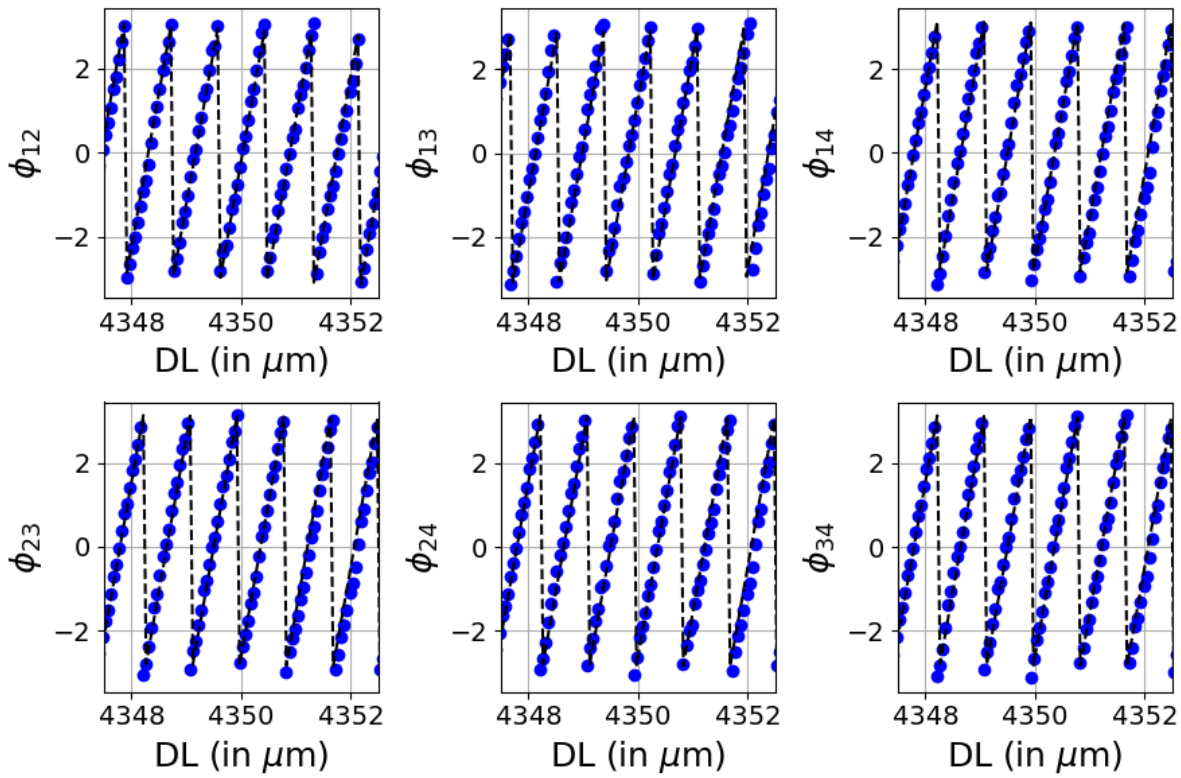

Figure 6.21: Visibility phase for $\lambda_0 = 1.6\,\mu$m. Theoretical value is shown in black. A zoomed view of $5\,\mu$m is shown. The x-axis values are absolute as recorded by the DL.

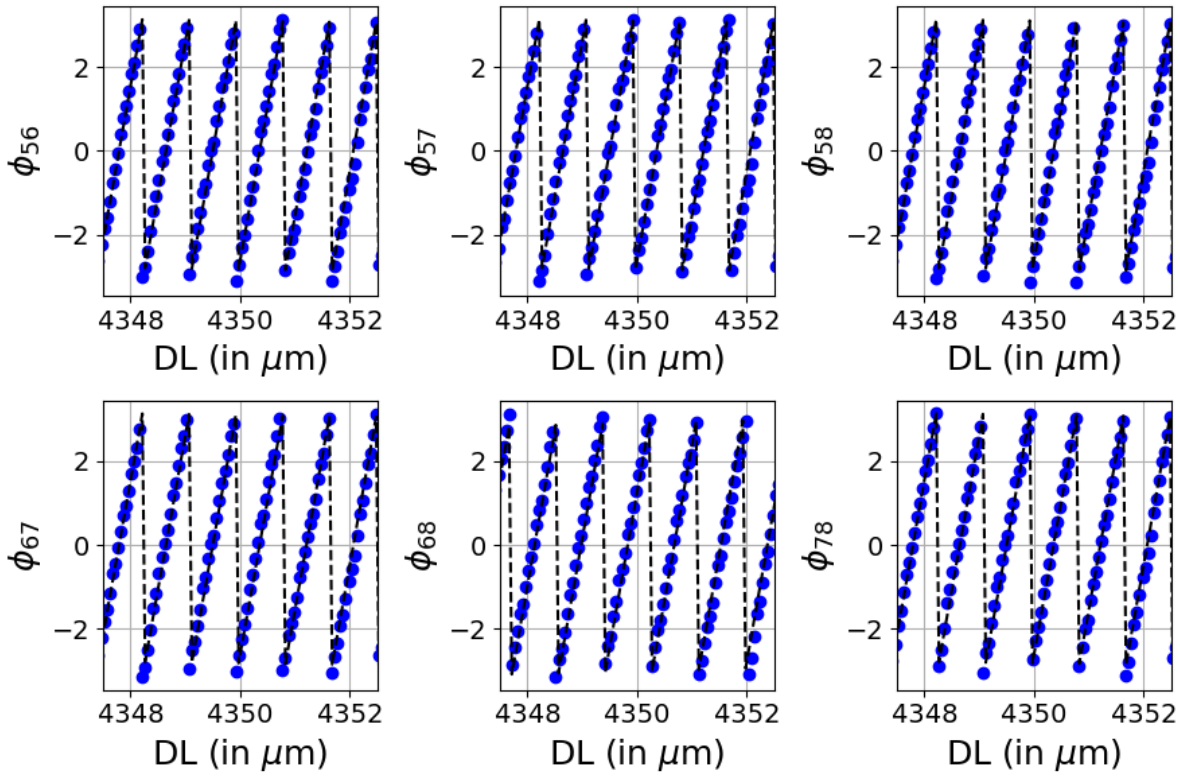

Figure 6.22: Visibility phase for $\lambda_0 = 1.6\,\mu$m. Theoretical value is shown in black. A zoomed view of $5\,\mu$m is shown. The x-axis values are absolute as recorded by the DL.

6.5.2 Retrieval of polychromatic visibilities

The visibility amplitude using a filter with $\lambda_0 = 1600$ nm and FWHM = 50 nm for all the combinations is shown in Fig. 6.23 and Fig. 6.24. The oscillations in the visibility amplitude around the retrieved curve can be seen in the inset, indicating the limited bandwidth operation of the DBC. In the retrieved visibilities of both the DBCs, OPD shifts between the pairwise baselines are due to the long arms of the Michelson setup and the tip/tilt offered by the kinematic mirror mounts. However, due to low separation ($\approx 250\,\mu$m) for the pupil remapper pairs at location 5,6,7 and 8; the shifts in the central OPD for all the visibility pairs in Fig. 6.24 are less[xii] when compared to Fig. 6.23. This is due to the "balanced" condition of the tip/tilt by the kinematic mirror mount while coupling light in locations 5,6,7, and 8 – the reason already stated Section 6.4.2.

The visibility phase for a $5\,\mu$m path length around the central OPD is shown in Fig. 6.25 and Fig. 6.26. A close resemblance between the retrieved visibility phase and the theoretical curve is seen around the central OPD. The experiment was repeated with a filter at $\lambda_0 = 1550$ nm, FWHM $= 40$ nm, but the visibilities plots are not shown here. However, the MSE both for visibility amplitude and phase are shown in Fig. 6.27, and the values from both the filters are compared. The MSE for phase is higher than amplitude due to the reasons already mentioned in Section 6.4 and Section 6.3. The MSE for either the visibility amplitude or the visibility phase is of the same order of magnitudes for all the combination pairs, which indicates that the two DBCs at different heights have almost identical optical properties. The MSE is of the same order of magnitude for both the band-pass filters, indicating that the quality of the retrieved visibilities is similar from both the DBCs when operated at moderate bandwidth – a result already inferred for the other two devices.

Finally, by comparing Fig. 6.27 and Fig. 6.10, it can be seen that the retrieved visibilities have MSE of the same order of magnitude, indicating that the retrieved visibilities have similar error propagation. This concludes that although the DBCs are manufactured in different glass substrates, they have excellent repeatability in terms of their geometrical and optical properties, indicating that the process parameters used in the ULI are reliable.

6.6 Polarization effects

It is well known that the difference in the polarization states of the light, when interfered with, can reduce the fringe visibility. The polarization state is generally defined as whether the light

[xii] A relative difference of $\approx 25\,\mu$m.

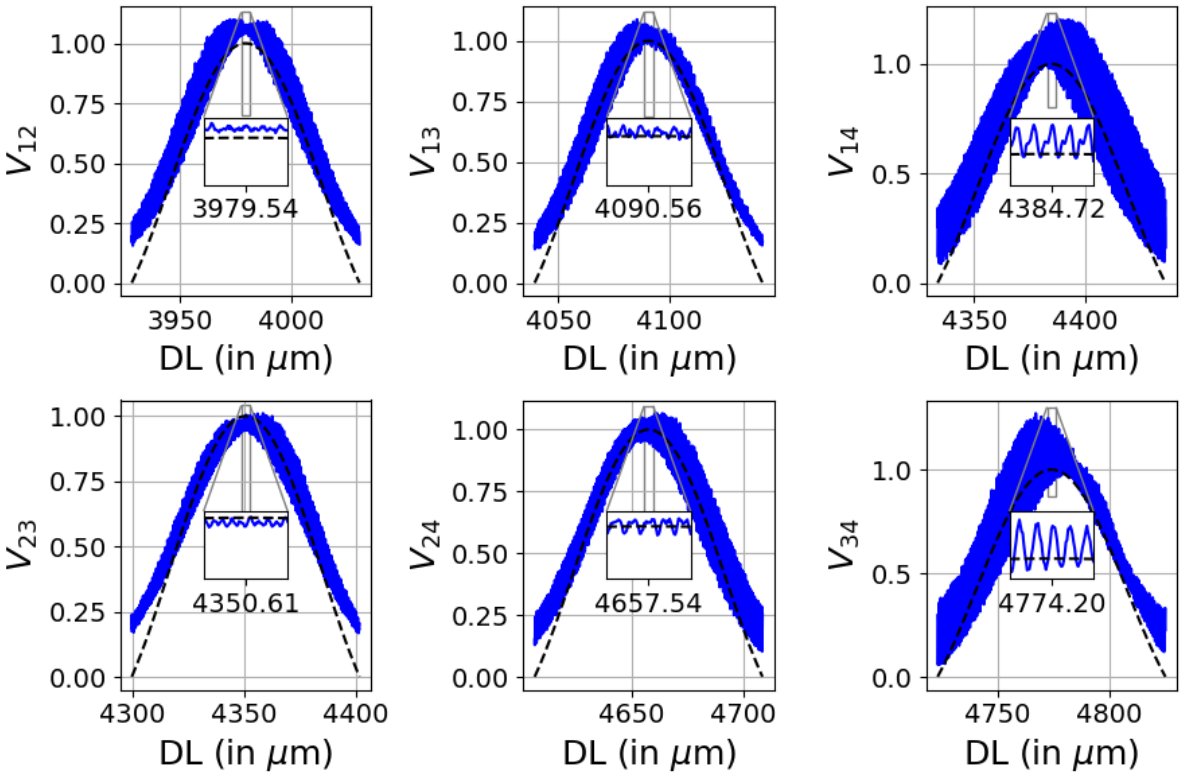

Figure 6.23: Visibility amplitude for $\lambda_0 = 1600\,\text{nm}$ and FWHM of 50 nm. Theoretical value is shown in black. A zoomed view around the center is shown in the inset. The x-axis values are absolute as recorded by the DL.

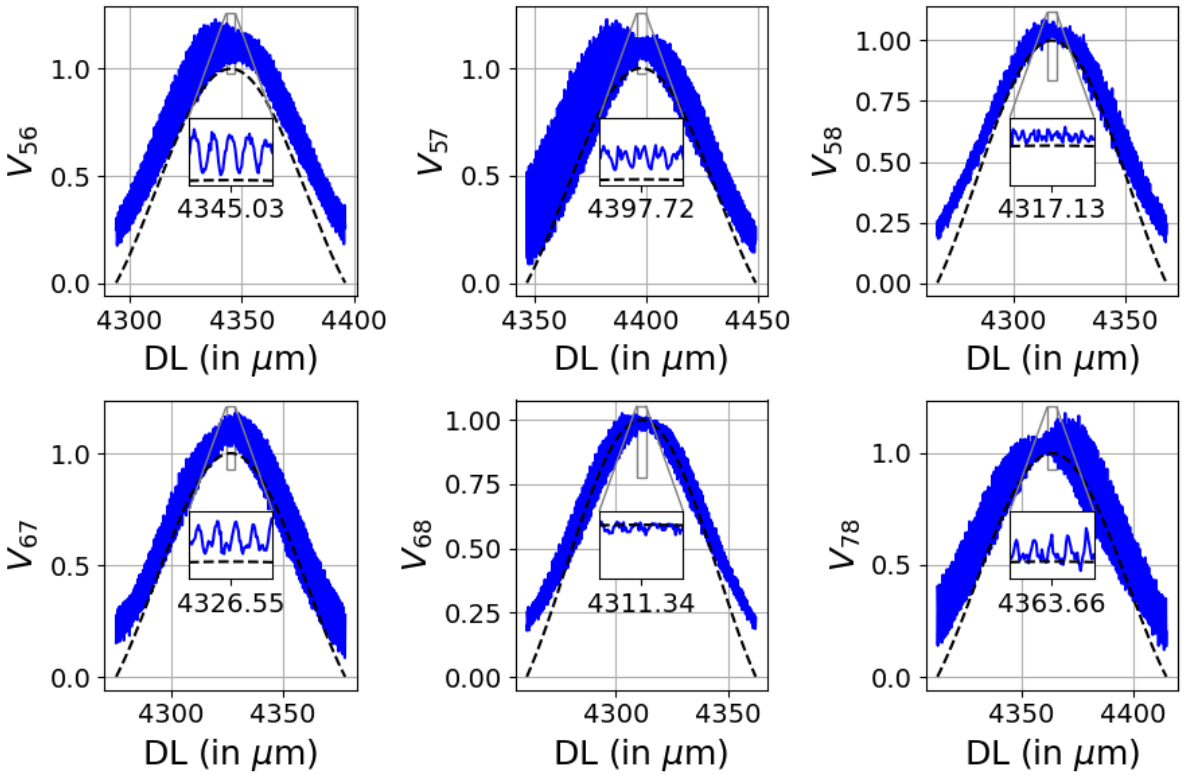

Figure 6.24: Visibility amplitude for $\lambda_0 = 1600$ nm and FWHM of 50 nm. Theoretical value is shown in black. A zoomed view around the center is shown in the inset. The x-axis values are absolute as recorded by the DL.

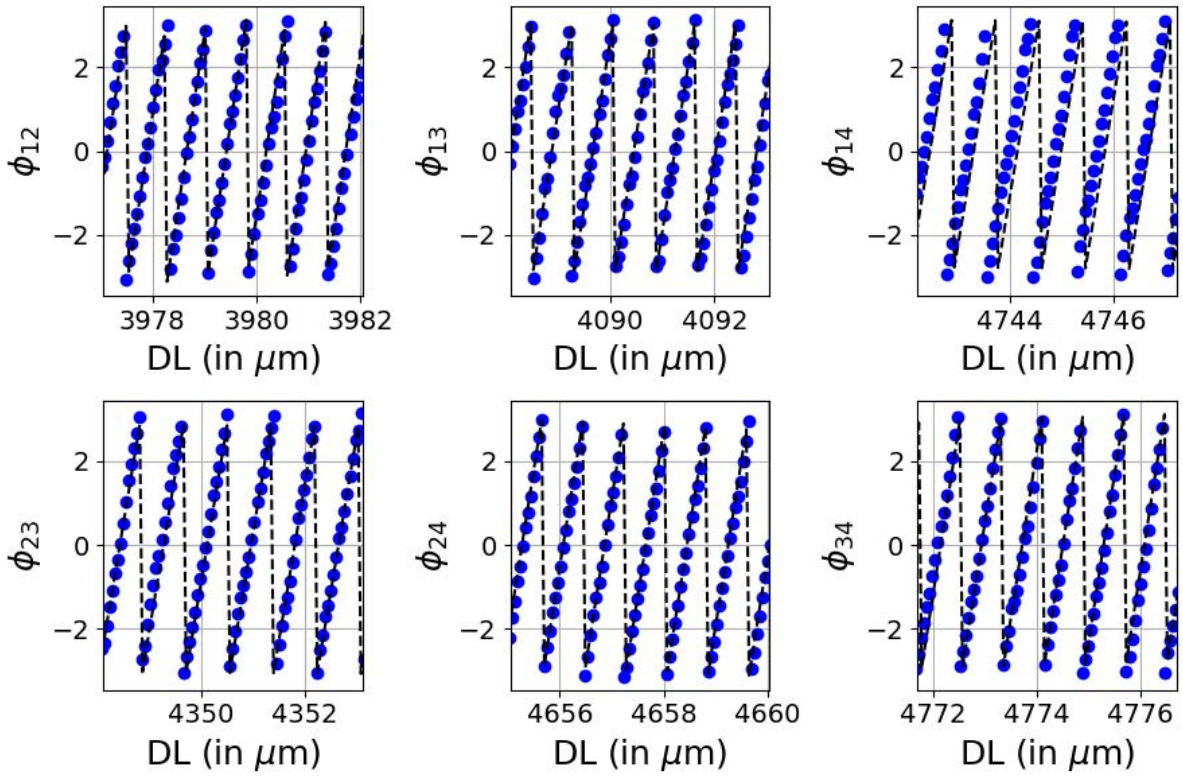

Figure 6.25: Visibility phase for $\lambda_0 = 1600\,\text{nm}$ and FWHM of 50 nm. Theoretical value is shown in black. A zoomed view of $5\,\mu$m is shown. The x-axis values are absolute as recorded by the DL.

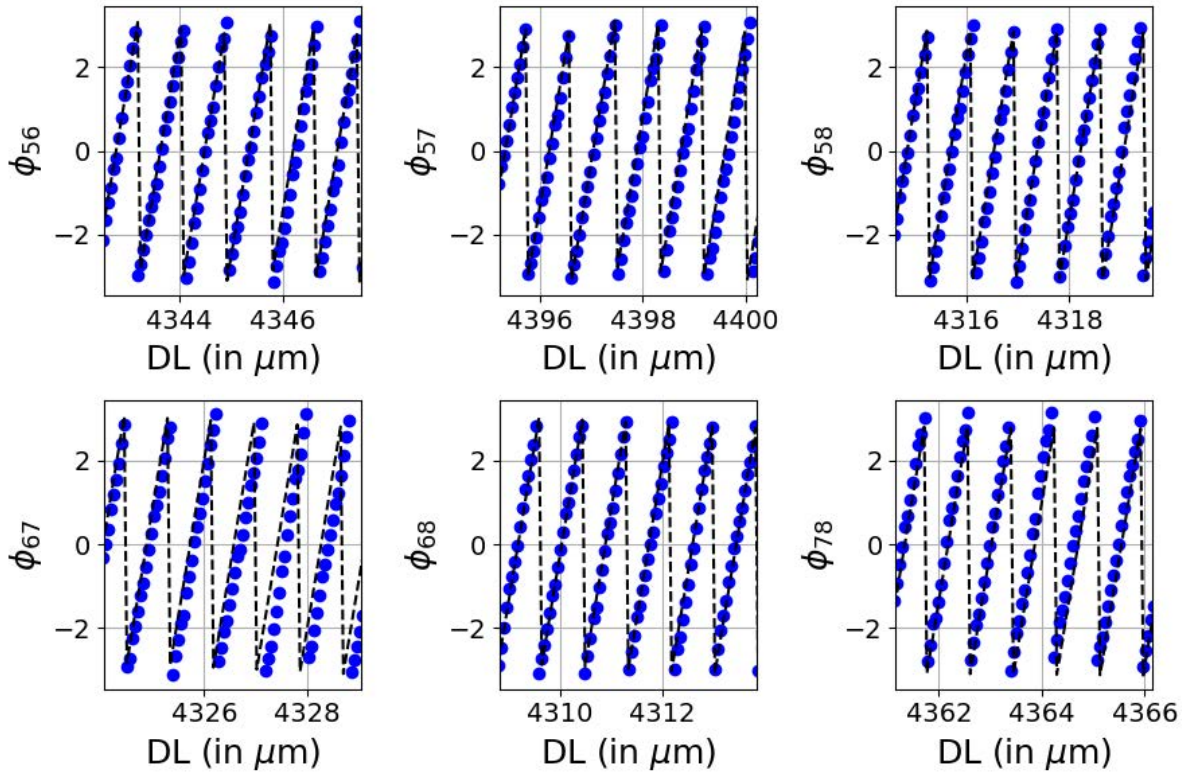

Figure 6.26: Visibility phase for $\lambda_0 = 1600\,\text{nm}$ and FWHM of $50\,\text{nm}$. Theoretical value is shown in black. A zoomed view of $5\,\mu\text{m}$ is shown. The x-axis values are absolute as recorded by the DL.

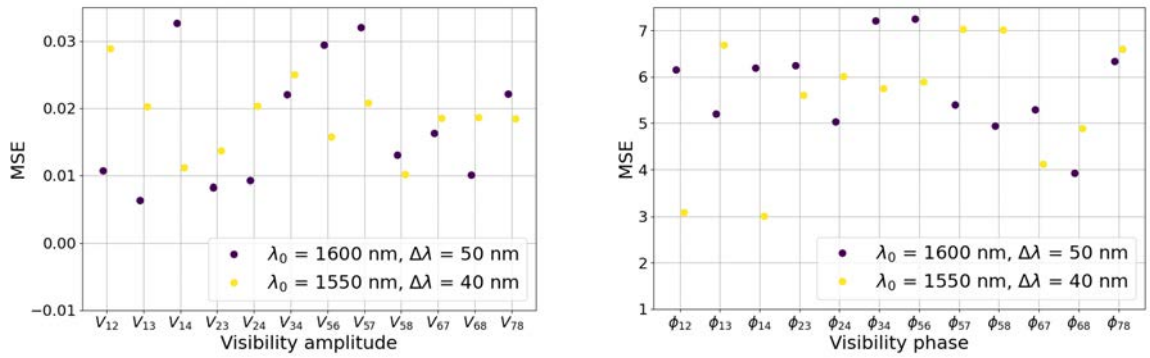

(a) (b)

Figure 6.27: MSE with the legends showing the two H-band filters. (a) Visibility amplitude. (b) Visibility phase.

is s-polarized or p-polarized. The electric field component perpendicular to the plane of incidence is called p-polarized light. The electric field component parallel to the plane of incidence is called s-polarized light. Thus, any other polarization state of light is written as a linear superposition of the basis vectors – given by s- and p- states. If ϕ_{sp} is the phase shift between the interfering s- and p-polarized light, then the interferogram will have the visibility term, V_{pol} given by [4, Chapter 3]:

$$V_{pol} = \left|\cos(\frac{\phi_{sp}}{2})\right|. \tag{6.1}$$

If V_{exp} is the expected visibility, then due to the difference in the interfering polarization states of the light (i.e. V_{pol}), one can expect a reduction in the visibility. Thus, the total visibility, V_{tot} is expressed as:

$$V_{tot} = V_{pol} \cdot V_{exp}. \tag{6.2}$$

In stellar interferometers, if polarization effects are not taken into account, then V_{pol} can drastically reduce the overall interferometric efficiency of the instrument, which also amplifies the photon noise amongst other noise sources. Thus, some of the ways that can mitigate the differential phase shifts between the two polarization states of light to enhance the V_{tot} will be discussed. One way is to use polarization-maintaining fibers, which maintain the polarization state of the input light along the optical train, thus maximizing the V_{pol} [150]. If non-polarization-maintaining fibers are used, then a dynamic control of the polarization using Lefevre loops [151] can be used, where fibers in each recombination arm are bent in loops to minimize the ϕ_{sp}. This was implemented in the FLUOR instrument at the IOTA facility to reduce the polarization mismatch between the two recombination fibers up to 20 % [65]. Furthermore, the mirrors used in the IOTA were designed using the direction cosine rule [152]. This rule implies that any reflection in one arm of the interferometer is duplicated in the other arm, in the same time order, from the point of view of the incident light. Thus, any polarization differences between the light paths are eliminated, giving true visibility. The PIONIER instrument at the VLTI facility implements a thin plate of birefringent material ($LiNbO_3$) in the beam paths such that the incident angle of the beam paths is adjusted to cancel the instrumental differential birefringence (i.e. $V_{pol} \approx 1$), thus reaching instrumental visibility of 98.5 % [153].

ULI written waveguides can tune the birefringence of the waveguides in the range $10^{-6} - 10^{-4}$, thus producing polarization sensitive and insensitive devices [154, 155]. As already mentioned in Chapter 4, the fabricated devices in this work are insensitive to the state of the polarization of the light. Thus in this section, the interferometric results will be shown to prove the

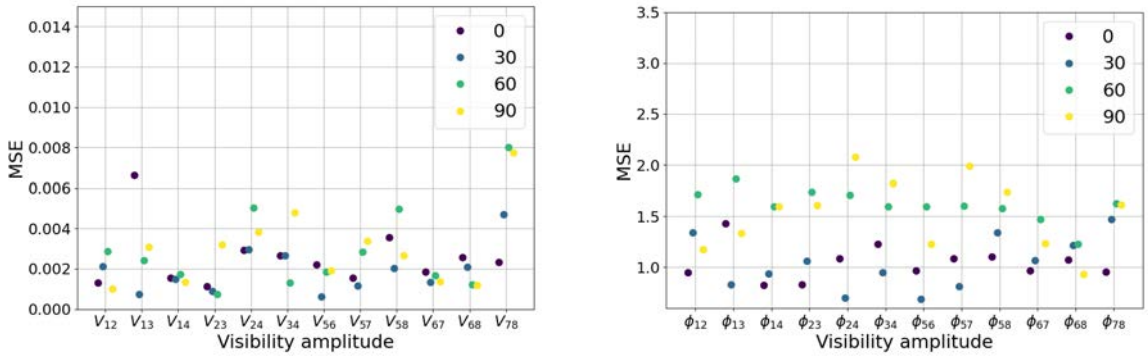

(a) (b)

Figure 6.28: MSE for the 8-input pupil remappers with 2x4-input DBC device characterized at $\lambda_0 = 1600\,\text{nm}$. The legend shows the orientation angle of the input linear polarizer used in Fig. 6.1. Here 0° corresponds to the transmission axis of the polarizer which is orthogonal to the plane of optical table. (a) Visibility amplitude. (b) Visibility phase.

polarization insensitive behavior of the devices. For this purpose, the 8-input pupil remappers (i.e. Fig. 3.8 – the device that used in Section 6.5) was selected and characterized with the monochromatic laser source at $\lambda_0 = 1600\,\text{nm}$. The setup shown in Fig. 6.1 is used, where now the linear polarizer (i.e. shown by POL) is rotated at different angles to change the orientation of the input polarized light coming out of the polarizer. To ensure a quadrature, the polarizer was rotated at four different angles of 0°, 30°, 60°, and 90°. Here 0° is the transmission axis of the polarizer, which is perpendicular to the plane of the optical table. The interferometric data is recorded, reduced, and the visibilities are extracted with each rotation angle. For the sake of simplicity and comparison, the MSE calculated both for amplitude and phase are shown in Fig. 6.28a and Fig. 6.28b, respectively.

One would expect that the rotation of the polarizer would lead to a difference in the amount of s- and p-states in the incident light. But, the MSE for all the visibility pairs have roughly a same order of magnitude despite different orientation angles of the polarizer. The relatively low birefringence of these ULI waveguides $\sim 10^{-6}$ [141, 3] indicates that the phase delay between the interfering s- and p-polarized light is relatively constant across the input polarization angle. As a result, V_{tot} in Eq. (6.2) is unaffected thus, giving similar MSE values in Fig. 6.28. Hence, these results provide quantitative proof that the DBC devices written using ULI are resistant to polarized light.

This page was intentionally left blank.

Chapter 7

On-sky tests

This Chapter describes the design of the pupil remapping experiment, construction of the tranfer matrix of the system using a calibration source, and the retrieval of the stellar visibilities obtained at the William Herschel Telescope (WHT). After conducting systematic laboratory characterization of various devices in Chapter 6, the 4-input pupil remappers with DBC and reformatters that has $L = 20\,\text{mm}$ was identified to be the most suitable device for operating the on-sky test at the WHT.

All the sections of this Chapter are published in Nayak et al. [3].

7.1 Design of the experiment

To interface the device with the WHT, an experimental layout using Zemax modeling was designed. In this case, two main components are required for pupil remapping of the WHT. Firstly, the re-imaged WHT pupil has to be hexagonally segmented using a deformable mirror (DM). Secondly, the light from the individual segments have to be coupled into the pupil remappers, for which a microlens array (MLA) was used. Recent examples of such a configuration can be found in Refs. [87, 90]. Note that in the rest of the sections the expression *deformable mirror* (and its acronym DM) is used to indicate the segmented deformable mirror, which is used in the on-sky experiment. This is not to be confused with the deformable mirror used by the adaptive optics (AO) system of the WHT itself. For doing the pupil remapping, a DM consisting of 37 hexagonal segments from Iris AO, Inc and a MLA from SUSS-Micro optics with a back focal length of $910\,\mu\text{m}$ was used, the schematic of the setup is shown in Fig. 7.1, Fig. 7.2. The coordinates of the four sub-apertures projected onto the WHT primary are provided in Table 7.1 in the reference frame of Fig. 4.2b.

From the WHT, the f/11 corrected beam enters the setup, where the achromatic lens L1 collimates the light to a beam with diameter of 11.4 mm. The collimated beam after lens L5 had a diameter of 5.1 mm, which is $\sim$20% larger than the 4.2 mm diameter of the inscribed circle of the DM. The DM has a pitch of $606.2\,\mu\text{m}$ and that of the MLA is $250\,\mu\text{m}$. Hence, two sets of achromatic lenses L6 and L7 was used to reduce the beam by a factor of 2.4 to achieve good conjugation between the DM and MLA pitches. By reducing the beam size, one can also avoid unwanted overlap of different segments of the DM on the same MLA lenset as well as spurious injection of light from a nearby MLA lenslet into the integrated optics device [156].

The average total throughput of the system is shown in Table 7.2, which is at most $\sim 4\%$. The numerical calculations based on the overlap integral showed that a coupling efficiency of $\approx 78\%$ could in principle be achieved when considering the numerical aperture of the individual MLA lenslet and the MFD of the input single mode WGs of the device. Each individual

	sub-pupil 1	sub-pupil 2	sub-pupil 3	sub-pupil 4
x (meters)	+1.52	0	-0.24	-1.52
y (meters)	0	+0.85	+1.32	0

Table 7.1: Coordinates of the sub-pupils projected onto the telescope primary in the reference frame of Fig. 4.2b.

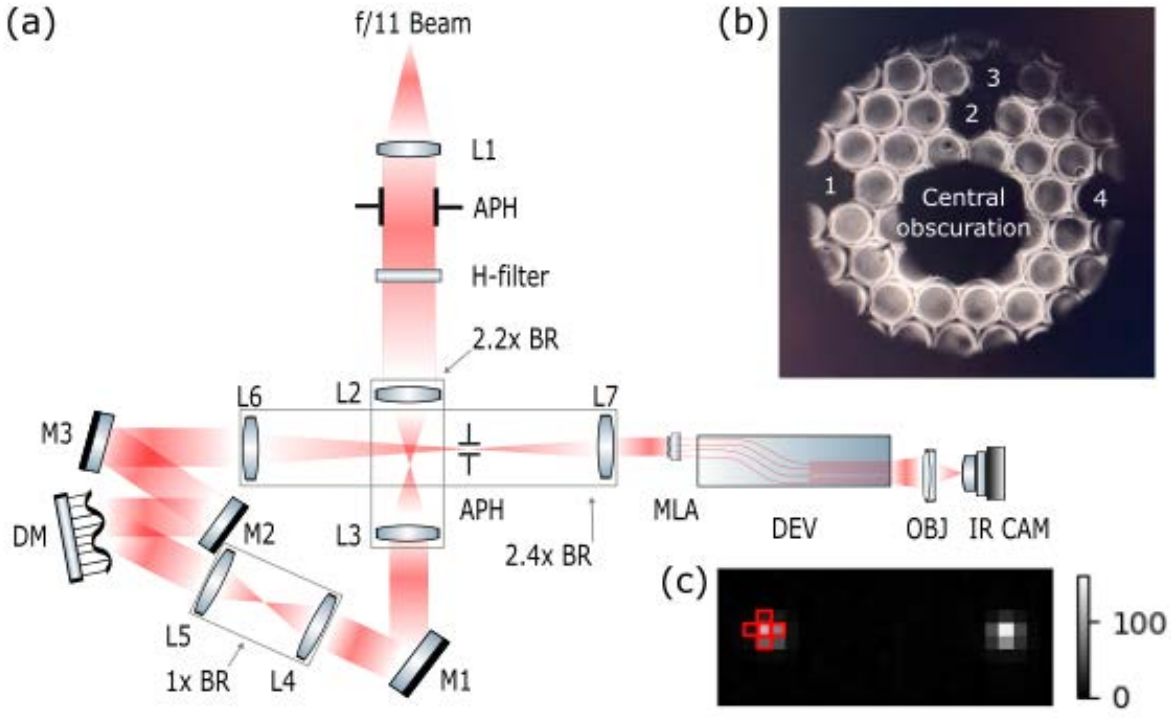

Figure 7.1: (a) Schematic of the optical setup that was used on the WHT Nasmyth bench *(not to scale)*. f/11 is the AO corrected beam that is received from the WHT. The following acronyms are used, L: lens, H-filter: H-band filter (λ_0 = 1600 nm, $\Delta\lambda$ = 50 nm), APH: adjustable pin hole, BR: beam reducer, M: mirror, DM: segmented deformable mirror, MLA: microlens array, DEV: device under test, OBJ: objective, IR CAM: infrared camera. The various focal lenghts are f1 = f4 = f5 = f7 = 125 mm, f2 = 100 mm, f3 = 45 mm, f6 = 300 mm. (b) Image to verify the conjugation of the DM onto the MLA before injection into the integrated optics (IO) device. The sub-apertures to be coupled into the IO device are steered out by tilting the corresponding segments of the DM and appear therefore in black. (c) Two of the output waveguides of the DBC after bias subtraction with Vega's starlight injected into the device. The image is magnified by a factor of ≈ 3.4 and the colorbar shows the analog to digital units (ADU). Also shown is a red augmented area consisting of 5 pixels, which is used to calculate the power across each output waveguide.

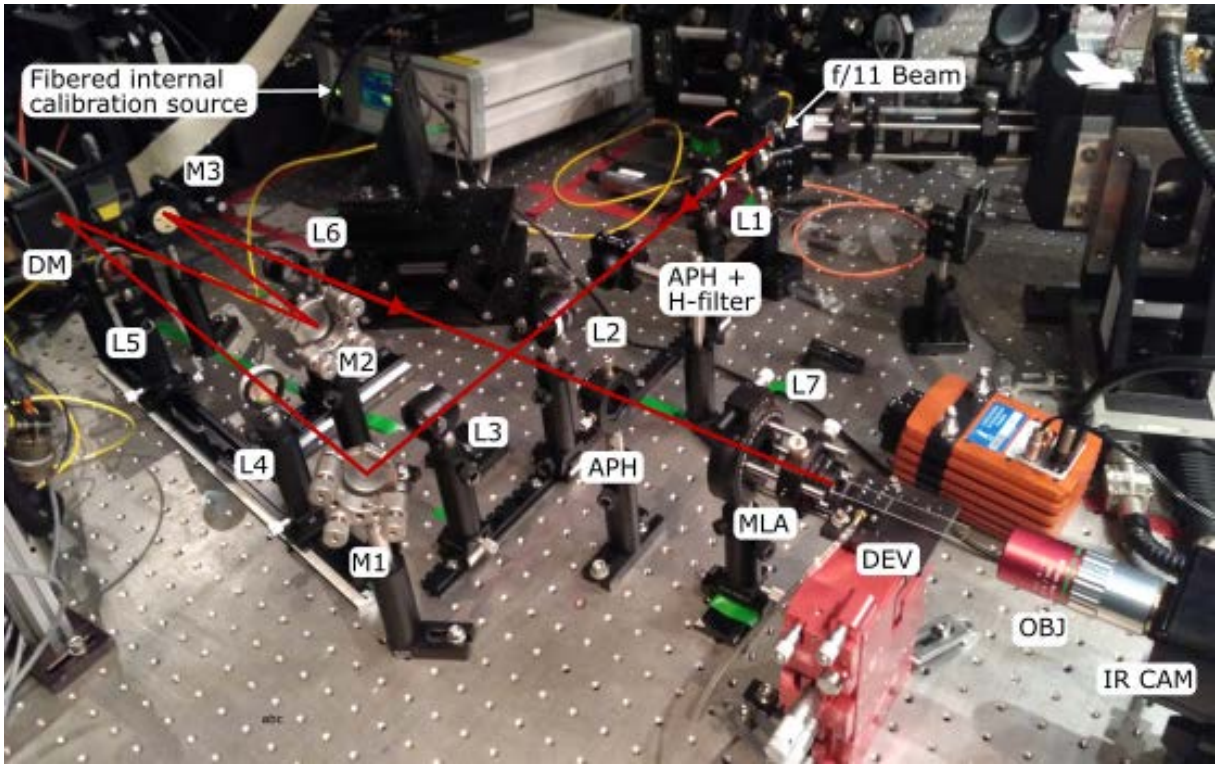

Figure 7.2: Photograph of the optical setup as installed on the Nasmyth platform with the red beam illustrating the light path from the telescope to the IO device. The acronyms used in Fig. 7.1 follows here as well.

Components	Throughput (in %)
CANARY (e)	< 15
Optics (e)	66
Coupling efficiency (e)	78
DBC device (m)	$\sim$ 50
Total	$\sim$ 3.9

Table 7.2: Estimated throughput of the system down to the infrared camera. In brackets, "m" refers to measured, "e" to estimated throughput. For the coupling efficiency, the optimistic upper limit is reported. The effective on-sky coupling efficiency could not be measured. The optics includes H-band pass filter (T = 90 %), lenses (T = 99.5%), mirror (R = 96%) and MLA (T = 90 %). T: Transmittance, R: Reflectance.

MLA lenslet produces a 49.4 cm aperture when projected on-sky, which is less than the Fried parameter calculated at 1600 nm, as shown in Table 7.3. Hence, the wavefront across the MLA aperture can be assumed to be parallel and the on-sky coupling efficiency could, if the optimal alignment is reached, be close to the theoretical limit. However, one in practice is limited by the thermo-mechanical stability of the setup, which ultimately probably decreases the effective coupling efficiency. A long distance ($\approx$ 80 cm) between the DM and MLA was kept to make sure that the individual DM segments could be steered out of the optical path when maximum tip/tilt (+/- 2 mrad) was applied.

Two InGaAs cameras were used: Ninox 640 from Raptor photonics and CRED2 from FIRST Light. All images recorded by the camera were stored in the *.fits*[i] file format. For characterization and extraction of the V2PM, the Ninox 640 was used, since the software for synchronous control was available. For the on-sky measurements, the CRED2 was used because of its lower dark current and readout noise. However, the necessary software for synchronous control of the CRED2 with the DM, which is required to determine the V2PM was inaccessible.

7.2 Characterization at the telescope

The broad band source from Amonics was used as an internal calibration source to obtain the V2PM at the WHT. The light from the broad band source was launched into the optical path such that it could include all the necessary components to obtain the transfer function of the system located after the Nasmyth focus of the telescope. This included the CANARY AO system [157, 158] as well as the optical elements of the DBC experiment (see Fig. 7.1, Fig. 7.2). The AO system was turned off during calibration, which corresponds to a close to flat configuration of the ALPAO[ii] deformable mirror. For the initial calibration, the DM used in Fig. 7.1 was also flattened, corresponding to a configuration of zero phase reference for the four injected beams.

With the calibration source launched into the optical path, the DM and MLA was used to couple the chosen four sub-apertures into the device as shown in Fig. 4.2b. The remaining 33 unwanted focal spots formed by the MLA were steered away. The coupling in each input waveguide was optimized by tip-tilting the corresponding segment. As the default $\pm 2.5\,\mu$m piston range of the DM segments was influenced by the applied tip-tilt, this resulted in each segment having a slightly different total travel range. However, within this travel range, the piston sampling was fixed at 5 nm/frame.

The usual V2PM characterization was proceeded: first, by injecting only one input beam

[i] A commonly used digital file format for storing and processing of data in astronomy.
[ii] A company that manufactures deformable mirror.

to record the single excitation and second, by injecting two input beams to record the pairwise excitation. The temporal fringes at the output were recorded by delaying the corresponding DM segment. With this process, 4 single excitations and 6 pairwise excitations of the input light beams were recorded to generate the 16×23 elements of the V2PM. The visibility amplitudes is shown in Fig. 7.3 extracted from one of the low-conditioned V2PM that was acquired at the WHT with the calibration source. The CN was 12.5, slightly higher than that obtained in the lab using the 2-beam Michelson setup (see Section 6.4). The oscillations in the visibility amplitude are due to residual phase errors obtained from a chromatic V2PM [2] – a result already obtained in Section 6.4.

The MSE between the theoretical value and the experimental data in blue for visibility amplitudes in Fig. 7.3 is in the range $0.4 \times 10^{-2} - 7.4 \times 10^{-2}$ for all visibility pairs. This range of MSE is of the same order of magnitudes as the visibility amplitude obtained from the 2-beam Michelson setup in the lab. However, the MSE of the visibility amplitude pairs, especially (V_{12} = 5.0×10^{-2}, V_{13} = 7.4×10^{-2} and V_{14} = 2.8×10^{-2}) is slightly higher in comparison to the other three pairs, which is evident in Fig. 7.3. A statistical approach is used where a confidence interval is defined and showed only those frames for the retrieved visibility amplitudes, whose value was within 50% of the theoretical value of visibility amplitude in Fig. 7.3. Those frames that were outside the 50 % confidence interval were discarded, which happened due to larger imbalance originating in the retrieved photometry (i.e. Γ_{ii} in Eq. (2.14)) of the input waveguide numbered 1. The photometry imbalance ($=\Gamma_{ii}/\Gamma_{jj}$) for V_{12} and V_{13} was a magnitude higher than the remaining four visibility pairs. As a result, the V_{ij} value given by Eq. (2.20) deviates from the expected amplitude value and fall outside of the confidence interval defined above, implying missing values for V_{12} and V_{13} in Fig. 7.3. This might have happened due to coupling errors at input numbered 1 from the DM segment in between the pairwise excitation of two input beams, while obtaining the V2PM.

The confidence interval defined above for the visibility amplitudes was then used to calculate the retrieved visibility phases as shown in blue in Fig. 7.4. The theoretical phase is shown in black with a spatial frequency of $\sim \frac{4\pi}{\lambda}$. There is a factor two in the spatial frequency due to the reflection on the DM. Fig. 7.4 shows a close match between the retrieved and the theoretical values, except for ϕ_{12}, ϕ_{13}. The phase deviation for the latter is suspected to be due to residual phases caused by coupling errors as mentioned above, as well as uncertainties in the piston positioning of the DM segment.

The above calibrated P2VM obtained at the WHT is applied to the stellar targets and the visibilities are extracted in the subsequent sections.

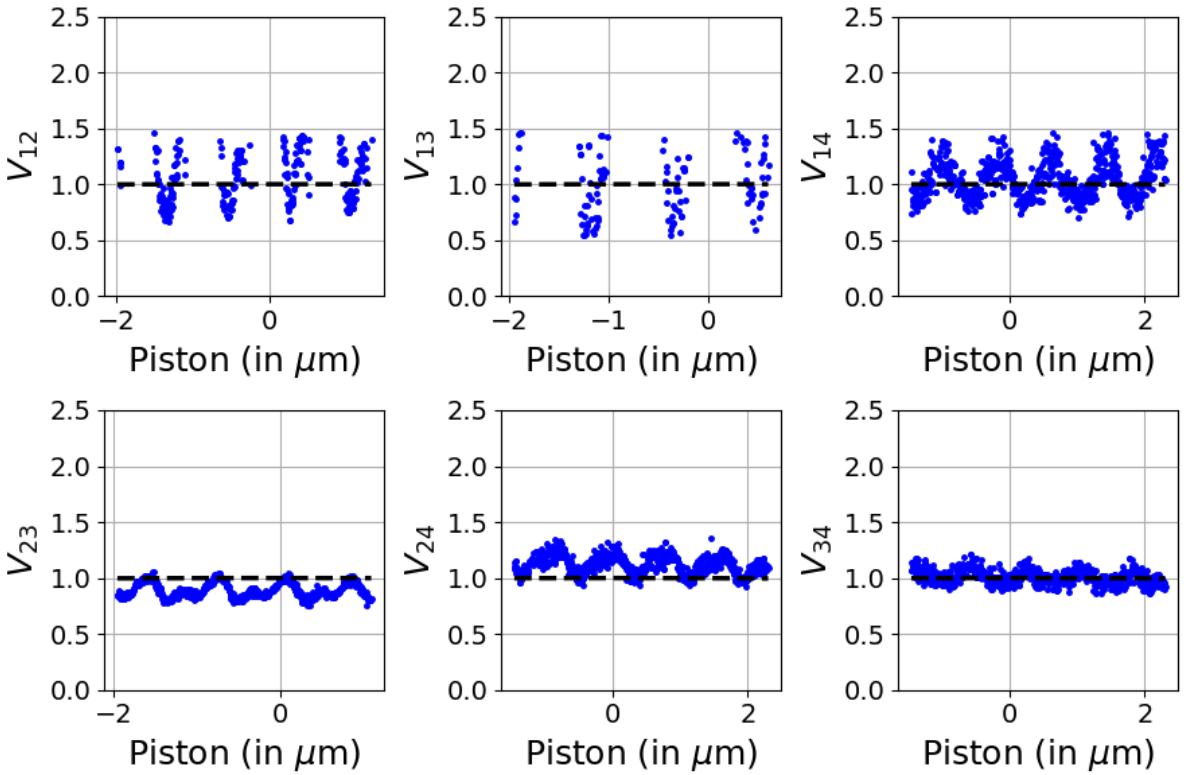

Figure 7.3: Retrieved visibility amplitudes from the V2PM data shown in blue, obtained at the telescope using the calibration light source ($\lambda_0 = 1600\,\text{nm}$, $\Delta\lambda = 50\,\text{nm}$). The missing amplitude values for V_{12} and V_{13} are due to the photometry imbalance (see Section 7.2).

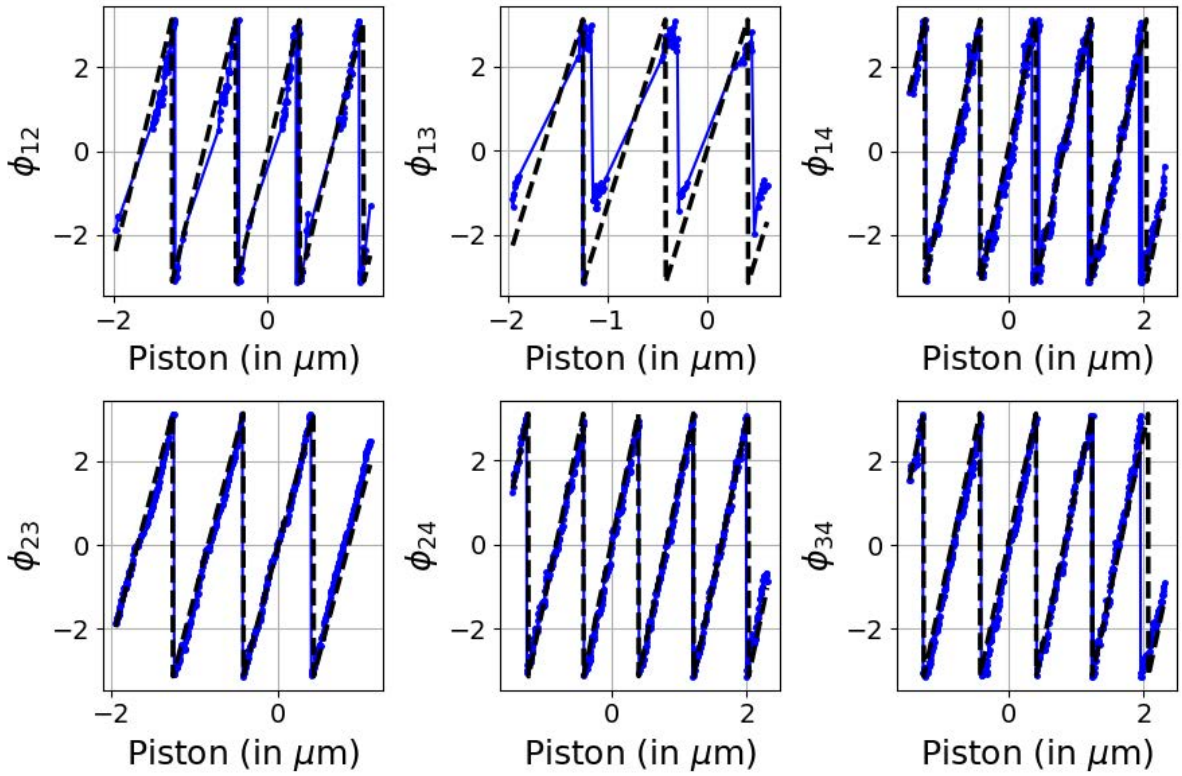

Figure 7.4: Retrieved visibility phases from the V2PM data shown in blue, obtained at the telescope with the calibration source. The black line shows the theoretical value.

Nights	seeing (as)	r_0 (cm)	v (km/hr)	τ_0 (ms)	σ_λ (nm)	Targets
10-11	0.7	58.3	20	32.5	169.2 – 276.5	Altair
11-12	0.8	50.8	20	28.3	295.9 – 432.3	Vega

Table 7.3: Table showing different averaged quantities describing the observing conditions for the nights: seeing values recorded from the metrology archive of the WHT at 500 nm, the Fried parameter (r_0) calculated at 1600 nm, wind speed (v), atmospheric time constant (τ_0), range of root-mean squared (rms) wavefront errors (σ_λ) from CANARY and stellar targets that were observed per night.

7.3 On-sky experiment

The on-sky experiments were performed during the nights of August 09-12, 2019, with observing conditions summarized in Table 7.3. Two bright stars Vega and Altair (H$\sim$0) were observed subtending an angular resolution of a few milli-arcsecond (mas) and thus appearing as point sources at the spatial resolution of the WHT. These two sources, which are among the brightest stars in the Northern hemisphere, were selected based on their observability (right ascension and declination) during the entire night. The on-sky experiment was operated with the support of the CANARY AO system to compensate for the atmospheric turbulence. Therefore, the AO system is briefly described from where the f/11 corrected beam was obtained. CANARY is a multi-guide star AO system that was developed to demonstrate multi-object AO correction. CANARY was configured in single conjugate adaptive optics (SCAO) mode with an expected throughput of $< 15\,\%$ for this experiment. In this mode, CANARY uses a 14x14 sub-aperture Shack-Hartmann wavefront sensor controlling a 241-actuator deformable mirror from ALPAO at a frame rate of 150 Hz [157, 158, 159]. When CANARY is operated in SCAO mode, and depending on the seeing conditions, an average Strehl ratio of 0.3 is obtained. In Table 7.3, the actual range of wavefront errors delivered by CANARY is reported during the observation of our sources.

The four segments of the DM were used to couple light into four inputs of the pupil remapper via the MLA (see Fig. 7.1). With an average total throughput of our system of at most $\sim 4\%$ (see Table 7.2), the CRED2 camera water-cooled at 233 K was used and affected by a read-out noise of $\sim 22\,\mathrm{e}^-$ [148] to record the DBC outputs. Since, the routines for a synchronous control of the CRED2 and DM was not available, the CRED2 and DM interfaces separately was used separately. The DM interface was used to steer in the four DM segments without adding any additional piston. The CRED2 interface was used to record various sets of 1500 frames in one continuous shot. All the frames were bias-subtracted. The bias frames were recorded by blocking starlight path with a physical aperture placed before L1 (see Fig. 7.1).

The exposure time per frame was chosen to be $t_e = 250$ ms with the CRED2 camera in high gain mode. The choice of this value was motivated by the necessary compromise between the SNR and risk of fringe smearing. As the quality of the delivered AO correction and the delivered SNR at the DBC outputs could not be analyzed in real-time, values adopted by other similar near-IR experiments [87] were adopted, for which the interferometric fringes were detected using $t_e = 200$ ms and without any assistance of external adaptive optics acting as a fringe tracker.

For the subsequent data reduction, a crossed region of five pixels around the peak value is selected (see Fig. 7.1c). For the analysis of stellar targets, the frame selection according to the following criteria was applied: firstly, the extracted power of the output WGs has to be positive. The frames with power of < 0.1 counts were discarded. Secondly, when retrieving the input power (Γ_{ii} in Eq. (2.14)) by applying the P2VM to the data, the frames resulting in negative values were removed. Third, only those frames with the retrieved visibility amplitudes in the range (0,4) were considered to show the on-sky results. Fig. 7.5 reports the typical SNR measured at each of the 23 outputs of the DBC when observing Vega after the frame selection.

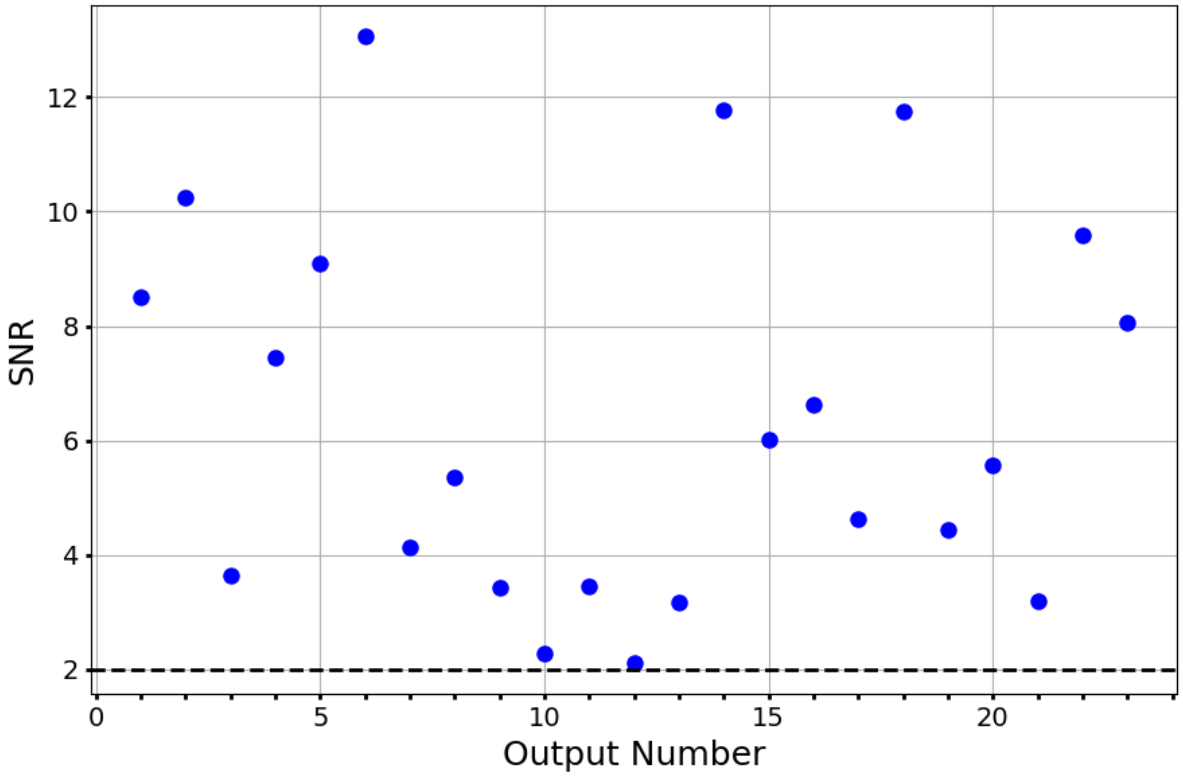

Figure 7.5: Measured flux SNR at each of the 23 outputs while observing Vega after frame selection. The dashed black line corresponds to SNR = 2.

	Visibility amplitudes						Closure phases (in rad)			
	V_{12}	V_{13}	V_{14}	V_{23}	V_{24}	V_{34}	Φ_{123}	Φ_{124}	Φ_{134}	Φ_{234}
Vega										
Mean	0.81	0.64	0.91	0.60	0.69	0.85	-0.85	0.08	0.67	-0.02
Std	0.48	0.43	0.52	0.28	0.38	0.47	2.11	1.99	2.05	2.34
Median	0.73	0.55	0.84	0.58	0.64	0.78	-1.10	-0.23	0.89	0.13
Altair										
Mean	0.65	0.58	0.70	0.72	0.75	0.76	-0.13	0.72	-0.13	-0.04
Std	0.19	0.23	0.63	0.16	0.39	0.51	1.59	1.64	2.70	1.92
Median	0.65	0.56	0.51	0.72	0.69	0.67	-0.53	0.49	-0.66	-0.39

Table 7.4: Mean, standard deviation (Std) and median values for the visibilities and closure phases obtained for Vega and Altair.

Γ_{ii} (in camera counts)	Calibration Source	Vega	Altair
Input 1	56000 ± 3000	800 ± 400	1700 ± 500
Input 2	128000 ± 6000	2300 ± 700	2500 ± 600
Input 3	41000 ± 4000	1400 ± 500	1500 ± 300
Input 4	51000 ± 3000	900 ± 300	700 ± 300

Table 7.5: Retrieved photometry of the four inputs when injected simultaneously into the DBC combiner.

7.3.1 Vega

Fig. 7.6 and Fig. 7.7, respectively reports the histograms of the retrieved visibility amplitudes and closure phases obtained on Vega. With the selection criteria defined above, 84 % of the frames out of 10500 frames contributed to the pool of data. The calculated mean, standard deviation and median values are reported in Table 7.4. The histograms exhibit a Gaussian skewed shape peaking to $\sim$ 0.6–0.9. While the expected visibility value for a point source is close to 1, the measurements are impacted by partial AO correction and longer integration times, which may result in fringe smearing (see Section 5.4.4). The visibility spread is significant, about 0.4 on average. This suggests that the retrieval process through the inverse V2PM is unstable, possibly due to the overall low flux level (see Section 5.4). The mean value of the CP is ~ 0 for Φ_{124}, Φ_{134} as expected for a point source, whereas it is offset for the other two triplets. Similarly, a significant spread is seen in the CP histograms. From the P2VM, the four input photometries corresponding to the Γ_{ii} terms in Eq. (2.14) (see Fig. 7.8) are retrieved and reported in Table 7.5 for comparison between Vega, Altair and the calibration source.

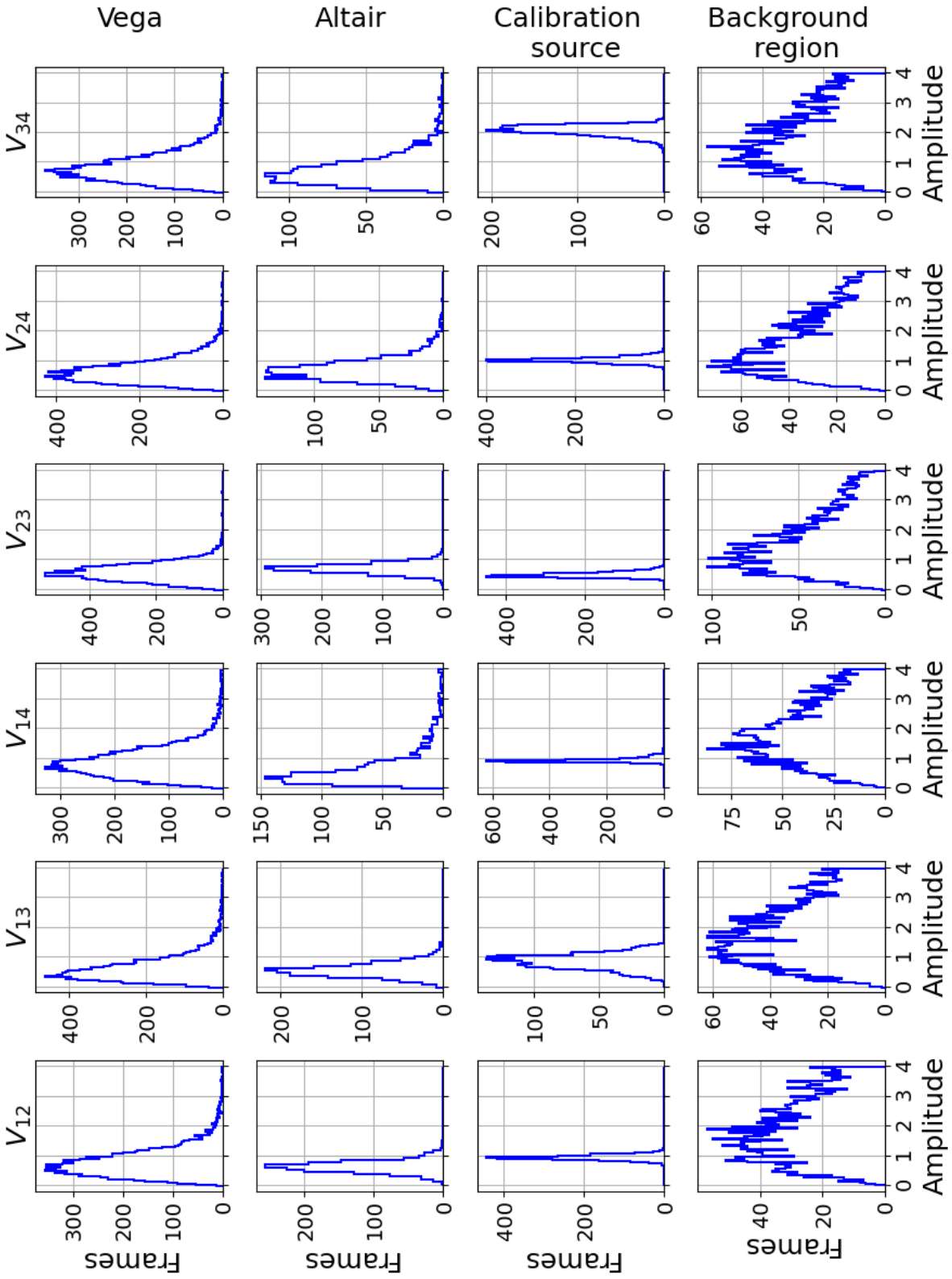

Figure 7.6: Histograms of the visibility amplitudes for Vega, Altair, the calibration source and a background region.

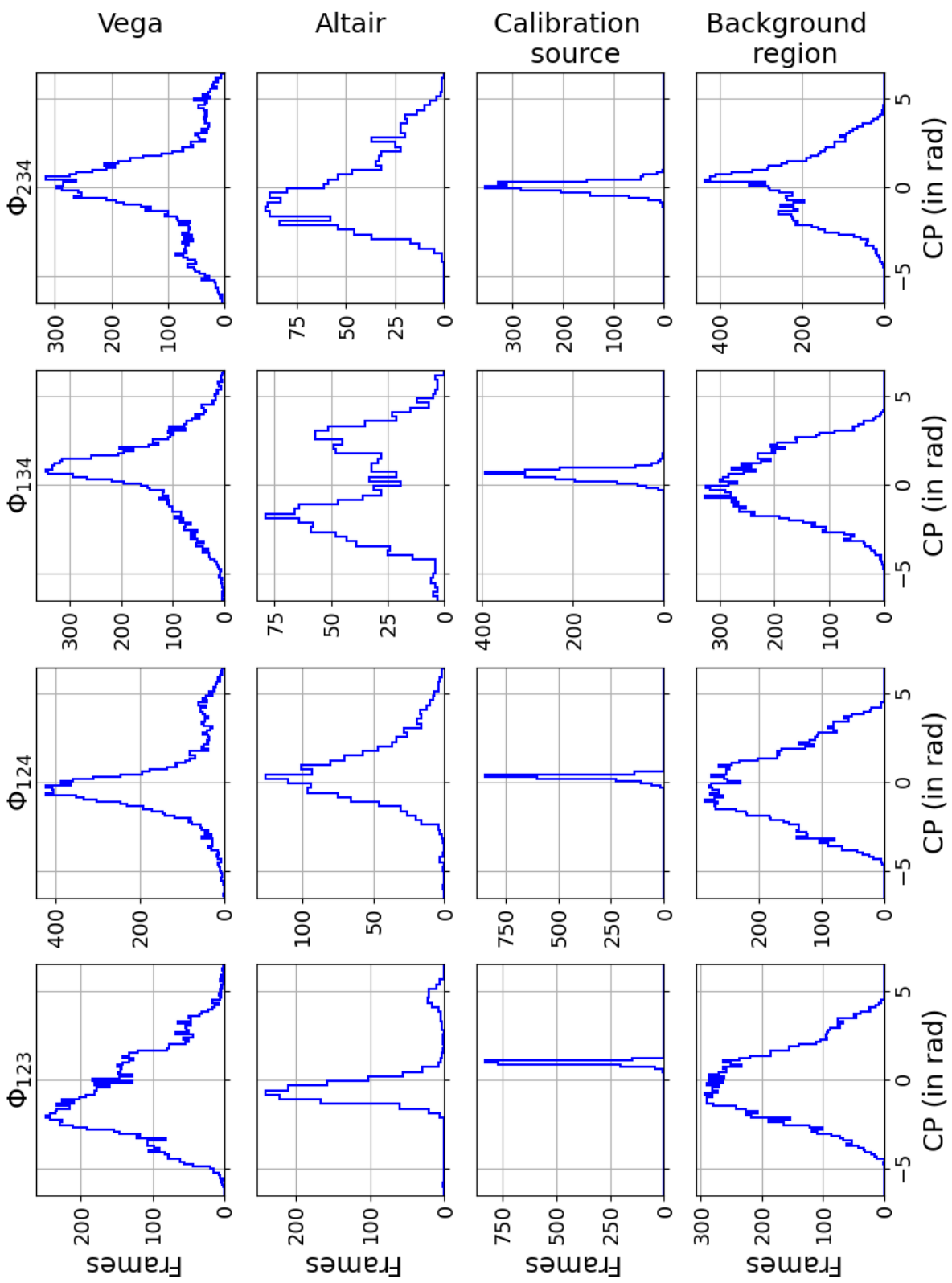

Figure 7.7: Histograms of the closure phases for Vega, Altair, the calibration source and a background region.

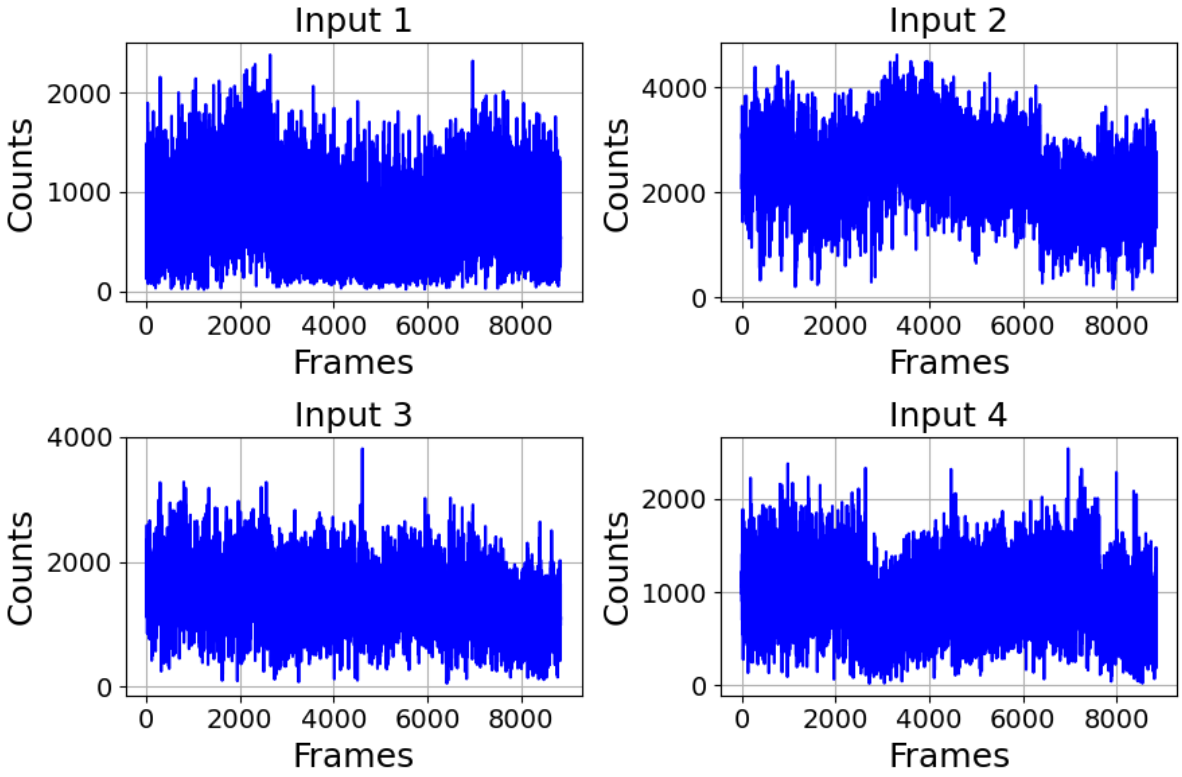

Figure 7.8: Plots of the retrieved photometry for the four inputs of the DBC for Vega.

7.3.2 Altair

Only one continuous shot for Altair with a total of 1500 frames was recorded. As shown in Table 7.5, the photon number from Altair are comparable to the case of Vega, which suggests that the error analysis and potential impact of noise sources in low photon regime may apply to the Altair data as well. The visibility amplitudes and closure phases for Altair is shown in Fig. 7.6 and Fig. 7.7 respectively, where contributions from 94 % of the frames are shown for the analysis of the visibilities with the selection criteria defined above. The mean, standard deviation and median values of the visibilities for all combinations from Altair are shown in Table 7.4.

7.4 Discussion of on-sky results

The Fig. 7.6 and Fig. 7.7 presents the results on the retrieval of the coherence function in a way that several hypothesis can be advanced to explain the spread of our data. The third column reports the visiblities retrieved from the observation of the internal calibration source, which

corresponds to a high-flux level case at the inputs of the DBC (see Table 7.5). The last column shows the results of the visibilities retrieval from a region of the detector fully dominated by the background and its noise. For all of these four cases, the *identical* V2PM obtained from Section 7.2 has been employed.

7.4.1 Impact of photon noise and detector noise

Considering the low throughput of the experiment together with intrinsically small diameter of the individual sub-apertures, there is a probability that the experiment faced a photon-starving regime despite observing two of the brightest stars in the northern hemisphere. In Fig. 7.6, Fig. 7.7, it can be observed that the histogram of the retrieved coherence function for the calibration source is much more peaked, owing to the much larger amount of flux collected as seen in Table 7.5. On the contrary, when applying the retrieval process to a detector region totally dominated by the background noise, the corresponding histograms present the widest spread both for the visibilities and closure phases. In the case of Vega, despite stellar photons are collected at the 23 outputs, the modest SNR measured (see Fig. 7.5) clearly point at a photon-starving regime. Note that the visibilty amplitude histograms obtained for Altair appears slightly less spread than in the case of Vega. It could be that an improvement of the throughput (see Table 7.5), caused for instance by the better AO correction on Altair (see Table 7.3), or a more stable coupling has helped towards more stable results. However, the effect remains marginal and cannot be fully proven at this point. A simulation of the impact of the photon shot noise and detector noise is presented in Section 5.4 to support these findings.

7.4.2 Partial AO correction and decoherence

In the experiment, adaptive optics correction was used as an external fringe tracker to maintain coherence between the sub-apertures. Because of partial AO correction, the relatively long integration time adopted may still lead to temporal decoherence, hence decreasing the values of the retrieved visibilities. When looking at the visibility amplitude distribution obtained with the calibration source, the histograms show a rather limited spread and have a median value close to V=1, except for V_{23} and V_{34} for a reason that cannot be clarified at this point. Similarly, the CP histograms are also comparatively narrow, with a median value for Φ_{124}, Φ_{234} triplets close to 0° when compared to other two triplets. Clearly, the partial AO correction combined to a longer integration time leads to some decoherencing, which explains partly the retrieved visibility amplitudes smaller than 1 for Vega and Altair. Since the CP is an observable more

robust to external phase errors, one may have expected a more peaked distribution for the two stars. But again, the overall low-level of light flux might result in random phase errors, which is detrimental for a robust calibration of the CP signal. This effect is also analysed through simulations in Section 5.4.

7.4.3 V2PM calibration

Finally, it is suspected that the process to derive the V2PM of the system may also lead to the generation of systematic biases that are difficult to identify. Indeed, due to configuration issues, the Ninox 640 have been used to establish the V2PM and the CRED2 for the on-sky and internal calibration measurements. Because of the different levels of detector noise between the two cameras, this may lead to the presence of biases. This fact is confirmed for the calibration source, where the retrived visibilities are not same for all the pairs and CP triplets.

Chapter 8

Summary and future outlook

8.1 Summary

In the context of interferometry, IO components have primarily been developed either as pupil remappers, where the pupil of the telescope is remapped with single-mode waveguides [87] or as beam combiners that combine light from two or more telescopes using 2-D [136] or 3-D photonic circuits [104]. This work aimed to blend these two concepts of pupil remappers and discrete beam combiners (DBC) for the realization of a monolithic 3-D IO-based *astrophotonics* device, followed by an interferometric characterization step to qualify the device for on-sky testing at the William Herschel Telescope (WHT) and finally, validate the DBC as a possible beam combination scheme for long baseline interferometry. The summary is carried out chapter-wise:

Design – The design of the monolithic IO-based *astrophotonics* device containing both the pupil remappers and the DBC, which was developed in this work, was optimized on several fronts. The coherent reformatters were path length matched to $PaL \sim 0.1\,\mu$m to preserve the coherence length of the light passing through the turbulent atmosphere. In addition to path length matching, the minimum radius of curvature of the reformatters was constrained to $R_c \geq 30\,$mm to maximize the attainable throughput.[i] The design of the DBC was a zig-zag-based 3D photonic lattice, which is composed of 4-inputs and 23-outputs single-mode waveguides that can combine light from 4 telescopes and simultaneously extract the complex visibilities. Building on concepts of previous work [104], this Thesis verified the optimum input configuration of this kind of DBC, which was calculated to be at input waveguide's position: 5-10-14-19. Following the numerical analysis, the required length[ii] and coupling ratio[iii] of the DBC was found in order to minimize the condition number (CN) of the transfer matrix of the DBC, $\{U\}$, which is also known as the V2PM. A minimum CN[iv] is generally required to have the least propagation error when the inverse of the V2PM, i.e. P2VM, is calculated. As any light source, in reality, has a certain finite bandwidth, this work revisited the theory of transfer matrix calibration of a DBC in the presence of a real light source. Here, a quasi-monochromatic $\{U\}$ was defined, where the matrix elements are frequency-dependent after a certain bandwidth. As a result, it was found that the DBC should be operated in a narrow bandwidth[v] within which the frequency dependent terms of quasi-monochromatic V2PM can be ignored.

Fabrication – Considering the above parameters of the coherent reformatters and the

[i] Throughput of $> 80\%$ has been achieved using simulations when considering the bending losses and transition losses of such reformatters.

[ii] $L = 1.35\,L_c$.

[iii] $\kappa_H = \kappa_D$.

[iv] ideally ~ 1.

[v] $\frac{\Delta\nu}{\nu_0} \ll 1$.

DBC, three IO devices were designed containing photonic circuits that manipulated the light spatially in 3-D. The following naming convention for the devices are used for the rest of this section: 1) Device-A, 2) Device-B, and 3) Device-C. Device-A consisted of 4-input non-redundant pupil remappers[vi] connected with the 4-input DBC. Device-B was a replica of Device-A but had reformatters that spatially distributed the 23-outputs of the DBC into a linear configuration for spectro-interferometric measurements. And Device-C consisted of 8-input non-redundant pupil remappers connected with two 4-input DBCs that were stacked vertically. The initial designs and parameters were sent to *Politecnico di Milano*, which they further optimized. Afterward, these devices were fabricated using their state-of-the-art ultra-fast laser inscription (ULI) facility. The single-mode waveguides of the pupil remappers were polarization insensitive and could be efficiently coupled with standard single-mode bare fibers at $\lambda_0 = 1.55\,\mu$m. A throughput of $\sim 50\%$ was achieved for all three devices.

Simulation – A simulation was done to find the wavelength and bandwidth response of the 4-input DBC region (see Fig. 3.5b). It was assumed that pupil remappers before the DBC region or coherent reformatters after the DBC region introduced negligible phase errors[vii] because these were path length matched. The CN was low (< 15) at the design wavelength in H-band.[viii] The retrieved visibilities[ix] were in good agreement with the theoretical values with mean squared error (MSE) values of $\sim 10^{-7}$. It was found that CP did not give a feasible result when calculated from the data that is used for the calibration of the V2PM (see Appendix A on how the V2PM is filled). But, when the same calibrated P2VM is used to extract the visibilities of different data that is taken with simultaneous injection of 4-input light beams, the CP provides a feasible result. Thus, it can be generalized to an N-input DBC that CP must be calculated when the calibrated P2VM is applied to the power output vectors – with all N-input beams injected simultaneously into the DBC. With the increasing bandwidth of light, the CN increases, indicating the chromaticity of the V2PM. The MSE of the retrieval visibilities and CP also increases with increasing bandwidth. It was found that there were high frequency oscillations in the retrieved visibility amplitude at higher bandwidths which were due to residual phase errors of $\geq \frac{\pi}{2}$ between the real and imaginary parts of mutual-coherence terms γ_{ij}. This resulted in the MSE values for the polychromatic visibilities to be higher than the monochromatic visibilities because of the phase errors obtained from the quasi-monochromatic P2VM due to the finite bandwidth of the source. A simulation was done where all the four input beams injected simultaneously into the device had an amplitude value of 1 and a linear phase ramp in one of the arms of the input waveguides. It was found that the retrieved visibilities and CP were as expected. The retrieved CP was close to $\sim 0^\circ$ showing the robustness of CP to external phase

[vi] When coherent reformatters are used to collect light from a re-imaged pupil of a telescope, they are defined as pupil remappers.

[vii] Errors of $\frac{\lambda}{16}$ at $\lambda_0 = 1.6\,\mu$m.

[viii] $\lambda_0 = 1.6\,\mu$m.

[ix] Refers to both visibility amplitude and phase, unless stated otherwise.

errors.

The impact of different noise sources on retrieved visibilities was further studied by simulating wavefront perturbations[x] in the form of amplitude and phase errors at all four input waveguide locations of the DBC. Neglecting the effects of both photon and detector noise, it was found that the retrieved visibility amplitude ~ 1 and CP ~ 0 for a set of 500 random realizations. However, when simulated photon noise[xi] was taken into account, the histograms for both the visibility amplitude and CP changed and started to spread out: the peak's height decreased, and the width increased due to the increase in photon noise. Adding detector noise to the photon noise worsened the retrieved visibility amplitude and CP. A significant deviation was observed, the median visibility amplitude < 1 and median CP $\neq 0$, along with an increase in the spread of the retrieved values. To simulate a realistic scenario, the camera's exposure time was included. Longer camera exposure times in addition to photon and detector noise further decreases the median values of the retrieved visibility amplitude. The retrieved amplitude median value decreases even more if the level of Strehl ratio or the correction from an AO system is poorer.[xii]

Characterization – The characterization of the three different IO devices was done using a 2-beam Michelson interferometer setup, which is capable of acquiring the V2PM of the DBC. The characterization was performed using a tunable laser source which produced the monochromatic visibilities, and using a broad-band light source with two different bandpass filters[xiii] producing the polychromatic visibilities. For all three devices, the monochromatic and polychromatic visibilities were successfully retrieved. The calculated CN of the measured V2PM of all devices was low (< 20), which is roughly similar to the CN values obtained from simulation across the H-band ($1.54 - 1.64\,\mu$m). Due to residual phase errors, simulations predicted high-frequency oscillations around the retrieved visibility amplitude. These oscillations could be observed in the measurements, which confirmed the simulations. Additionally, a shift of the central OPD for all the three devices (e.g. see Fig. 6.15) was observed while retrieving the polychromatic visibility amplitude. This is suspected to be due to the long arms[xiv] of the Michelson experimental setup. The tip/tilt applied to the mirrors in order to couple light into the pupil remappers creates an optical path delay in the long arms of the setup, which are seen as shifts in the central OPD of the retrieved visibility amplitude. To test whether the mirror tip/tilt introduces phase errors while retrieving the visibilities from the experimental V2PM, an artificial global phase term was applied to the columns of the V2PM. No change in the CN or the retrieved visibility amplitude was found, concluding that phase errors in the form of central

[x] The statistics of the wavefront perturbations was calculated based on Strehl ratio that was delivered by the CANARY AO system.

[xi] The relative contribution of photon noise increases with a lower number of photons.

[xii] As the Strehl ratio decreases, it implies significant perturbation in the incoming wavefront.

[xiii] One at $\lambda_0 = 1.6\,\mu$m, $\Delta\lambda = 50$ nm and other at $\lambda_0 = 1.55\,\mu$m, $\Delta\lambda = 40$ nm.

[xiv] The distance between the mirrors and the coupling lens.

OPD shifts from the Michelson setup do not affect the retrieved instrumental visibilities.

The MSE of the retrieved visibilities for all the three devices[xv] had the same order of magnitude[xvi], which indicates two things. The first indication is that the phase errors, which are a combination of systematic and random errors from the experiment, affected the V2PM of all three devices identically. This agrees with the CN being very similar for all three devices and the level of accuracy in the retrieved visibilities being identical. Thus, the MSE has the same order of magnitude. The second point refers to the reliability of the ULI process and the parameters used to fabricate these three devices. In one of the works on ULI fabrication [160, Chapter 7], it has been reported that the performance of photonic circuits varied despite using the same ULI parameters, identifying defect states present in the glass as the main culprit. That kind of variation in performance has not been observed with the devices used for this Thesis. Note that the substrate used in Ref [160, Chapter 7] is different from the substrate used in this work, which could play a role as well. However, the results in this Thesis indicate that with the state-of-the-art ULI facility and fabrication method at *Politecnico di milano*, the variation in performance is low: in particular, the DBCs have almost identical optical properties, leading to similar experimental MSE values among the three devices.

However, while the MSE for the experimental visibilities was consistent between the devices, it was generally higher than the MSE values obtained from simulations[xvii], which comes from various experimental factors. Notably, the MSE for the visibility phase was higher than the MSE for visibility amplitude by a factor of ~ 100. This is because the visibility phase is more sensitive to external phase errors in the experiment than the visibility amplitude. The phase errors are a combination of systematic errors from the delay line, random coupling errors due to the positioning of the DL, retrieval errors from the quasi-monochromatic V2PM due to the finite bandwidth of the light source and non-ideal detectors. A study was carried out where the V2PM of a device captured on one day was applied to data captured on a completely different day with the same laser parameters and coupling conditions. It was found that the retrieved visibilities from both days had similar MSE values indicating a repeatable and predictable behavior of the experimental factors in the Michelson setup.

Finally, a polarization study was done for Device-C by rotating the polarizer at different angles. It was found that the retrieved visibilities had similar MSE values[xviii] independent of

[xv] Though three devices are different in design, the commonality they all share is the DBC – a 4-input and 23-output single-mode waveguides lattice in a zig-zag geometry. The DBC combines the light such that complex visibilities could be extracted simultaneously.

[xvi] For all three devices, MSE for the polychromatic visibility amplitudes were $\sim 10^{-2}$ and that for phases were $\sim 10^{1}$.

[xvii] In the simulation, MSE for monochromatic visibility amplitude was $\sim 10^{-7}$, while in the experiment it was $\sim 10^{-3}$.

[xviii] For all rotation angle of the polarizer, MSE for visibility amplitudes were $\sim 10^{-3}$ and that for phases were $\sim 10^{0}$.

the orientation of the polarized light, thus confirming the polarization insensitive behavior of the single-mode waveguides fabricated using ULI.

On-sky results – The visibilities and CP results from the lab characterization and overall performance of the devices presented above provided the foundation and motivation to proceed with the on-sky campaign at the WHT. Within the available space at the Nasmyth table of the WHT, an optical setup was prepared using a segmented deformable mirror and an MLA to perform the pupil remapping of the WHT. For this purpose, the substrate containing the Device-B was selected. Light coupling into the IO chip was maximized by carefully positioning the DM, MLA, and various optical components. The V2PM was acquired with a broad-band calibration light source using a bandpass filter of $\Delta\lambda = 50$ nm. With the DM and MLA, starlight was successfully coupled into 4 input WGs of the DBC, enabling 6 baseline measurements simultaneously. Stellar photons from Vega and Altair were recorded, and the P2VM obtained from the calibration measurements was applied to the data captured from the star. After the data analysis, several points were found that should be discussed to interpret the results:

- Using the high-flux, turbulence-free, broad-band calibration source, it was observed that, in most of the baselines, the retrieved visibility distributions were in agreement with $V \sim 1$ and $CP \sim 0^\circ$. However, one change had to be introduced to the setup between the calibration and starlight measurement: the camera had to be replaced due to technical challenges. It is strongly believed that the calibrated V2PM might have been affected by biases, which are partly due to different cameras used for the V2PM calibration and the on-sky observation. Unfortunately, this was detrimental to obtaining the precisely calibrated visibilities and CPs.

- For all baselines, the visibility amplitude distributions peaked below the expected value of $V = 1$ for an unresolved source, typically around $\sim 0.6 - 0.8$, with a significant spread around the mean value. The measured CPs also exhibited a significant spread around 0°, and showed in some cases departures from 0°, which is not interpreted as an astrophysical signal.

- To further investigate effects on the retrieval of visibilities and CPs from the on-sky measurements, the signal level was considered. A comparison between the high-flux case[xix] and a case where no signal is detected at the DBC outputs indicates that the shape, spread, and peak in the histograms of the retrieved quantities is strongly influenced by the SNR measured at the 23 outputs. For Vega, an SNR $\sim 2 - 14$ was reached, which is considered at the edge of measuring a coherent signal. Therefore, we expect higher flux – e.g. through larger telescope sub-apertures – is required to obtain reliable results for the visibilities.

[xix] With the calibration source.

- In this experiment, some of the typical challenges of similar experiments [85, 87] were encountered: With single apertures of ~ 60 cm in diameter and the need for short integration times, the measurements ended up in the low photon regime. Here, the level of the AO correction from CANARY did not permit exposure times significantly longer than the atmospheric coherence time. In addition, the noise figure of the camera played a significant role, leading to an overall low SNR.
- To better understand the origin of the low visibilities and high spread of the on-sky results, several simulations were performed to obtain a more realistic situation. It was found that:
  - The partial AO correction from CANARY of $\sim 200-300$ nm rms is not by itself the main cause for the large spread of the data. Still, this level of correction and the relatively large exposure time compared to the atmospheric coherence time would result in fringe smearing, decreasing the value of the retrieved visibilities to ~ 0.5.
  - In the low photon regime of this experiment, the impact of the detector noise is also very significant in shifting the distribution peaks and increasing the spread of the results. This also clearly affects the retrieved CPs, which would otherwise be more robust to the residual phase errors in high-flux conditions.

8.2 Future outlook

After several successful feasibility studies that were limited only to laboratory environments [103, 104, 2], this is the first time that an ULI-manufactured *astrophotonics* device using the DBC-based matricial beam combination scheme was tested on-sky, where it collected starlight from Vega and Altair. Although the performance of retrieved CPs were not yet satisfactory when compared to similar work on pupil reformatting [85, 87], this does not lead us to conclude that the phase retrieval process of the DBC-based beam combination scheme is inherently flawed. On the contrary, as other noise sources strongly impacted the on-sky measurements, laboratory and calibration characterization at the WHT indicate that much better performance could be expected in an experiment where more focus is given to better control of environmental parameters and the transfer function, and to increase the SNR. On the other hand, the retrieval of visibility amplitudes delivered a better outcome, even though there were effects from fringe smearing. It is to be noted that visibility amplitude values were not reported in other, similar works [85, 87]. It is expected that the results would have been improved from a repeated and optimized on-sky experiment under better controlled conditions. Hence, from the encouraging outcomes of this Thesis work, the following upgrades could be done in the future:

- To address some of the issues encountered during the on-sky test, the pupil remapping

setup in Fig. 7.1 could be improved on the following fronts:

  - 3-D printing of the MLA [161] could be done directly on the front facet of the pupil remappers to increase the injection efficiency of light and enable higher signals.
  - The setup can be extended to include resolution test targets [162] and an AO testbed [163] to simulate artificial observational astronomy in the laboratory, which could be used to study the retrieval of visibilities, CP, and image formation. Thus, a more rigorous validation for DBC-based beam combination scheme could be done.

- The spectro-interferometric capabilities of DBC could be explored using a bulk-optics dispersing element[xx] or using IO-based arrayed-waveguide gratings (AWGs) [164]. The advantage of using IO-based AWG is that it could be glued to the outputs of the ULI-based DBC, forming a hybridized single-photonic component with minimum mechanical alignment, which can perform both interferometry and spectroscopy. There are ongoing developments in hybridization towards *astrophotonics* components, which use different photonic fabrication technologies [91, 90].

- Current state-of-the-art pupil remapping interferometry is limited to the lab experiment forming 8-inputs and 28-baselines simultaneously [91]. With the growing size of ground-based telescopes such as ELT [165],[xxi] there is a need for utilizing the whole pupil of the telescope for performing pupil remapping to have access to several baselines simultaneously. The results of the 8-input pupil remapper and 3-D capability of ULI in this work are an encouraging step for a scalable photonic device, which can have $>$ 8-pupil remappers with a cascade of DBCs.

- To enable interferometry with a larger number of telescopes, work is ongoing to develop DBC that can combine light from $>$ 4-telescopes simultaneously [149]. This could be used, e.g. in the context of the CHARA array. However, while preliminary results for 6 inputs are promising, more investigation is needed for this kind of DBC.

- Due to retrieval of phase information from the DBC, it can be used as wavefront sensors in AO [121]. If a prototype was fabricated and validated, this could find applications beyond astronomy, in fields of biophotonics [166] and quantum optics [167].

To summarize, this Thesis described a monolithic 3-D IO-based *astrophotonics* device that consisted of both *pupil remappers* and *DBC*, from design to on-sky testing. This is a first step for validating the concept of DBC-based beam combination for applications in long-baseline interferometry. Especially when the above upgrades are considered, this IO device has the great potential to be implemented in a large-sized telescope,[xxii] at an interferometric facility, or as

[xx] A prism or grating.
[xxi] Extremely large telescope.
[xxii] Primary mirror with $>$ 6 m diameter.

part of a future mission for stellar interferometry in space [168].

This page was intentionally left blank.

Appendix A

How to fill the V2PM?

This Appendix is dedicated to show the step-by-step process of filling the elements of a V2PM obtained from a 4-input DBC. The experimental data that was used to produce Fig. 6.15 and Fig. 6.16 in Section 6.4 will be used as an example in this section. It is to be reminded that this was the device that used for on-sky testing to collect the stellar photons at the WHT. The standard *numpy*, *scipy*, *lmfit*, *astropy.io* and *matplotlib* packages for *python 3* or higher will be extensively used to reduce the data.

The experimental data performed using 2-beam Michelson setup as shown in Fig. 6.1 consists of a folder where 21 *.fits* files are recorded. There are 6 baselines, and for each baseline, there are three *.fits* files: 1 file for when two beams are excited simultaneously, and 2 files each for when one of the beams is blocked while the other beam is injected into the device. The remaining three files correspond to 2 files – when the device is excited with the beam but with no additional delay,[i] and 1 file with both the beams blocked.[ii] The 21 *.fits* files are stacked and summed to get the output image of the DBC as shown in Fig. A.1. The outputs are detected, and coordinates of the 23 output waveguides are stored by finding the peak intensity. After performing the bias subtraction (see Footnote below), a trapezoidal summation corresponding to a 1 pixel radius as shown in Fig. 7.1c is performed to extract and store the power of each waveguide for all *.fits* files.

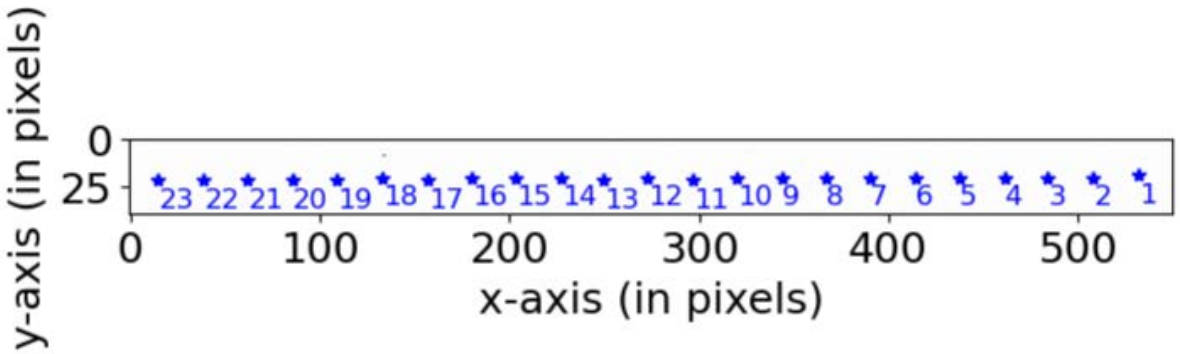

Figure A.1: Summed output image of the DBC.

After the above steps are followed, individual baselines are now analyzed. Consider the baseline pair 1 and 2, as shown in Fig. 3.5a. The following definition is now used for the data set, each containing 23 output WGs:

- BL12: Both the beams are present, but the delayed beam is at input 2.

[i] It is to be made sure that at least one *.fits* file exists for the 4 input waveguides – when the device is excited with one of the input beams, while the other beam blocked. There should not also be any kind of phase delay from the delay line to this coupled input beam.

[ii] It is a file that will be used for subtraction to all the remaining files that are excited with at least one input beam to remove any biases from the camera.

- $P1$: Only input beam numbered 1 is present due to contribution from the straight mirror.
- $P2^d$: Only input beam numbered 2 is present due to contribution from the delayed mirror.

The following steps are now followed:

I To BL12 data set, a fast fourier transfrom (FFT) algorithm is used to filter out the high frequency components by setting a threshold value, and the result for some of the waveguides is shown in Fig. A.2.

II A polynomial fitting of the 4^{th} power or less, $y = a + bx + cx^2 + dx^3 + ex^4$ is applied to $P1$ and $P2^d$ through NLLS method. x is the DL scan from $3.7 - 4$ mm with 5700 samples, y is the data, and unknowns are a, b, c, d, e. The result for some of the WGs is shown in Fig. A.3.

III A photometric correction, $BL12^c$ is applied using:

$$BL12^c = \frac{BL12 - P1 - P2^d}{2\sqrt{P1P2^d}}. \tag{A.1}$$

The fringes for some of the waveguides are shown in Fig. A.4.

IV A Hilbert transformation is used to find the envelope of the temporal fringes and the center of the envelope is located. This gives the central OPD (in μm) of each of the 23 output fringes. An average is carried out across the central OPD for 23 output WGs. Then, a few number of fringes (~ 11) around the averaged-central OPD is used for the next step. The corresponding DL scan values for the 11 number of fringes[iii] are also noted down.

V A model fitting is applied:

$$y = DC_{12} + A_{12}\cos(f_c(x - x_0) + \phi_{12})\frac{\sin(f_s(x - x_0))}{f_s(x - x_0)}. \tag{A.2}$$

Where, $y = BL12^c$, $f_c = \frac{4\pi}{\lambda_0}$ and $f_s = \frac{\pi\Delta\lambda}{\lambda_0^2}$. $x =$ DL values and $x_0 =$ average of 23 central OPD from the fringes found in Step IV. The unknowns are $A_{12} =$ amplitude, $\phi_{12} =$ phase and $DC_{12} =$ constant term. The model is applied using NLLS method and the fitting is shown in Fig. A.5 for the 11 number of fringes. The fitting parameters are saved for later use while filling the V2PM. It is to be noted that for a monochromatic light source $\Delta\lambda \to 0$. Hence, the same Eq. (A.2) is used for the monochromatic data as well,[iv] with the exception that $\frac{\sin(0)}{0} \to 1$ in Eq. (A.2).

[iii] Here, 1 number of fringe corresponds to a cosine or sine cycle from 0 to 2π.

[iv] See the monochromatic retrieved visibilities – Fig. 6.12 and Fig. 6.13.

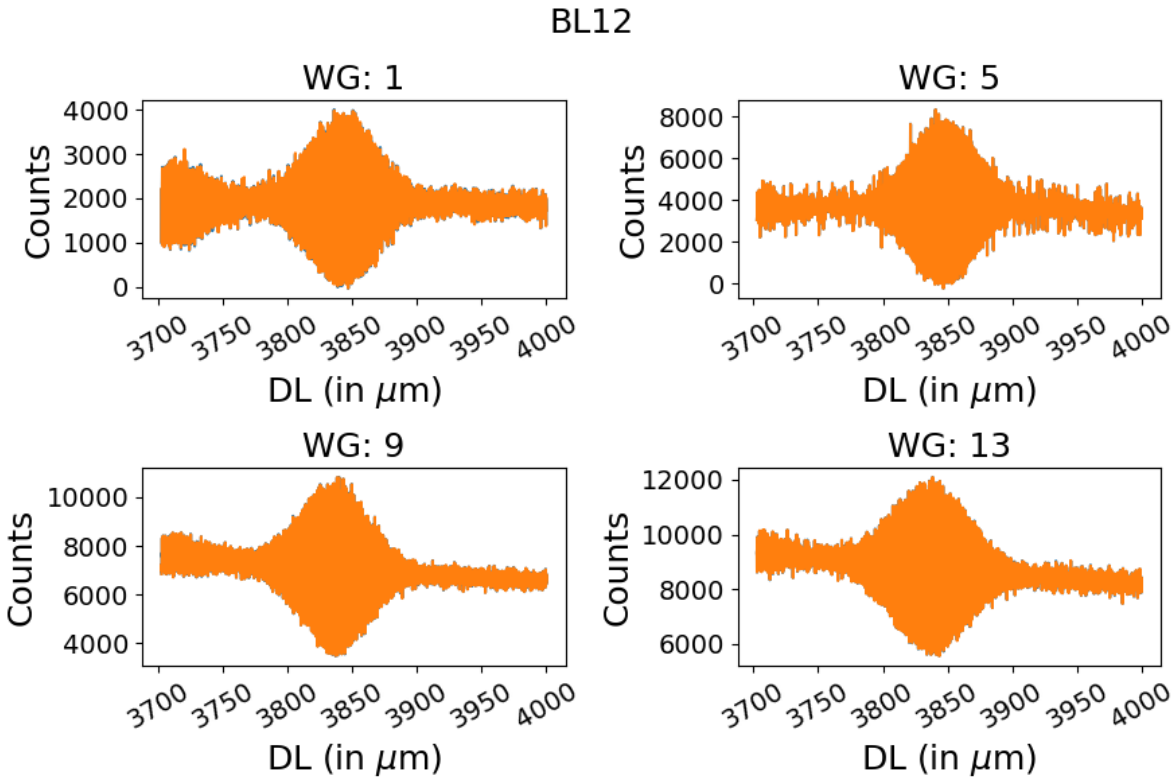

Figure A.2: FFT filtering is used to filter the high frequency components when both the beams are present. The orange is the filtered curve, while blue is the original data.

The Steps I to V are repeated for the remaining 5 baselines.[v]

A.1 Self-coherence terms

The first 4 columns of the 23×16 V2PM are filled with the coefficients of self-coherence terms.[vi] Consider the 1^{st} column of the 23×16 V2PM, which is filled with input beam numbered 1 from the contribution of the straight mirror. The filling of the i^{th} row, 1^{st} column element, U_{i1} can be written mathematically as:

$$U_{i1} = \frac{P1^i}{\sum_{i=1}^{23} P1^i}. \tag{A.3}$$

Where, $P1^i$ is the power extracted for i^{th} WG of input beam numbered 1 (see the definition above). The Eq. (A.3) can then easily be extended to the remaining first three columns, thus

[v] This particular example uses 4 inputs/telescopes. Therefore, there are 6 unique baselines.

[vi] Γ_{ii} in Eq. (2.14).

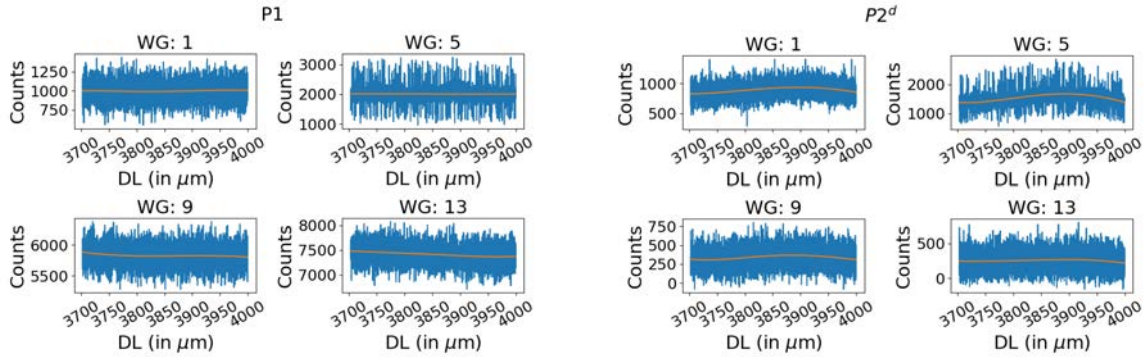

(a) (b)

Figure A.3: Polynomial fitting to the data when only 1 of the beam is present. Blue is the original data, and orange is the fitting curve. (a) $P1$ (b) $P2^d$. The coupling variation due to DL can be easily seen for WG: 5.

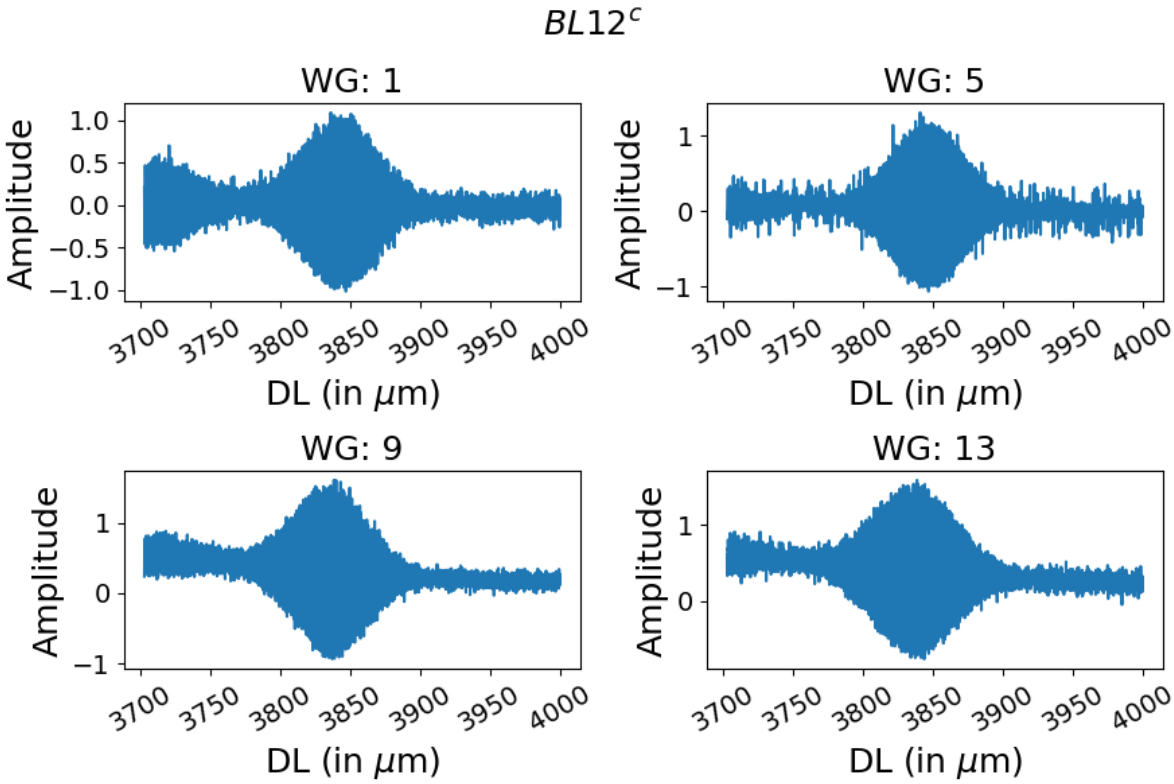

Figure A.4: Photometric correction of fringes using Eq. (A.1). It can be seen that when photometric correction is performed, amplitude range of the fringes is in range -1 to 1.

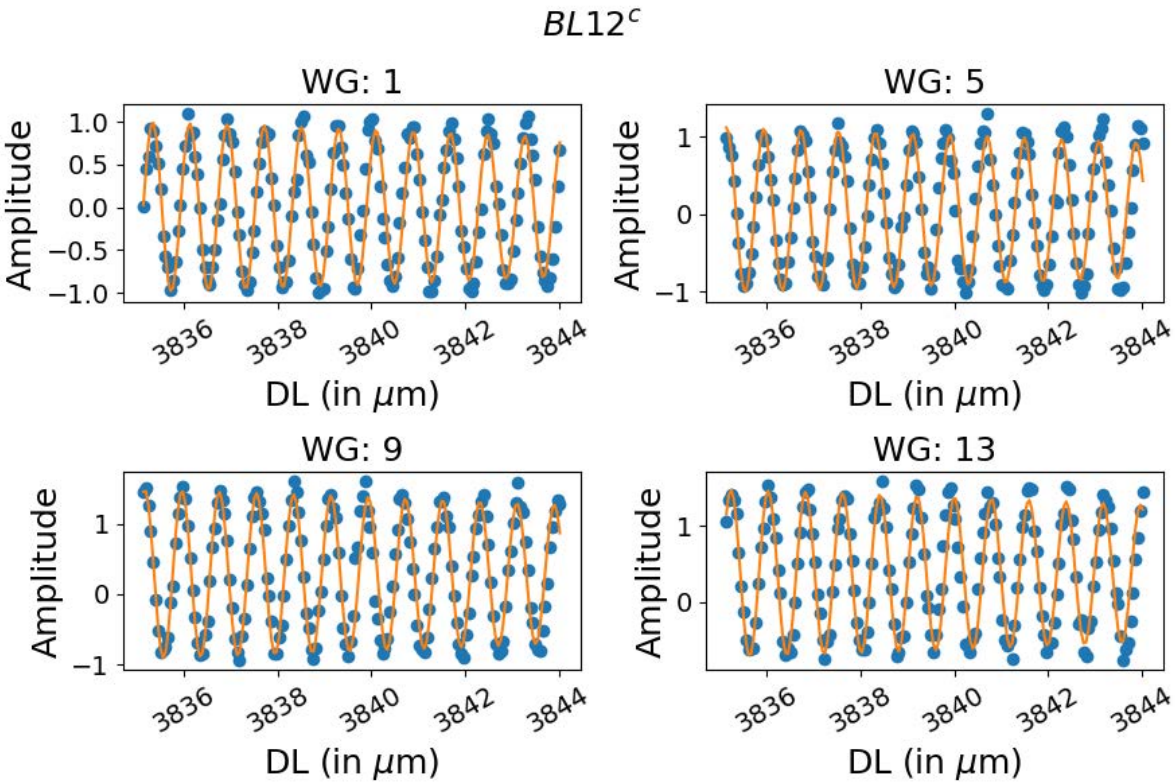

Figure A.5: Model fitting using Eq. (A.2). The A^i_{12} = amplitude and ϕ^i_{12} = phase of the temporal fringes is found for the i^{th} output WG. Blue is the photometrically corrected data from Fig. A.4, while orange is the fitting curve.

filling the coefficients of self-coherence terms. It is advisable that one should not use the $P1^d$ data, which has a contribution from the delayed mirror due to coupling errors as shown in Fig. A.3b.

A.2 Mutual-coherence terms

The remaining 12 columns of the 23×16 V2PM are filled with the coefficients of mutual-coherence terms.[vii] Consider the fifth column of the V2PM, which is filled with parameters extracted from Step V. The filling of the i^{th} row, 5^{th} column element, U_{i5} can be written mathematically as:

$$U_{i5} = 2\sqrt{P1^i P2^i} A^i_{12} \cos(\phi^i_{12}). \tag{A.4}$$

Where, $P1^i$ and $P2^i$ are the power extracted for i^{th} WG of input beam numbered 1 and 2, respectively (see the definition above). ϕ^i_{12} and A^i_{12} are the parameters extracted from Eq. (A.2) for i^{th} WG, when both the beams numbered 1 and 2 are present. The Eq. (A.4) can then easily be extended to fill the 6^{th}, 7^{th}, 8^{th}, 9^{th}, and 10^{th} columns from the contributions of baselines BL^c_{13}, BL^c_{14}, BL^c_{23}, BL^c_{24}, and BL^c_{34}, respectively.

Finally, the last 6 columns are reserved for the imaginary part of Γ_{ij}. The filling of the i^{th} row, 11^{th} column element, U_{i11} is done using:

$$U_{i11} = -2\sqrt{P1^i P2^i} A^i_{12} \sin(\phi^i_{12}). \tag{A.5}$$

Where, all the definitions are defined above. Thus, Eq. (A.5) can then easily be extended to fill the 12^{th}, 13^{th}, 14^{th}, 15^{th}, and 16^{th} columns from the contributions of baselines BL^c_{13}, BL^c_{14}, BL^c_{23}, BL^c_{24}, and BL^c_{34}, respectively.

A.3 Elements of the V2PM

The procedures mentioned above are followed, filling all the elements of a 23×16 V2PM, which is shown in Fig. A.6. The pseudoinverse[viii] of the V2PM, which is the P2VM is calculated

[vii] Γ_{ij} in Eq. (2.14).

[viii] Also known as Moore-Penrose inverse.

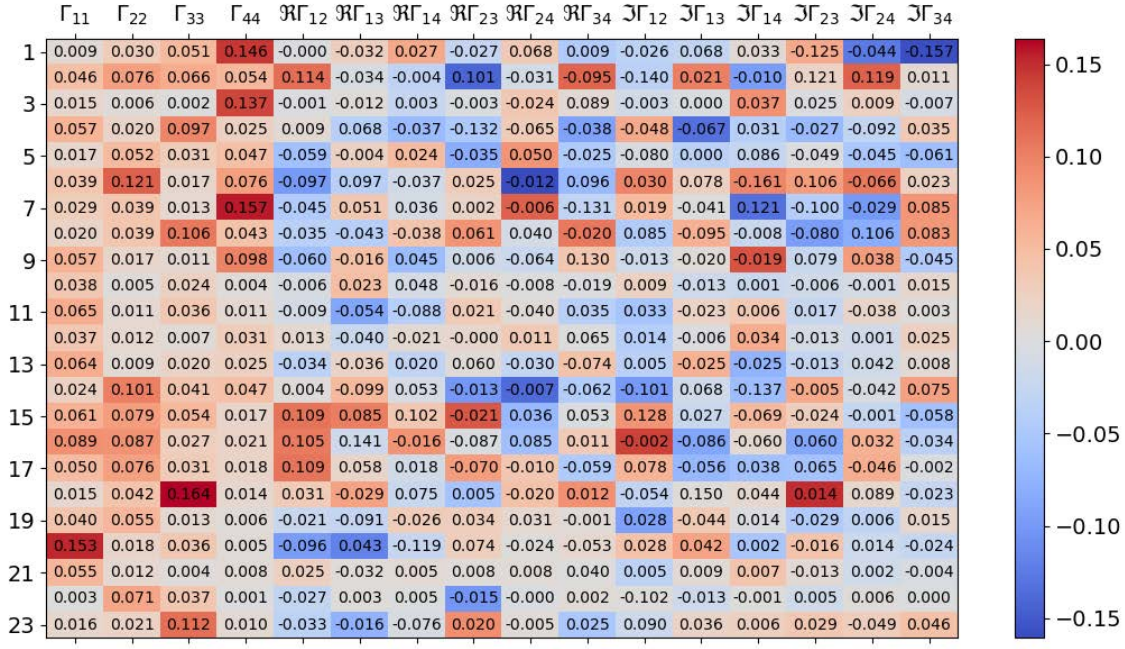

Figure A.6: The elements of a 23×16 V2PM. This was the V2PM that was used to obtain the visibilities of Fig. 6.15 and Fig. 6.16 in Section 6.4.

and applied to the $\vec{P}^{\text{ix}}$ of 23 output WGs for 6 of the *BLpq* data set. *pq* in *BLpq* refers to pairwise combination when both the beams are present at input numbered p and q without any photometric correction of Step III. The corresponding rows of the matrix, $\{P2VM.\vec{P}\}$ are extracted and using Eq. (2.20), the visibilities of Fig. 6.15 and Fig. 6.16 in Section 6.4 are produced. It is to be noted that the elements of the V2PM can be filled in any order, but one should make sure that the consistency is being followed while extracting the corresponding rows of the $\vec{J}$ from the matrix $\{P2VM.\vec{P}\}$. Thus, the DBC encodes the fringes matricially (see Section 1.4.4). Once the transfer matrix or V2PM of the optical system is known, it allows for the simultaneous extraction of visibilities without any scanning element.[x]

[ix] Power vectors from Eq. (2.13).

[x] Scanning element refers to any optical component that introduces a phase delay.

References

[1] M. A. Johnson, A. L. Betz, and C. H. Townes. 10-μm heterodyne stellar interferometer. *Phys. Rev. Lett.*, 33:1617–1620, Dec 1974.

[2] Abani Shankar Nayak, Thomas Poletti, Tarun Kumar Sharma, Kalaga Madhav, Ettore Pedretti, Lucas Labadie, and Martin M. Roth. Chromatic response of a four-telescope integrated-optics discrete beam combiner at the astronomical l band. *Opt. Express*, 28(23):34346–34361, Nov 2020.

[3] Abani Shankar Nayak, Lucas Labadie, Tarun Kumar Sharma, Simone Piacentini, Giacomo Corrielli, Roberto Osellame, Éric Gendron, Jean-Tristan M. Buey, Fanny Chemla, Mathieu Cohen, Nazim A. Bharmal, Lisa F. Bardou, Lazar Staykov, James Osborn, Timothy J. Morris, Ettore Pedretti, Aline N. Dinkelaker, Kalaga V. Madhav, and Martin M. Roth. First stellar photons for an integrated optics discrete beam combiner at the william herschel telescope. *Appl. Opt.*, 60(19):D129–D142, Jul 2021.

[4] Peter Lawson. *Principles of long baseline stellar interferometry*. JPL, 2000.

[5] Andreas Glindemann. *Principles of stellar interferometry*. Springer Science & Business Media, 2011.

[6] VLTI facility photograph. `https://commons.wikimedia.org/wiki/File:Paranal_and_the_Pacific_at_sunset_(dsc4088,_retouched,_cropped).jpg`.

[7] A Quirrenbach, D Mozurkewich, DF Buscher, CA Hummel, and JT Armstrong. Angular diameter and limb darkening of arcturus. *Astronomy and Astrophysics*, 312:160–166, 1996.

[8] P. G. Tuthill, W. C. Danchi, D. S. Hale, J. D. Monnier, and C. H. Townes. Near- and mid-infrared subarcsecond structure of the dusty symbiotic star r aquarii. *The Astrophysical Journal*, 534(2):907–914, may 2000.

[9] M. Zhao, D. Gies, J. D. Monnier, N. Thureau, E. Pedretti, F. Baron, A. Merand, T. ten Brummelaar, H. McAlister, S. T. Ridgway, N. Turner, J. Sturmann, L. Sturmann, C. Farrington, and P. J. Goldfinger. First resolved images of the eclipsing and interacting binary β lyrae. *The Astrophysical Journal*, 684(2):L95–L98, aug 2008.

[10] Lena Murchikova. S0-2 star, g1- and g2-objects, and flaring activity of the milky way's galactic center black hole in 2019. *The Astrophysical Journal Letters*, 910(1):L1, mar 2021.

[11] GRAVITY Collaboration, Abuter, R., Amorim, A., Anugu, N., Bauböck, M., Benisty, M., Berger, J. P., Blind, N., Bonnet, H., Brandner, W., Buron, A., Collin, C., Chapron, F., Clénet, Y., dCoudé u Foresto, V., de Zeeuw, P. T., Deen, C., Delplancke-Ströbele, F., Dembet, R., Dexter, J., Duvert, G., Eckart, A., Eisenhauer, F., Finger, G., Förster Schreiber, N. M., Fédou, P., Garcia, P., Garcia Lopez, R., Gao, F., Gendron, E., Genzel, R., Gillessen, S., Gordo, P., Habibi, M., Haubois, X., Haug, M., Haußmann, F., Henning, Th., Hippler, S., Horrobin, M., Hubert, Z., Hubin, N., Jimenez Rosales, A., Jochum, L., Jocou, L., Kaufer, A., Kellner, S., Kendrew, S., Kervella, P., Kok, Y., Kulas, M., Lacour, S., Lapeyrère, V., Lazareff, B., Le Bouquin, J.-B., Léna, P., Lippa, M., Lenzen, R., Mérand, A., Müler, E., Neumann, U., Ott, T., Palanca, L., Paumard, T., Pasquini, L., Perraut, K., Perrin, G., Pfuhl, O., Plewa, P. M., Rabien, S., Ramírez, A., Ramos, J., Rau, C., Rodríguez-Coira, G., Rohloff, R.-R., Rousset, G., Sanchez-Bermudez, J., Scheithauer, S., Schöller, M., Schuler, N., Spyromilio, J., Straub, O., Straubmeier, C., Sturm, E., Tacconi, L. J., Tristram, K. R. W., Vincent, F., von Fellenberg, S., Wank, I., Waisberg, I., Widmann, F., Wieprecht, E., Wiest, M., Wiezorrek, E., Woillez, J., Yazici, S., Ziegler, D., and Zins, G. Detection of the gravitational redshift in the orbit of the star s2 near the galactic centre massive black hole. *A&A*, 615:L15, 2018.

[12] GRAVITY Collaboration, Abuter, R., Accardo, M., Amorim, A., Anugu, N., Ávila, G., Azouaoui, N., Benisty, M., Berger, J. P., Blind, N., Bonnet, H., Bourget, P., Brandner, W., Brast, R., Buron, A., Burtscher, L., Cassaing, F., Chapron, F., Choquet, É., Clénet, Y., Collin, C., Coudé du Foresto, V., de Wit, W., de Zeeuw, P. T., Deen, C., Delplancke-Ströbele, F., Dembet, R., Derie, F., Dexter, J., Duvert, G., Ebert, M., Eckart, A., Eisenhauer, F., Esselborn, M., Fédou, P., Finger, G., Garcia, P., Garcia Dabo, C. E., Garcia Lopez, R., Gendron, E., Genzel, R., Gillessen, S., Gonte, F., Gordo, P., Grould, M., Grözinger, U., Guieu, S., Haguenauer, P., Hans, O., Haubois, X., Haug, M., Haussmann, F., Henning, Th., Hippler, S., Horrobin, M., Huber, A., Hubert, Z., Hubin, N., Hummel, C. A., Jakob, G., Janssen, A., Jochum, L., Jocou, L., Kaufer, A., Kellner, S., Kendrew, S., Kern, L., Kervella, P., Kiekebusch, M., Klein, R., Kok, Y., Kolb, J., Kulas, M., Lacour, S., Lapeyrère, V., Lazareff, B., Le Bouquin, J.-B., Lèna, P., Lenzen, R., Lévêque, S., Lippa, M., Magnard, Y., Mehrgan, L., Mellein, M., Mérand, A., Moreno-Ventas, J., Moulin, T., Müller, E., Müller, F., Neumann, U., Oberti, S., Ott, T., Pallanca, L., Panduro, J., Pasquini, L., Paumard, T., Percheron, I., Perraut, K., Perrin, G., Pflüger, A., Pfuhl, O., Phan Duc, T., Plewa, P. M., Popovic, D., Rabien, S., Ramírez, A., Ramos, J., Rau, C., Riquelme, M., Rohloff, R.-R., Rousset, G., Sanchez-Bermudez, J., Scheithauer, S., Schöller, M., Schuhler, N., Spyromilio, J., Straubmeier, C., Sturm, E., Suarez, M., Tristram, K. R. W., Ventura, N., Vincent, F., Waisberg, I., Wank, I., Weber, J., Wieprecht, E., Wiest, M., Wiezorrek, E., Wittkowski, M., Woillez, J., Wolff, B., Yazici, S., Ziegler, D., and Zins, G. First light for gravity: Phase referencing optical interferometry for the

very large telescope interferometer. *A&A*, 602:A94, 2017.

[13] P. G. Tuthill, J. D. Monnier, W. C. Danchi, E. H. Wishnow, and C. A. Haniff. Michelson interferometry with the keck i telescope. *Publications of the Astronomical Society of the Pacific*, 112(770):555–565, apr 2000.

[14] Primary mirror of the JWST. `https://www.nasa.gov/press-release/nasa-to-provide-update-on-james-webb-space-telescope`.

[15] A prototype of the non-redundant mask used in the JWST. `https://jwst-docs.stsci.edu/jwst-near-infrared-imager-and-slitless-spectrograph/niriss-observing-modes/niriss-aperture-masking-interferometry`.

[16] G. Perrin, S. Lacour, J. Woillez, and É. Thiébaut. High dynamic range imaging by pupil single-mode filtering and remapping. *Monthly Notices of the Royal Astronomical Society*, 373(2):747–751, 10 2006.

[17] TA Ten Brummelaar, J Sturmann, ST Ridgway, L Sturmann, NH Turner, HA McAlister, CD Farrington, U Beckmann, G Weigelt, and M Shure. The CLASSIC/CLIMB beam combiner at the CHARA array. *Journal of Astronomical Instrumentation*, 2(02):1340004, 2013.

[18] Max Born and Emil Wolf. *Principles of optics: electromagnetic theory of propagation, interference and diffraction of light*. Elsevier, 2013.

[19] Chris Haniff. An introduction to the theory of interferometry. *New Astronomy Reviews*, 51(8-9):565–575, 2007.

[20] Albert Abraham Michelson. On the application of interference methods to astronomical measurements. *The Astrophysical Journal*, 51:257, 1920.

[21] Eugene Hecht. *Optics*. Addison Wesley, 2002.

[22] Albert A Michelson and Francis G Pease. Measurement of the diameter of alpha-orionis by the interferometer. *Proceedings of the National Academy of Sciences of the United States of America*, 7(5):143, 1921.

[23] V. Coudé du Foresto, Ridgway, S., and Mariotti, J.-M. Deriving object visibilities from interferograms obtained with a fiber stellar interferometer. *Astron. Astrophys. Suppl. Ser.*, 121(2):379–392, 1997.

[24] S. Lacour and G. Perrin. Remapping the pupil. In John C. Mather, Howard A. MacEwen, and Mattheus W. M. de Graauw, editors, *Space Telescopes and Instrumentation I: Optical, Infrared, and Millimeter*, volume 6265, pages 825 – 829. International Society for Optics and Photonics, SPIE, 2006.

[25] A Labeyrie. Attainment of diffraction limited resolution in large telescopes by fourier analysing speckle patterns in star images. *Astronomy and Astrophysics*, 6:85, 1970.

[26] VLTI facility. `https://www.eso.org/sci/facilities/paranal/telescopes/vlti.html`.

[27] A Richard Thompson, James M Moran, and George W Swenson. *Interferometry and synthesis in radio astronomy*. Springer Nature, 2017.

[28] S. Gillessen, F. Eisenhauer, G. Perrin, W. Brandner, C. Straubmeier, K. Perraut, A. Amorim, M. Schöller, C. Araujo-Hauck, H. Bartko, H. Baumeister, J.-P. Berger, P. Carvas, F. Cassaing, F. Chapron, E. Choquet, Y. Clenet, C. Collin, A. Eckart, P. Fedou, S. Fischer, E. Gendron, R. Genzel, P. Gitton, F. Gonte, A. Gräter, P. Haguenauer, M. Haug, X. Haubois, T. Henning, S. Hippler, R. Hofmann, L. Jocou, S. Kellner, P. Kervella, R. Klein, N. Kudryavtseva, S. Lacour, V. Lapeyrere, W. Laun, P. Lena, R. Lenzen, J. Lima, D. Moratschke, D. Moch, T. Moulin, V. Naranjo, U. Neumann, A. Nolot, T. Paumard, O. Pfuhl, S. Rabien, J. Ramos, J. M. Rees, R.-R. Rohloff, D. Rouan, G. Rousset, A. Sevin, M. Thiel, K. Wagner, M. Wiest, S. Yazici, and D. Ziegler. GRAVITY: a four telescope beam combiner instrument for the VLTI. In William C. Danchi, Françoise Delplancke, and Jayadev K. Rajagopal, editors, *Optical and Infrared Interferometry II*, volume 7734, pages 318 – 337. International Society for Optics and Photonics, SPIE, 2010.

[29] Le Bouquin, J.-B., Berger, J.-P., Lazareff, B., Zins, G., Haguenauer, P., Jocou, L., Kern, P., Millan-Gabet, R., Traub, W., Absil, O., Augereau, J.-C., Benisty, M., Blind, N., Bonfils, X., Bourget, P., Delboulbe, A., Feautrier, P., Germain, M., Gitton, P., Gillier, D., Kiekebusch, M., Kluska, J., Knudstrup, J., Labeye, P., Lizon, J.-L., Monin, J.-L., Magnard, Y., Malbet, F., Maurel, D., Ménard, F., Micallef, M., Michaud, L., Montagnier, G., Morel, S., Moulin, T., Perraut, K., Popovic, D., Rabou, P., Rochat, S., Rojas, C., Roussel, F., Roux, A., Stadler, E., Stefl, S., Tatulli, E., and Ventura, N. Pionier: a 4-telescope visitor instrument at vlti. *A&A*, 535:A67, 2011.

[30] Peter Tuthill, Nemanja Jovanovic, Sylvestre Lacour, Andrew Lehmann, Martin Ams, Graham Marshall, Jon Lawrence, Michael Withford, Gordon Robertson, Michael Ireland, Benjamin Pope, and Paul Stewart. Photonic technologies for a pupil remapping interferometer. In William C. Danchi, Françoise Delplancke, and Jayadev K. Rajagopal, editors, *Optical and Infrared Interferometry II*, volume 7734, pages 596 – 604. International Society for Optics and Photonics, SPIE, 2010.

[31] NPOI facility. `https://lowell.edu/research/telescopes-and-facilities/npoi/`.

[32] J. T. Armstrong, H. R. Schmitt, D. Mozurkewich, A. M. Jorgensen, M. W. Muterspaugh, E. K. Baines, J. A. Benson, Robert T. Zavala, and D. J. Hutter. Multi-baseline bootstrapping at the Navy precision optical interferometer. In Jayadev K. Rajagopal, Michelle J. Creech-Eakman, and Fabien Malbet, editors, *Optical and Infrared Interferometry IV*, volume 9146, pages 181 – 185. International Society for Optics and Photonics, SPIE, 2014.

[33] François Roddier. Redundant versus nonredundant beam recombination in an aperture synthesis with coherent optical arrays. *J. Opt. Soc. Am. A*, 4(8):1396–1401, Aug 1987.

[34] R. C. Jennison. A Phase Sensitive Interferometer Technique for the Measurement of the Fourier Transforms of Spatial Brightness Distributions of Small Angular Extent. *Monthly Notices of the Royal Astronomical Society*, 118(3):276–284, 06 1958.

[35] D. H. Rogstad. A technique for measuring visibility phase with an optical interferometer in the presence of atmospheric seeing. *Appl. Opt.*, 7(4):585–588, Apr 1968.

[36] Christopher A Haniff, CD Mackay, David J Titterington, D Sivia, JE Baldwin, and PJ Warner. The first images from optical aperture synthesis. *Nature*, 328(6132):694–696, 1987.

[37] ACS Readhead, TS Nakajima, TJ Pearson, G Neugebauer, JB Oke, and WLW Sargent. Diffraction-limited imaging with ground-based optical telescopes. *Astronomical Journal*, 95(4):1278–1296, 1988.

[38] CHARA facility. `http://www.chara.gsu.edu/`.

[39] Distance measurement in astronomy. `https://starchild.gsfc.nasa.gov/docs/StarChild/questions/question39.html`.

[40] Theo Ten Brummelaar, Michelle Creech-Eakman, and John Monnier. Probing stars with optical and near-ir interferometry. *Phys. Today*, 62(6):28–33, 2009.

[41] Wittkowski, M., Kervella, P., Arsenault, R., Paresce, F., Beckert, T., and Weigelt, G. Vlti/vinci observations of the nucleus of ngc 1068 using the adaptive optics system macao *. *A&A*, 418(3):L39–L42, 2004.

[42] John D Monnier. Optical interferometry in astronomy. *Reports on Progress in Physics*, 66(5):789–857, apr 2003.

[43] D. H. Berger, D. R. Gies, H. A. McAlister, T. A. ten Brummelaar, T. J. Henry, J. Sturmann, L. Sturmann, N. H. Turner, S. T. Ridgway, J. P. Aufdenberg, and A. Merand. First results from the CHARA array. IV. the interferometric radii of low-mass stars. *The Astrophysical Journal*, 644(1):475–483, jun 2006.

[44] Andrew W. Mann, Gregory A. Feiden, Eric Gaidos, Tabetha Boyajian, and Kaspar von Braun. How to constrain your M dwarf: measuring effective temperature, bolometric luminosity, mass, and radius. *The Astrophysical Journal*, 804(1):64, may 2015.

[45] D. Burns, J. E. Baldwin, R. C. Boysen, C. A. Haniff, P. R. Lawson, C. D. Mackay, J. Rogers, T. R. Scott, D. St.-Jacques, P. J. Warner, D. M. A. Wilson, and J. S. Young. Large-amplitude periodic variations in the angular diameter of R Leonis. *Monthly Notices of the Royal Astronomical Society*, 297(2):462–466, 06 1998.

[46] Montargès, M., Kervella, P., Perrin, G., Chiavassa, A., Le Bouquin, J.-B., Aurière, M., López Ariste, A., Mathias, P., Ridgway, S. T., Lacour, S., Haubois, X., and Berger, J.-P. The close circumstellar environment of betelgeuse - iv. vlti/pionier interferometric monitoring of the photosphere. *A&A*, 588:A130, 2016.

[47] J. S. Young, J. E. Baldwin, R. C. Boysen, C. A. Haniff, P. R. Lawson, C. D. Mackay, D. Pearson, J. Rogers, D. St.-Jacques, P. J. Warner, D. M. A. Wilson, and R. W. Wilson. New views of Betelgeuse: multi-wavelength surface imaging and implications for models of hotspot generation. *Monthly Notices of the Royal Astronomical Society*, 315(3):635–645, 07 2000.

[48] Rachael M Roettenbacher, John D Monnier, Heidi Korhonen, Alicia N Aarnio, Fabien Baron, Xiao Che, Robert O Harmon, Zs Kővári, Stefan Kraus, Gail H Schaefer, et al. No sun-like dynamo on the active star ζ andromedae from starspot asymmetry. *Nature*, 533(7602):217–220, 2016.

[49] Netolický, M., Bonneau, D., Chesneau, O., Harmanec, P., Koubský, P., Mourard, D., and Stee, P. The circumbinary dusty disk around the hydrogen-deficient binary star ν sagittarii. *A&A*, 499(3):827–833, 2009.

[50] Be star information. `https://www.oca.eu/fr/philippe-stee-research/1270-be-stars-stee`.

[51] C Thom, P Granes, and F Vakili. Optical interferometric measurements of gamma cassiopeiae's envelope in the h-alpha line. *Astronomy and Astrophysics*, 165:L13–L15, 1986.

[52] Antoine Labeyrie. Interference fringes obtained on vega with two optical telescopes. *The Astrophysical Journal*, 196:L71–L75, 1975.

[53] F Vakili, D Mourard, Ph Stee, D Bonneau, P Berio, O Chesneau, N Thureau, F Morand, A Labeyrie, and I Tallon-Bosc. Evidence for one-armed oscillations in the equatorial disk of zeta tauri from gi2t spectrally resolved interferometry. *Astronomy and Astrophysics*, 335:261–265, 1998.

[54] Meilland, A., Stee, Ph., Zorec, J., and Kanaan, S. Be stars: one ring to rule them all? *A&A*, 455(3):953–961, 2006.

[55] Young Stellar Object information. `http://www.reinervogel.net/index_e.html?/YSO/YSO_e.html`.

[56] R. Millan-Gabet, F. P. Schloerb, W. A. Traub, F. Malbet, J. P. Berger, and J. D. Bregman. Sub–astronomical unit structure of the near-infrared emission from AB aurigae. *The Astrophysical Journal*, 513(2):L131–L134, mar 1999.

[57] RJHM van Boekel, M Min, Ch Leinert, LBFM Waters, A Richichi, O Chesneau, C Dominik, W Jaffe, Anne Dutrey, U Graser, et al. The building blocks of planets within the 'terrestrial'region of protoplanetary disks. *Nature*, 432(7016):479–482, 2004.

[58] Active Galactic Nuclei information. `https://webbtelescope.org/resource-gallery/articles/pagecontent/filter-articles/what-are-active-galactic-nuclei?filterUUID=a776e097-0c60-421c-baec-1d8ad049bfb0`.

[59] Weigelt, G., Hofmann, K.-H., Kishimoto, M., Hönig, S., Schertl, D., Marconi, A., Millour, F., Petrov, R., Fraix-Burnet, D., Malbet, F., Tristram, K., and Vannier, M. Vlti/amber observations of the seyfert nucleus of ngc 3783. *A&A*, 541:L9, 2012.

[60] Klaus Meisenheimer, David Raban, Konrad Tristram, Marc Schartmann, Walter Jaffe, Huub Röttgering, and Leonard Burtscher. Mid-infrared interferometry of active galactic nuclei: an outstanding scientific success of the vlti. *The ESO Messenger*, 133:36–41, 2008.

[61] Reinhard Genzel, Frank Eisenhauer, and Stefan Gillessen. The galactic center massive black hole and nuclear star cluster. *Rev. Mod. Phys.*, 82:3121–3195, Dec 2010.

[62] GRAVITY Collaboration, Abuter, R., Amorim, A., Bauböck, M., Berger, J. P., Bonnet, H., Brandner, W., Cardoso, V., Clénet, Y., de Zeeuw, P. T., Dexter, J., Eckart, A., Eisenhauer, F., Förster Schreiber, N. M., Garcia, P., Gao, F., Gendron, E., Genzel, R., Gillessen, S., Habibi, M., Haubois, X., Henning, T., Hippler, S., Horrobin, M., Jiménez-Rosales, A., Jochum, L., Jocou, L., Kaufer, A., Kervella, P., Lacour, S., Lapeyrère, V., Le Bouquin, J.-B., Léna, P., Nowak, M., Ott, T., Paumard, T., Perraut, K., Perrin, G., Pfuhl, O., Rodríguez-Coira, G., Shangguan, J., Scheithauer, S., Stadler, J., Straub, O., Straubmeier, C., Sturm, E., Tacconi, L. J., Vincent, F., von Fellenberg, S., Waisberg, I., Widmann, F., Wieprecht, E., Wiezorrek, E., Woillez, J., Yazici, S., and Zins, G. Detection of the schwarzschild precession in the orbit of the star s2 near the galactic centre massive black hole. *A&A*, 636:L5, 2020.

[63] GRAVITY Collaboration, Lacour, S., Nowak, M., Wang, J., Pfuhl, O., Eisenhauer, F., Abuter, R., Amorim, A., Anugu, N., Benisty, M., Berger, J. P., Beust, H., Blind, N., Bonnefoy, M., Bonnet, H., Bourget, P., Brandner, W., Buron, A., Collin, C., Charnay, B., Chapron, F., Clénet, Y., Coudé du Foresto, V., de Zeeuw, P. T., Deen, C., Dembet, R., Dexter, J., Duvert, G., Eckart, A., Förster Schreiber, N. M., Fédou, P., Garcia, P., Garcia Lopez, R., Gao, F., Gendron, E., Genzel, R., Gillessen, S., Gordo, P., Greenbaum, A., Habibi, M., Haubois, X., Haußmann, F., Henning, Th., Hippler, S., Horrobin, M., Hubert, Z., Jimenez Rosales, A., Jocou, L., Kendrew, S., Kervella, P., Kolb, J., Lagrange, A.-M., Lapeyrère, V., Le Bouquin, J.-B., Léna, P., Lippa, M., Lenzen, R., Maire, A.-L., Mollière, P., Ott, T., Paumard, T., Perraut, K., Perrin, G., Pueyo, L., Rabien, S., Ramírez, A., Rau, C., Rodríguez-Coira, G., Rousset, G., Sanchez-Bermudez, J., Scheithauer, S., Schuhler, N., Straub, O., Straubmeier, C., Sturm, E., Tacconi, L. J., Vincent, F., van Dishoeck, E. F., von Fellenberg, S., Wank, I., Waisberg, I., Widmann, F., Wieprecht, E., Wiest, M., Wiezorrek, E., Woillez, J., Yazici, S., Ziegler, D., and Zins, G. First direct detection of an exoplanet by optical interferometry - astrometry and k-band spectroscopy of hr 8799 e. *A&A*, 623:L11, 2019.

[64] Étienne Artigau, Anand Sivaramakrishnan, Alexandra Z. Greenbaum, René Doyon, Paul Goudfrooij, Alex W. Fullerton, David Lafrenière, Kevin Volk, Loïc Albert, André Martel, K. E. Saavik Ford, and Barry L. McKernan. NIRISS aperture masking interferometry: an overview of science opportunities. In Jacobus M. Oschmann Jr., Mark Clampin, Giovanni G. Fazio, and Howard A. MacEwen, editors, *Space Telescopes and Instrumentation 2014: Optical, Infrared, and Millimeter Wave*, volume 9143, pages 1185 – 1194. International Society for Optics and Photonics, SPIE, 2014.

[65] Vincent Coudé du Foresto, Guy Perrin, Jean-Marie Mariotti, Marc Lacasse, and Wes Traub. The fluor/iota fiber stellar interferometer. *Integrated Optics for Astronomical Interferometry*, page 115, 1997.

[66] Joss Bland-Hawthorn and Pierre Kern. Astrophotonics: a new era for astronomical instruments. *Optics express*, 17(3):1880–1884, 2009.

[67] Robert R Thomson, Ajoy K Kar, and Jeremy Allington-Smith. Ultrafast laser inscription: an enabling technology for astrophotonics. *Optics express*, 17(3):1963–1969, 2009.

[68] Peter Tuthill, James Lloyd, Michael Ireland, Frantz Martinache, John Monnier, Henry Woodruff, Theo ten Brummelaar, Nils Turner, and Charles Townes. Sparse-aperture adaptive optics. In Brent L. Ellerbroek and Domenico Bonaccini Calia, editors, *Advances in Adaptive Optics II*, volume 6272, pages 1064 – 1073. International Society for Optics and Photonics, SPIE, 2006.

[69] Francoise Delplancke, Samuel A. Leveque, Pierre Kervella, Andreas Glindemann, and Luigi D'Arcio. Phase-referenced imaging and micro-arcsecond astrometry with the VLTI. In Pierre J. Lena and Andreas Quirrenbach, editors, *Interferometry in Optical Astronomy*, volume 4006, pages 365 – 376. International Society for Optics and Photonics, SPIE, 2000.

[70] WT Rhodes and JW Goodman. Interferometric technique for recording and restoring images degraded by unknown aberrations. *JOSA*, 63(6):647–657, 1973.

[71] JE Baldwin, Christopher A Haniff, CD Mackay, and PJ Warner. Closure phase in high-resolution optical imaging. *Nature*, 320(6063):595–597, 1986.

[72] K-H Hofmann and G Weigelt. Speckle masking observation of the central object in the giant h ii region ngc 3603. *Astronomy and Astrophysics*, 167:L15, 1986.

[73] John D. Monnier, Rafael Millan-Gabet, Peter G. Tuthill, Wesley A. Traub, Nathaniel P. Carleton, Vincent Coude du Foresto, William C. Danchi, Marc G. Lacasse, Sebastien Morel, Guy S. Perrin, and Irene L. Porro. Aperture synthesis using multiple facilities: Keck aperture masking and the IOTA interferometer. In Wesley A. Traub, editor, *Interferometry for Optical Astronomy II*, volume 4838, pages 379 – 386. International Society for Optics and Photonics, SPIE, 2003.

[74] H. C. Woodruff, P. G. Tuthill, J. D. Monnier, M. J. Ireland, T. R. Bedding, S. Lacour, W. C. Danchi, and M. Scholz. The keck aperture masking experiment: Multiwavelength observations of six mira variables. *The Astrophysical Journal*, 673(1):418–433, jan 2008.

[75] H. C. Woodruff, M. J. Ireland, P. G. Tuthill, J. D. Monnier, T. R. Bedding, W. C. Danchi, M. Scholz, C. H. Townes, and P. R. Wood. THE KECK APERTURE MASKING EXPERIMENT: SPECTRO-INTERFEROMETRY OF THREE MIRA VARIABLES FROM 1.1 TO 3.8 μm. *The Astrophysical Journal*, 691(2):1328–1336, feb 2009.

[76] J. D. Monnier, R. Millan-Gabet, P. G. Tuthill, W. A. Traub, N. P. Carleton, V. Coude du Foresto, W. C. Danchi, M. G. Lacasse, S. Morel, G. Perrin, I. L. Porro, F. P. Schloerb, and C. H. Townes. High-resolution imaging of dust shells by using keck aperture masking and the IOTA interferometer. *The Astrophysical Journal*, 605(1):436–461, apr 2004.

[77] Anand Sivaramakrishnan, David Lafrenière, K. E. Saavik Ford, Barry McKernan, Anthony Cheetham, Alexandra Z. Greenbaum, Peter G. Tuthill, James P. Lloyd, Michael J. Ireland, René Doyon, Mathilde Beaulieu, André Martel, Anton Koekemoer, Frantz Martinache, and Peter Teuben. Non-redundant Aperture Masking Interferometry (AMI) and segment phasing with JWST-NIRISS. In Mark C. Clampin, Giovanni G. Fazio,

Howard A. MacEwen, and Jacobus M. Oschmann Jr., editors, *Space Telescopes and Instrumentation 2012: Optical, Infrared, and Millimeter Wave*, volume 8442, pages 1018 – 1031. International Society for Optics and Photonics, SPIE, 2012.

[78] Pierre Kern, Fabien Malbet, Isabelle Schanen-Duport, and Pierre Benech. Integrated optics single-mode interferometric beam combiner for near infrared astronomy. *Integrated Optics for Astronomical Interferometry*, page 115, 1997.

[79] Mark P. J. L. Chang and David F. Buscher. Monomode fiber interferometer for single telescopes. In Robert D. Reasenberg, editor, *Astronomical Interferometry*, volume 3350, pages 2 – 13. International Society for Optics and Photonics, SPIE, 1998.

[80] AJOY AUTOR GHATAK, Ajoy Ghatak, K Thyagarajan, and K Thyagarajan. *An introduction to fiber optics*. Cambridge university press, 1998.

[81] Vincent Coude du Foresto, Guy S. Perrin, Cyril Ruilier, Bertrand P. Mennesson, Wesley A. Traub, and Marc G. Lacasse. FLUOR fibered instrument at the IOTA interferometer. In Robert D. Reasenberg, editor, *Astronomical Interferometry*, volume 3350, pages 856 – 863. International Society for Optics and Photonics, SPIE, 1998.

[82] S. Lacour, E. Thiébaut, and G. Perrin. High dynamic range imaging with a single-mode pupil remapping system: a self-calibration algorithm for redundant interferometric arrays. *Monthly Notices of the Royal Astronomical Society*, 374(3):832–846, 12 2006.

[83] T. Kotani, S. Lacour, G. Perrin, G. Robertson, and P. Tuthill. Pupil remapping for high contrast astronomy: results from an optical testbed. *Opt. Express*, 17(3):1925–1934, Feb 2009.

[84] Mark Peter Joe-Ling Chang. *DAFI: a single mode optical fibre interferometer for astronomy*. PhD thesis, Durham University, 1998.

[85] Huby, E., Perrin, G., Marchis, F., Lacour, S., Kotani, T., Duchêne, G., Choquet, E., Gates, E. L., Woillez, J. M., Lai, O., Fédou, P., Collin, C., Chapron, F., Arslanyan, V., and Burns, K. J. First, a fibered aperture masking instrument - i. first on-sky test results. *A&A*, 541:A55, 2012.

[86] Huby, E., Duchêne, G., Marchis, F., Lacour, S., Perrin, G., Kotani, T., Choquet, É., Gates, E. L., Lai, O., and Allard, F. First, a fibered aperture masking instrument - ii. spectroscopy of the capella binary system at the diffraction limit. *A&A*, 560:A113, 2013.

[87] N. Jovanovic, P. G. Tuthill, B. Norris, S. Gross, P. Stewart, N. Charles, S. Lacour, M. Ams, J. S. Lawrence, A. Lehmann, C. Niel, J. G. Robertson, G. D. Marshall, M. Ireland, A. Fuerbach, and M. J. Withford. Starlight demonstration of the Dragonfly instru-

ment: an integrated photonic pupil-remapping interferometer for high-contrast imaging. *Monthly Notices of the Royal Astronomical Society*, 427(1):806–815, 11 2012.

[88] Barnaby Norris, Nick Cvetojevic, Simon Gross, Nemanja Jovanovic, Paul N. Stewart, Ned Charles, Jon S. Lawrence, Michael J. Withford, and Peter Tuthill. High-performance 3d waveguide architecture for astronomical pupil-remapping interferometry. *Opt. Express*, 22(15):18335–18353, Jul 2014.

[89] Ronald N Bracewell. Detecting nonsolar planets by spinning infrared interferometer. *Nature*, 274(5673):780–781, 1978.

[90] Barnaby R M Norris, Nick Cvetojevic, Tiphaine Lagadec, Nemanja Jovanovic, Simon Gross, Alexander Arriola, Thomas Gretzinger, Marc-Antoine Martinod, Olivier Guyon, Julien Lozi, Michael J Withford, Jon S Lawrence, and Peter Tuthill. First on-sky demonstration of an integrated-photonic nulling interferometer: the GLINT instrument. *Monthly Notices of the Royal Astronomical Society*, 491(3):4180–4193, 11 2019.

[91] Nick Cvetojevic, Barnaby R. M. Norris, Simon Gross, Nemanja Jovanovic, Alexander Arriola, Sylvestre Lacour, Takayuki Kotani, Jon S. Lawrence, Michael J. Withford, and Peter Tuthill. Building hybridized 28-baseline pupil-remapping photonic interferometers for future high-resolution imaging. *Appl. Opt.*, 60(19):D33–D42, Jul 2021.

[92] Berger, J. P., Rousselet-Perraut, K., Kern, P., Malbet, F., Schanen-Duport, I., Reynaud, F., Haguenauer, P., and Benech, P. Integrated optics for astronomical interferometry - ii. first laboratory white-light interferograms. *Astron. Astrophys. Suppl. Ser.*, 139(1):173–177, 1999.

[93] LeBouquin, J. B., Rousselet-Perraut, K., Kern, P., Malbet, F., Haguenauer, P., Kervella, P., Schanen, I., Berger, J. P., Delboulbé, A., Arezki, B., and Schöller, M. First observations with an h-band integrated optics beam combiner at the vlti*. *A&A*, 424(2):719–726, 2004.

[94] Jean-Philippe Berger, Pierre Haguenauer, Pierre Y. Kern, Karine Rousselet-Perraut, Fabien Malbet, Stephane Gluck, Laure Lagny, Isabelle Schanen-Duport, Emmanuel Laurent, Alain Delboulbe, Eric Tatulli, Wesley A. Traub, Nathaniel Carleton, Rafael Millan-Gabet, John D. Monnier, Ettore Pedretti, and S. Ragland. Integrated-optics 3-way beam combiner for IOTA. In Wesley A. Traub, editor, *Interferometry for Optical Astronomy II*, volume 4838, pages 1099 – 1106. International Society for Optics and Photonics, SPIE, 2003.

[95] S. Kraus, F. P. Schloerb, W. A. Traub, N. P. Carleton, M. Lacasse, M. Pearlman, J. D. Monnier, R. Millan-Gabet, J.-P. Berger, P. Haguenauer, K. Perraut, P. Kern, F. Malbet,

and P. Labeye. Infrared imaging of capella with the IOTA closure phase interferometer. *The Astronomical Journal*, 130(1):246–255, jul 2005.

[96] J. D. Monnier, J.-P. Berger, R. Millan-Gabet, W. A. Traub, F. P. Schloerb, E. Pedretti, M. Benisty, N. P. Carleton, P. Haguenauer, P. Kern, P. Labeye, M. G. Lacasse, F. Malbet, K. Perraut, M. Pearlman, and M. Zhao. Few skewed disks found in first closure-phase survey of herbig ae/be stars. *The Astrophysical Journal*, 647(1):444–463, aug 2006.

[97] Benisty, M., Berger, J.-P., Jocou, L., Labeye, P., Malbet, F., Perraut, K., and Kern, P. An integrated optics beam combiner for the second generation vlti instruments. *A&A*, 498(2):601–613, 2009.

[98] Jean-Baptiste J. B. LeBouquin, Jean-Philippe Berger, Pierre R. Labeye, Eric Tatulli, Fabien Malbet, Karine Rousselet-Perraut, and Pierre Y. Kern. Comparison of integrated optics concepts for a near-infrared multi-telescope beam combiner. In Wesley A. Traub, editor, *New Frontiers in Stellar Interferometry*, volume 5491, pages 1362 – 1369. International Society for Optics and Photonics, SPIE, 2004.

[99] Stefano Minardi, Sylvestre Lacour, Jean-Philippe Berger, Lucas Labadie, Robert R. Thomson, Chris Haniff, and Michael Ireland. Beam combination schemes and technologies for the Planet Formation Imager. In Fabien Malbet, Michelle J. Creech-Eakman, and Peter G. Tuthill, editors, *Optical and Infrared Interferometry and Imaging V*, volume 9907, pages 461 – 477. International Society for Optics and Photonics, SPIE, 2016.

[100] David J Richardson, John M Fini, and Lynn E Nelson. Space-division multiplexing in optical fibres. *Nature photonics*, 7(5):354–362, 2013.

[101] S Gross and MJ Withford. Ultrafast-laser-inscribed 3d integrated photonics: challenges and emerging applications. *Nanophotonics*, 4(3):332–352, 2015.

[102] Stefano Minardi and Thomas Pertsch. Interferometric beam combination with discrete optics. *Optics letters*, 35(18):3009–3011, 2010.

[103] Allar Saviauk, Stefano Minardi, Felix Dreisow, Stefan Nolte, and Thomas Pertsch. 3d-integrated optics component for astronomical spectro-interferometry. *Appl. Opt.*, 52(19):4556–4565, Jul 2013.

[104] Romina Diener, Jan Tepper, Lucas Labadie, Thomas Pertsch, Stefan Nolte, and Stefano Minardi. Towards 3d-photonic, multi-telescope beam combiners for mid-infrared astrointerferometry. *Optics express*, 25(16):19262–19274, 2017.

[105] E. Tatulli and J-B LeBouquin. Comparison of Fourier and model-based estimators in single-mode multi-axial interferometry. *Monthly Notices of the Royal Astronomical Society*, 368(3):1159–1168, 04 2006.

[106] Robert J. Harris, Jan Tepper, John J. Davenport, Ettore Pedretti, Dionne M. Haynes, Philipp Hottinger, Theodoros Anagnos, Abani Shankar Nayak, Yohana Herrero Alonso, Pranab Jyoti Deka, Stefano Minardi, Andreas Quirrenbach, Lucas Labadie, and Roger Haynes. NAIR: novel astronomical instrumentation through photonic reformatting. In Ramón Navarro and Roland Geyl, editors, *Advances in Optical and Mechanical Technologies for Telescopes and Instrumentation III*, volume 10706, pages 157 – 171. International Society for Optics and Photonics, SPIE, 2018.

[107] Robert J. Harris, Tarun Kumar Sharma, John J. Davenport, Philipp Hottinger, Theodoros Anagnos, Abani Shankar Nayak, Andreas Quirrenbach, Lucas Labadie, Kalaga V. Madhav, and Martin M. Roth. NAIR: Novel Astronomical Instrumentation through photonic Reformatting. In Ramón Navarro and Roland Geyl, editors, *Advances in Optical and Mechanical Technologies for Telescopes and Instrumentation IV*, volume 11451, pages 18 – 31. International Society for Optics and Photonics, SPIE, 2020.

[108] François Roddier. *Adaptive optics in astronomy*. Cambridge university, 1999.

[109] Ned Charles, Nemanja Jovanovic, Simon Gross, Paul Stewart, Barnaby Norris, John O'Byrne, Jon S. Lawrence, Michael J. Withford, and Peter G. Tuthill. Design of optically path-length-matched, three-dimensional photonic circuits comprising uniquely routed waveguides. *Appl. Opt.*, 51(27):6489–6497, Sep 2012.

[110] John H Mathews and Kurtis D Fink. *Numerical methods using MATLAB*. Prentice hall, 1999.

[111] Classroom notes on floquet-bloch theorem. `http://photonics.intec.ugent.be/download/ocs132.pdf`.

[112] Thomas Pertsch, Ulf Peschel, Falk Lederer, Jonas Burghoff, Matthias Will, Stefan Nolte, and Andreas Tünnermann. Discrete diffraction in two-dimensional arrays of coupled waveguides in silica. *Opt. Lett.*, 29(5):468–470, Mar 2004.

[113] Demetrios N Christodoulides, Falk Lederer, and Yaron Silberberg. Discretizing light behaviour in linear and nonlinear waveguide lattices. *Nature*, 424(6950):817–823, 2003.

[114] S. Minardi. Photonic lattices for astronomical interferometry. *Monthly Notices of the Royal Astronomical Society*, 422(3):2656–2660, 05 2012.

[115] Stefano Minardi. Nonlocality of coupling and the retrieval of field correlations with arrays of waveguides. *Phys. Rev. A*, 92:013804, Jul 2015.

[116] Ettore Pedretti, Romina Diener, Abani Shankar Nayak, Jan Tepper, Lucas Labadie, Thomas Pertsch, Stefan Nolte, and Stefano Minardi. Beam combination schemes and

technologies for the Planet Formation Imager. In Michelle J. Creech-Eakman, Peter G. Tuthill, and Antoine Mérand, editors, *Optical and Infrared Interferometry and Imaging VI*, volume 10701, pages 758 – 765. International Society for Optics and Photonics, SPIE, 2018.

[117] Ilse CF Ipsen. *Numerical matrix analysis: Linear systems and least squares*. SIAM, 2009.

[118] Abani Shankar Nayak, Simone Piacentini, Tarun Kumar Sharma, Giacomo Corrielli, Roberto Osellame, Lucas Labadie, Stefano Minardi, Ettore Pedretti, Kalaga Madhav, and Martin M. Roth. Integrated optics-interferometry using pupil remapping and beam combination at astronomical H-band. In Simon C. Ellis and Céline d'Orgeville, editors, *Advances in Optical Astronomical Instrumentation 2019*, volume 11203, pages 55 – 56. International Society for Optics and Photonics, SPIE, 2020.

[119] Bahaa EA Saleh and Malvin Carl Teich. *Fundamentals of photonics*. john Wiley & sons, 2019.

[120] J. Crank and P. Nicolson. A practical method for numerical evaluation of solutions of partial differential equations of the heat-conduction type. *Mathematical Proceedings of the Cambridge Philosophical Society*, 43(1):50–67, 1947.

[121] Momen Diab and Stefano Minardi. Modal analysis using photonic lanterns coupled to arrays of waveguides. *Optics letters*, 44(7):1718–1721, 2019.

[122] Kok Yeow You. *Emerging Waveguide Technology*. BoD–Books on Demand, 2018.

[123] Martijn J. R. Heck, Jared F. Bauters, Michael L. Davenport, Daryl T. Spencer, and John E. Bowers. Ultra-low loss waveguide platform and its integration with silicon photonics. *Laser & Photonics Reviews*, 8(5):667–686, 2014.

[124] Jan Tepper, Lucas Labadie, Simon Gross, Alexander Arriola, Stefano Minardi, Romina Diener, and Michael J Withford. Ultrafast laser inscription in zblan integrated optics chips for mid-ir beam combination in astronomical interferometry. *Optics express*, 25(17):20642–20653, 2017.

[125] SJ Ben Yoo, Binbin Guan, and Ryan P Scott. Heterogeneous 2d/3d photonic integrated microsystems. *Microsystems & Nanoengineering*, 2(1):1–9, 2016.

[126] Nicolás Sherwood-Droz and Michal Lipson. Scalable 3d dense integration of photonics on bulk silicon. *Opt. Express*, 19(18):17758–17765, Aug 2011.

[127] Shiyang Zhu and Guo-Qiang Lo. Vertically stacked multilayer photonics on bulk silicon toward three-dimensional integration. *Journal of Lightwave Technology*, 34(2):386–392, 2016.

[128] M. Weidenbach, D. Jahn, A. Rehn, S. F. Busch, F. Beltrán-Mejía, J. C. Balzer, and M. Koch. 3d printed dielectric rectangular waveguides, splitters and couplers for 120 ghz. *Opt. Express*, 24(25):28968–28976, Dec 2016.

[129] P Bollgruen, T Wolfer, U Gleissner, D Mager, C Megnin, L Overmeyer, T Hanemann, and J G Korvink. Ink-jet printed optical waveguides. *Flexible and Printed Electronics*, 2(4):045003, oct 2017.

[130] Jun Feng, Yijun Zheng, Shardul Bhusari, Maria Villiou, Samuel Pearson, and Aránzazu del Campo. Printed degradable optical waveguides for guiding light into tissue. *Advanced Functional Materials*, 30(45):2004327, 2020.

[131] Robert Infuehr, Niklas Pucher, Christian Heller, Helga Lichtenegger, Robert Liska, Volker Schmidt, Ladislav Kuna, Anja Haase, and Jürgen Stampfl. Functional polymers by two-photon 3d lithography. *Applied Surface Science*, 254(4):836–840, 2007. Laser synthesis and processing of advanced materials.

[132] Aleksandr Ovsianikov and Boris N. Chichkov. *Two-Photon Polymerization – High Resolution 3D Laser Technology and Its Applications*, pages 427–446. Springer New York, New York, NY, 2008.

[133] Matthias Blaicher, Muhammad Rodlin Billah, Juned Kemal, Tobias Hoose, Pablo Marin-Palomo, Andreas Hofmann, Yasar Kutuvantavida, Clemens Kieninger, Philipp-Immanuel Dietrich, Matthias Lauermann, et al. Hybrid multi-chip assembly of optical communication engines by in situ 3d nano-lithography. *Light: Science & Applications*, 9(1):1–11, 2020.

[134] Onur Tokel, Ahmet Turnalı, Ghaith Makey, Parviz Elahi, Tahir Çolakoğlu, Emre Ergeçen, Özgün Yavuz, René Hübner, Mona Zolfaghari Borra, Ihor Pavlov, et al. In-chip microstructures and photonic devices fabricated by nonlinear laser lithography deep inside silicon. *Nature photonics*, 11(10):639–645, 2017.

[135] Koji Sugioka and Ya Cheng. Ultrafast lasers—reliable tools for advanced materials processing. *Light: Science & Applications*, 3(4):e149–e149, 2014.

[136] Aurélien Benoît, Fraser A. Pike, Tarun K. Sharma, David G. MacLachlan, Aline N. Dinkelaker, Abani S. Nayak, Kalaga Madhav, Martin M. Roth, Lucas Labadie, Ettore Pedretti, Theo A. ten Brummelaar, Nic Scott, Vincent Coudé du Foresto, and Robert R. Thomson. Ultrafast laser inscription of asymmetric integrated waveguide 3 db couplers

for astronomical k-band interferometry at the chara array. *J. Opt. Soc. Am. B*, 38(9):2455–2464, Sep 2021.

[137] Fraser A. Pike, Tarun K. Sharma, Aurélien Benoît, David G. MacLachlan, Aline N. Dinkelaker, Abani S. Nayak, Kalaga Madhav, Martin M. Roth, Lucas Labadie, Ettore Pedretti, Theo A. ten Brummelaar, Nicholas J. Scott, Vincent Coudé du Foresto, and Robert R. Thomson. K-band integrated optics beam combiners for CHARA fabricated by ultrafast laser inscription. In Peter G. Tuthill, Antoine Mérand, and Stephanie Sallum, editors, *Optical and Infrared Interferometry and Imaging VII*, volume 11446, pages 118 – 123. International Society for Optics and Photonics, SPIE, 2020.

[138] Simone Piacentini, Giacomo Corrielli, Abani Shankar Nayak, Tarun Kumar Sharma, Kalaga V. Madhav, Ettore Pedretti, Stefano Minardi, Lucas Labadie, and Roberto Osellame. Integrated discrete beam combiner with a pupil remapper for stellar interferometry (Conference Presentation). In Yakov Soskind and Lynda E. Busse, editors, *Photonic Instrumentation Engineering VII*, volume 11287. International Society for Optics and Photonics, SPIE, 2020.

[139] S. Piacentini, G. Corrielli, A. S. Nayak, E. Pedretti, S. Minardi, and R. Osellame. Direct writing of 3d integrated photonic circuits for astrophotonics. In *2019 Conference on Lasers and Electro-Optics Europe European Quantum Electronics Conference (CLEO/Europe-EQEC)*, pages 1–1, 2019.

[140] Alexander Arriola, Simon Gross, Nemanja Jovanovic, Ned Charles, Peter G Tuthill, Santiago M Olaizola, Alexander Fuerbach, and Michael J Withford. Low bend loss waveguides enable compact, efficient 3d photonic chips. *Optics express*, 21(3):2978–2986, 2013.

[141] Giacomo Corrielli, Simone Atzeni, Simone Piacentini, Ioannis Pitsios, Andrea Crespi, and Roberto Osellame. Symmetric polarization-insensitive directional couplers fabricated by femtosecond laser writing. *Optics express*, 26(12):15101–15109, 2018.

[142] Simone Piacentini, Giacomo Corrielli, Abani Shankar Nayak, Tarun Kumar Sharma, Kalaga V. Madhav, Andrea Adami, Ettore Pedretti, Stefano Minardi, Lucas Labadie, and Roberto Osellame. Femtosecond laser writing of 3D polarization insensitive integrated devices for astrophotonics (Conference Presentation). In Peter R. Herman, Michel Meunier, and Roberto Osellame, editors, *Frontiers in Ultrafast Optics: Biomedical, Scientific, and Industrial Applications XX*, volume 11270. International Society for Optics and Photonics, SPIE, 2020.

[143] D. Marcuse. Gaussian approximation of the fundamental modes of graded-index fibers. *J. Opt. Soc. Am.*, 68(1):103–109, Jan 1978.

[144] Somenath Sarkar, K. Thyagarajan, and Arun Kumar. Gaussian approximation of the fundamental mode in single mode elliptic core fibers. *Optics Communications*, 49(3):178–183, 1984.

[145] A. Ankiewicz and G. . Peng. Generalized gaussian approximation for single-mode fibers. *Journal of Lightwave Technology*, 10(1):22–27, 1992.

[146] Frederik Michel Dekking, Cornelis Kraaikamp, Hendrik Paul Lopuhaä, and Ludolf Erwin Meester. *A Modern Introduction to Probability and Statistics: Understanding why and how*. Springer Science & Business Media, 2005.

[147] C-RED 2 data sheet. `https://www.first-light-imaging.com/wp-content/uploads/2019/02/Datasheet_C-RED-2_17.11.2020.pdf`.

[148] Rose K Gibson, Rebecca Oppenheimer, Christopher T Matthews, and Gautam Vasisht. Characterization of the c-red 2: a high-frame rate near-infrared camera. *Journal of Astronomical Telescopes, Instruments, and Systems*, 6(1):011002, 2019.

[149] Ettore Pedretti, S. Piacentini, G. Corrielli, Roberto Osellame, and Stefano Minardi. A six-apertures discrete beam combiners for J-band interferometry. In Michelle J. Creech-Eakman, Peter G. Tuthill, and Antoine Mérand, editors, *Optical and Infrared Interferometry and Imaging VI*, volume 10701, pages 316 – 325. International Society for Optics and Photonics, SPIE, 2018.

[150] François Reynaud and Hervé Lagorceix. Stabilization and control of a fiber array for the coherent transport of beams in a stellar interferometer. *Integrated Optics for Astronomical Interferometry*, page 115, 1997.

[151] HC Lefevre. Single-mode fibre fractional wave devices and polarisation controllers. *Electronics letters*, 16(20):778–780, 1980.

[152] Wesley A Traub. Polarization effects in stellar interferometers. In *European Southern Observatory Conference and Workshop Proceedings*, volume 29, pages 1029–1038, 1988.

[153] Lazareff, B., Le Bouquin, J.-B., and Berger, J.-P. A novel technique to control differential birefringence in optical interferometers - demonstration on the pionier-vlti instrument. *A & A*, 543:A31, 2012.

[154] Luís A. Fernandes, Jason R. Grenier, Peter R. Herman, J. Stewart Aitchison, and Paulo V. S. Marques. Femtosecond laser writing of waveguide retarders in fused silica for polarization control in optical circuits. *Opt. Express*, 19(19):18294–18301, Sep 2011.

[155] Luís A. Fernandes, Jason R. Grenier, Peter R. Herman, J. Stewart Aitchison, and Paulo V. S. Marques. Stress induced birefringence tuning in femtosecond laser fabricated waveguides in fused silica. *Opt. Express*, 20(22):24103–24114, Oct 2012.

[156] Abani Shankar Nayak, Tarun Kumar Sharma, Lucas Labadie, Simone Piacentini, Giacomo Corrielli, Roberto Osellame, Éric Gendron, Jean-Tristan M. Buey, Fanny Chemla, Mathieu Cohen, Nazim A. Bharmal, Lisa F. Bardou, Lazar Staykov, James Osborn, Timothy J. Morris, Ettore Pedretti, Aline N. Dinkelaker, Kalaga V. Madhav, and Martin M. Roth. First on-sky results with an interferometric discrete beam combiner (DBC) at the William Herschel Telescope. In Peter G. Tuthill, Antoine Mérand, and Stephanie Sallum, editors, *Optical and Infrared Interferometry and Imaging VII*, volume 11446, pages 360 – 372. International Society for Optics and Photonics, SPIE, 2020.

[157] Richard M. Myers, Zoltán Hubert, Timothy J. Morris, Eric Gendron, Nigel A. Dipper, Aglaé Kellerer, Stephen J. Goodsell, Gérard Rousset, Eddy Younger, Michel Marteaud, Alastair G. Basden, Fanny Chemla, C. Dani Guzman, Thierry Fusco, Deli Geng, Brice Le Roux, Mark A. Harrison, Andrew J. Longmore, Laura K. Young, Fabrice Vidal, and Alan H. Greenaway. CANARY: the on-sky NGS/LGS MOAO demonstrator for EAGLE. In Norbert Hubin, Claire E. Max, and Peter L. Wizinowich, editors, *Adaptive Optics Systems*, volume 7015, pages 52 – 60. International Society for Optics and Photonics, SPIE, 2008.

[158] Gendron, E., Vidal, F., Brangier, M., Morris, T., Hubert, Z., Basden, A., Rousset, G., Myers, R., Chemla, F., Longmore, A., Butterley, T., Dipper, N., Dunlop, C., Geng, D., Gratadour, D., Henry, D., Laporte, P., Looker, N., Perret, D., Sevin, A., Talbot, G., and Younger, E. Moao first on-sky demonstration with canary. *A & A*, 529:L2, 2011.

[159] E. Gendron, T. Morris, A. Basden, F. Vidal, D. Atkinson, U. Bitenc, T. Buey, F. Chemla, M. Cohen, C. Dickson, N. Dipper, P. Feautrier, J.-L. Gach, D. Gratadour, D. Henry, J.-M. Huet, C. Morel, S. Morris, R. Myers, J. Osborn, D. Perret, A. Reeves, G. Rousset, A. Sevin, E. Stadler, G. Talbot, S. Todd, and E. Younger. Final two-stage MOAO on-sky demonstration with CANARY. In Enrico Marchetti, Laird M. Close, and Jean-Pierre Véran, editors, *Adaptive Optics Systems V*, volume 9909, pages 126 – 142. International Society for Optics and Photonics, SPIE, 2016.

[160] Jan Tepper. *Towards high-resolution and high-contrast imaging in mid-infrared astronomy: Integrated optics beam combiners for astrointerferometry*. PhD thesis, Universität zu Köln, 2017.

[161] Philipp-Immanuel Dietrich, Robert J. Harris, Matthias Blaicher, Mark K. Corrigan, Tim J. Morris, Wolfgang Freude, Andreas Quirrenbach, and Christian Koos. Printed

freeform lens arrays on multi-core fibers for highly efficient coupling in astrophotonic systems. *Opt. Express*, 25(15):18288–18295, Jul 2017.

[162] Resolution test targets. `https://www.edmundoptics.eu/knowledge-center/application-notes/imaging/testing-and-targets/`.

[163] Momen Diab, Aline N Dinkelaker, John Davenport, Kalaga Madhav, and Martin M Roth. Starlight coupling through atmospheric turbulence into few-mode fibres and photonic lanterns in the presence of partial adaptive optics correction. *Monthly Notices of the Royal Astronomical Society*, 501(2):1557–1567, 12 2020.

[164] Andreas Stoll, Kalaga Madhav, and Martin Roth. Design, simulation and characterization of integrated photonic spectrographs for astronomy ii: low-aberration generation-ii awg devices with three stigmatic points. *Opt. Express*, 29(22):36226–36241, Oct 2021.

[165] ELT facility. `https://elt.eso.org/`.

[166] Aurel Ymeti, Johannes S. Kanger, Jan Greve, Paul V. Lambeck, Robert Wijn, and Rene G. Heideman. Realization of a multichannel integrated young interferometer chemical sensor. *Appl. Opt.*, 42(28):5649–5660, Oct 2003.

[167] James G. Titchener, Alexander S. Solntsev, and Andrey A. Sukhorukov. Two-photon tomography using on-chip quantum walks. *Opt. Lett.*, 41(17):4079–4082, Sep 2016.

[168] Gary H. Blackwood, Oliver P. Lay, William D. Deininger, MiMi A. Gudim, Asif Ahmed, Riley M. Duren, Charley Noecker, and Brian Barden. StarLight mission: a formation-flying stellar interferometer. In Michael Shao, editor, *Interferometry in Space*, volume 4852, pages 463 – 480. International Society for Optics and Photonics, SPIE, 2003.